EXPERIMENTAL STUDIES OF BUBBLE DOMAIN MATERIALS

by

Susan Jane Thornley

Thesis presented for the degree of
Doctor of Philosophy
University of Edinburgh

1975

PREFACE

This dissertation is not substantially the same as any that I have submitted for a degree or diploma or other qualification at any other University. The work described was done in the Department of Electrical Engineering, University of Edinburgh, between 1971 and 1974. I am grateful to the Science Research Council for the award of a Research Studentship.

I should like to thank Professor W.E.J. Farvis and Professor J.H. Collins for the provision of facilities in the Department of Electrical Engineering, and Dr A.D. Milne, my supervisor, for his guidance and the provision of facilities in the Wolfson Microelectronics Liaison Unit.

Thanks are also due to Mr F. Day who polished the slices and to Dr J.M. Owens, Dr J.D. Adam and Dr S.A. Mughal who grew the CVD and pure YIG LPE epitaxial films. Dr B. Jefferies of the Department of Geology kindly performed the microprobe measurements and Dr T. Page of the University of Cambridge performed the EDAX analysis.

Miss J. Clarke, who typed this thesis, successfully overcame the considerable challenge of my handwriting. Lastly, many thanks to my husband, Richard, for his support and a steady supply of chocolate biscuits.

SUMMARY

Measurements were made on synthetic garnets suitable for bubble domain devices. Defects in the substrate material and in epitaxial films were observed by x-ray topography and by optical techniques.

The following defects were found to have been formed during the growth of the substrate crystal: inclusions of iridium, growth bands, faceting and dislocations. The dislocations were found to be of two main types. In one type the dislocation line was straight and approximately parallel to the growth direction. In the other type the dislocation line was in the form of a helix. Very large helical dislocations, ~700 μm in diameter, were found and these had a helicoidal fault surface of impurity associated with them. Smaller helical dislocations, ~100 μm in diameter, were without this impurity surface.

The defects in the epitaxial films produced during the growth of the film were: variations in thickness, variations in composition, cracks, inclusions and, in one sample, misfit dislocations.

The defects already present in the substrate also affect the growing film. Dislocations propagate into the film, scratches left from poor surface preparation cause poor film growth. Variations in lattice parameter in growth bands and core produce a complementary variation in the film.

The effect of these defects on the magnetic properties, in particular bubble mobility, was investigated. Of the defects present, only growth banding produced little or no effect on the bubble properties. All other defects perturbed, and sometimes pinned, the bubble motion.

CONTENTS

C H A P T E R 1

INTRODUCTION

1.1 Magnetic Bubble Domains

A thin sheet of some ferro-or ferrimagnetic material may be obtained such that the uniaxial easy direction of magnetisation is normal to the plane of the sheet. A material of low saturation magnetisation and high magnetic anisotropy will cause the magnetic domains to have their magnetisation directed either 'up' or 'down' normal to the sheet. The domain walls are also normal to the sheet and extend from surface to surface. In the absence of an applied field the net magnetisation of the sheet will be approximately zero and thus the 'up' and 'down' domains will be of equal volume. Since the domains extend right through the sheet the 'up' and 'down' domains will occupy equal area on the surface of the slice. If the sheet has low anisotropy in its in-plane properties then the domains will form an irregular serpentine pattern. This domain configuration is illustrated in fig. 1.1.1.

Application of a D.C. magnetic field perpendicular to the surface of the magnetic plate will cause the domains having the same magnetic sense as the applied field to increase in volume. The domains of opposite magnetic sense will contract and may form right, circular cylinders normal to the plate. Such a cylindrical domain is known as a magnetic 'bubble' domain hereafter known as a bubble. Magnetic bubbles are shown in fig. 1.1.2.

An increase in the D.C. bias field will cause the bubbles to shrink until, ultimately, they collapse and the plate contains only a single domain. A decrease in

Domains in serpentine pattern.

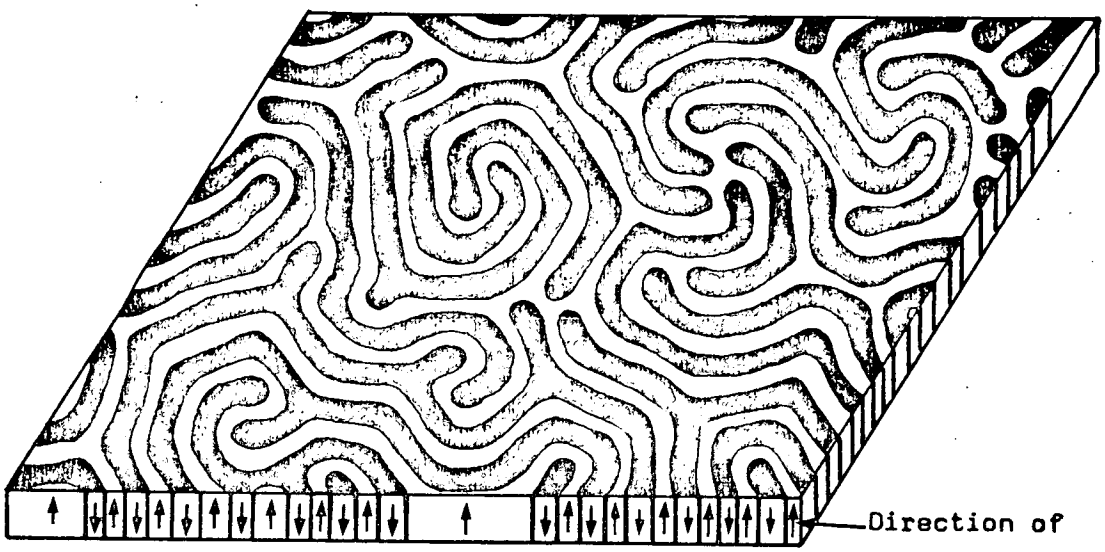

Figure 1.1.1

Magnetic 'bubble' domains.

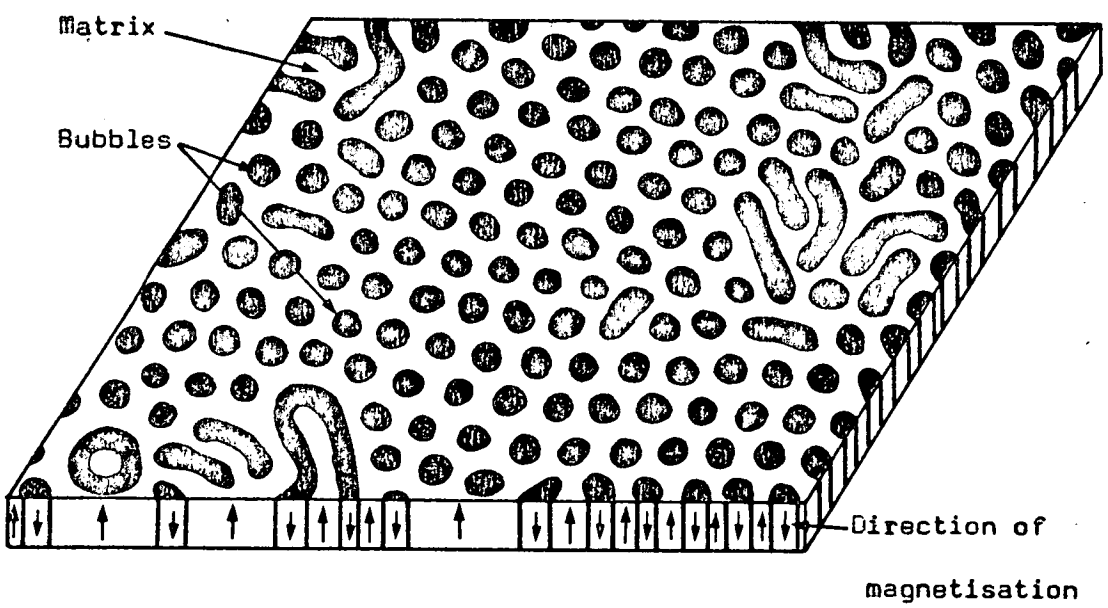

Figure 1.1.2

the bias field causes the bubbles to expand until they 'run out' into serpentine domains. The stability of bubbles in an applied field is discussed in chapter 4.1.

1.2 Bubble Domain Devices

The magnetic bubble can be made to move to a region of reduced field by the application of a field gradient. A bubble will undergo a mutual repulsion from other bubbles since they are magnetic dipoles. The magnetisation is perpendicular to the plane of the slice and so the bubble will be mobile in two dimensions and this allows its use in a memory device.(1)

A binary number may be represented by a string of bubble domains, the 'ones' represented by bubbles and the 'zeros' by absence of bubbles. This string may be propagated along a defined path at a particular velocity. The information is transmitted but there is no movement of the material of the device, only the domain walls move. Compare this with magnetic disc and tape store where the recording medium moves past a reading head. The bubbles are small, a few microns in diameter, and can move at velocities of several metres per second and so high data rates are possible. Logic can be performed on the binary data because of the interaction between bubbles and because of the two-dimensional nature of the store.

A brief description of the various types of element employed in a bubble domain device is given in the next two sections. This will provide a context and background to this work which investigates the effect of crystal

defects on magnetic bubble properties. A more detailed description and summary of bubble devices may be found in the book on magnetic bubbles by O'Dell,[2] and in that by others.[24]

The description below indicates the type of behaviour which is required from a bubble material.

1.3 Bubble Propagation

Several different approaches have been made to the problem of defining the track along which a bubble will move. For use in shift registers and memories the bubble should move in discrete steps at specified times, thus localised drive fields are needed.

1.3.1 Conductor loops

Field gradients can be created by current loops.[3],[4] Adjacent loops are energised with opposite currents such that one loop repels and the next loop attracts the bubble. If this circuit is used in conjunction with permalloy dots, the 'rest' position of the bubble is offset slightly with respect to the current loops and so directionality is obtained.

This type of circuit is fairly easy to design but it becomes difficult to fabricate the circuit for the small bubble sizes needed for a high data rate. The current needed to propagate the bubble may also be rather high.

1.3.2 Magnetic overlay patterns

A 'soft' magnetic material such as permalloy can be applied as a thin film in a defined pattern on the magnetic

sheet. The presence of the permalloy produces local variations in the magnetic field and the bubbles interact with these.

One approach is known as an angelfish circuit.[3] The bubble diameter is varied by modulating the bias field. Asymmetric energy traps are provided by wedge-shaped films of permalloy. The bubble will move in the direction of the points of the wedges. Changing from one track to another is not easy and the drive field operates at a fairly high power level.

A more common form of overlay has involved the interaction between the permalloy and a small, rotating, in-plane field. The T- and I-bar pattern is the archetype. This exploits the fact that a rectangle of permalloy will produce a much larger external field when the magnetisation lies along its length rather than its breadth. Other arrangements of permalloy, e.g. Y's,[6] X's,[7] etc. have been used to make corners and transfer between loops more reliable but the principle of propagation remains the same.

For large bubbles, ~15μm in diameter, conventional photolithographic techniques may be used to define the permalloy pattern. Bubbles of one micron size or less require a technique such as ion milling[8],[9] to define the pattern.

1.3.3 Local control of magnetisation

Propagation tracks on garnet films have been made by varying the local magnetisation on a fine scale.[10] A thin film of silicon is deposited in the desired pattern

and the crystal is annealed in oxygen or inert gas. The region of the crystal under the silicon has a large reduction in the saturation magnetisation. As a bias field is increased, the bubbles in the region under the silicon collapse first leaving bubbles in the required tracks. Propagation is obtained by means of current conductors. The advantage of this method of defining the track is that the magnetic layer remains planar after the track has been defined since the silicon may be removed after the anneal. This makes further processing easier.

1.3.4 Local change in thickness

A groove of approximately a half micron in width can be ion-milled in a magnetic bubble material and will locate the bubble at known positions.[11] A serpentine conductor is used for propagation which requires a rather high current and allows occasional errors in propagation.

A related means of locating bubbles, raised scalloped tracks, has been studied.[12] The bubble material is thinned by etching everywhere except for the track which is masked. Propagation is again by a serpentine conductor.

Both these methods are susceptible to difficulties in processing because the bubble material is non-planar.

1.4 Other Device Elements

1.4.1 Bubble generation

Two methods of bubble generation have been used separately and in conjunction. A bubble will be nucleated if a pulsed current is passed through a hairpin conductor.

The pulsed currents are rather large and this method would be unsuitable for a high rate of generation of bubbles.[3],[13] New bubbles are formed more readily by splitting them off from an existing bubble. This is particularly suitable for devices using permalloy tracks and a rotating field.[5] The generation can be controlled by a small current in a loop which will inhibit the transfer of a bubble onto the track.[14] For this bubble generator to work there must be a bubble already attached. This can be obtained by 'seeding' when necessary, which should be infrequently, by the use of the pulsed current through a hairpin conductor.[13]

1.4.2 Bubble replication and steering

A string of bubbles may be duplicated by splitting each bubble in two in a method similar to that of bubble generation. These strings of bubbles may be shifted to different tracks depending on the state of a conductor loop or the presence, or absence, of another bubble. This allows logic to be performed on the stored data.

1.4.3 Bubble annihilation

Bubbles may be destroyed by the reverse process to generation. They can be incorporated into a bubble held on a large block of permalloy or they may be collapsed by the application of a local field. The latter process may be a part of the detection of bubbles.

1.4.4 Bubble detection

An ideal sensor would detect the information without destroying it at a fast rate and giving a large signal.

Several types of non-destructive sensor have been designed for bubble devices.[15],[16]

1.4.4 (i) Magneto-optic detection

The presence or absence of a bubble is made to modulate the intensity of a beam of plane-polarised light which requires the material to have a large coefficient of Faraday rotation. No electrical contacts need be made to the device but difficulties may occur in getting the beam of light in and out of the package. The minimum size of domain which may be detected is limited by the wavelength of the light.

1.4.4 (ii) Hall effect and magneto-restrictive detectors

The two detectors employ the effect of the stray field of a bubble on the carriers in a semiconductor (Hall effect) or the change in resistance of a permalloy film (magneto-resistance). The signal for a magnetoresistive detector can be increased by stretching the bubble but without destroying it.

1.4.4 (iii) Inductive sensor

A destructive technique is by means of an inductive sensor.[14] The bubble is collapsed thus all the energy in the bubble can be detected instead of just the fraction detected by the Hall and magnetoresistive detectors. This produces a much larger signal. This method becomes effectively non-destructive if the bubble string is duplicated before detection, then the inductive sensor destroys

only the copy of the data.

1.5 Applications of Bubble Devices

A bubble memory would have a high bit density (10^6 bits per cm^2) and a good data rate (10^6 bits per sec) with the possibility of performing logic on the same chip. If the bias field required to maintain a stable bubble is supplied by a permanent magnet then the data will be retained even in the event of a power failure and re-starting is straightforward compared with disk and drum stores. The power required to drive the device is very low since it can be made as an integrated unit.

A major advantage, as mentioned previously, is the lack of moving parts which would give a higher reliability than, for example, tape store particularly in such applications as airborne computers and recorders.[17] The bubble memory is fairly compact and insensitive to radiation damage[18],[19] and by suitable choice of bubble and permanent magnet material, can operate over a wide range of temperature.

As well as very large stores for computer operation, either replacing disk and drum stores or as an intermediary between disk and core store, small stores, e.g. a repertory dialler for automatic dialling of telephone numbers, have been developed.[20] A bubble device has also been designed for use as a text-editing system which combines the use of large volumes of storage and logic.[21]

1.6 Experimental Studies of Bubble Domain Materials

The successful operation of a bubble domain device depends on a bubble being able to move readily on each part of the track, moving a fixed distance at each step, and not being allowed to escape from the track. This depends partly on good circuit design but local inhomogeneities may come from the bubble domain material itself and produce unwanted energy wells which may trap a bubble. This project was intended to find what inhomogeneities may occur, how they are formed, and which of them are particularly harmful to the propagation of bubble domains. The methods of preparation and choice of materials are examined in chapter 2. The defects in materials, with particular reference to garnets, are examined by x-ray and optical techniques and illustrated in chapters 5 and 6.

Static and dynamic magnetic properties and their correlation with particular defects are described in chapter 7.

C H A P T E R 2

BUBBLE MATERIALS

2.1 Introduction

For a thin film or plate of a magnetic material to contain stable cylindrical domains the easy direction of magnetisation must be normal to the plate and the uniaxial anisotropy field must be greater than $\mu_o M_s$.[22] This anisotropy can be due to the crystal structure as in non-cubic materials or it may be produced during growth.

Device applications require a high packing density of bits which implies a small bubble diameter. This means that the plate must be very thin since the bubble diameter depends directly on the thickness of the plate. The magnetic properties must be tailored to give the best stability and operation of the bubble device. The Curie temperature should be well above the operating temperature and the magnetic properties need to be reasonably independent of temperature over the range of ambient temperatures likely to be encountered.

There now follows a summary of some of the groups of materials used, or able, to support bubble domains.

2.2 Orthoferrites

Rare-earth orthoferrites were the first materials used for bubble domain devices since the growth technology was available. Orthoferrites are materials of the general formula R Fe O_3 where R is any rare earth or yttrium. They have an orthorhombic crystal structure with unit cell edges $a<b<c$. The magnetic structure is that of a canted antiferromagnet with the spin systems canted by approximately

half a degree. Except in Sm Fe O_3, where it is in the [100] direction, the uniaxial anisotropy axis at room temperature is along [001].

The crystals of orthoferrite are generally grown as bulk crystals by the flux method[23] and then sliced and polished to the required thickness of ~50μm. The bubble diameters in orthoferrites are rather too large for high storage densities and the compositions giving smaller bubbles are too temperature dependent.[3] The in-plane magnetic properties are not isotropic which affects the movement and shape of a bubble.

Thin slices are difficult to support, particularly during processing. Growth of a magnetic orthoferrite epitaxially on a substrate is difficult since two sets of lattice parameters must be matched.[25]

2.3 Hexagonal Ferrites and Ferromagnets

Materials such as (Sr, Ba, Pb) Fe_{12} O_{19} (magnetoplumbites) and Ba Fe_{18} O_{27} have the easy axis of magnetisation parallel to the hexagonal axis. Other hexagonal ferrimagnets can have the easy axis in the basal plane.

The room temperature values of μ_o M_s are large and so the bubbles are quite small, ~0.3μm. Substitution of Al for Fe in the magnetoplumbites reduces the saturation magnetisation and thus increases the size of the domains.[22] Difficulties are found in producing flux grown platelets of uniform coercive force and the bubble mobilities are rather low.[26]

Bubble domains have been observed by electron microscopy in thin films of cobalt [27],[28] and in cobalt-chromium alloys.[29]

2.4 Amorphous Materials

It is not necessary for a material to be a single crystal or even crystalline in order for there to be a magnetic easy axis. Metallic films, in particular Gd Co and Gd Fe, have been prepared by r.f. sputtering onto a variety of substrates such as glass, mica and Na Cl.[30],[31] The compositions can easily be tailored to give a wide range of bubble diameters with high mobilities. However, these materials are temperature sensitive and the film may crystallise under adverse conditions.

2.5 Cubic Materials - Garnets

The conditions of growth of a magnetic garnet platelet can induce an anisotropy sufficient for the plate to support bubbles, even though the material is nominally cubic. A detailed description of the garnet crystallographic and magnetic structure and methods of growth of the garnets is to be found in the following sections.

2.5.1 The garnet structure

The garnet structure was first established for the large group of silicates of the general composition $A_3 B_2 (SiO_4)_3$ and in particular for $Ca_3 Al_2 (SiO_4)_3$.[32],[33] The same cubic structure has been found for many complex oxides, and fluorides, with other elements replacing silicon, notably in the rare

earth and yttrium iron garnets, $R_3 Fe_2 (Fe O_4)_3$.

There are eight formula units in the body-centred cubic cell (Space group Ia3d, no. 230 in the International Tables for X-ray Crystallography)[34] and the cell edge is about 12Å for all these garnets. The atomic positions are described in detail for $Y_3 Fe_2 (Fe O_4)_3$, YIG, by Wyckoff.[35]

The yttrium or rare earth atoms are in 24(c) sites[34],[35] in an eight-fold coordination group with oxygen, two of the five iron atoms in the formula unit are in 16(a) sites octahedrally surrounded by oxygen and the remaining three iron atoms are on 24(d) tetrahedrally surrounded sites. The oxygen atoms are in general positions. Figure 2.5.1 compares a photograph of a model of the garnet structure [36] with a diagram showing the three types of coordination polyhedra.

There is a negative superexchange (antiferromagnetic) interaction between the Fe^{3+} ions on the (a) and (d) sites through the intermediate oxygens and thus in YIG there is a net magnetic moment of $5\mu_B$ per formula unit. If non-magnetic ions are substituted for iron then the net moment will be altered by changing the relative number of magnetic ions in octahedral and tetrahedral sites. A non-magnetic substituting M^{3+} ion will predominately occupy an octahedral (a) site if it is larger than Fe^{3+} and thus increase the magnetic moment, and if it is smaller than Fe^{3+} it will occupy the tetrahedral (d) sites and thus reduce the net magnetic moment.[37] For some ions such as Ga^{3+} and Al^{3+} there is a complete range of solid solution. Cr^{3+} will substitute for Fe^{3+} in the octahedral site to a limited

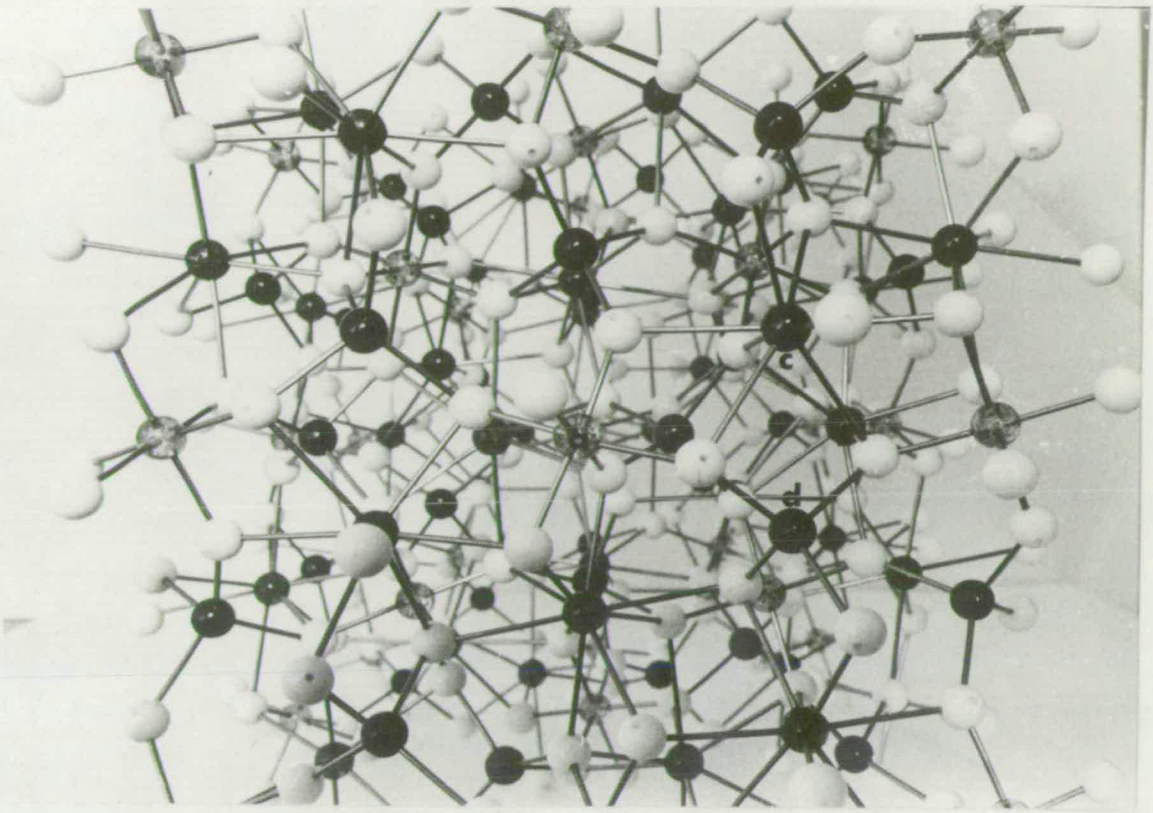

Model of one unit cell of the garnet structure, viewed along a cube axis.

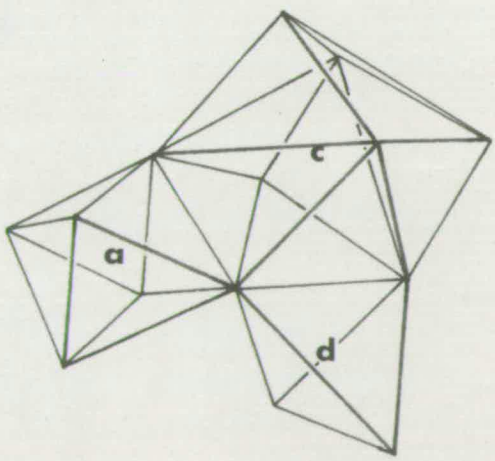

Oxygen coordination of the a, c and d sites.

Figure 2.5.1

extent even though it is smaller.

The magnetostriction coefficients can be adjusted by substituting rare earth ions in the (c) sites.[26] By a suitable combination of rare earths the magnetostriction coefficients can be reduced to zero in order to reduce coercivity. The lattice parameter will also change and will vary approximately linearly with composition. Not all rare earths can be substituted. An iron garnet is not formed with the rare earths La, Ce, Pr, Nd and gallium garnets are not formed with La, Ce, Pr, Nd, Sm and Eu.[38]

The magnetic rare earth ions are coupled to the resultant moment of the two Fe sublattices by antiparallel exchange forces which are weak compared to the forces between the Fe ions. Complete ordering will be found at absolute zero with the moments of the (d) site ions directed in one direction, along <111>, and the moments of the (a) and (c) site ions in the opposite direction.

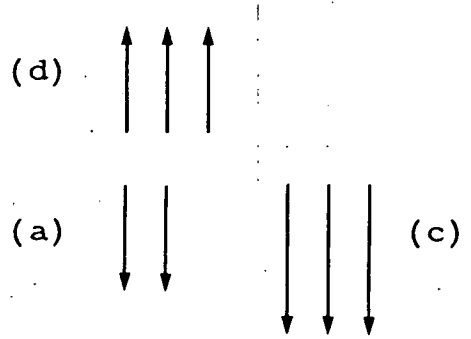

Gadolinium, terbium, dysprosium, holmium and technetium ions all have large moments compared to the Fe^{3+} ion thus near absolute zero the spontaneous magnetisation of these garnets should be predominantly due to the rare earth elements. Lutetium and yttrium ions have zero moment so the spontaneous magnetisation for these two garnets must be due

to the Fe^{3+} ions alone. Ytterbium has a moment equal to Fe^{3+}.

As the temperature is increased the alignment of the rare earth ions decreases rapidly since the antiparallel coupling to the iron ions is weak. Close to the Curie temperature the magnetic properties are due to the iron ions since the rare earth ions contribute very little. The Curie points are determined almost entirely by the interactions between the Fe^{3+} ions on the (a) and (d) sublattices and since these interactions must be the same for all rare earth iron garnets they will all have a similar Curie point at $\sim 560^{o}K$.

A garnet for which the rare earth moment is large must show a 'compensation temperature' at which the rare earth sublattice is sufficiently disordered for its magnetisation to be equalled by the oppositely directed net moment of the iron sublattices.[39] This behaviour is important if variations in temperature are not to produce large changes in magnetisation. A composition for which the operating temperature is near the compensation temperature should not be chosen. Garnets have a much lower sensitivity to temperature changes than the orthoferrites.[40]

2.5.2 Bulk growth of magnetic garnets

The growth of orthoferrites from a lead oxide flux was first demonstrated by Remeika.[23] The magnetic garnets consist of the same components as the orthoferrites and it was suggested[41] that a lead oxide flux would also be suitable for the growth of garnets. YIG was the first

garnet grown by this method. To produce larger, more perfect crystals of YIG certain modifications were made to the method of growth and Pb F_2 was added to the flux to lower the viscosity of the melt.

Garnets suitable for bubble domain devices were grown by the flux method.[26] These crystals grow with {211} and {110} habit planes. These planes have the closest packing of atoms in the crystal structure and thus <211> and <110> are the slowest growth directions. <111> is a fast growth direction and so no {111} facets are formed. This morphology is also found in natural garnets. It was found[26] that if the growth sectors under {211} facets were sliced along particular {111} planes then there will be a uniaxial magnetic easy axis perpendicular to the plate. For garnets such as $Er_1\ Tb_1\ Al_{1.1}\ Fe_{3.9}\ O_{12}$ and $Gd_{0.94}\ Tb_{0.75}\ Er_{1.31}\ Al_{0.5}\ Fe_{4.5}\ O_{12}$,a 'Type 1' cut, where the slices are perpendicular to the <111> axis nearest perpendicular to the {211} facet plane, is needed. A 'Type 2' cut is required for $Gd_{2.31}\ Tb_{0.60}\ Eu_{0.09}\ Fe_5\ O_{12}$, where the slices are perpendicular to the {211} facet and to the <111> direction in that facet.

A cubic crystal should have all <111> directions equivalent so parts of these crystals are not exactly cubic. An ordering of the rare earth atoms during growth will lead to a rhombohedral distortion.[42],[43],[44]

To produce small bubbles thin platelets have to be cut and polished on both sides as in the case of the orthoferrites. This leads to difficulties in preparation in handling, especially during processing. Crystals grown

by this method are liable to flux inclusions and variations in composition and thus variations in magnetic properties. Large uniform platelets are difficult to produce.

2.6 Epitaxy

The problem of supporting a thin magnetic platelet can be overcome by growing a magnetic film on a non-magnetic substrate. The garnet system is particularly well-suited to this as there is a large range of possible compositions for the substrate and for the film. The lattice parameters can be controlled and a single crystal film can be grown in the same orientation as the substrate and without cracks or misfit dislocations.

The following sections discuss some of the criteria for choosing the composition of film and substrate and the method of growth of the substrate material.

2.6.1 Choice of substrate/film compositions

The choice of composition of the magnetic garnet to control the magnetisation and magnetostriction has already been discussed. This section describes the control over lattice parameter mismatch between substrate and film and also the effect of thermal expansion.

It might be expected that epitaxial growth of two different garnets would be easiest if the lattice parameters were the same. A large mismatch, where the film has a smaller lattice parameter, would lead to tensile stresses in the film. The film would crack if the film thickness were greater than the length of the Griffith

half-crack.[45] In some cases a small amount of tension is employed in the film to produce a uniaxial easy axis normal to the film using the magnetostriction effect[46] when there is little, or no, growth induced anisotropy.[47] Growth induced anisotropy can be modified by annealing[48] or ion-implantation.[49]

The rare-earth gallium garnets (non-magnetic) have lattice parameters which span those of the iron garnets (magnetic) and so are suitable for use as substrate materials. Data[35] on the lattice parameters of flux-grown garnets is given in table 2.6.1. Garnets grown by other means may not grow exactly stoichiometric and thus the lattice parameters will differ slightly.[50]

The lattice parameters of the substrate and/or the film could be adjusted by suitable mixtures of rare earths to differ by less than 0.01Å.[26] In practice it is more convenient to choose one, or possibly two compositions of substrate and tailor the film composition to match. For film compositions based on YIG the best substrate to use is gadolinium gallium garnet (GGG)[51] and this is the material which has been most used as a substrate, although some have been used with Dy substituting partially or completely for Gd.

Non-Magnetic Garnets		Ferri-Magnetic Garnets	
Composition	a Å	Composition	a Å
$Dy_3 Ga_5 O_{12}$	12.307	$Dy_3 Fe_5 O_{12}$	12.414
$Er_3 Ga_5 O_{12}$	12.255	$Er_3 Fe_5 O_{12}$	12.349
$Eu_3 Ga_5 O_{12}$	12.401	$Eu_3 Fe_5 O_{12}$	12.498
$Gd_3 Ga_5 O_{12}$	12.376	$Gd_3 Fe_5 O_{12}$	12.44
$Lu_3 Ga_5 O_{12}$	12.183	$Lu_3 Fe_5 O_{12}$	12.277
$Nd_3 Ga_5 O_{12}$	12.506	$Nd_3 Fe_5 O_{12}$	12.60
$Y_3 Ga_5 O_{12}$	12.277	$Y_3 Fe_5 O_{12}$	12.376
$Yb_3 Ga_5 O_{12}$	12.200	$Tb_3 Fe_5 O_{12}$	12.447
$Sm_3 Ga_5 O_{12}$	12.432	$Sm_3 Fe_5 O_{12}$	12.530

TABLE 2.6.1

The above discussion has considered the lattice parameters at room temperature. The film growth takes place at elevated temperatures, $\sim 900^{\circ}C$, and so the thermal expansions of substrate and film should also be matched.[52] The match is not too good for thick films of gallium substituted YIG (Ga:YIG) if the gallium content is high and the substrate is GGG but is quite good for YIG and rare earth iron garnet films and GGG substrate.

A substrate material which is transparent in the visible range of wavelengths is to be preferred since the magnetic films are absorbing and a transparent substrate makes optical examination easier. Thus, of the gallium garnets, gadolinium would be preferred to dysprosium gallium garnet.

2.6.2 Growth of substrate material

The rare earth gallium garnets are congruent melting compounds and thus are suitable for growth by the Czochralski technique. The growth of these, and in particular GGG, has been reported by several authors.[53],[54],[55],[56] In all cases a mixture of high purity, dry, rare earth and gallium oxides, in proportions near to the stoichiometric ratio, are melted in an iridium crucible under a controlled atmosphere of nitrogen or nitrogen/oxygen. The particular compositions of starting material and atmosphere needed for optimum growth seem to depend on the particular furnace configuration. An iridium crucible is used since iridium has a melting point of 2455^{o}C, the garnet melt of approximately 1700^{o}C and platinum a melting point of 1769^{o}C. A seed crystal of the required orientation is dipped into the melt and withdrawn slowly while being rotated. The quality of the crystal depends on the rotation and pulling rates and on the temperature gradients in the melt. The types of defect which are formed are illustrated in chapter 5.

Single rare earth garnets can be grown quickly but solid solutions of mixed rare earth garnets must be grown slowly to avoid constitutional supercooling and segregation of the components.

2.7 Growth of Epitaxial Films

2.7.1 Liquid Phase Epitaxy (LPE)

YIG was grown as epitaxial thin films from a solvent melt using a tipping technique by which the melt was made

to flow over the substrates.[57] This demonstrated that YIG would grow epitaxially on GGG but there was difficulty in producing a smooth film unless there was a low growth temperature, high growth rate and low lattice parameter mismatch.[58] Melts of the B_2O_3 - PbO - garnet system can be supersaturated with respect to garnet and remain stable without spontaneous nucleation of the garnet.[59] A substrate dipped in the supercooled melt will allow growth of the garnet on the substrate but nowhere else. This process can be repeated many times and the films deposited in a well-controlled, isothermal zone of the furnace. The crystal phase deposited depends on the $B_2O_3/PbO/RO_3/Fe_2O_3$ compositions and on the lattice parameter of the substrate.[60]

The apparatus of Levinstein was modified by several workers to allow the rotation of a horizontal sample in the horizontal plane. The kinetics of growth have been investigated for various compositions, supersaturations, rates of rotation and times of growth.[61],[62],[63],[64] The growth rate increases approximately linearly with the undercooling and increases as the square root of the rotation rate. The rotated samples reach a steady state of constant growth rate fairly quickly but this is not reached for zero rotation. The film composition will depend on the growth rate and also slightly on the film thickness, particularly if the melt is of small mass. Some lead may also be incorporated from the flux, especially at high rates of growth.[62],[65] Lead-free fluxes have been tried[66],[67] such as BaO - BaF_2 - B_2O_3 but these tend to

LPE apparatus

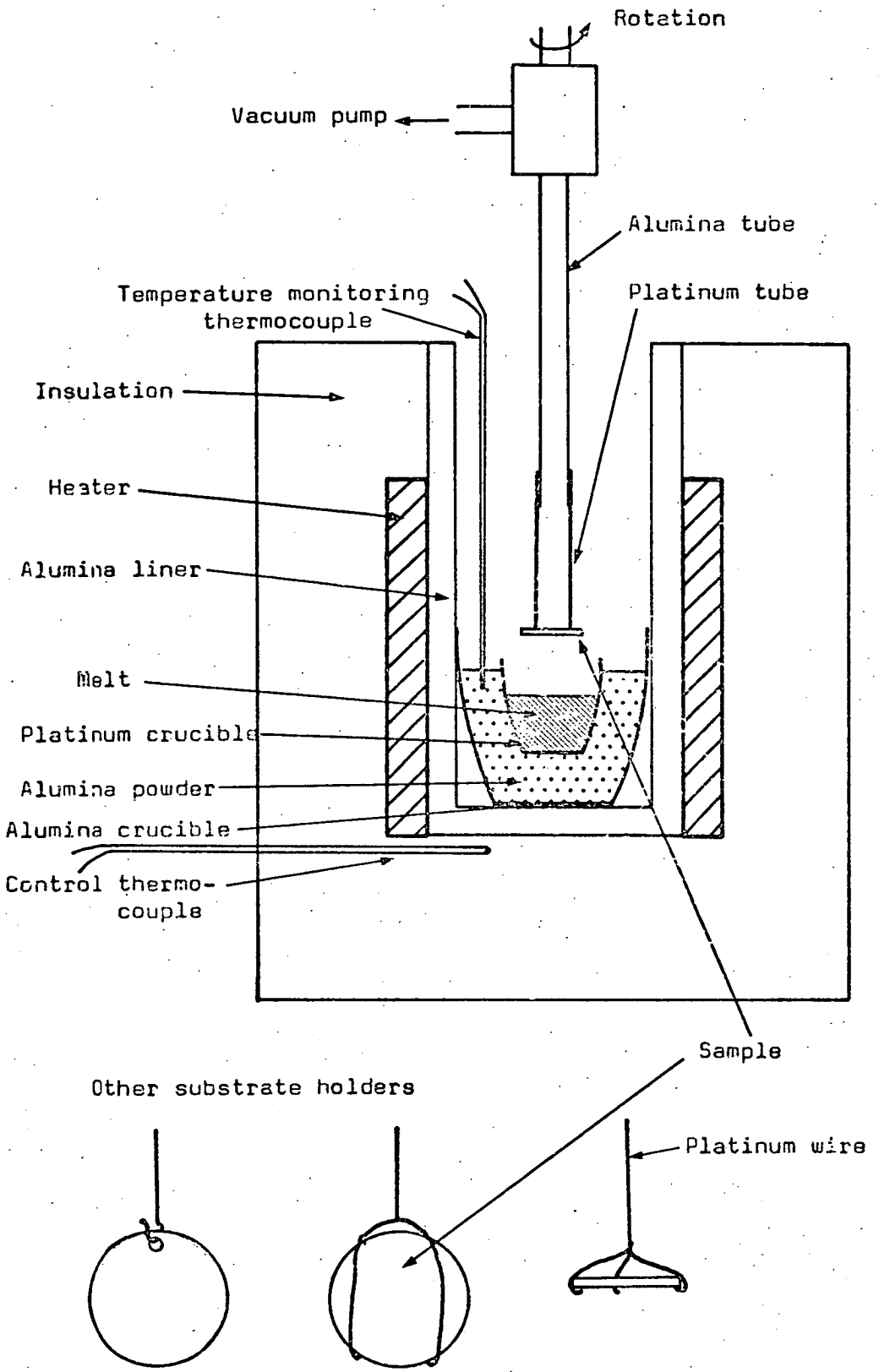

Figure 2.7.1

have rather a high viscosity and be retained on the substrate and cause pitting. It has been shown that the undercooling is the most important parameter to control to produce reproducible thickness and composition of films.

Figure 2.7.1 shows a diagram of the LPE apparatus used in the work on bubbles at Edinburgh University. The melt is held in a 75 ml platinum crucible supported in an alumina crucible packed with powdered alumina. The temperature is monitored by a Pt/Pt-Rh thermocouple.

The original design of substrate holder held the substrate either vertically or horizontally using platinum wire clips. The entire substrate was submerged and so a film would grow on both sides making optical examination of the domain pattern more difficult and depleting the melt more quickly. The clips also tend to trap drops of the melt when the sample is withdrawn. A platinum vacuum chuck was a later design which held the substrate horizontal. The substrate could not be submerged in the melt and film growth takes place with the substrate on the surface of the melt and rotated at 50-300 rpm. The film is spun 'dry' on removal from the melt by rotating the sample at a high rate. This technique has grown films on substrates up to 3 cm in diameter and the thickness of the film from one to 100 μm. The various compositions of melt used to grow epitaxial garnet films in this furnace are given in Table 2.7.1

A typical procedure for growing a bubble film is as follows: The melt is heated to 1100°C and allowed to come

Material	Melt Composition, grm.	
$Er_2Eu_1Ga_{0.7}Fe_{4.3}O_{12}$	Er_2O_3	1.35
	Eu_2O_3	0.63
	Fe_2O_3	10.00
	Ga_2O_3	0.9
	B_2O_3	2.86
	Pb O	140.00
$Y_3Fe_5O_{12}$	Y_2O_3	1.13
	Fe_2O_3	11.5
	B_2O_3	2.8
	Pb O	190.00
$Sm_{0.25}Y_{2.75}Ga_1Fe_4O_{12}$	Sm_2O_3	0.25
	Y_2O_3	1.4
	Ga_2O_3	1.7
	Fe_2O_3	10.00
	B_2O_3	2.8
	Pb O	140.0
$Gd_3Ga_5O_{12}$	Ga_2O_3	2.93
	Gd_2O_3	2.85
	B_2O_3	2.45
	Pb O	91.77

TABLE 2.7.1

to equilibrium. The temperature is then reduced to ~950°C at which the supersaturated melt is fairly stable. The sample is lowered slowly into the furnace to minimise the effects of thermal shock and lowered down to the surface of the melt. The descent is halted when a meniscus is formed. The sample is rotated slowly during growth. At the end of the required growth time the sample is raised to just above the surface of the melt and then spun at very high speed to remove any retained flux. The sample is removed slowly from the furnace and when the sample is completely cooled any remaining flux is removed with glacial acetic acid.

2.7.2 Chemical Vapour Deposition (CVD)

The epitaxial growth of metal oxides by vapour transport has been studied in open and closed systems for many years. An open system is better for bubble materials since uniformity is important and may be obtained by a constant replenishment of the reactants. In crystal growth of metal oxide films from the vapour phase the constituents of the desired compound are transported separately in a gaseous form to the deposition zone where the vapours mix and react at a substrate surface and form the required solid phase. The metallic elements are usually transported as volatile chlorides or other halides and then react with oxygen and/or water vapour. The reaction is moderated by excess of either HCl or Cl_2.

The overall reaction for YIG may be written:

$$3YCl_3\,(g) + 5FeCl_2\,(g) + \frac{19}{2}\,H_2O\,(g) + \frac{5}{4}\,O_2\,(g) \xrightarrow{\text{substrate}} Y_3Fe_5O_{12}\,(s) + 19HCl\,(g)$$

Other components such as rare earths or gallium may also be included to produce a bubble domain film.

Depending on the gas flow conditions and the concentrations of the various constituents, other compounds may be produced in the reactor. These compounds include Y_2O_3, $YFeO_3$, $Y_3Fe_5O_{12}$, Fe_2O_3, Fe_3O_4 in the case where YIG is required. The order of appearance in the direction of gas flow is well-defined and occurs as follows: Y_2O_3 white, $YFeO_3$ red, $Y_3Fe_5O_{12}$ yellowish-green, Fe_2O_3 red. The position and extent of each zone can be varied by altering the gas flow rates and chloride concentrations. Vertical T-reactors [68] and horizontal, concentric-tube reactors [69],[70] have been used, the principles of operation are the same in each.

The reactor used here was of the horizontal concentric tube type and is shown in the diagram in fig. 2.7.2. The reactor tubes were of fused quartz. There were three independently controlled metal chloride source zones since only YIG or Ga:YIG was grown in this reactor. The iron and yttrium chlorides were contained in silica crucibles; the gallium metal crucible, in a different tube of the furnace because of the low boiling point of $GaCl_3$, was divided into sections to prevent the gallium metal remaining as a single drop. The gallium concentration in the garnet depends on the HCl flow over the gallium metal. The crucibles were loaded into the inner tubes using a drybox to prevent contamination by moisture since oxychlorides will float on the surface of the melt and make evaporation

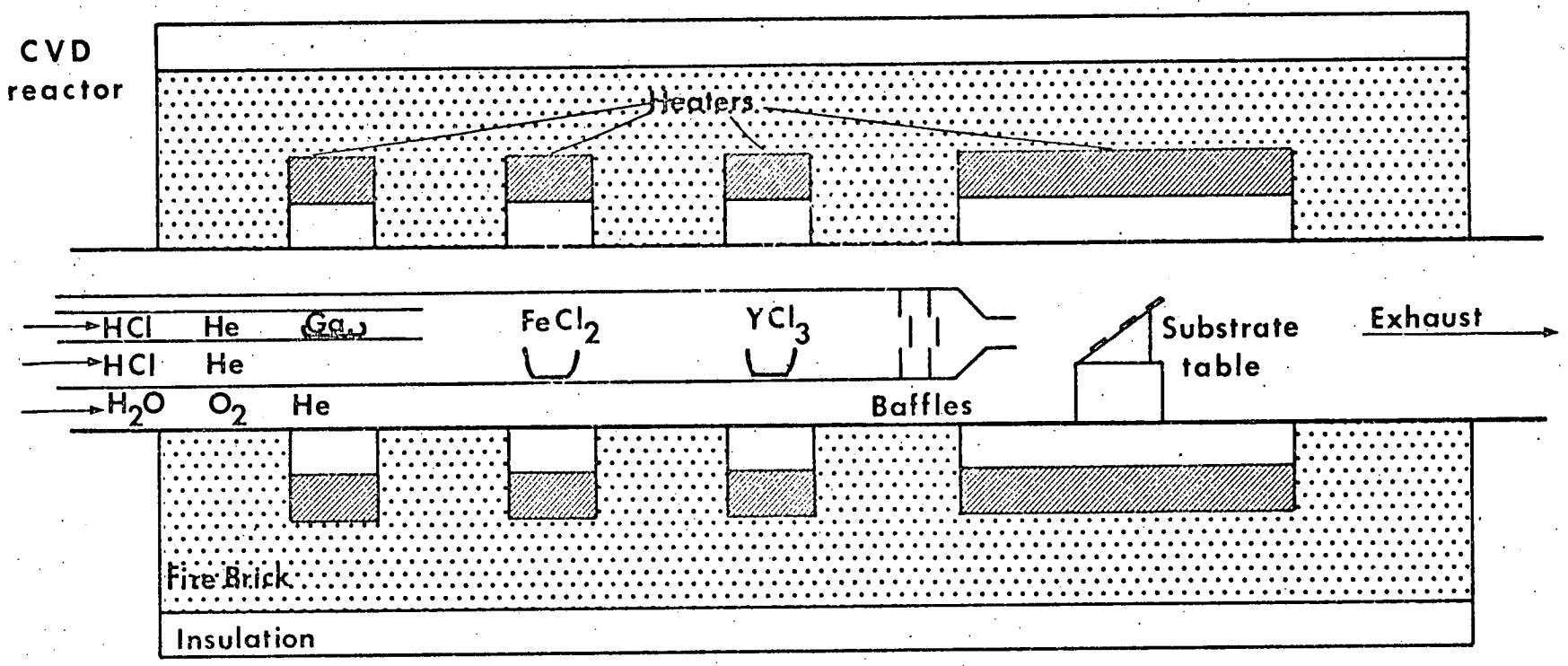
CVD
reactor
Heaters
HCl He Ga
HCl He
H2O O2 He
FeCl2
YCl3
Baffles
Substrate
table
Exhaust
Fire Brick
Insulation

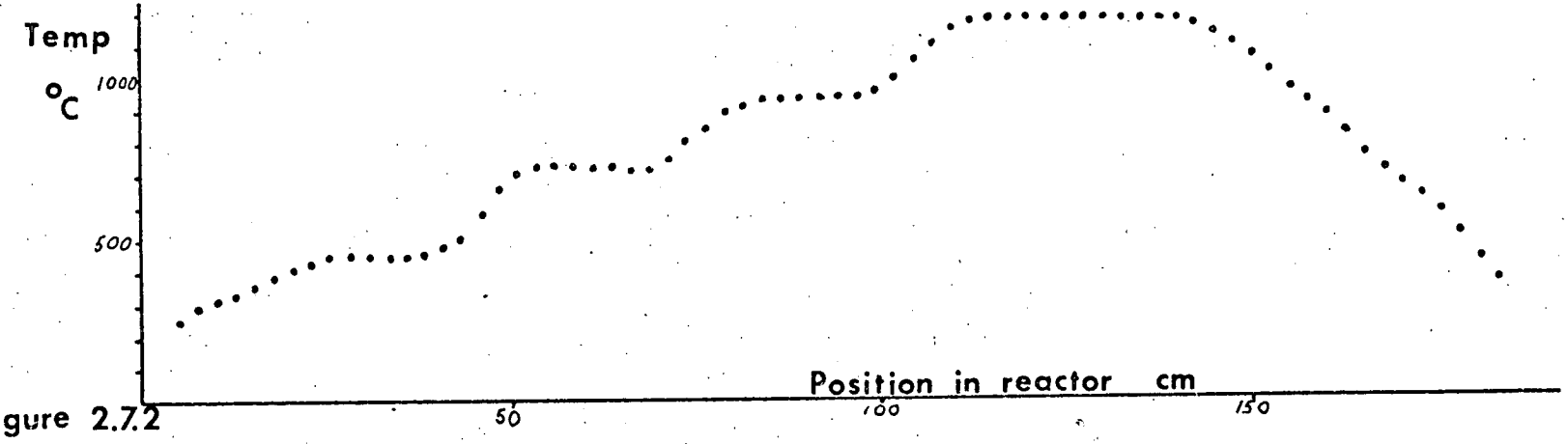
Temp
°C
1000
500
Position in reactor cm
50
100
150

Figure 2.7.2

difficult.

The chloride vapours are swept along by helium carrier gas and mixed as they pass through the baffles. Oxygen or water vapour is introduced in the outer tube and mixes with the chloride vapours under laminar flow conditions. The metal oxides are deposited downstream. HCl is added to the inner tube gas flow to moderate the reaction rate. Adjustment of the various gas flows allows optimisation of the growth of iron garnets.

2.8 Magnetic Anisotropy

There are three basic components of uniaxial anisotropy in garnets. These are magnetocrystalline anisotropy, growth induced anisotropy and anisotropy induced by strain. All three types operate in LPE films but there is no growth induced anisotropy in CVD films.

The growth induced anisotropy is similar to that found in bulk garnets[47] and particularly occurs when there is more than one rare-earth ion and there is an ordering occurring in the occupation of the dodecahedral sites by these ions. The greater the difference of radius of the two rare earth ions and the lower the growth temperature, the greater will be the growth induced anisotropy. This anisotropy can be removed by annealing the sample at 1200°C[60] CVD films are grown at ~1200°C and so any growth induced anisotropy is annealed out during growth.

The stress in a thin, uniformly strained film depends on the lattice parameter mismatch, thermal expansion

coefficients and degree of stress relief by the formation of dislocations.[60],[71],[72] These quantities are linked by the following relation:

$$\sigma_o = \left\{ (1-\eta) \left(\frac{a_s - a_f}{a_f} \right) + \eta (\alpha_s - \alpha_f) \Delta T \right\} \frac{E}{1-\mu} \quad (60)$$

where η is the fractional stress relief and a_s and a_f are the room temperature lattice parameters of substrate and film respectively. α_s and α_f are the linear expansion coefficients.* The stress induced anisotropy for <111> oriented films is directly proportional to the stress and to the coefficient of magnetostriction, λ_{111}.[60] The mismatch and λ_{111} can be tailored by appropriate choice of rare earth.

It is difficult to form dislocations in garnets because the lattice parameter is so large and so a film in tension is more likely to crack than relieve the stress by misfit dislocations. This means that, except in exceptional circumstances, the degree of stress relief, η, will be zero.

An unstrained magnetic garnet has its easy directions of magnetisation along <111> and the hard directions along <100> due to the magnetocrystalline anisotropy. The effect of this anisotropy is generally small compared with the growth and strain induced anisotropies.

* E = Young's modulus, μ = Poisson's ratio
ΔT = Growth temp. - Room temp.

2.9 Preparation of Substrates

Boules grown by the Czochralski technique in <111> orientation were bought from various suppliers. They were oriented accurately on <111> by x-ray techniques and

sliced into wafers 0.75 mm thick using a Capco high speed diamond saw. The saw damage was removed by grinding the wafers with successively finer grades of carborundum powder mixed into a slurry with water. The final polish was chemical/mechanical using twice-filtered alkaline colloidal silica (Syton by Monsanto) on a vibratory polisher. The polishing pad was of polypropylene. The reasons for this particular choice of procedure are given in chapter 5.

A quick method of producing a damage-free, but not very smooth, surface is by dissolving some of the crystal in hot orthophosphoric acid at about 300°C.[73],[74],[75] There is a danger that the slice will crack due to thermal shock.

CHAPTER 3

X-RAY AND OPTICAL TECHNIQUES

3.1 X-Ray Topography

This section describes the apparatus and experimental techniques used to determine the distribution of strain in garnet crystals. There are several topographic techniques available for mapping defects in crystals.[76] The choice of technique depends on the degree of sensitivity to strain that is required and on the degree of perfection of the crystal. For example, a very sensitive technique would be wasted on a crystal with a high density of dislocations since the dislocation image is large and the various images would overlap. This sensitivity would, however, be required to detect small composition fluctuations in an otherwise perfect crystal.

Two topographic techniques, Lang[77],[78],[79],[80] and Double Crystal,[81] are described here. Both techniques employ the fact that a perfect crystal will produce a uniform diffracted beam if the incident beam is uniform but a crystal with defects will give local variations in the diffracted intensity. Details of experimental procedure are given for the apparatus used here.

3.1.1 Lang topography

The x-ray beam from a fine-focus (point) source is collimated to a ribbon beam by narrow slits of tantalum at 50 cm from the source. The width of the slit is such that when the crystal is set in the diffracting position for a particular characteristic wavelength then no other wavelength will diffract. As the crystal is rotated $k\alpha_1$ and $k\alpha_2$ radiations will diffract at different angular positions

of the crystal. Figure 3.1.1 shows the crystal set such that the diffracted beam is transmitted through the crystal. The diffracted ribbon passes through another slit which prevents either the direct beam or air-scattered radiation reaching the photographic plate. The plate is set normal to the diffracted beam since the emulsion on the plate is thick and oblique incidence would reduce the resolution. The sample and photographic plate are scanned together to give complete coverage of the crystal.

The second set of slits is fixed in space so the position of the diffracted beam is defined. If the diffracted beam is to reach the photographic plate at all parts of the scan then the plane of the crystal slice must be parallel to the direction of traverse. The line of intersection of the incident beam with the crystal surface should be normal to the beam direction to avoid the need to tilt the second set of slits.

Rare-earth garnets combine the problems of a large lattice parameter, a structure which leads to a large number of systematic absences or weak reflections and a very large absorption coefficient for x-rays. This last is the main difficulty for transmission topography. The linear absorption coefficients for the characteristic wavelengths used most often in crystallography are as follows:

	μ cm^{-1}
Ag kα	190
Mo kα	360
Cu kα	1600

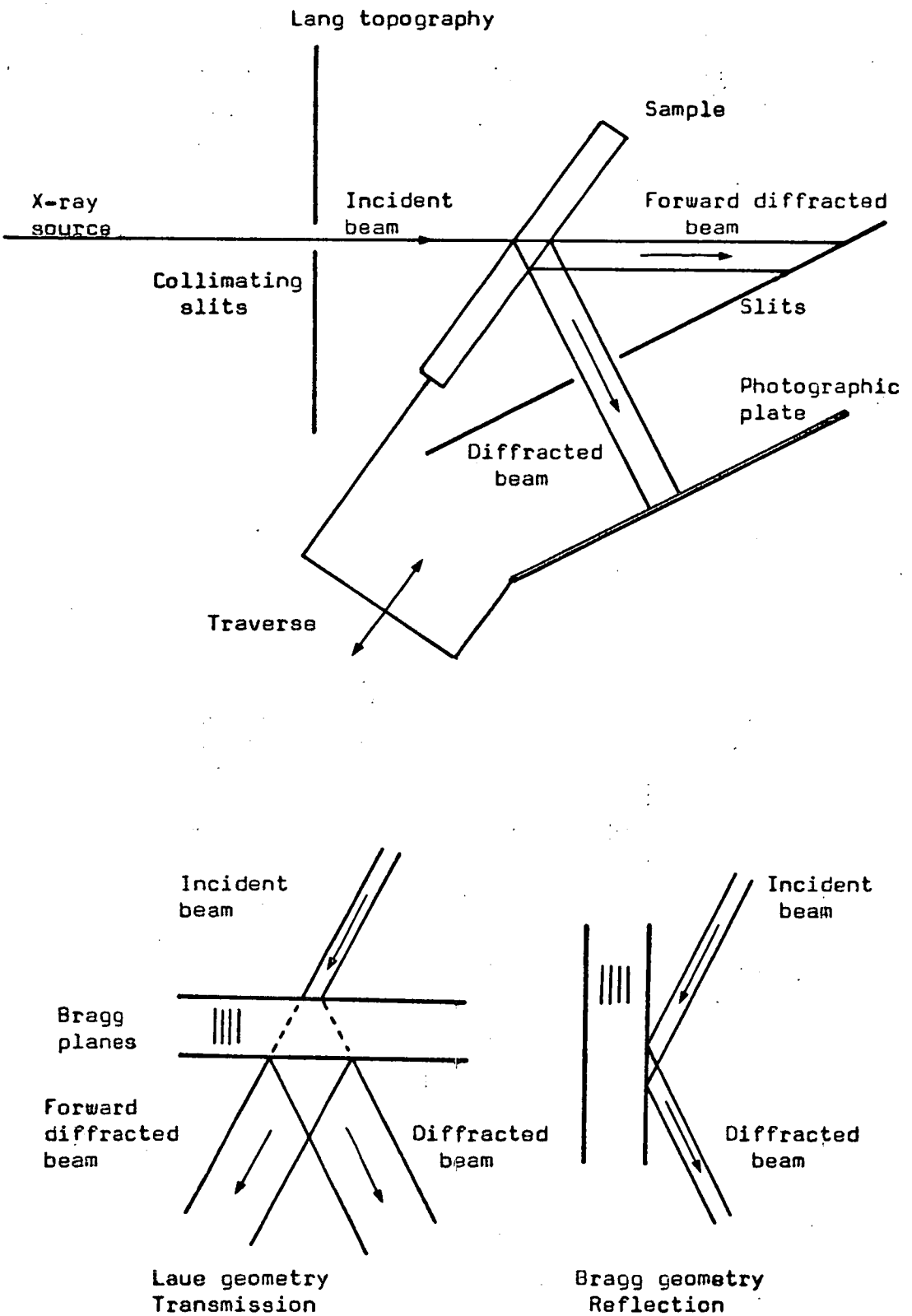
Lang topography
Sample
X-ray source
Incident beam
Forward diffracted beam
Collimating slits
Slits
Photographic plate
Diffracted beam
Traverse
Incident beam
Bragg planes
Forward diffracted beam
Diffracted beam
Laue geometry
Transmission
Incident beam
Diffracted beam
Bragg geometry
Reflection

Figure 3.1.1

These figures are for GGG but would be similar for other rare earth garnets. A sample would have to be 100 μm or less in thickness for there to be low absorption, even using the most penetrating radiation, Ag kα. A thin sample with two damage-free surfaces is required and can be prepared by grinding with carborundum and polishing with Syton or by etching in hot phosphoric acid, as described in section 2.9. The former method is to be preferred since variations in thickness produce changes in transmitted x-ray intensity because of absorption. Such thin slices are difficult to handle and so were mounted inside a large, non-metallic washer with small pieces of adhesive wax.

This technique is useful for determining the type of defects present in the substrate material, but it is not suitable for the examination of films ~5 μm in thickness nor for routine examination since such a thin slice is of no use for crystal growth. This apparatus can be used in a slightly different geometry to overcome this. The diffracted beam is 'reflected' off the surface of the crystal which can be a thick slice with, or without, a film. The difference between the two geometries is shown in fig. 3.1.1. The film and substrate have different lattice parameters and so the film and substrate will diffract for different angular positions of the sample[82] thus separate topographs of the film and substrate can be obtained. The higher the Bragg angle used the better the angular resolution between film and substrate peaks, and

this will also minimise the distortion of the crystal image, particularly if Bragg planes not parallel to the surface are used. The large lattice parameter for garnets means that a long wavelength radiation, e.g. Cu kα and/or a high order reflection must be used. This is likely to mean a rather lower diffracted intensity. This problem does not arise for the transmission geometry since a low Bragg angle is required to minimise distortion. This is obtained from low order reflections and a short wavelength. The minimum distortion occurs when the diffracted beam is normal to the crystal slice. Some of the reflections used for a (111) slice in transmission and in reflection are listed in table 3.1.1.

In the reflection geometry only a few microns depth of the crystal is sampled, thus only a short segment of a dislocation line running normal to the slice would go towards forming the image. In transmission the whole of the dislocation would form an image, thus making detection easier. Scattered radiation is more troublesome in the reflection case and tends to reduce contrast. Small variations in lattice parameter are rather difficult to detect because the change in Bragg angle is small compared to the divergence of the incident beam. Reflection topographs are useful in that they are non-destructive and films can be examined in situ. To increase the resolution of defects and lattice parameter mismatch double crystal topography is used.

Reflection	Geometry	Angle between diffracted beam and {111} surface Degrees	Structure Factor F
16 16 16*	R	52.55	781
8 8 8	R	59.55	1305
8 8 0	R	80.0	1476
8 8 0†	T	75.19	1476
8 8 0†	T	54.8	1476
12 4 4	R	85.1	880
12 4 4†	T	75.9	880
8 6 4	R	57.2	830
16 8 8*	R	53.6	1010
8 0 0†	T	65.1	1793

R = reflection T = transmission

* Mo radiation

† Ag radiation

Other reflection Cu radiation

TABLE 3.1.1

3.1.2 Double crystal topography

An 'uncollimated' beam of x-rays from a fine-focus line source is diffracted from a reference crystal which, ideally, should be perfect. An asymmetric reflection will give a diffracted beam of large cross-sectional area but of small angular divergence in the horizontal plane. This beam is incident on the sample crystal where it is diffracted. If the crystals are set up in the 'parallel' orientation, fig. 3.1.2, the two sets of diffracting planes are parallel and of equal spacing and all wavelengths will diffract for the same angular setting of the sample crystal. This gives a very narrow rocking curve, i.e. the width of the intensity versus angular position curve is only a few seconds of arc, and is close to the theoretical width for perfect crystals. This property is used in lattice parameter measurements, see section 3.2.1.

A parallel crystal setting will give a doubling of the image of a defect in the topograph. Although all wavelengths diffract for the same position of the crystal, the diffracted beams leave the crystal at different angles. Unless the photographic plate is very close or very far away from the sample the two images ($k\alpha_1$ and $k\alpha_2$) will occur at different positions on the plate. If the reference and sample diffracting planes are not of exactly the same spacing (Si 440, GGG 888) a topograph can be taken with either $k\alpha_1$ or $k\alpha_2$ radiation. The angular separation of the α_1 and α_2 peaks is $(\theta_r^{\,2}+\theta_s^{\,1}) - (\theta_r^{\,1}+\theta_s^{\,2})$ where θ is the Bragg angle, r and s denote

Double crystal topography

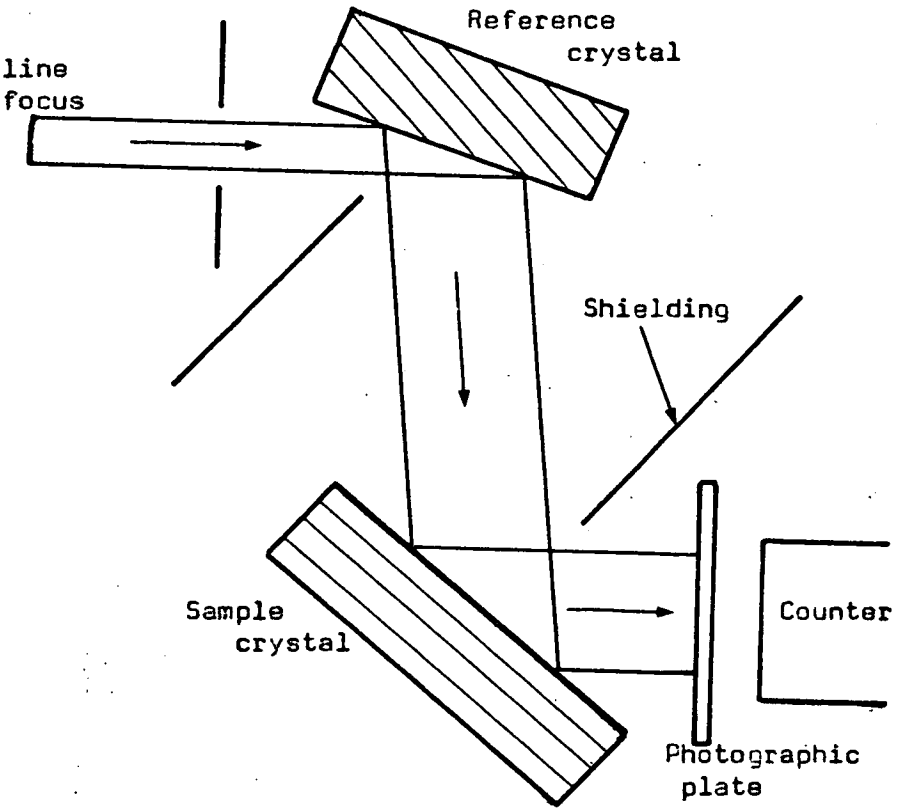

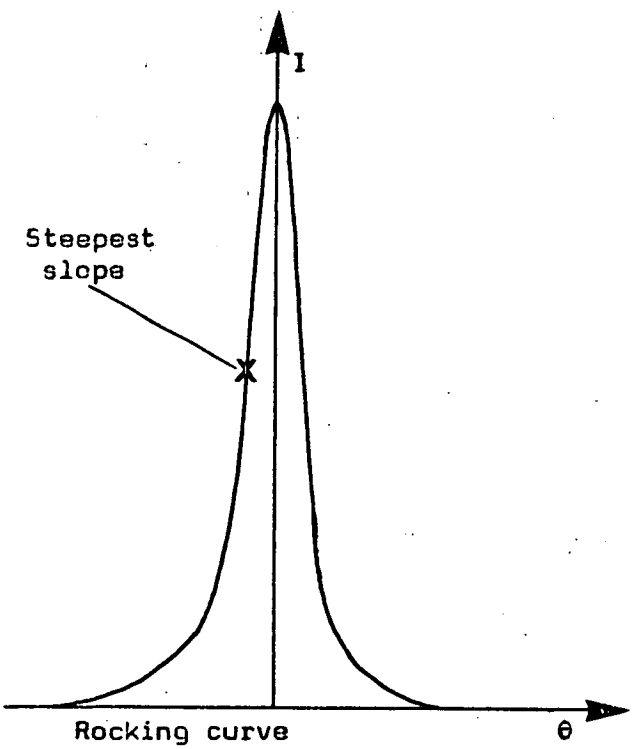

Figure 3.1.2

reference and sample, and $_2$ and $_1$ refer to $k\alpha_1$ and $k\alpha_2$. The $k\alpha_1$ and $k\alpha_2$ peaks are also slightly broader than in the parallel setting.

As the crystal is rotated through the diffracting position the diffracted intensity increases from a very low level, through a maximum and back to the background level. The shape of the curve is approximately Lorentzian. This is the rocking curve and the greatest sensitivity to defects can be obtained by setting the crystal such that the intensity is at half maximum. Here the slope of the rocking curve is at its greatest and so a small change in local orientation or lattice parameter will give a large change in diffracted intensity. If the crystal is set for the other side of the peak the contrast for a given defect would be reversed.(81) The change in intensity I caused by a distortion is given by:

$$\Delta I = I K \left(\frac{\delta d}{d} \tan \theta + \delta \theta \right)$$

where K is the slope of the rocking curve, θ the Bragg angle, δd the change in spacing, and $\delta \theta$ the change in orientation of the diffracting planes.

The width of the rocking curve, and thus the sensitivity to defects, depends on the radiation and reflection used, table 3.1.2. Copper radiation was used for GGG since the rocking curve width is comparable to the spread of effective orientations in the crystals.

The diffracted intensity is very sensitive to the angular position of the crystal and drifting from the required position due to temperature fluctuations or

Reflection widths at half maximum intensity

Reflection	Chromium = 2.289 Å		Copper = 1.540 Å		Molybdenum = 0.709 Å	
	2θ deg	w sec arc	2θ deg	w sec arc	2θ deg	w sec arc
4 0 0	43.4	16.2	28.8	10.46	13.2	4.69
4 2 0	48.8	16.5	32.3	10.53	14.2	4.69
4 4 4	79.6	13.6	51.0	7.83	22.9	3.32
6 4 0	83.6	12.0	53.2	6.75	23.8	2.84
8 0 0	95.4	18.3	59.6	9.58	26.5	3.98
8 6 4			84.1	3.85	35.9	1.38
8 8 0			89.4	6.81	37.8	2.35
12 4 4			111.2	4.35	44.6	1.22
8 8 8			159.1	6.89	46.8	1.75
16 0 0			169.1	2.75	54.5	1.35
16 8 0					61.6	1.23
16 8 8					68.3	1.06
16 16 16					105.1	0.79

$$w = 1.32 \times \frac{2C}{\sin 2\theta} \frac{r_e}{\pi} \lambda^2 \frac{F_h}{V}$$

C = 1 or $\cos 2\theta$ depending on polarisation

r_e is classical electron radius

V is volume of the unit cell

TABLE 3.1.2

relaxation in the crystal mounting must be corrected. The intensity is monitored through the photographic plate and if it moves out of certain pre-set limits the crystal is automatically rotated to bring the intensity back to the correct level. Confining the angular motion of the crystal in this way gives very sharp images of defects and is essential since the crystal can easily drift the few seconds of arc necessary for it not to diffract at all.

Short segments of dislocations can be seen by this method. Topographs of films and substrates can be taken for a lattice parameter mismatch as small as 0.001 Å. This method is, however, rather sensitive to bending of the crystal and may thus be less suitable for thick films of large mismatch.

3.1.3 Zebra patterns

Contours of constant Bragg angle may be obtained by a variation of the double crystal technique.[83] The reference and sample crystal are set in the parallel configuration. The first diffracted beam is well-defined in the horizontal plane but diverges in the vertical plane. If the sample crystal is tilted about a horizontal axis, ϕ, shown in fig. 3.1.3, only part of this crystal will be able to diffract. This will be a straight, horizontal band if the two crystals are perfect and the x-ray source is a line. As the crystal is rotated about θ different parts of the crystal will diffract in turn and the horizontal band will move over the crystal. Local changes in orientation or lattice parameter will produce a similar, but

Double crystal apparatus set for Zebra patterns.

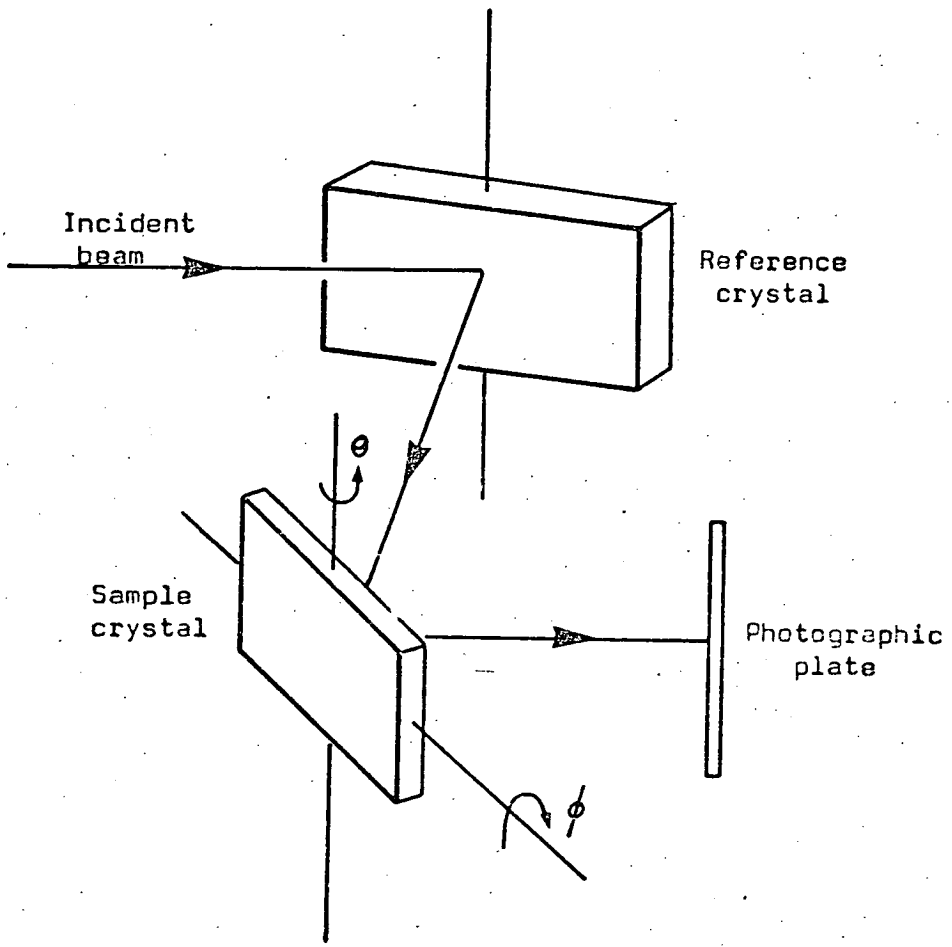

Figure 3.1.3

local, movement of the band which will not now be straight. This may be recorded on film and the amount of strain present can be calibrated by rotating about θ by a known amount between successive exposures on the same piece of film. The effects due to bending and dilatation can be separated by rotating the sample 180° about the diffraction vector between successive experiments.

Fast dental x-ray film is used for this experiment to cut the exposure time to a few minutes. The flattened rocking curve does not allow for control against crystal drift which may be appreciable over a long exposure.

3.1.4 Photography

Nuclear emulsion fine grain plates, type L.4 made by Ilford, were used for all topographs except Zebra patterns. Emulsions of 50 μm thickness were used for Mo and Ag radiations and 25 μm thickness for Cu radiation. The monitoring of the double crystal diffracted intensity required the emulsion to be plastic backed so the Cu radiation could penetrate. The plates were glass backed for all other applications.

The topographs were developed at ice temperature in Kodak D19 x-ray developer, diluted 1+3 with water and filtered. This gives more control over the development of the thick emulsions. After fixing, washing and drying the emulsions were protected by thin glass coverslips. A coverslip was also put on the back of the plastic backed plates since this plastic was also rather susceptible to scratching.

Negatives of whole or part of the topograph were made on fine grain film with some enlargement. These are then printed to give a positive print such that black means a higher diffracted x-ray intensity than grey.

3.2 Lattice Parameter Measurements

3.2.1 Lattice parameter mismatch

The double crystal apparatus can be used to measure the difference in lattice parameter between substrate and epitaxial film. If the apparatus is set in the non-dispersive configuration (GGG sample and reference crystals set on the same reflection) then the rocking curve width will be $\sim 7''$, thus small mismatches of $\sim 0.001\text{Å}$ can be detected. Similar measurements can be made as part of the procedure for taking a topograph with Si (440) as the reference although the $k\alpha_1$ and $k\alpha_2$ separation can cause problems. Rocking curves of the same sample but different reference crystals are compared in fig. 3.2.1.

The sample axis was calibrated for rotation per pulse applied to the motor using an optical lever arrangement. This gave a rotation of 0.05" per pulse. The rocking curve measurements were made by recording the intensity output on a chart recorder, for routine measurement. To check the shape of the rocking curve the x-ray intensity was obtained digitally and recorded by hand at every few steps of rotation. The difference in lattice parameter is given by the expression:

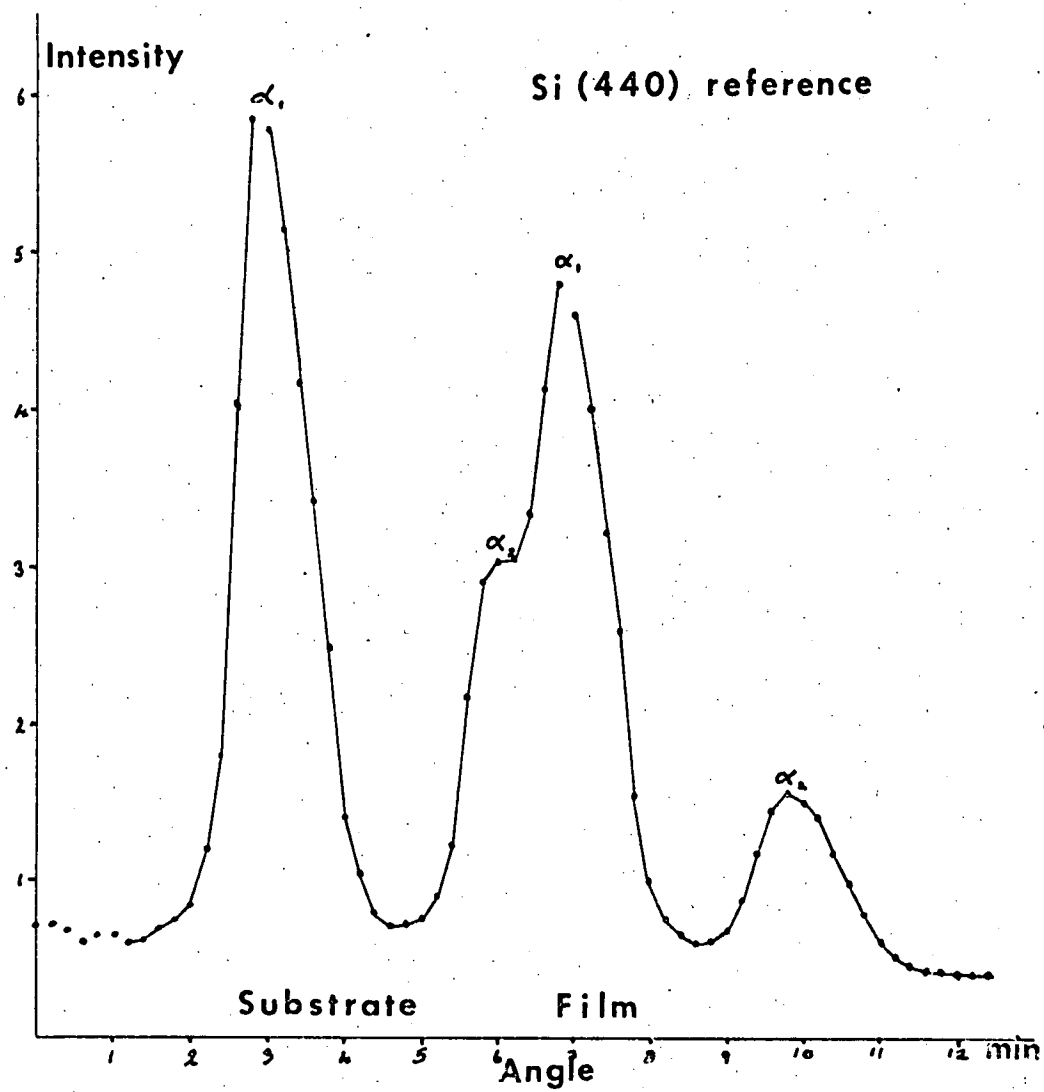
Intensity
Si (440) reference
α_1
α_2
α_1
α_2
Substrate
Film
Angle
min

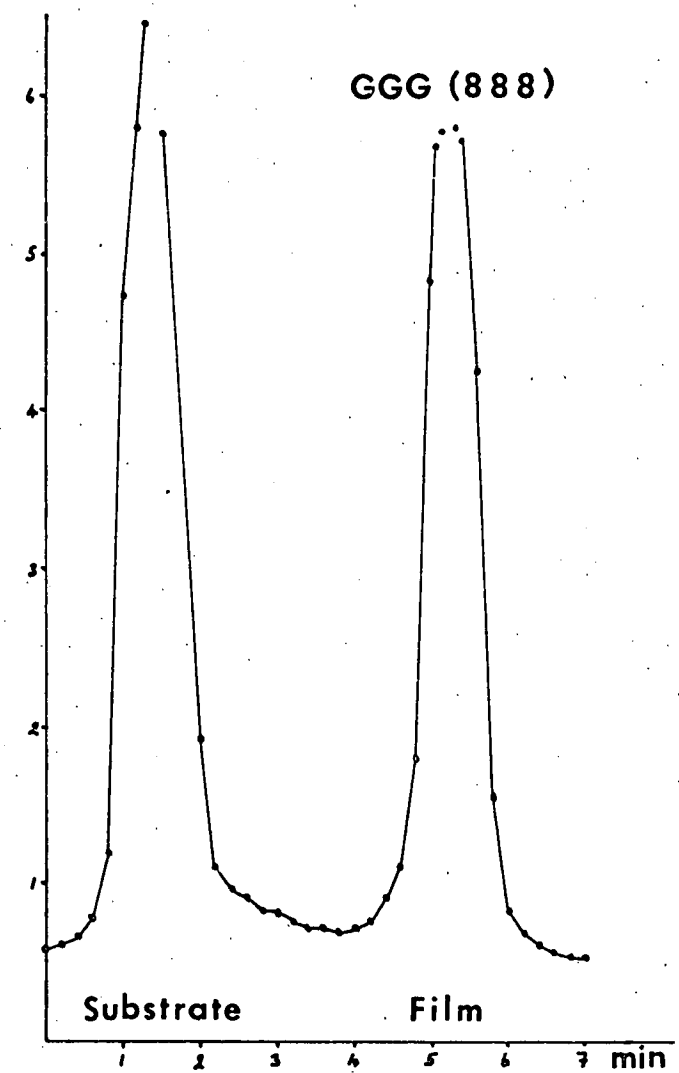
GGG (888)
Substrate
Film
min

Figure 3.2.1

$$\Delta a = (\cot\theta - \frac{\Delta\theta}{2})\, a.\Delta\theta$$

$$= \cot\theta\, a\, \Delta\theta \quad \text{for small mismatch}$$

The average lattice parameter mismatch over the whole film is found if the whole sample is illuminated. These results can be misleading if the sample is bent, so the size of the beam is reduced. This allows measurement of lattice parameter mismatch at different points in the film and may reveal the presence of several film layers of slightly different lattice parameter.

A symmetric reflection will give the change in lattice parameter normal to the slice, $\Delta a^{\perp}$. This can be related to the free lattice parameter of the film if it is assumed that the substrate is unstrained and the film is elastically strained.

$$\Delta a_f = \Delta a^{\perp} \quad (1 - \frac{2\mu}{1-\mu} \quad \frac{\Delta a^{\perp}}{a})$$

μ = Poisson's ratio

Asymmetric reflections will give a combination of the change in orientation of the planes and the change in spacing.[84] These can be separated by repeating the experiment with the sample rotated 180° about the scattering vector, the diffracting planes being vertical, i.e. parallel to θ, for each measurement.

3.2.2 Absolute lattice parameters

Standard Debye-Scherrer powder photographs were used to obtain absolute lattice parameter measurements of substrate material. The Straumanis film-setting and copper

$k\alpha$ radiation were used. The powdered samples were mixed with gum tragacanth and water and rolled into small cylinders. This is a destructive technique.

3.3 Crystal Orientation

The crystal boules are required to be sliced on known orientations. The crystal to be cut is mounted such that its orientation can be adjusted relative to a cylinder. The cylinder is placed in a V-block near a collimated x-ray beam. The tilt of the crystal is adjusted so that the required Bragg reflection((8 8 8) if a (111) slice is required) is obtained for all positions of the cylinder in the V-block. This occurs when the required plane is perpendicular to the cylinder axis. A similar V-block is mounted perpendicular to the saw blade. The slices can be cut to an accuracy of 1' or better.

Approximate orientations are obtained using back-reflection Laue photographs.

3.4 X-Ray Theory

3.4.1 Intensity of Bragg reflection

The condition for diffraction of x-rays by a particular set of crystal planes is given by Bragg's Law:

$$n\lambda = 2\, d_{hkl} \sin\theta$$

where λ is the x-ray wavelength

d_{hkl} is the interplanar spacing of the planes (hkl)

2θ is the angle the diffracted beam makes to the incident beam

The intensity of the diffracted beam will depend on the crystal structure but also on the perfection of the crystal and the absorption of x-rays in the sample. The effect of the atomic positions is given by the structure factor F_{hkl}

$$F_{hkl} = 2\sum_{n} (f_n \cos 2\pi (hx_n + ky_n + lz_n))$$

for a centrosymmetric structure.

f_n is the atomic scattering factor which depends on $\sin \theta / \lambda$.

x_n, y_n, z_n is the position of the n^{th} atom.

The summation is over the pairs of atoms related by the centre of symmetry. The values of $|F|$ in table 3.1.1 were calculated from this formula and analytical expressions for the atomic scattering factor.(85)

When a beam of monochromatic x-rays falls on an absorbing material of thickness t, the transmitted intensity, I, is related to the incident intensity, I_o, by the relation:

$$I = I_o \exp(-\mu t)$$

where μ is a constant known as the linear absorption coefficient.

The reduction in intensity of the beam occurs because some of the x-ray beam is Compton scattered and some is transformed into other types of radiation.

The values of μ have been measured for most elements and these values can be used to obtain μ for any crystal.

If the size of the unit cell and the contents of the cell are known then the formula below is used.

$$\mu = \sum_{\text{cell}} \frac{(\mu_a)_{\text{cell}}}{V} \qquad \text{Sum over all atoms in cell}$$

V is the volume of the cell

μ_a is the atomic absorption coefficient.

The values of μ_a for particular wavelengths can be found in the International Tables.[86] Absorption increases rapidly as the wavelength of the x-rays increases except near an absorption edge. Values of μ for GGG were given in section 3.1.1. The contribution from the oxygen ions was neglected since this value was small compared with the uncertainty in the value of μ_a for gadolinium.

In thin samples where the absorption is low the integrated diffracted intensity from an imperfect region of crystal will be greater than for a perfect region. The core of a dislocation can be considered as a rod of imperfect material embedded in a matrix of perfect crystal. The image produced by diffraction from this core is known as the direct image. An additional image, the dynamical image, is formed under conditions of moderate absorption. In a typical transmission experiment the angular divergence of the beam of x-rays is greater than the range of angles over which Bragg reflection occurs and x-ray energy flows throughout the triangle bounded by the incident beam direction and the diffracted beam direction drawn through the position of incidence.

3.4.2 Images of dislocations

If a dislocation or other imperfection is present this will diffract energy which would otherwise flow into the triangle bounded by the incident and diffracted beam directions, apex at the dislocation, and form a shadow, lighter than the background.[87],[88] Smaller distortions away from the core of the dislocation will also cause a redistribution of the beam energy between the forward and diffracted components. If the absorption of x-rays is high most of the energy flows in directions close to the Bragg planes under conditions of anomalous transmission. A defect will diffract more energy into a direction away from the Bragg planes and so this energy will be absorbed. The image of the dislocation (the Borrmann image) is lighter than the background and there is no shadow.

The direct image of the dislocation may not be a single line. If the wavelength and reflection are chosen to give a narrow perfect crystal rocking curve then the direct image may appear double in a transmission topograph.[89]

3.4.3 Determination of Burgers vectors

The Burgers vector of a dislocation is determined, in ideal cases, by finding reflections in which the dislocation line becomes invisible. This determines the Burgers vector since displacements in the crystal parallel to the reflecting plane should produce no contrast.

The elastic strain around a straight dislocation is summarised below for a pure screw and for a pure edge dislocation in an elastically isotropic crystal.[90]

u, v and w are the x, y and z components of the displacement of the material (x, y and z are rectangular coordinates with the z axis along the dislocation line). b is the modulus of the Burgers vector, θ is an angular coordinate measured from the x-axis about the z-axis, r is the distance from the z-axis in the x-y plane and ν is Poisson's ratio.

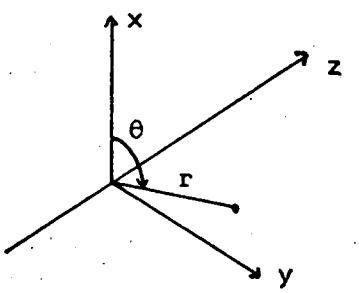

For a pure screw dislocation the discontinuity in displacements has

$$\Delta u = 0, \quad \Delta v = 0, \quad \Delta w = b$$

and the displacements are

$$u = 0, \quad v = 0, \quad w = \frac{b}{2\pi}\theta$$

For a pure edge dislocation, $\Delta u = b$, $\Delta v = 0$, $\Delta w = 0$, and

$$u = \frac{b}{2\pi}\left(\theta + \frac{\sin 2\theta}{1-\nu}\right)$$

$$v = \frac{-b}{2\pi}\left\{\frac{1-2\nu}{2(1-\nu)}\ln r + \frac{\cos 2\theta}{4(1-\nu)}\right\}$$

$$w = 0$$

It can be seen that the components of displacement parallel and normal to the dislocation are separable.

If $\underline{b}$ is the Burgers vector, $\underline{l}$ the line vector of the

dislocation and $\underline{g}$ the normal to the Bragg planes then for a screw dislocation the line will be invisible if $\underline{g}.\underline{b} = 0$, i.e. if the vector $\underline{g}$ is normal to the dislocation line. Thus any reflection in the zone normal to $\underline{l}$ will cause the dislocation to be invisible. Maximum contrast will be obtained when $\underline{g}$ and $\underline{b}$ are parallel or anti-parallel.

There are two components of displacement for an edge dislocation. One is parallel to the Burgers vector and the other normal to the slip plane. The condition $\underline{g}.\underline{b} = 0$ is not sufficient for there to be zero contrast in the image, $\underline{g}$ must also be normal to the displacement, v. Thus $\underline{g}$ must be parallel or anti-parallel to $\underline{l}$ and there are only two reflections for which the dislocation image will vanish. Under favourable conditions the dislocation image will almost vanish if $\underline{g}.\underline{b} = 0$ and $\underline{g}$ not parallel to $\underline{l}$.

3.4.4 Images of magnetic domains

Magnetic domains are visible in x-ray topographs due to the magnetostrictive deformation of the crystal[91] and have been observed by this method in terbium iron garnet - [92],[93],[94] and in YIG.[95] There should be no strain between 180° domains and so these should not be visible for any Bragg reflection, though weak contrast may occur.[91]

3.5 Optical Techniques

3.5.1 Determination of film thickness

The interference between monochromatic light reflected at the top and bottom surfaces of a film, the film/substrate interface providing a reference flat, is a non-destructive

Measurement of variations in film thickness.

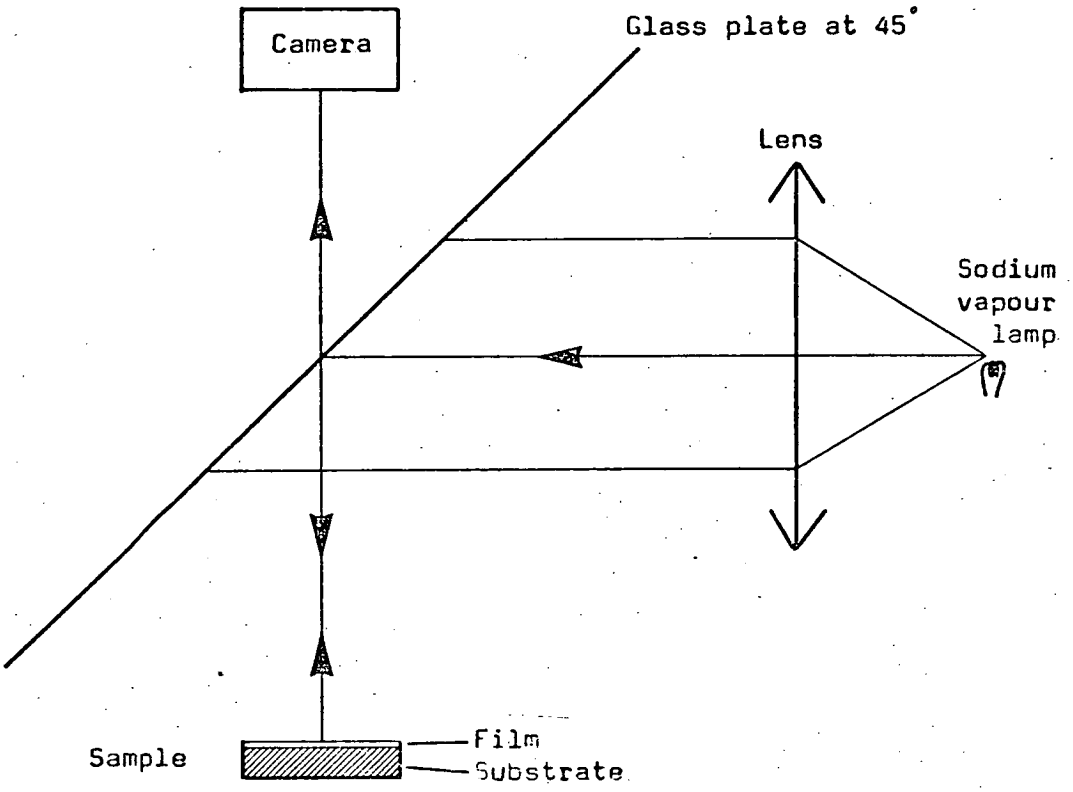

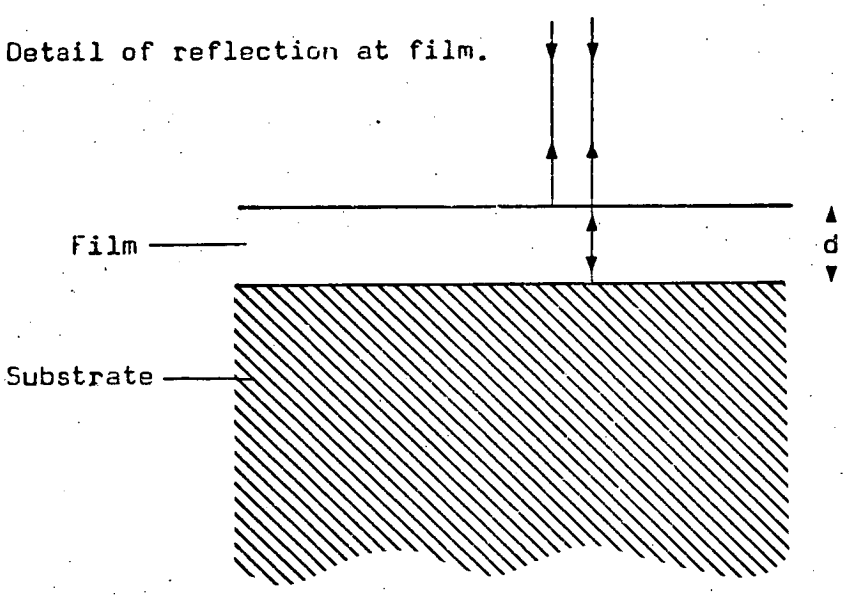

Figure 3.5.1

method of determining variations in the thickness of the film. Yellow light from a sodium vapour lamp was used in the experimental arrangement shown in fig. 3.5.1. Dark fringes corresponding to destructive interference will occur at intervals corresponding to a thickness change of Δd where $r \Delta d = \lambda/2$, r is the refractive index. Changes in thickness are readily seen. Absolute values are more difficult to obtain since the refractive index and phase changes on reflection need to be known.

A method of obtaining an absolute thickness, though by destroying part of the film, is by a ball penetrometer. This is a steel ball, coated with abrasive, which is rotated at high speed and brought into contact with the sample for a sufficient time for the hole formed to penetrate the film/substrate interface. When the hole is viewed in the microscope two circles are seen, the larger being the film surface. The thickness of the film, h, may be determined from the radii of these circles and of the steel ball.

$$h = \frac{1}{2R} (r_1^2 - r_2^2)$$

where R is the radius of the steel ball

r_1 is the radius at the film surface

r_2 is the radius at the substrate surface

3.5.2 Observation of strain

An isotropic, transparent material put between crossed polarisers will allow no light to be transmitted. A stress applied to the material will cause some

anisotropy and in general light will be transmitted, except when either of the optic axes is parallel to the polariser or the analyser. This property is used to investigate macrostresses in the polariscope and microstresses, e.g. round dislocations, in the polarising microscope.

The polariscope consists of a light source, a polariser and analyser which can be crossed and then rotated together and two removeable quarter-wave plates.

With the quarter-wave plates removed and a white-light source in use the stress pattern observed will be of black isoclinics,which are contours of inclination of the optic axes parallel to polariser and analyser superimposed on a background of coloured isochromatics. Rotating the polariser and analyser moves the isoclinics. The isochromatics are contours of equal retardation and can be observed without the isoclinics by the addition of the quarter-wave plates which can be arranged to produce circularly polarised light. A sodium vapour lamp can also be used as light source. This method will determine the location of the long-range strains.

An application of the photoelastic method to slices of the substrate material means that short-range stresses around dislocations can be detected using the polarising microscope with the polars crossed. The confusions between isoclinics and isochromatics does not arise here since the retardations are small. Under suitable circumstances the edge component of Burgers vector for a dislocation line normal to the slice can be determined from the

characteristic 'rosette' pattern.[96],[97],[98] This pattern depends on the angle between the Burgers vector and the direction of the polariser. The contours of equal transmitted intensity are given in polar coordinates r and ψ by:

$$r = K \cos(2\psi) \cos(\psi - \beta)$$

β is the angle between $\underline{b}$ and the polariser direction. Long-range strains may distort the contrast but the Burgers vector may still be determined.[99] Dislocations with the line parallel to the surface of the slice may also be observed but with much lower contrast. An edge dislocation becomes invisible when either the polariser or analyser is parallel to the dislocation line, a screw dislocation is invisible when the line is at 45° to the polariser.[99]

3.5.3 Observation of magnetic domains

Domains where the magnetisation direction is normal, or near normal, to the transparent slice may be observed by the Faraday effect[100],[101],[102],[103] using the polarising microscope. The plane of polarisation of a beam of light is rotated by the magnetic field in the domain. The sense of rotation depends on the direction of magnetisation. The magnitude of the rotation depends on the strength of the field, i.e. on the composition of the film, and on the thickness of the film. The polars are set almost crossed. The maximum contrast between domains occurs when the analyser is set to transmit no light from

one set of domains. The polars can also be set to observe the domain walls. An absorbing impurity such as lead will reduce the domain contrast.

CHAPTER 4

MAGNETIC TECHNIQUES

4.1 Magnetic Theory

4.1.1 Static behaviour

For a plate of magnetic material to support a cylindrical bubble domain there must be uniaxial anisotropy, an easy direction of magnetisation, normal to the surface. The anisotropy field must also be greater than the saturation magnetisation.

Thiele[104] gives a detailed theoretical treatment of the stability of bubble domains in materials of low coercivity. The analysis requires plates to be of uniform thickness, bubbles to be cylindrical and the domain wall width to be negligible. This theory has been the basis for the determination of magnetic bubble film parameters by measurements on stripe and bubble domains and their variation with applied field.[105],[106] The problem has been approached from a different view, from which the physical situation is more readily appreciated, by O'Dell[2] and approximations to Thiele's expressions have been obtained[2],[107] which are more amenable to further analysis. Except where otherwise stated, the expressions given below have been taken from O'Dell's book and numbered accordingly.

The range of bias fields and bubble diameters over which the bubble is stable needs to be known and should be controllable. The forces acting on a domain, and hence its static properties, are discussed below.

A straight stripe domain will have an expanding force due to its own field. This will be balanced by a contracting force due to an applied field or other stripe

domains. A bubble will have three forces acting on it. If an externally applied field B_o is directed along the axis of a bubble domain, diameter D, and opposed to the magnetisation M, then there will be a force F_o, acting radially, tending to contract the domain.

$$F_o = -(-B_o)\ (2Mh)\ (\pi D) \qquad 2.13$$

The thickness of the film is h. There will be an expanding force due to the field of the bubble domain

$$F_r = \frac{\mu_o M\ (2Mh)\ (\pi D)}{\pi/K\ (D/h)} \qquad 2.25$$

π/K is a constant $\simeq 0.726$.

Another contracting force is due to the domain wall energy. If σ_w is a constant energy per unit area of wall then,

$$F_w = -2\pi h\ \sigma_w$$

The force due to the field of the bubble and the force due to the wall energy can be considered as coming from applied fields $\bar{B}$ and B_w

$$\text{where} \quad \frac{\bar{B}}{\mu_o M} = \frac{1}{1 + 0.726\ (D/h)} \qquad 2.27$$

$$\text{and} \quad \frac{B_w}{\mu_o M} = \frac{-\sigma_w}{\mu_o M^2 h}\ (D/h)^{-1} \qquad 2.35$$

The bubble will be in equilibrium if all the fields cancel out, i.e.

$$\frac{1}{1 + 0.726\ (D/h)} - \frac{(\sigma_w/\mu_o M^2 h)}{(D/h)} = \frac{-B_o}{\mu_o M} \qquad 2.37$$

A quantity, λ, known as the 'characteristic length' is defined as

$$\lambda = \sigma_w/\mu_o M^2 \qquad 2.38$$

As the applied field is increased, a value B_o will be reached when the bubble is no longer stable and it will collapse. This occurs at the maximum of the curve of expression 2.37. Differentiating with respect to D/h and equating to zero,

$$\frac{0.726}{\left[1 + 0.726\ (^{D}col/h)\right]^2} + \frac{\lambda/h}{(^{D}col/h)^2} = 0 \qquad 2.40$$

$$^{D}col/h = \frac{(\lambda/h)^{1/2}}{(0.726)^{1/2}} \quad \frac{1}{(1-(0.726)^{1/2}(\frac{\lambda}{h})^{1/2})} \qquad 2.41$$

$$-^{B}col/\mu_o m = 1 - (0.726)^{1/2}\ (\frac{\lambda}{h})^{1/2} \quad 2 \qquad 2.42$$

A similar analysis can be applied to the runout field and diameter.

$$\frac{\lambda}{h} = \frac{1}{\pi} \left[\ln\ (\frac{\mu_o M}{-B_{ro}}) - \left\{1 - (\frac{-B_{ro}}{\mu_o M})\right\}\right] \qquad 2.51$$

These expressions are plotted in figs. 4.1.1 and 4.1.2. Measurement of the collapse and runout fields and bubble diameters thus allows the determination of λ/h and hence the saturation magnetisation, $\mu_o M_s$.

The ratio λ/h can also be determined from the period of straight stripe domains in a minimum energy configuration. The following expression[105] is for period p_o, $p' = P_o/h$:

Variation of bubble collapse and run-out diameters.

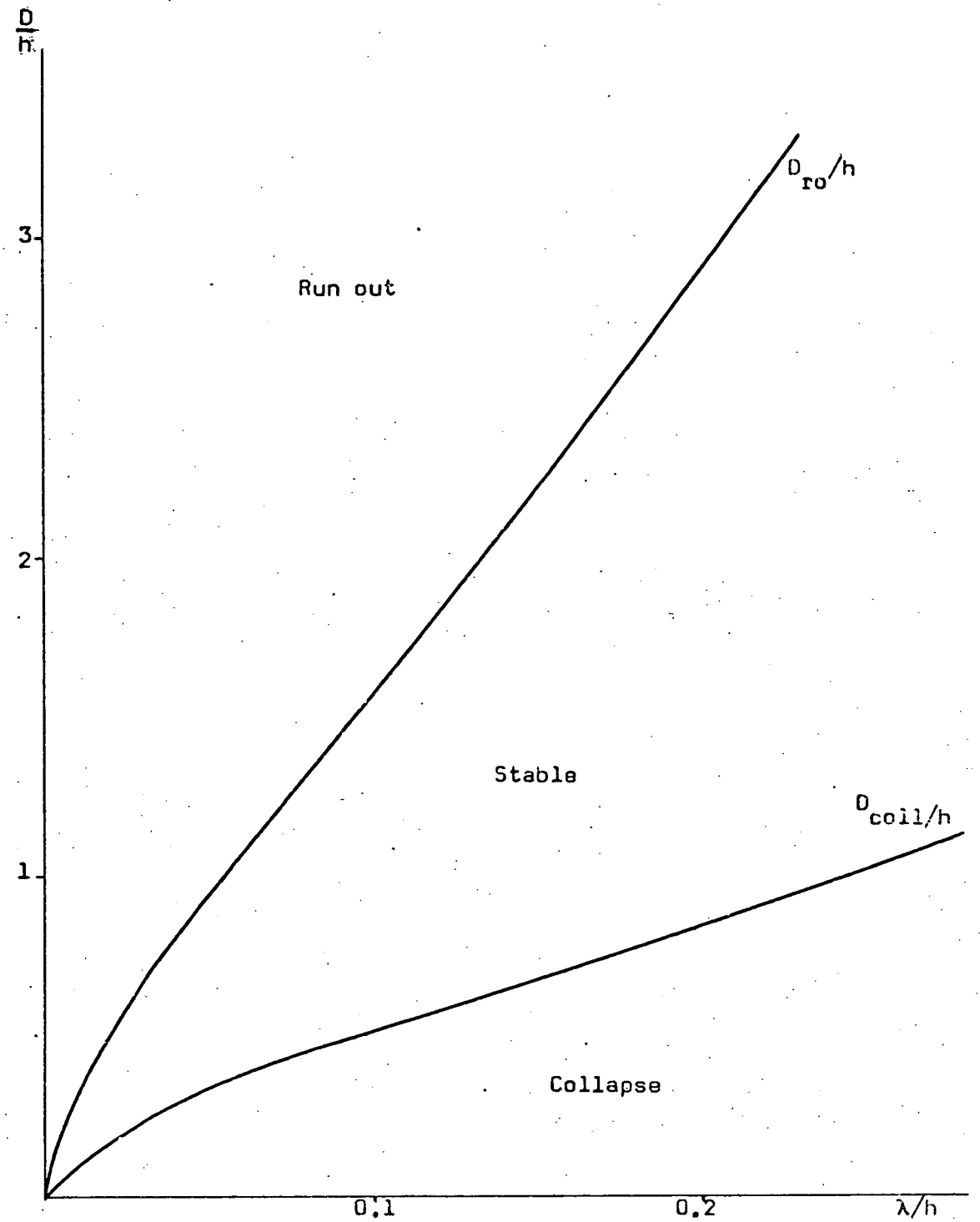

Figure 4.1.1

Variation of bubble collapse and run-out fields.

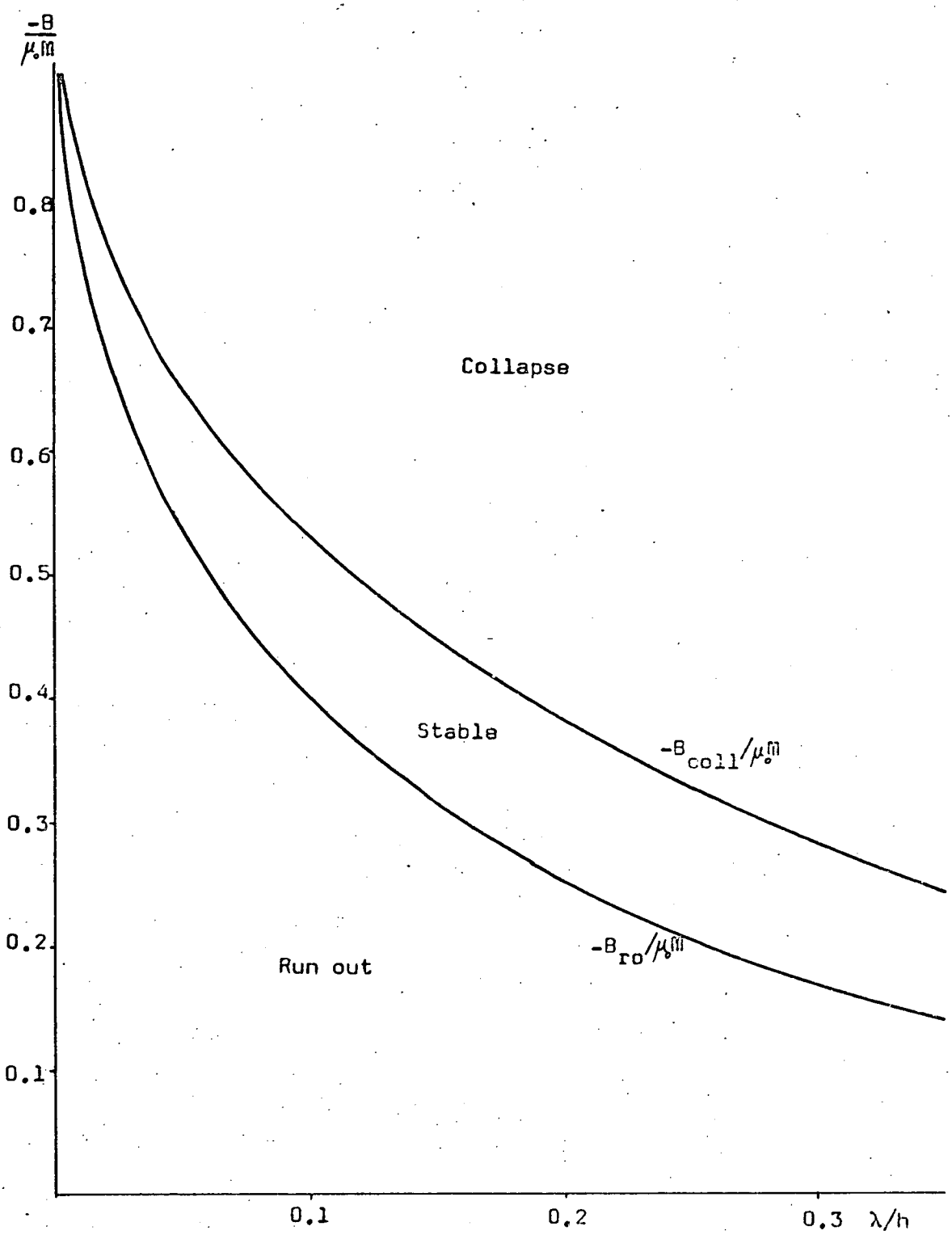

Figure 4.1.2

Variation of zero field stripe period.

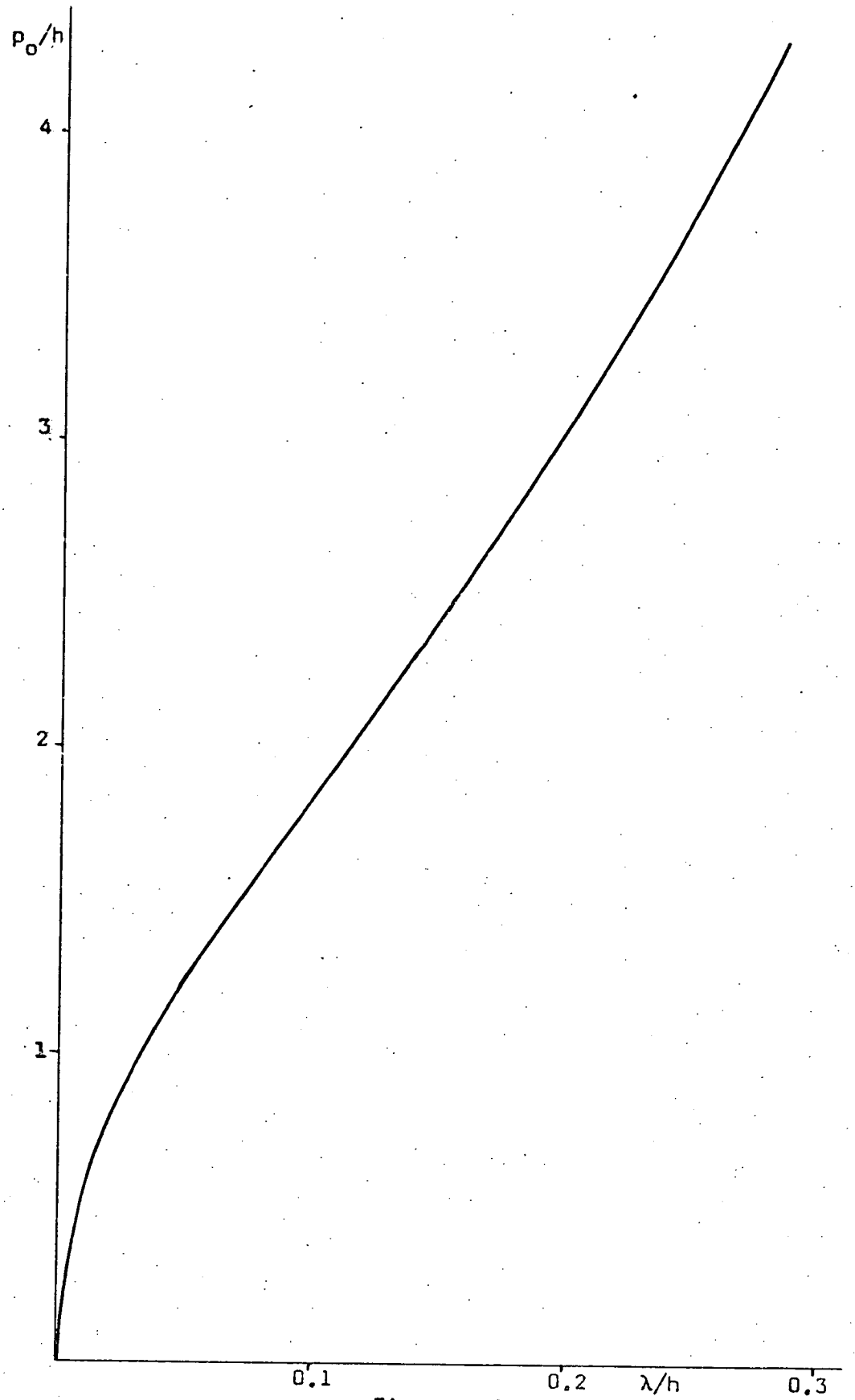

Figure 4.1.3

$$\frac{\lambda}{h} = \frac{(p')^2}{\pi^3} \left\{ \sum_{n\,\mathrm{odd}} \frac{1}{n^3} \left[1 - e^{-2n\pi/p'} \left(1 + \frac{2n\pi}{p'}\right) \right] \right\}$$

Numerical values of this expression[106] have been plotted in fig. 4.1.3.

When the value of the bias field is intermediate between the collapse field and the runout field, the diameter of the bubble will vary approximately linearly with field.[108]

4.1.2 Bubble dynamics

From the previous section, the data can be used to tailor a film composition and thickness for which the bubble is stable over the widest range of field. Dynamic properties of a bubble, in particular the bubble mobility, will determine, to a large extent, the maximum data rate of a device.

Several methods have been devised, originally for orthoferrites, which are applicable to garnets. The two methods discussed here are the bubble collapse method[109] and the translation of a bubble in a pulse gradient.[108] Both methods assume that there is a constant term, μ_w, known as the mobility of the domain such that the velocity of movement of the wall, $v = \mu_w B$, is proportional to the local field.

In the bubble collapse method a bubble domain is set up in a bias field, B, such that it has a stable diameter, D, greater than the collapse diameter, D_{col}. If a pulsed field, ΔB, is applied in the same direction as B then the bubble will collapse if the duration of the pulse, Δt, is

long enough. Measurements are made of the diameters of the bubbles D and of D_{col} and the amplitude and durations of the pulses required just to produce collapse. The wall mobility, μ_w, can be obtained from the simple expression,

$$\mu_w = \frac{D-D_{col}}{2\,\Delta t\,\Delta B} \quad (109)$$

This is an approximation to a very complex system[107] but is adequate for large values of ΔB. Other solutions have been found to yield the same equation.[167]

This type of experiment has limitations in that a maximum velocity of the domain wall may be reached as ΔB is increased. This is due to instabilities developing in the motion of the domain wall.[110],[111] Bubbles can, however, be translated at velocities higher than the collapse saturation velocities.

A bubble will move in a bias field gradient. The velocity will depend on the change in field, ΔB, across the diameter of the bubble and is given by:

$$v = \frac{1}{2}\,\mu_w \left\{ \Delta B - \frac{8}{\pi}\,\Delta B_c \right\} \quad (108)$$

This shows that the field gradient must be above a certain value in order to overcome the coercivity, ΔB_c. If the driving field gradient is a rectangular pulse of duration, Δt, then the bubble will travel a distance,

$$x = \frac{1}{2}\,\mu_w \left\{ \Delta B - \frac{8}{\pi}\,\Delta B_c \right\} \Delta t$$

The pulse field gradient is conveniently produced by passing equal, parallel currents down small parallel wires about 100 μm apart. At a point midway between the wires

there is no increase in bias field and the field gradient is proportional to I, the current in each wire, and inversely proportional to the square of the separation of the wires.[109] If the bubble is driven in the same direction for a series of steps it is possible to find average values of μ_w and coercive field over a large area. There can be a large variability in the distance moved per pulse.[109]

A modification to this comparatively simple method of producing a bias field gradient has been proposed[112] since as the bubble moves away from the centre, it will move into a region of different bias field. This effect is removed by applying a current to a second pair of conductors such that the field thus produced will increase linearly with time and be sufficient to cancel out the change in bias. However, the large variation in displacement per pulse means that the correction due to improvement of the bias field is small compared to the scatter.[113]

4.1.3 Hard bubbles

Some bubbles may not move parallel to a field gradient and have a lower mobility than other bubbles. They may also collapse at high bias fields and thus are known as hard bubbles.[114] This behaviour is due to a complex domain wall. The simplest type of wall is a simple Bloch wall.

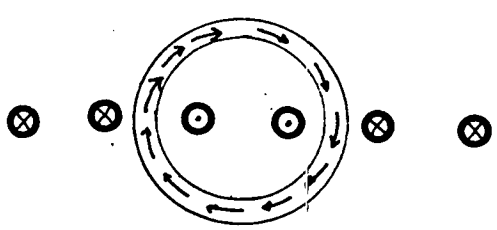

The rotation shown may be termed right-handed, going from the inside to the outside of the bubble. A left-handed rotation should be equally possible. The domain wall could be divided up into segments in which the magnetisation in the wall altered its direction of circulation. The boundaries to the segments, Bloch lines, are very narrow since the magnetisation is turning in a hard direction.

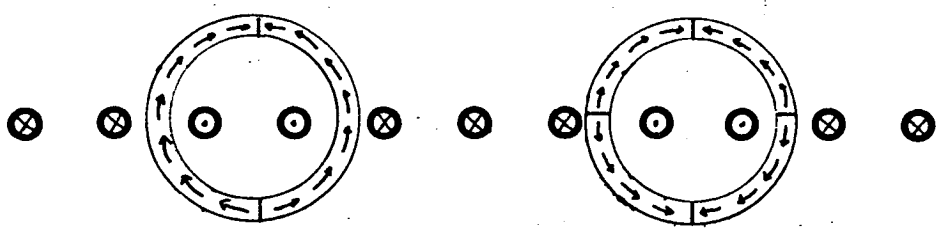

2n = 2 segments 2n = 4 segments

n is an integer

The wall structure cannot be observed using optical or Bitter pattern techniques but has been observed using Lorentz electron microscopy in the Fresnel (out-of-focus) mode in materials such as cobalt[115] and in magnetoplumbite.[116] This technique can determine the sense of rotation of the magnetisation in the domain wall and it was found in both these materials that most of the bubbles had the simplest domain walls with no Bloch lines. There were approximately equal numbers of bubbles of each hand. Bubbles containing two Bloch lines were also observed. The behaviour of the bubbles with two segments should be similar to that of the simplest form and should move parallel to a bias field gradient. Only the bubbles with

$2n > 2$ segments will cause trouble and these can be converted to $2n = 2$ by a two-layer film.[117]

4.1.4 Detection of defects

Defects in the film which are sufficient to impede the motion of a bubble domain may be seen by superimposing an A.C. bias field on the D.C. bias field. This causes the domains to move randomly, except where the domain is pinned. A time average, i.e. a photograph, will show a uniform grey where the sample is perfect but discrete domains will be visible where there is pinning.[118] This technique, after adjustment of the A.C. amplitude and D.C. bias to give optimum display, is fairly sensitive.[119] There are variations to this method which involve the distortion of the flow lines of a moving stream of bubbles by a defect[120],[121] or the monitoring of the size and shape of a single captive bubble scanned over the sample.[122]

These techniques will show up gross pinning points but will not show small variations in mobility.

4.2 Magnetic Apparatus

The magnetic domains in thin garnet films are visible in polarised light due to the Faraday effect. To make measurements on the static and dynamic properties the apparatus is built round a polarising microscope, in this case a Leitz Ortholux microscope. In order to use as many of the microscope facilities as possible, such as a condenser lens to get more light through a thicker film, the apparatus is required to be compact and conform to some of

the dimensions of the microscope. The largest part of the magnetic apparatus is the D.C. bias field coil and the design of this determines the design of the other parts of the apparatus.

4.2.1 D.C. bias field coil

A uniform magnetic field is required perpendicular to the sample plane and, ideally, this should not depend too critically on the position of the specimen relative to the coils for reproducible results. A Helmholtz pair of coils was made since for a separation of the coils equal to the radius of each coil there is a large volume of space over which the field is uniform. The field for the optimum configuration is given by:

$$B = \frac{8\ \mu_o\ nI}{5\sqrt{5}\ a}$$

where n is the number of turns in each coil,

I is the current and

a is the radius of the coil.

The sample is placed in between the coils and so the minimum radius is determined by the diameter of the objective lens which must pass through one of the coils. The field obtained from a given current depends on the number of turns and inversely on the mean radius. To keep the radius of the coil as small as possible the number of turns was restricted to 150 in each coil. The smaller bulk of the coil also means that it can cool more quickly and reach a lower, stabler temperature than a single coil giving the same field. The resistance of each coil made of laquered

Measurements of axial fields in Helmholtz pair and single coil.

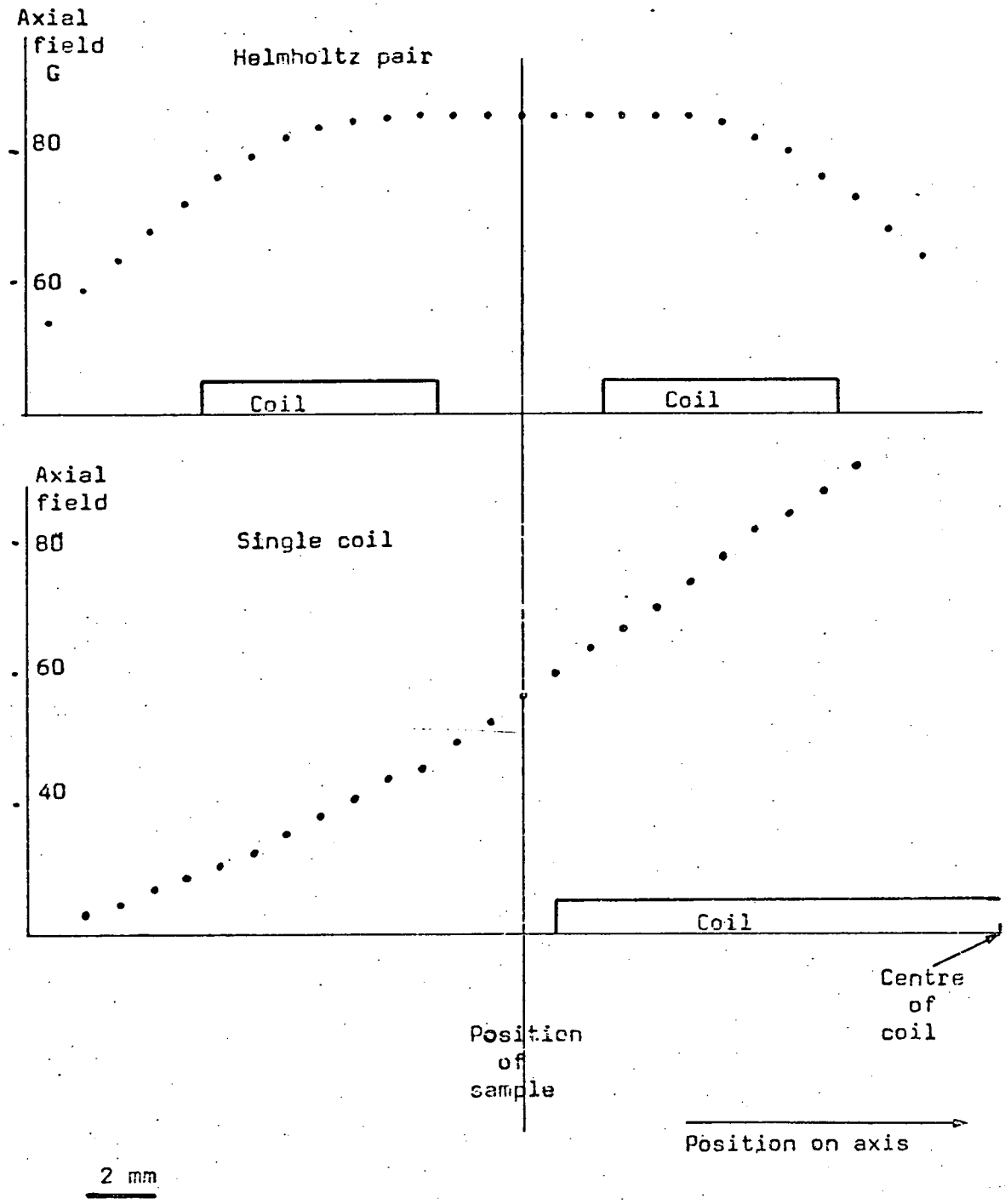

Figure 4.2.1

S.W.G. 26 copper wire was 1.4Ω. The turns of the coil were glued and bound together and each coil was sandwiched by two aluminium plates of much larger size than the coil, thus acting as cooling fins and giving a large, flat, working surface. The mean diameter of the coil was such that three microscope slides as spacers gave the correct separation between the coils. A sample, resting on a microscope slide, would thus have the film as near as possible to the centre of the coil assembly.

The uniformity of the field was checked and calibrated using a Hall probe and gaussmeter. The variation of field in the plane of the coil at the working position varied by less than ½% over the available area. Figure 4.2.1 compares the variation of field along the axis of the Helmholtz coil with a single coil capable of producing a similar field. The coil assembly is attached to the x-y stage of the microscope and positioned so that the objective lens will pass freely down the coil.

When a current of the order of one Amp passes through a coil of even a few ohms resistance, there will be a rise in temperature of the coil and therefore of the sample. The temperature was monitored with a copper/constantan thermocouple placed alongside the sample position.

4.2.2 A.C. / pulse field coil

A small coil, 5Ω resistance, 5mm diameter, underneath the sample microscope slide is used to supply the A.C. bias field, in conjunction with a D.C. bias, which will 'scramble' serpentine domains to create bubbles or reveal

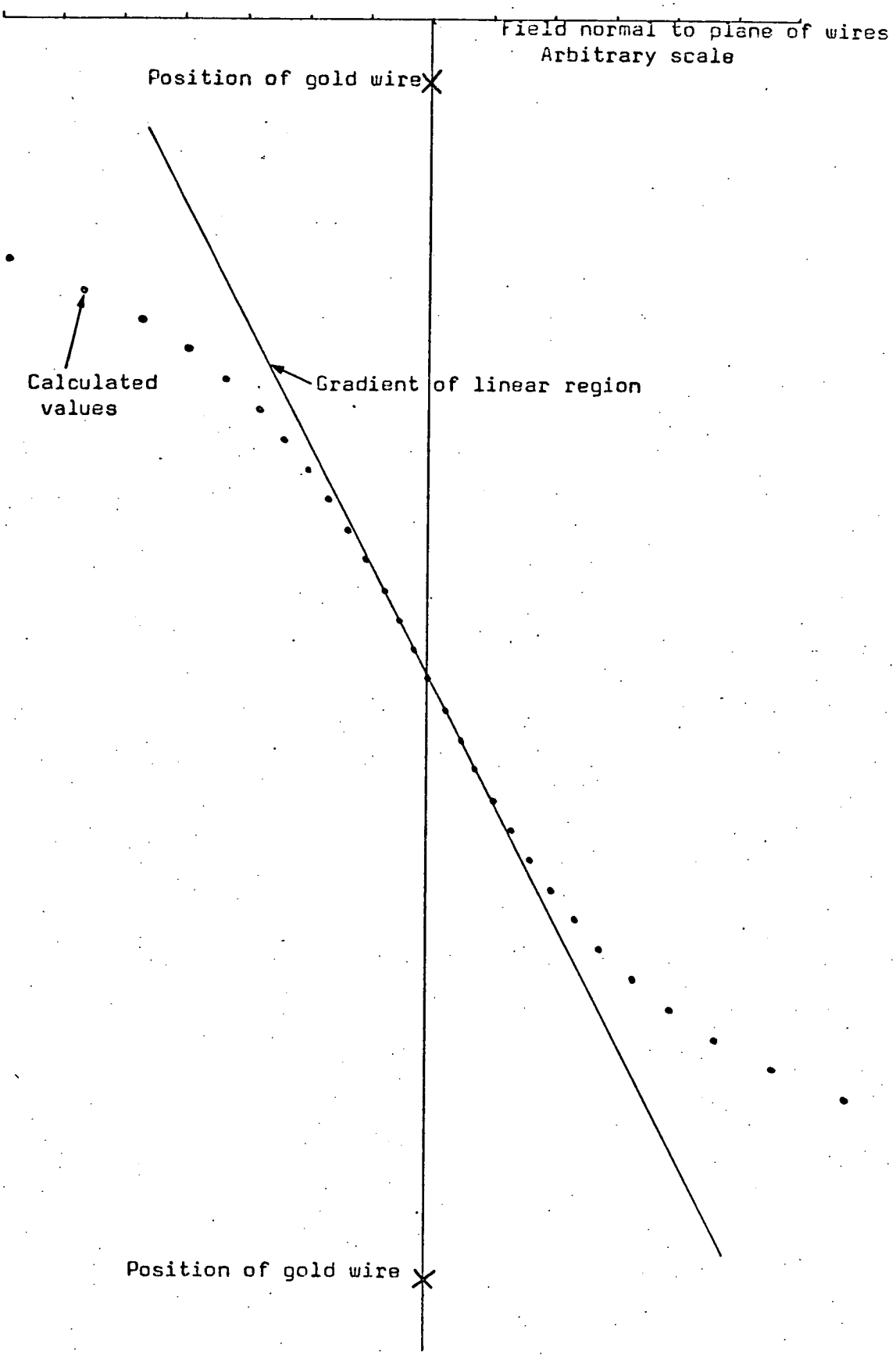
Field normal to plane of wires
Arbitrary scale
Position of gold wire
Calculated values
Gradient of linear region
Position of gold wire

Figure 4.2.2

pinning points. This coil can also be used for bubble collapse measurement of mobility. This was not entirely satisfactory since the inductance of the coil was rather high and the square pulse became distorted.

4.2.3 Bubble translation

The pulsed field gradient required for bubble translation experiments can be obtained by passing parallel currents through two thin, straight, parallel wires. The field normal to the plane of the wires, separation 2a, at a distance, x, from the centre line, is given by:

$$B(x) = \frac{\mu_o I}{2\pi} \frac{x}{a^2-x^2} \propto \frac{x}{a^2-x^2}$$

which is approximately linear if x is small compared to a. This function is plotted in fig. 4.2.2. x can be up to 30% of a and the deviation from linearity is still less than 10%.

Two 25 μm thick gold wires were wound over a microscope slide such that the wires were taut and separated by ~150 μm. To prevent the glass from cutting the gold wires and to enable good electrical contact to be made to the wires the gold wires were wound over thick copper wires which run along the two edges of the microscope slide and are held securely by adhesive tape. When the gold wires were positioned they were stuck down to the glass slide with 'Durafix' adhesive diluted with amyl acetate. The electrical contact between the gold and copper wires was reinforced by a small drop of high conductivity paint. This is illustrated in fig. 4.2.3.

Diagram of bubble translation apparatus - actual size.

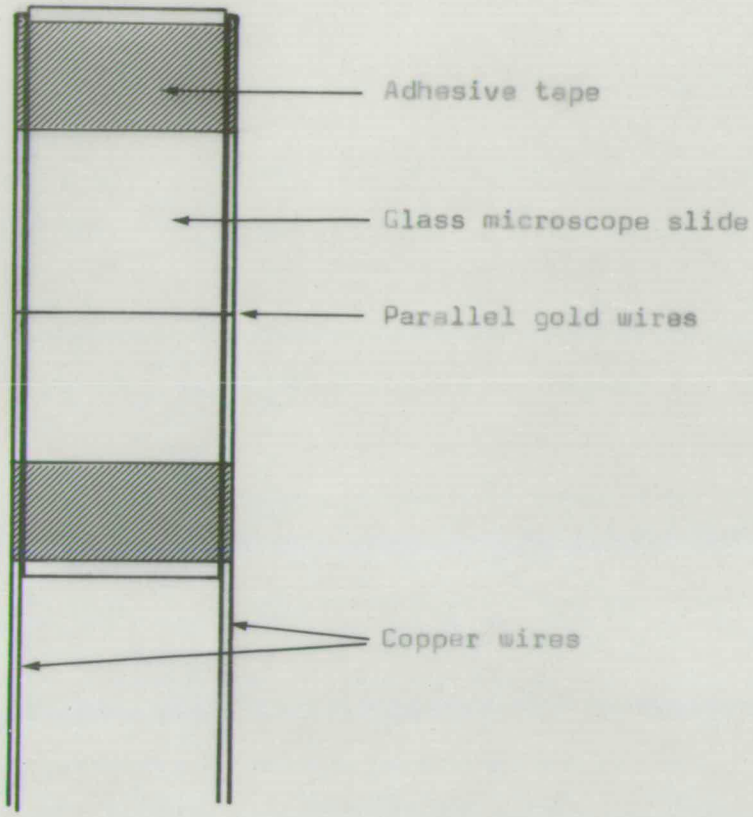

Detail of gold wires.

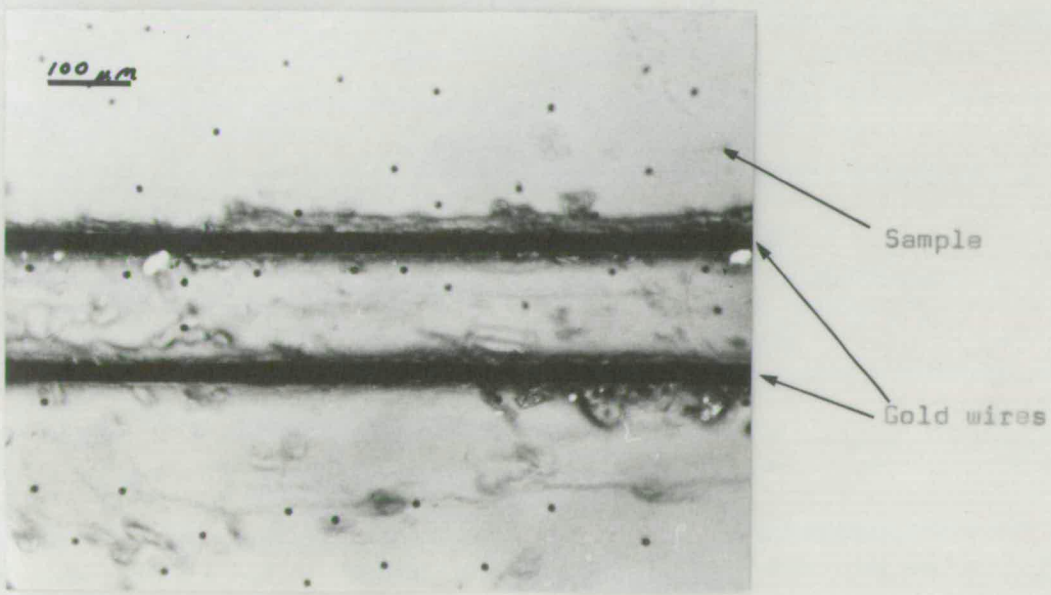

Figure 4.2.3

Magnetic coil assembly - actual size.

Side view - section

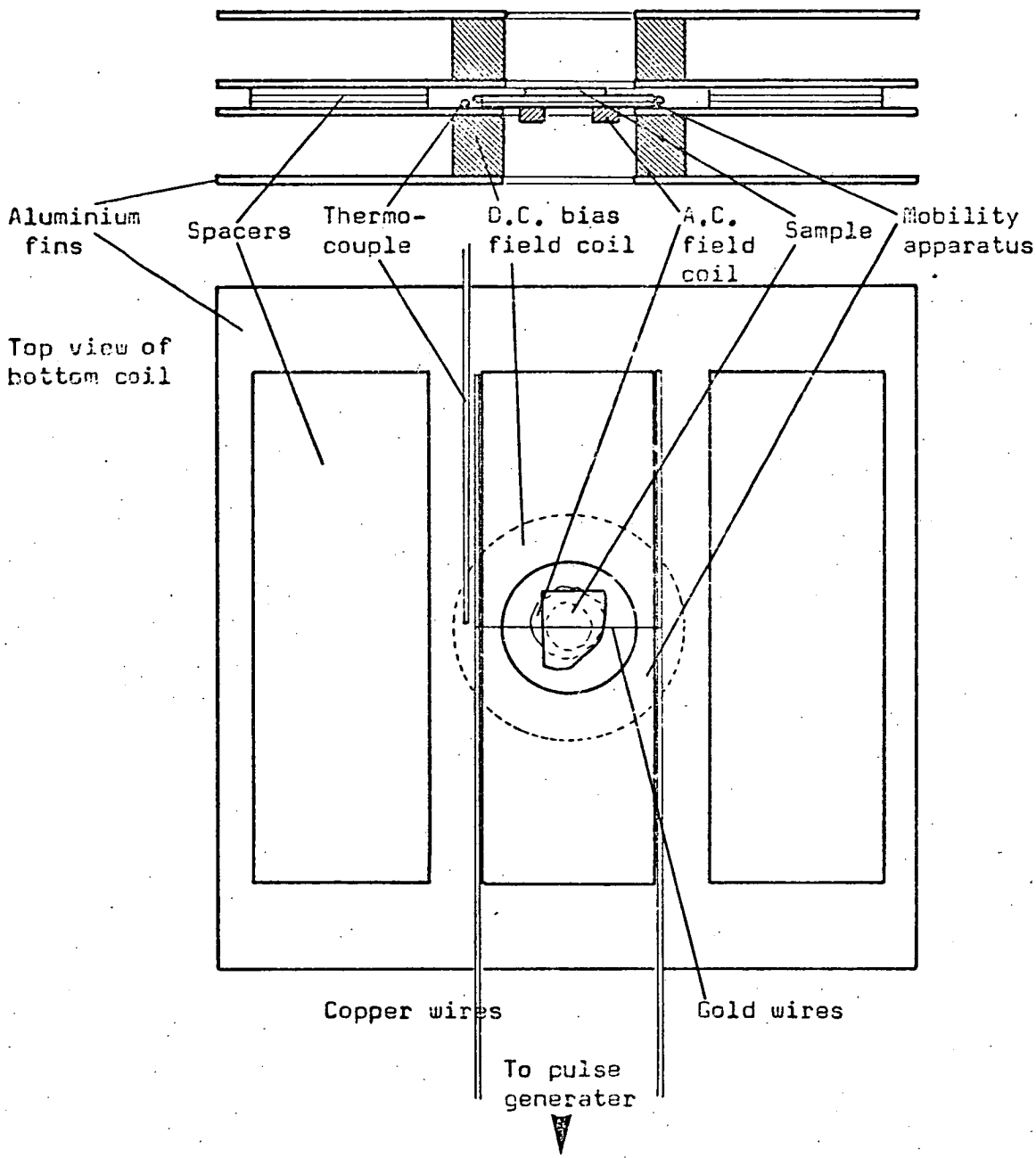

Figure 4.2.4

Optical and electrical scheme.

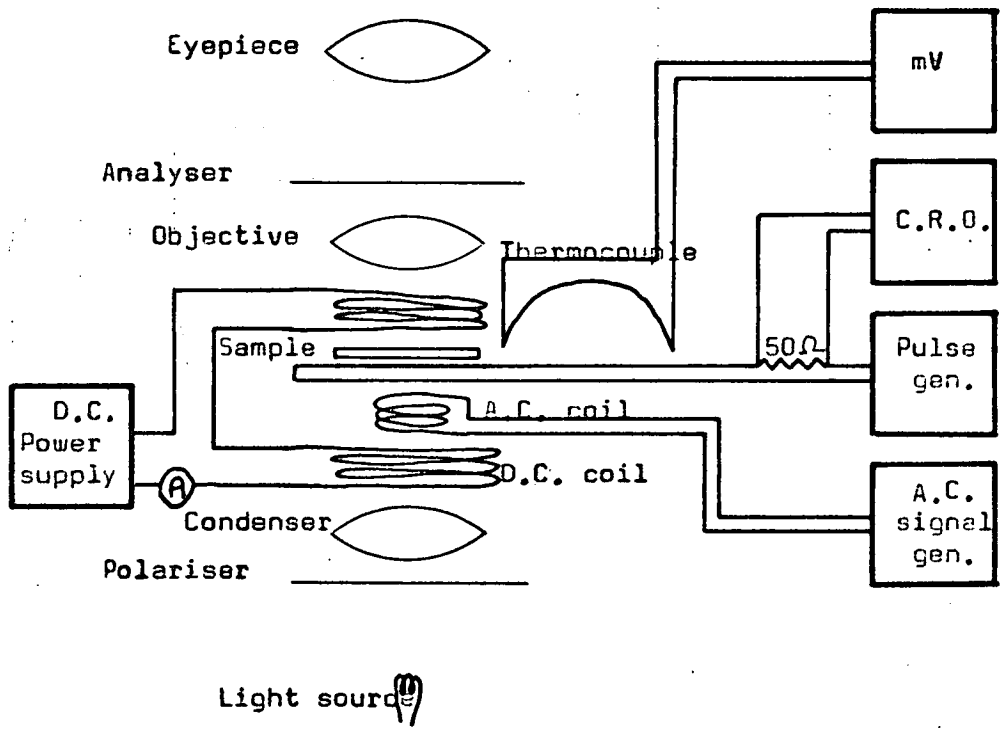

Figure 4.2.5

The slide with the gold wires is placed in the field coil assembly and the sample is placed face down such that the film is in contact with the gold wires which are in the microscope field of view. The position of the sample can be altered if necessary. The motion of the bubbles is viewed through the polished back of the substrate. The complete coil arrangement is shown in fig. 4.2.4 and fig. 4.2.5 shows the optical and electrical scheme.

4.3 Measurements and Methods

Distances a bubble moves, bubble diameters and stripe domain widths are measured in the microscope using a Leitz micrometer eyepiece which is calibrated for the optical system using a standard scale. The following quantities were measured:

i) film thickness

ii) zero field strip width

iii) bubble diameter versus field

iv) minimum stripe width

v) runout field and bubble diameter

vi) collapse field and bubble diameter

vii) pinning in A.C. field

viii) bubble mobility

The intrinsic length and saturation magnetisation may be determined from the static properties.

Results of measurements on bubble films grown by the author are given in Chapter 7.

C H A P T E R 5

DEFECTS IN SUBSTRATE MATERIALS

5.1 Preparation of Surface

The photolithographic techniques employed in the fabrication of devices require the surface to be flat since the scale of the device, with a bar width of ~2μm, needs a very high resolution. The requirement for flatness can be relaxed a little for this examination of the magnetic properties of films. The characteristics, advantages and disadvantages of three techniques for the preparation of damage-free surfaces are discussed below.

5.1.1 Polishing

The amount and depth of damage to a crystal will depend on the size and hardness of the abrasive used and whether it is fixed or free. A free abrasive will produce less damage since it will roll on the polishing lap and thus can carry less load.

The ideal polishing procedure will use progressively finer grades of particle, each grade removing the damage from the previous grade. Saw damage can be removed by successively finer grades of loose carborundum powder made into a slurry with either water or diamond lubricant. The diamond lubricant was less volatile and reduced clogging. A final grade of 800 carborundum powder will leave a damaged layer about 10 μm in depth. At this stage a polishing medium on a soft pad, the grinding uses a brass lap, should be used but there are many media from which to choose. Diamond paste and alumina powder polish quickly and are well-known from metallography. These will produce

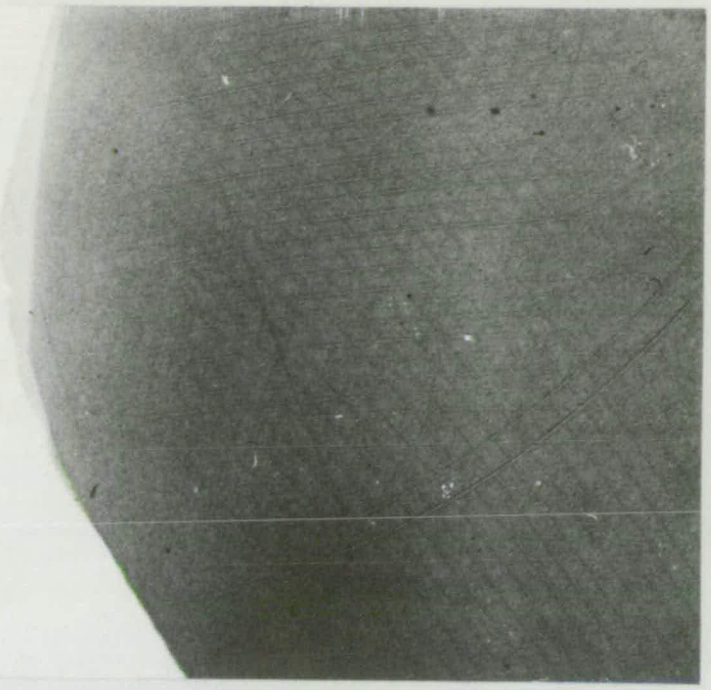

Lang reflection

(16 16 16) Mo K_α

Damage produced by

$\frac{1}{4}\mu$m diamond paste.

1 mm

Figure 5.1.1

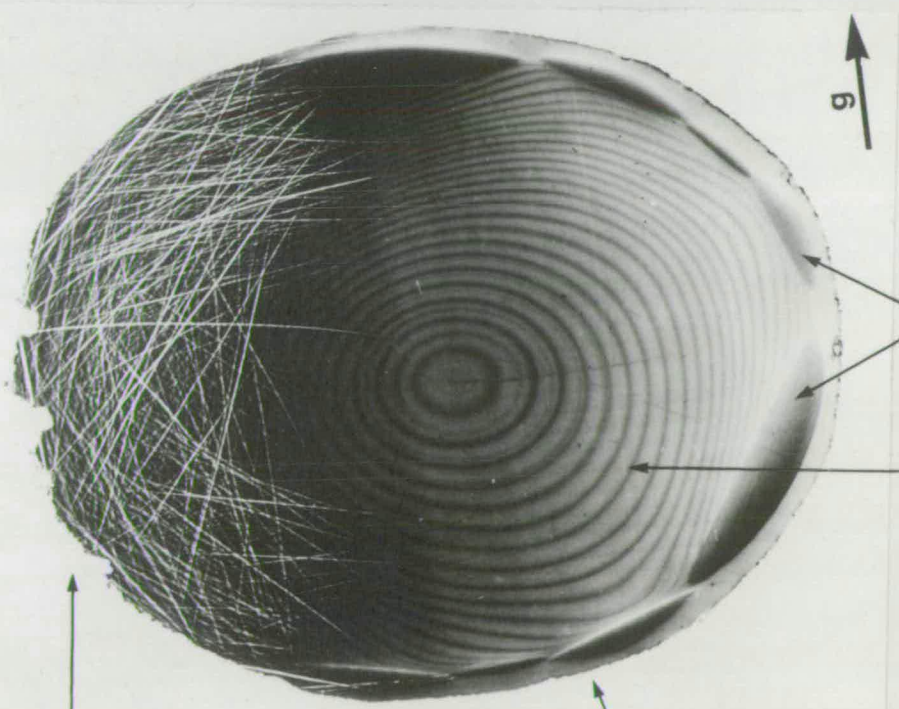

Figure 5.1.2

surfaces that appear free of scratches under optical examination. However, x-ray topography shows that even for ¼ μm diamond paste there are scratches present. The strains from these scratches mask the defect structure of the crystal, fig. 5.1.1 and, as will be shown in chapter 6, are sufficient to affect the growth of an epitaxial film.

Colloidal silica can be obtained with particle sizes of 0.03 μm dispersed in an aqueous solution (Syton by Monsanto). Care must be taken that larger particles do not form due to rise in temperature or pH. Any large particles present initially can be removed by filtration. Self-adhesive pads cannot be used since Syton will dissolve the adhesive. Cloths of nylon fabric are difficult to clamp and tend to wear rapidly if the cloth becomes wrinkled. Polypropylene pads were the most useful and easier to use with the raised rim of the lap necessary to retain the Syton since the pad could be waxed to the lap if necessary. Figure 5.1.2 shows a sample originally polished on 6 μm diamond which gave what appeared to be a good surface. It was then taper-polished on Syton with no intermediate polishing. The initial and final states can be compared and the improvement in the surface quality is self-evident and the underlying defect structure becomes visible.

5.1.2 Etching

The damaged layer produced by the sawing process or the thin Beilby layer left after Syton polishing can be

removed by dissolving the surface of the crystal in a suitable solvent. Garnets are fairly inert but will dissolve in hot orthophosphoric acid at a reasonable rate.[73],[74]

The phosphoric acid is held at ~300°C for a polishing etch although this does not produce a smooth surface if the sample is etched for a time much longer than a minute. The sample is supported by a platinum or Teflon cage and should be pre-heated if possible to avoid thermal shock. The surface damage is removed but there is a danger of cracking the slice, particularly if large internal stresses are present.

Phosphoric acid at a lower temperature, ~160°C, may be used as a selective etch to reveal scratches and dislocations.[74] Concentrated sulphuric acid at 110°C will also reveal scratches.

Other solvents such as molten PbO/B_2O_3 or molten V_2O_5 were tried but these were slow and the flux was retained on the crystal surface, particularly in the case of V_2O_5, and was very difficult to remove.

Etch polishing is less suitable than mechanical polishing for the production of a flat surface. The selective etch, ~30 sec in phosphoric acid at 160°C, will give a check on the efficacy of the mechanical polishing procedure but will not affect the overall surface flatness in that short time. This will also remove the Beilby layer of polishing debris which would otherwise dissolve in the flux during L.P.E. film growth.

5.1.3 Homoepitaxy

Liquid phase epitaxy can be used to grow a thin film of GGG on a GGG substrate.[123] If the temperature of the melt is initially above the saturation temperature a substrate lowered into the melt will dissolve slowly. Lowering the melt temperature below saturation will cause a thin film of GGG to grow on the substrate. This process will produce a smooth, damage-free surface on a platelet even from the as-sawn state but the surface will not be particularly flat. To produce a flatter surface there would need to be an initial lapping stage. The effect of defects is the same as for the LPE magnetic films discussed in chapter 6. Scratches have been removed if the initial dissolution stage has been employed. Without this stage there is little advantage in this method except that a very clean surface is produced. This can be taken advantage of by growing the magnetic layer immediately after the GGG layer has been grown.

Garnet grown by a flux method has a different lattice parameter from that grown by the Czochralski method.[50] The lattice parameter difference in the direction normal to the film was measured using the double crystal diffractometer for seven films of GGG and one film of GGG with some dysprosium substituted for the gadolinium. The lattice parameter of the film was less than that of the substrate for all these samples. The values are given below:

Sample	Film Composition	$\Delta a^{\perp r}$ Å
R19B	GGG	0.0088
E19	GGG	0.0025
E11	GGG	0.0058
R22B	GGG	0.0095
E10	GGG	0.0055
UC9	GGG	0.007
E9	GGG	0.0082
R24A	Dy:GGG	0.0140

5.2 Inclusions

During the Czochralski growth of GGG one of the components of the melt, Ga_2O_3, is liable to decompose and react to form lower oxides and oxygen. The suboxide may precipitate in the melt[56] and the oxygen will react with the iridium of the crucible to produce $Ir\ O_2$ in solution. This will react with Ga_2O to form Ga_2O_3 and a precipitate of iridium at the crystal interface.[126]

Precipitates of the suboxides have not been observed here but opaque inclusions of iridium, triangular or hexagonal in shape, have been seen occasionally. An optical micrograph of a sample containing a particularly high concentration of iridium inclusions is shown in fig. 5.2.1. The size of the inclusions ranges from 1 μm or smaller, to 30 μm. The largest number visible were triangular in shape and of about 2 μm in size. In this particular crystal the conditions leading to formation of the inclusions must have been fluctuating as the distribution of inclusions was not

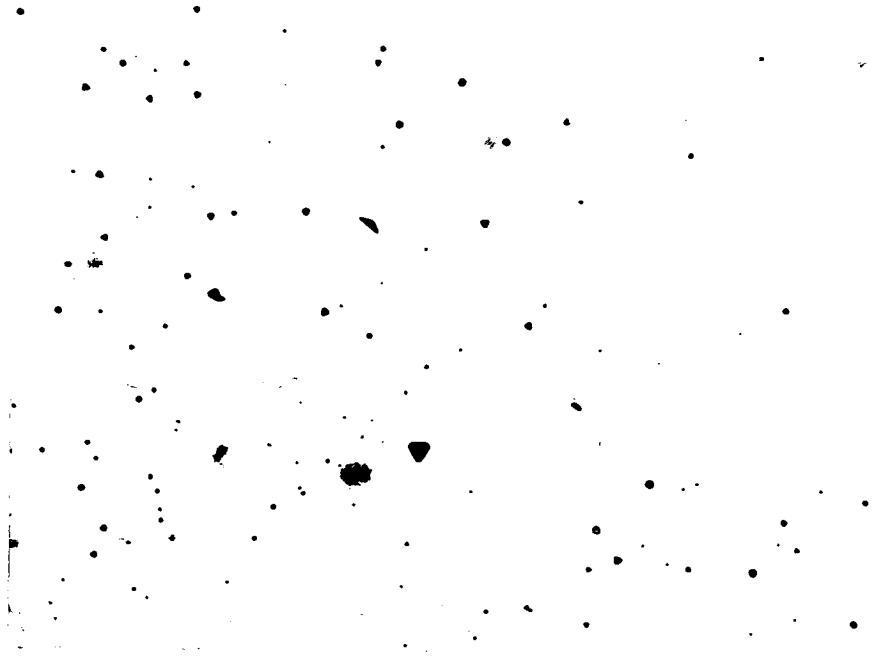

Figure 5.2.1

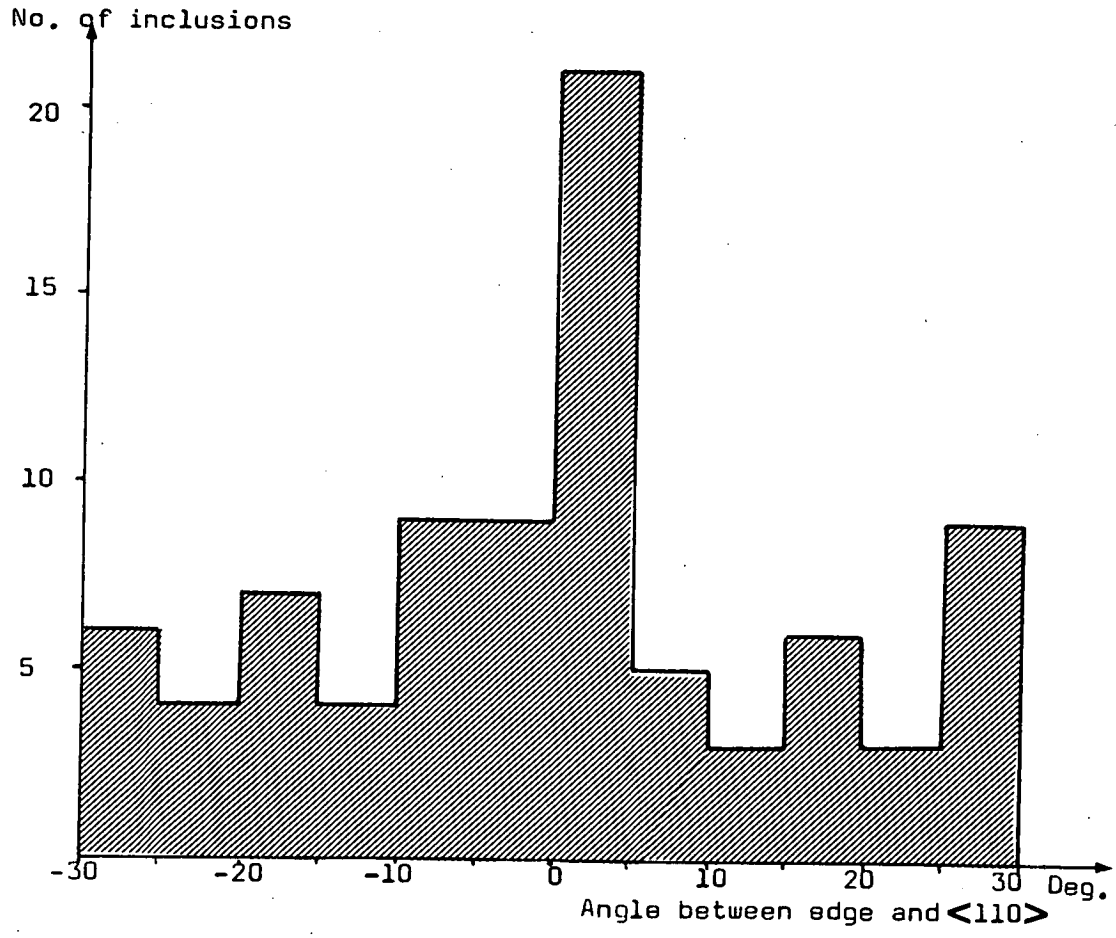

Figure 5.2.2

uniform. High concentrations of small particles occurred in bands perpendicular to the growth direction with, between the bands, a few, larger inclusions.

Inclusions formed in the melt, or swept from the crucible surface, and then incorporated into the growing crystal are likely to be oriented randomly. If the inclusions form at the crystal/melt interface some preferred orientation with respect to the parent crystal might be expected. Iridium metal has the cubic close-packed structure. The photographs show that the planes of the iridium plates are parallel to the {111} growth plane of the GGG crystal. A very few of the larger inclusions had the plane of the plate in some other orientation.

The histogram of fig. 5.2.2 shows the results of measurements of the angle an edge of the inclusion made with a ⟨110⟩ direction in the plane of the slice. The measurements were made on a fairly small number, 85, of the inclusions. The very small inclusions were difficult to measure and so are under-represented in the distribution.

There would be a uniform distribution if the inclusions were oriented randomly. The histogram indicates that some of the inclusions have a crystallographic relation to the GGG crystal but others, and these were mainly the larger inclusions, were oriented randomly. Iridium particles formed at the interface may be incorporated immediately into the parent crystal and thus lie in a particular crystallographic orientation. Some small Ir particles may be swept off the interface by strong

convection currents or high rotation rates or be produced by erosion of the crucible. These nuclei now in the melt but near to the interface will be able to grow to a larger size before being incorporated in the growing crystal. The plate-like shape of the inclusion would make it more liable to lie flat along the solid/liquid interface if it is not to be swept off again.

There was little or no strain around these inclusions as observed by optical means unlike some which have been observed by other authors.[127],[128]

5.3 Growth Bands

Small fluctuations in the temperature of the melt are difficult to avoid during crystal growth. These fluctuations will cause small variations in the composition of the crystal and thus cause small variations in the lattice parameter. These fluctuations may be observed by x-ray topography and have been induced by known temperature fluctuations for a flux-grown crystal.[129] If these variations are extreme they may be observed using polarised light but in general the variations are small.

The shape of the solid/liquid interface is determined from the shape of a lamella of a particular composition if it is known that this band runs completely across the crystal. Adjacent lamellae are slightly different in composition and are stacked up approximately normal to the growth direction.[130],[131] If the crystal is cut normal to the growth direction the effect

Growth bands in GGG.

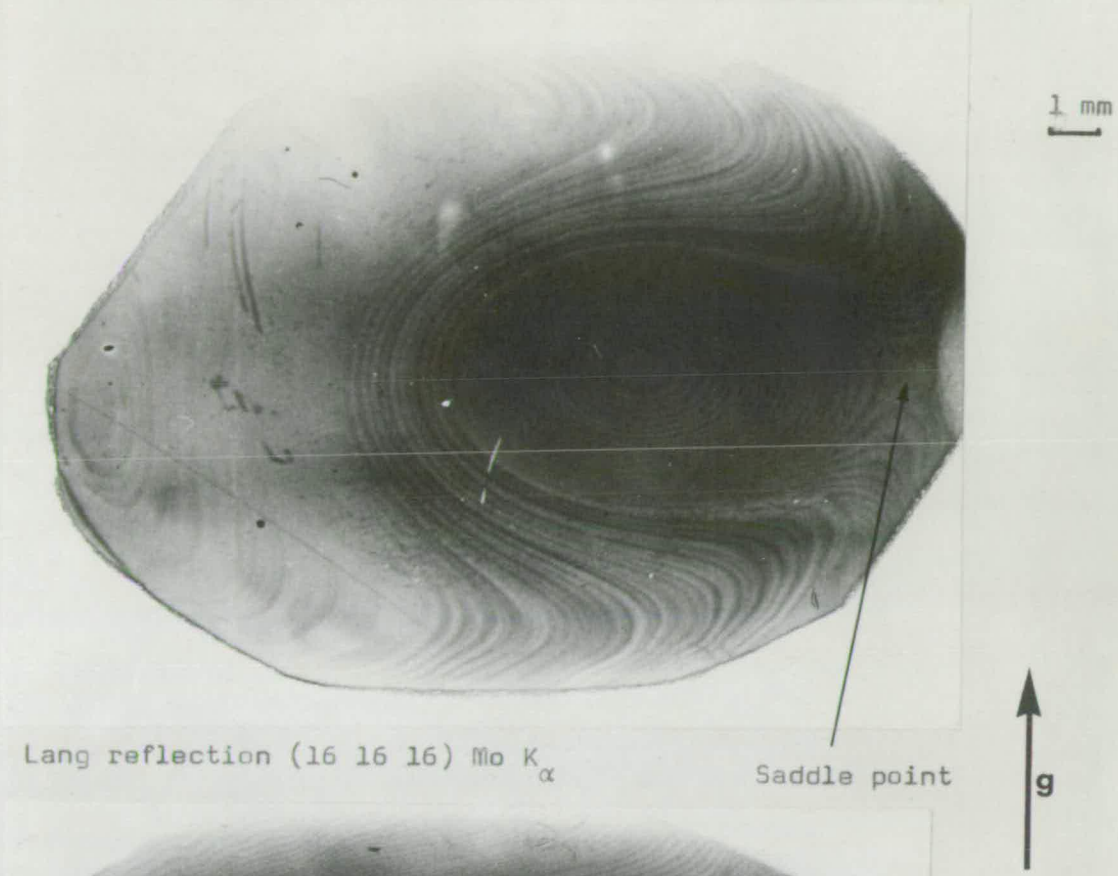

Lang reflection (16 16 16) Mo K_α

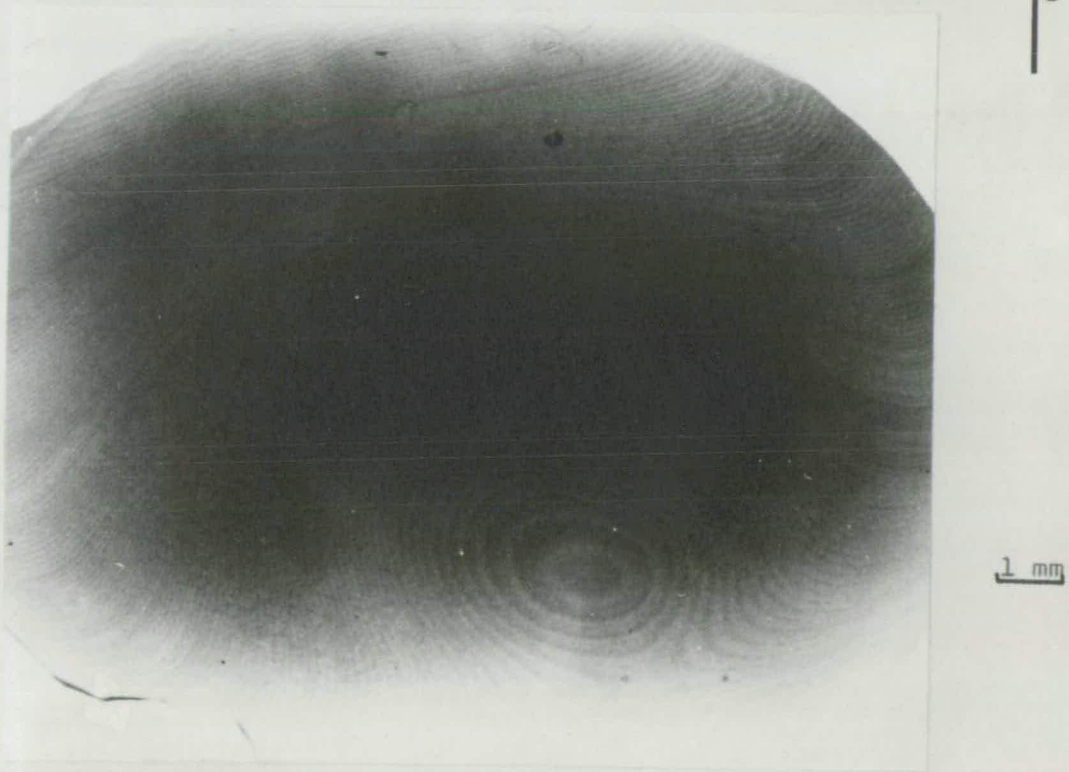

Figure 5.3.1

of non-planarity of the interface will give rise to a whorl-like pattern in a topograph. Once the interface shape has become established it will tend to continue throughout the crystal growth, as can be seen in fig. 5.3.1. This compares topographs of two slices from the same boule, the whorl-pattern is similar in each. Thus it seems reasonable that the whorl pattern reflects the shape of the solid/liquid interface and the banding can be considered as contour lines if no dissolution and regrowth of the crystal has occurred. In fig. 5.3.1 the crystal interface contained a saddle point. If the surface were symmetrically curved about the rotation axis the whorl pattern would be in the form of concentric circles, as in fig. 5.1.2. A flat surface, not normal to the growth direction, would have parallel, straight, equally spaced bands.

The curvature of the lamellae can be seen directly by cutting the crystal parallel to the growth direction which is approximately normal to the planes of the lamellae. This curvature is shown in fig. 5.3.2a, which is a transmission topograph of a thin sample and shows half the diameter of the boule. The centre of the boule is marked. The lamellae can be seen to extend right across the crystal in a smooth curve. There are scratches and dislocations, which will be discussed in section 5.6, also visible in the topograph. There are slight variations in the periodicity and x-ray contrast in the growth bands. The average periodicity of the striae for this crystal is 55 μm, another crystal had a periodicity of 38 μm in the growth

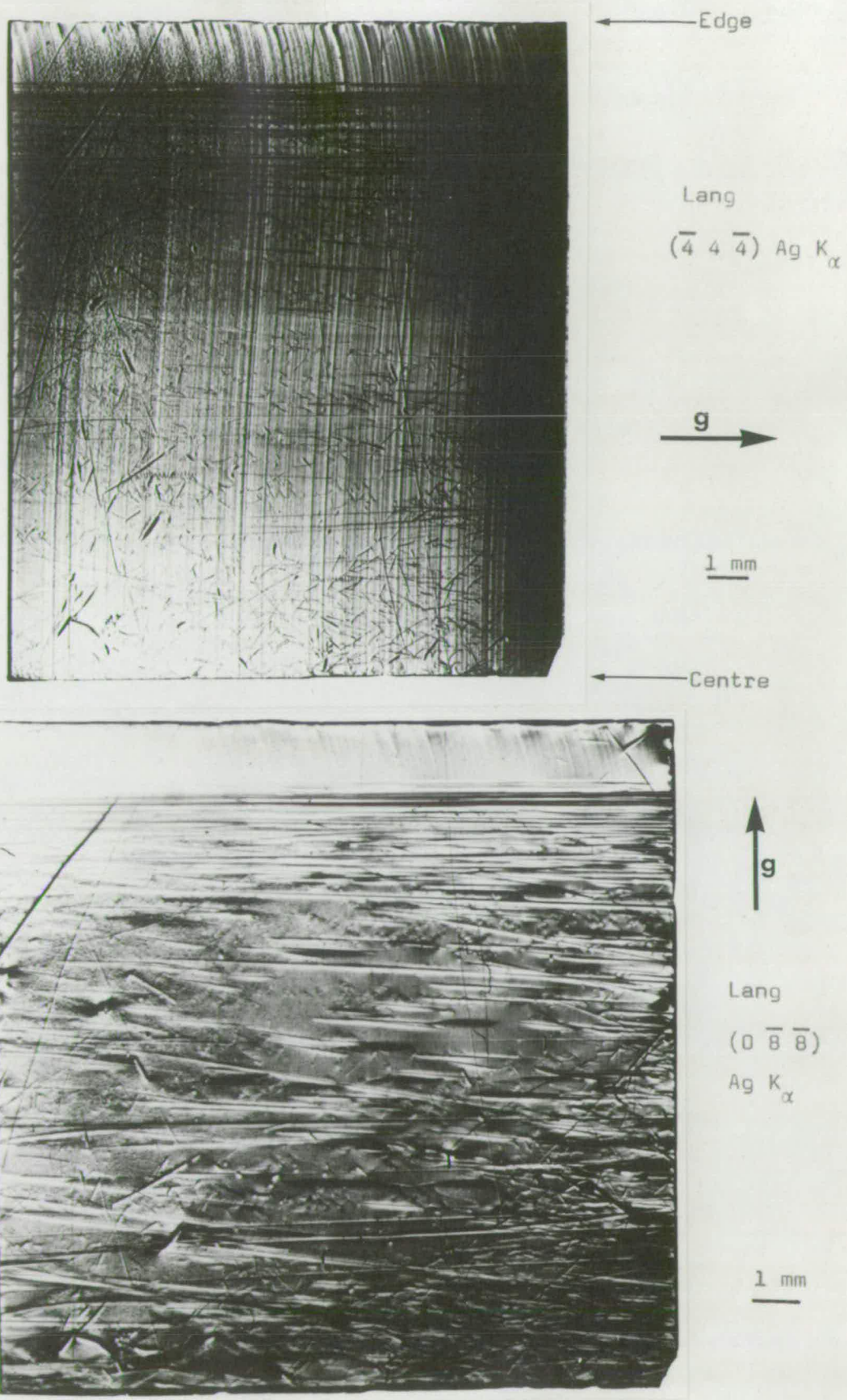

Figure 5.3.2

direction. Unfortunately, the information on growth rates and rotation rates of the crystal is unavailable. Comparison with the data in the paper by Belt and Moss[130] would indicate that the fluctuations producing the composition change last for the order of 40 seconds, while the time for one rotation is approximately two seconds. The detailed temperature fluctuations are likely to vary from one crystal growing system to another. In one particular case the growth band pattern indicated two superimposed composition fluctuations of different periodicity. The Lang reflection topograph of fig. 5.1.2 shows broad band variations. A double crystal topograph of the same sample, a small area of which is shown in fig. 5.3.3, shows, with its greater sensitivity, smaller fluctuations superimposed on the broad bands with six times the frequency.

As one lamella grows on another it is not free to take up its unstrained lattice parameter. In directions parallel to the planes of the lamellae a lamella of smaller lattice parameter than its neighbour will be under a tensile stress since the tendency is for all lamellae to have the same lattice parameter in directions in the plane. The lamellae can expand or contract freely in the growth direction. The lattice parameter differences will be increased over the free values by a proportion depending on Poisson's ratio. A topograph taken with the Bragg planes normal to the growth axis will thus show a high contrast and a topograph with the Bragg planes parallel to the growth axis will show very low contrast. This is seen by comparing figs. 5.3.2a and 5.3.2b. In (a) the

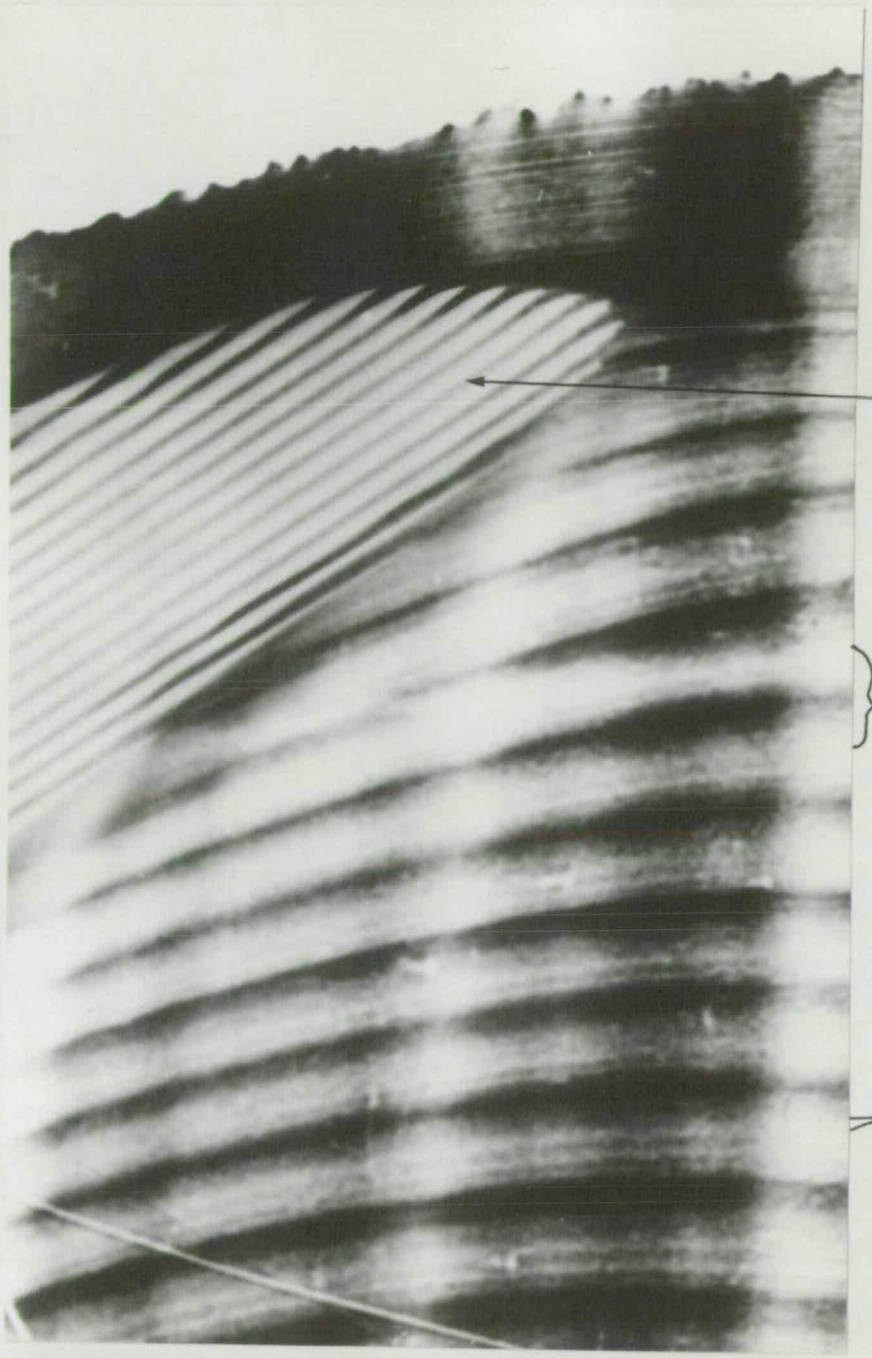
Double crystal
(8 8 8) Cu K_α
Facet
Long-term
variations.
Short-term
variations.
0.5 mm
g

Figure 5.3.3

bands are clearly visible while they are almost invisible in (b). This feature will be seen as an incidental part of many later topographs, particularly transmission topographs.

Numerical values of the changes in lattice parameter may be obtained from double crystal topographs, section 3.1. Transmission topographs are less amenable to numerical analysis since the width of the rocking curve depends largely on the width of the collimating slits. The optical density of an irradiated plate is proportional to the x-ray intensity up to optical densities of about two and this limit is not reached in the plates used here. A Joyce-Loebl microdensitometer was used to measure the optical density across a topograph. The minimum effective beam size obtainable in this instrument is $\sim$50 μm and so topographs of only one sample, which had broad bands 0.4 mm across in the (111) slice,could be used.

Double crystal topographs of one slice, using four different sets of planes, were measured across the same region. The same features were recognisable in each microdensitometer trace. Figure 5.3.4. shows one of these traces and compares it with the relevant strip of topograph. The contrast and therefore the measured $\frac{\delta d}{d}$ should decrease as the reflecting plane makes a greater angle with the plane of the slice. The greatest angle it was found possible to use for a topograph was 35.3° for {110} planes and this reflection should give a maximum reduction in $\frac{\delta d}{d}$ of 20% from the value measured for (111) planes. The value of $\frac{\delta d}{d}$ is very dependent on knowing the position

Double crystal topograph

Microdensitometer trace

1 mm

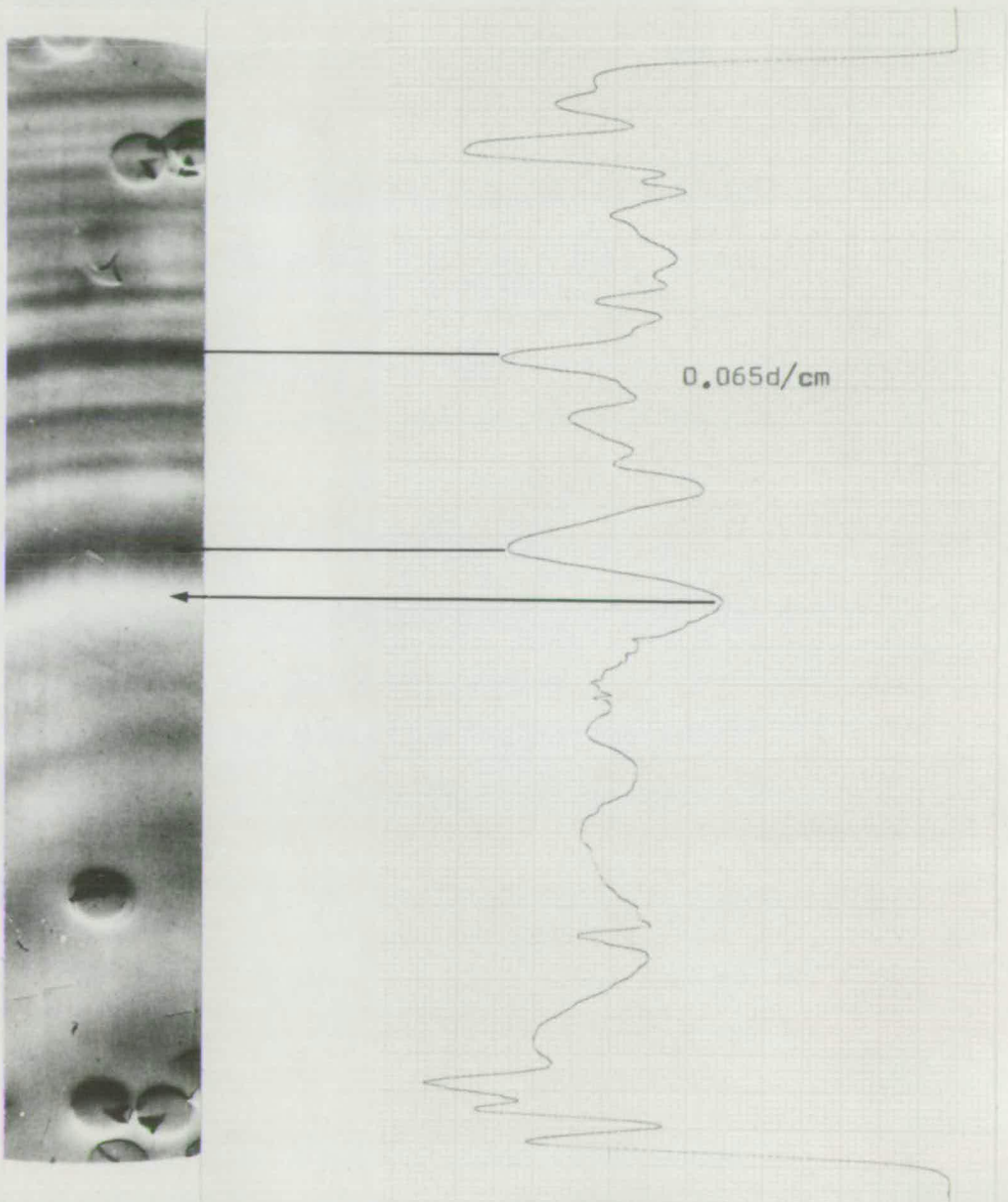

Figure 5.3.4

on the rocking curve at which the topograph was taken. This position is known to ± 10% and the level corresponding to this value must be determined on the microdensitometer trace. The following table 5.3.1 gives the average values of $\frac{\delta d}{d}$ for these reflections and the maximum value of $\frac{\delta d}{d}$ between neighbouring growth bands. The black/white contrast was the same for all of the topographs.

Reflection	Dir^n of $\underline{g}$	Angle of plane to (111)	$\frac{\delta \bar{d}}{d}$	$\frac{\delta d \text{ max}}{d}$
8 8 8	◄	0	1.0×10^{-5}	1.9×10^{-5}
8 6 4	▲	15.2	1.2×10^{-5}	3.0×10^{-5}
12 4 4	►	29.4	8×10^{-6}	1.8×10^{-5}
8 8 0	◄	35.3	1.3×10^{-5}	3.4×10^{-5}

TABLE 5.3.1

The effect of rotations of the atomic planes have been ignored and the dilatations alone considered. A constrained dilation will, in fact, produce some small rotations since the crystal is no longer cubic. In this case the rotations will be exceedingly small and produce a negligible effect on the intensity compared with the $\frac{\delta d}{d}$ effect.

The change in $\frac{\delta d}{d}$ as measured here corresponds to a maximum change in lattice parameter of 0.0002Å. If the growth bands were flat and parallel to the slice then the variation in lattice parameter across the slice could be reduced still further, although there still would be some

variation from slice to slice.

This particular sample was also measured using the Zebra pattern technique. Figure 5.3.5 shows the two horizontal stripes photographed at an angular separation of 48". The waviness of the lines corresponds to fluctuations of lattice parameter, measured from this photograph, of $\frac{\delta d}{d} = 2 \pm 1 \times 10^{-5}$, which confirms the value obtained by microdensitometry.

These lattice parameter variations are below those which can be detected easily by powder methods which gives a = 12.382 ± 0.001 for GGG. Similar lattice parameter variations to those found here have been found by Belt and Moss[130] and related to composition variations as found by electron beam x-ray microanalyser.

5.4 Coring and Faceting

The natural habit planes for garnet crystals are the slow growth planes {211} and {110}. During Czochralski growth of garnets at low rotation rates the solid/liquid interface is convex towards the melt. If the interface becomes parallel to one of these habit planes the interface will flatten locally into a facet which produces a strained region of crystal of slightly different lattice parameter. The extent of the facet depends on the curvature of the crystal interface since a flat, horizontal interface will not allow facets to form.[132] A flatter interface may be obtained by increasing the rate of rotation of the crystal. The angular relations between the facet planes are shown in the stereogram in fig. 5.4.1.

Zebra pattern

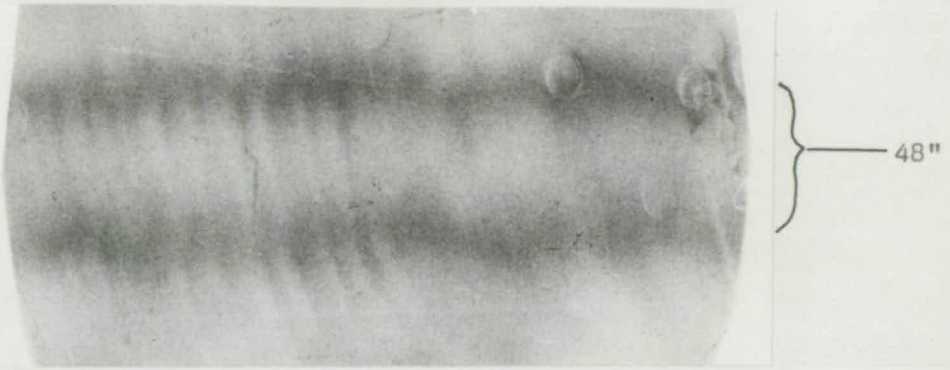

1 mm

Figure 5.3.5

Stereogram of facet planes round 111 growth axis.

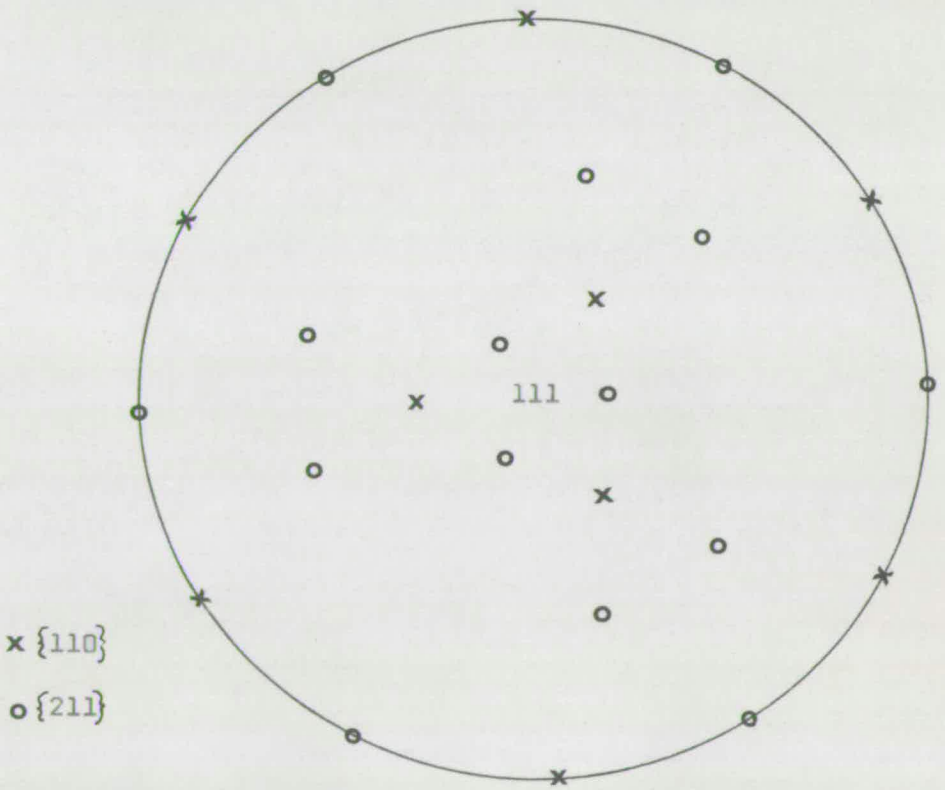

Figure 5.4.1

A smoothly curved crystal interface will give a curved growth band pattern. Faceting will give straight, parallel bands within the facet. The type of facet can be determined by measuring the spacing of these bands.[133] Facets of {211} and {110} type form and give a hexagonal morphology to [111] axis crystals by the formation of six {211} facets parallel to the growth axis. If the faceting occurs in the centre of the crystal it is known as a core; if it occurs towards the edge then it is known as a facet.

Strain is associated with the core since the slow growth planes grow having a slightly different lattice parameter. Cockayne et al[133] postulate a change in oxygen segregation since an effect of the same magnitude is observed in Czochralski-grown yttrium aluminium garnet. The strain produced at the boundary between core and matrix can be observed using polarised light, as shown in fig. 5.4.2. Details of the core and its growth band structure can be seen by reflection topography in fig. 5.4.3. Photograph (a) shows the other two lobes of the core in the same boule as that shown in fig. 5.4.2. Photograph (b) shows a complete slice across a small boule. The core occupies a large part of the crystal and shows the expected 3-fold symmetry. Comparison with the stereogram suggests that the centre trefoil is of {211} facets, the others are {110}.

Double crystal topography gives the value of the change in lattice parameter in the core. An extra peak in the rocking curve due to the core[134] was not found.

Circular polariscope

Figure 5.4.2

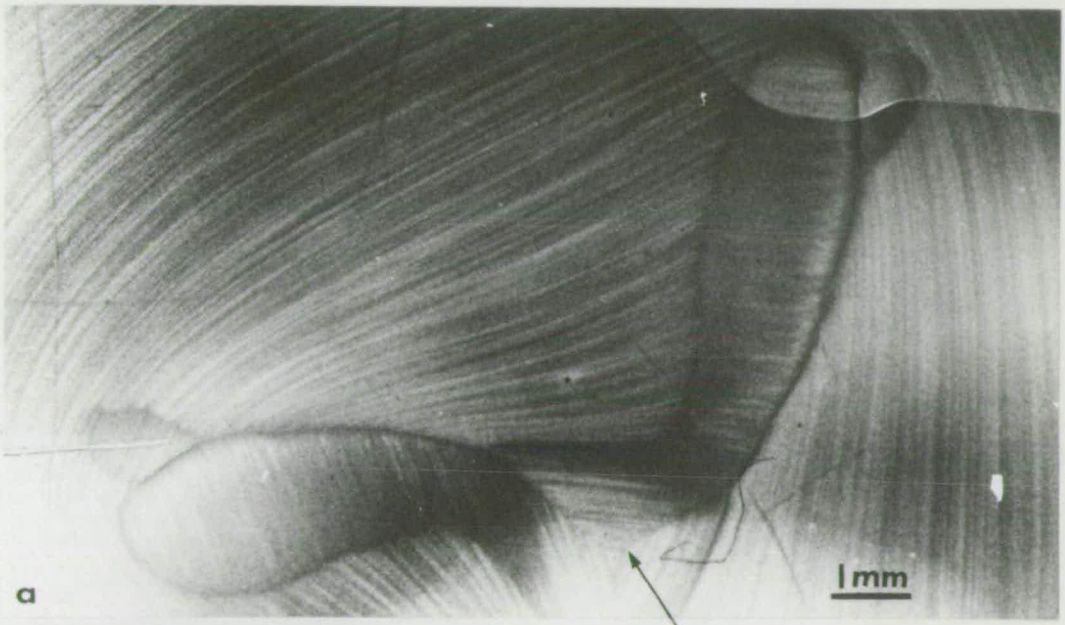

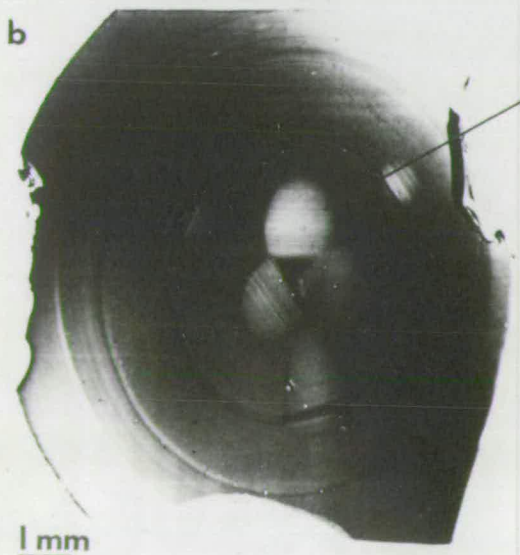

Lang reflection

(16 16 16) Mo K_{α}

Figure 5.4.3

The proportion of cored material was comparitively small and the x-ray wavelengths not long enough to give sufficient resolution. Changes in contrast of the following type were observed. For a topograph taken on the high θ side of the rocking curve the intensity from the core and an edge facet was less than the matrix which indicates that the lattice parameter in faceted regions is greater than in the matrix. There is also a difference between {211} and {110} facets. The central {211} facets show a greater decrease in intensity for this symmetric reflection than the {110} edge facet. The material of the {211} facet therefore has a larger lattice parameter than for {110} facets. Similarly, the intensity from the core is greater than that from the matrix if the topograph is set on the low θ side of the rocking curve.

The contrast across the core or edge facet, figs. 5.4.4 and 5.3.3, is not uniform, indicating either that the composition is not uniform in the core or that there is a bending outwards of the atomic planes at the boundary. The change in contrast gives a value for the change in lattice parameter of 0.001Å. Transmission topographs show that the contrast is less for reflections with the diffraction vector normal to the growth direction than for a reflection at some other angle, fig. 5.4.5. The core will be constrained by the matrix and, by symmetry, can relax only at the surface in the growth direction. Examination of slices taken parallel to the growth direction through the core would be useful, but such a sample was not available.

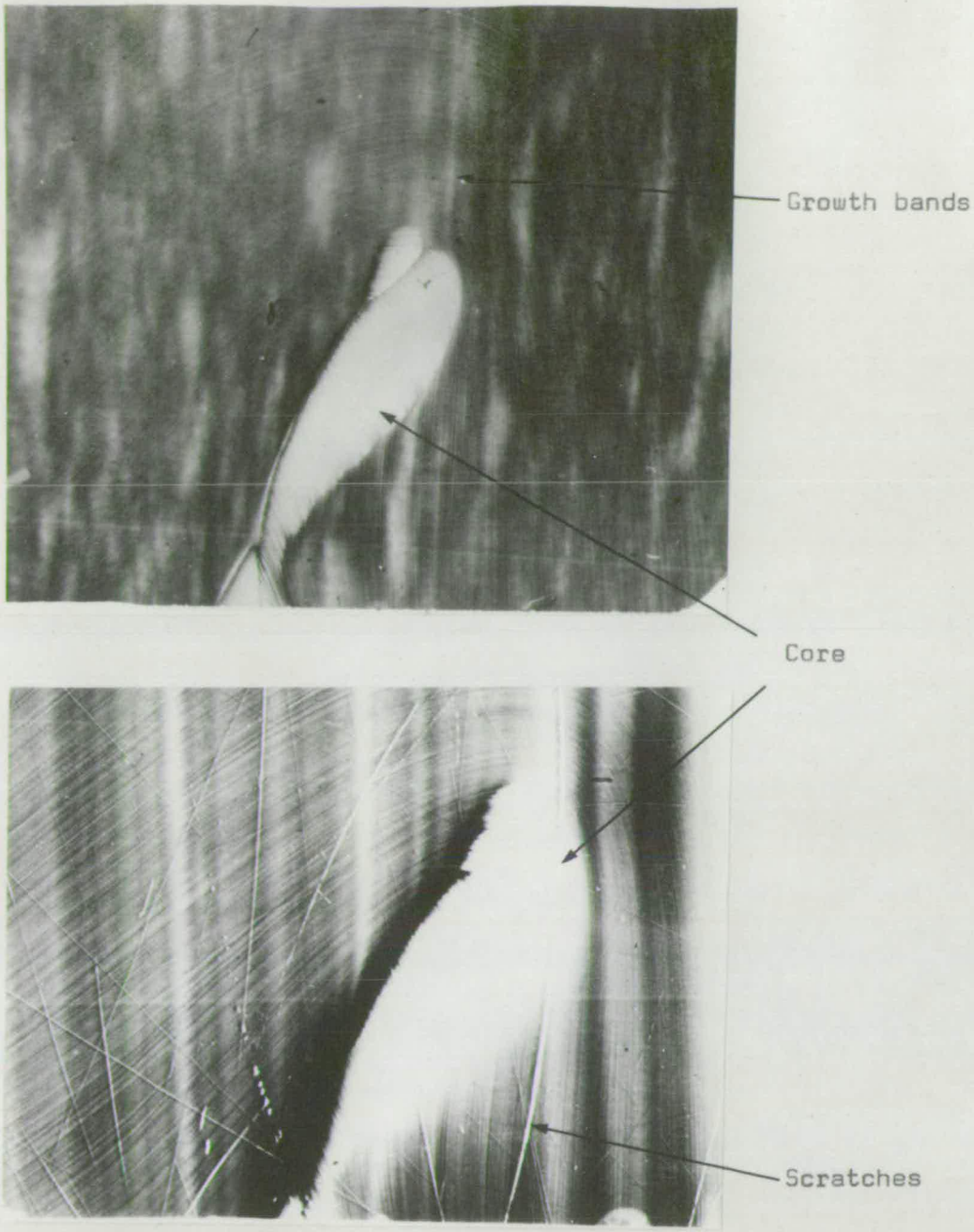

Double crystal (8 8 8) Cu K_α

High angle side of rocking curve

1 mm

Figure 5.4.4

Lang (8 8 0) Ag K_α symmetric

1 mm

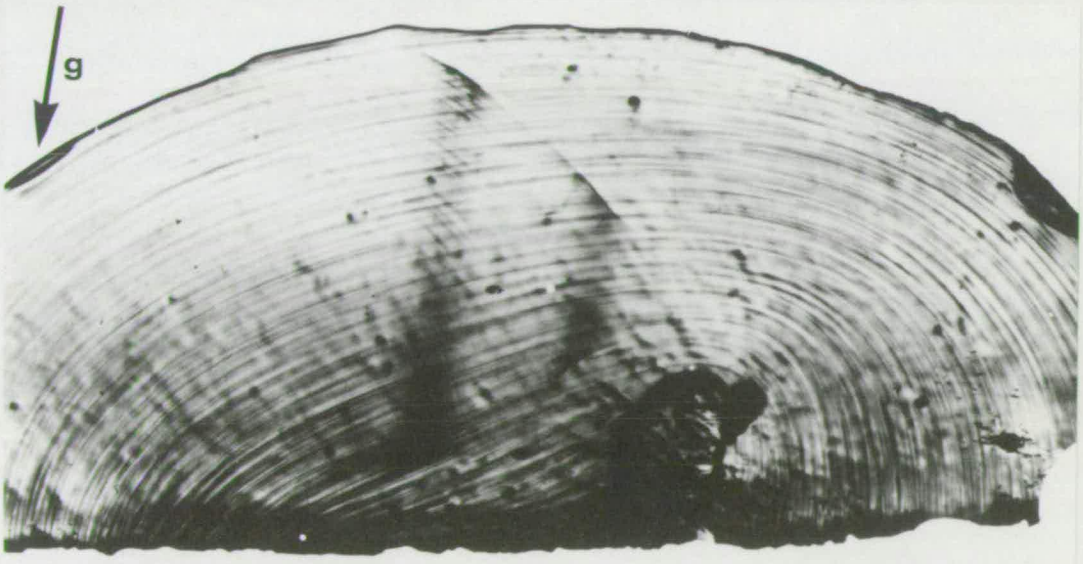

Lang (8 0 0) Ag K_α asymmetric

Figure 5.4.5

The facets can be kept small and at the edge of the crystal by flattening the crystal/melt interface through high rotation rates during growth. If necessary, the strain from these facets can be removed by grinding off the outer surface of the crystal.

Most of the samples examined contained edge facets at least. The one crystal which did not show facets had a ground surface.

5.5 Strained Rim

The growth bands shown in fig. 5.3.2(a) are almost flat except for a small region near the edge. There they curve steeply and indicate the direction of growth since the crystal is likely to be convex towards the melt at the periphery. An outer ring of this type was observed only in this crystal. It extended right round the crystal and is very highly strained. This strain is shown in fig. 5.5.1 by sodium isochromatics in the circular polariscope. The photograph is taken down the axis of the boule which is three centimetres in diameter and about eight centimetres long. The outer rim of width 2-3 mm is highly strained as can be seen from the sharp, closely spaced isochromatics. The crystal in the large central region is almost unstrained as there are very few broad, diffuse, low-order isochromatics even in this thick block.

This type of strain would occur if the material of the rim were of a different lattice parameter from the bulk. A smaller lattice parameter in the rim is indicated

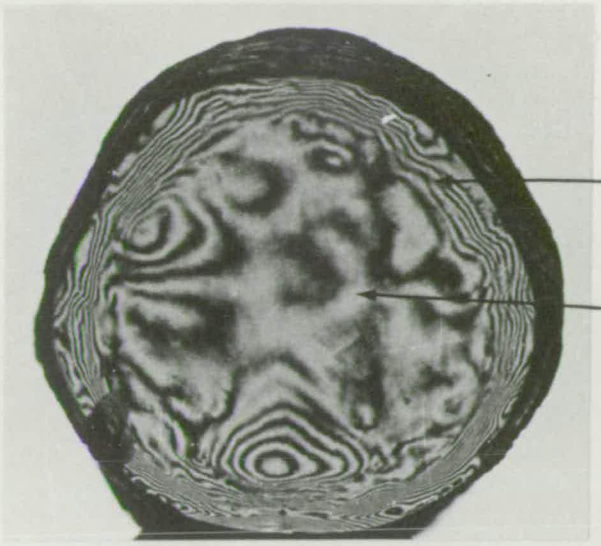

Figure 5.5.1

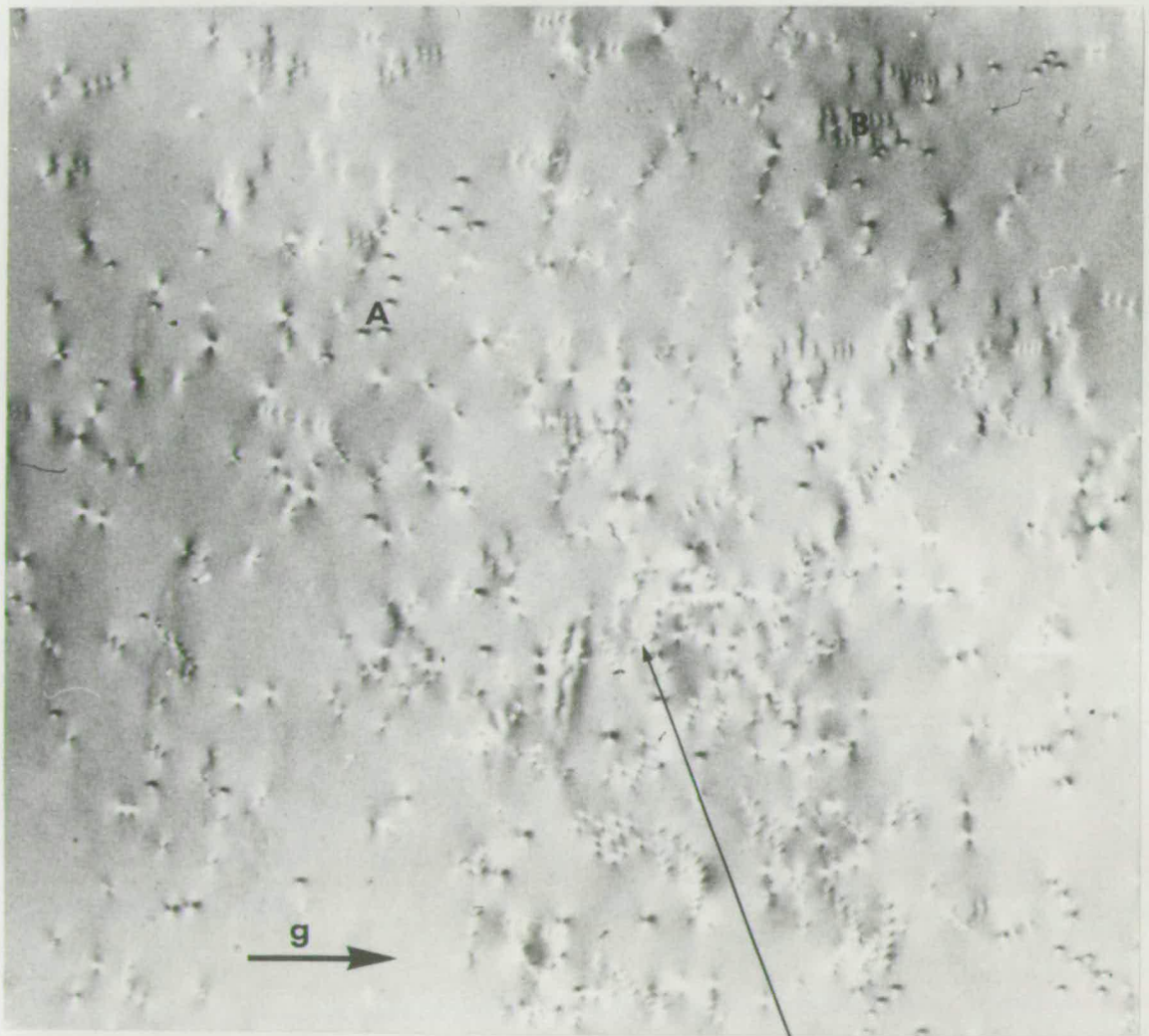

Lang (8 8 0) Mo K_α

Figure 5.6.1

by the presence of a crack in part of the boule at one end. This crack extends from the surface and runs normal to one of the 'flats' from a point midway along the 'flat' where the rim is at its thinnest to the internal boundary of the rim where it stops. Slices cut from this boule were susceptible to thermal shock and cracks would initiate from a similar point.

A rim which is in tension and the bulk which is in compression is also indicated by the contrast in x-ray topographs. Different conditions of melt composition, thermal distribution or melt flow may have combined to produce a region of crystal more nearly stoichiometric than the bulk of the crystal[130] and thus of a lower lattice parameter.

The compressive strain in the centre of the boule could be removed by grinding off the whole of the rim.

5.6 Dislocations

The defects in the crystals which have been considered so far have all produced only elastic distortions. Dislocations are line defects which occur when there is a discontinuity in the crystal lattice and result in a plastic distortion. Dislocations were observed by etching, x-ray topography and stress birefringence and were found in most of the crystal boules which were examined. The densities of dislocations varied between less than 10 lines/cm^2 to about 3000 lines/cm^2 and often appeared in 'bunches' rather than being uniformly distributed. There

is also a large variation in type of dislocation.

A dislocation cannot just stop inside a crystal but it can be terminated by interaction with another dislocation, an inclusion or the surface of the crystal. Thus any dislocations in the seed crystal for Czochralski growth, or formed at the seeding-on position, will propagate into the growing crystal. A dislocation line at a large angle to the growth direction should eventually reach the side surface and terminate there. Only those dislocations with their line approximately parallel to the growth axis will grow for a large distance in the crystal. Such dislocations are seen in fig. 5.3.2. Topographs taken of several (111) slices from the one boule show that the pattern of dislocations will persist although there may be some slight relative movement if the dislocation lines do not run exactly down the growth direction.

The cored samples shown in figs. 5.4 have few, if any, dislocations. The samples of figs. 5.3.1 and 5.3.2 are core-free but have a high density of dislocations. It would appear that a core in a sample blocks the propagation of dislocations down the axis of the boule and 'sweeps' them out to the side. This property has been used[54] to produce dislocation- and core-free boules by first growing a cored sample at low rotation rate to remove the dislocations and then increasing the rotation rate to flatten the solid/liquid interface and remove the core. Crystals produced recently have been found to be both core- and dislocation-free.

Careful examination of fig. 5.3.2 reveals the presence of two distinct types of dislocation. The dislocations near the edge by the rim are straight and run almost along the [111] direction. Nearer the centre of the boule there are many dislocation lines which appear wavy or as short, straight lines stacked up like plates along the growth direction. These are dislocations in which the line takes the form of a helix and will be discussed in subsection 5.6.2.

5.6.1 Straight-line dislocations

The straight dislocations occurring in two samples will be discussed. The sample shown in fig. 5.3.2, sample II, has already been mentioned. The sample of figs. 5.6.1 and 5.3.1, sample I, contains only straight dislocations which are seen end-on in the topographs. The boule from which these slices came was rather small and so no longitudinal slice was available for study.

Sample I

Figure 5.6.1 is a transmission topograph of a thin (111) slice and shows a large number of point-like images which occur in bunches and arrays. Each member of a particular group, e.g. group A, has the same type of contrast which may be different from that in a neighbouring group, e.g. group B. This shows that the point defects are dislocations with each group consisting of dislocations of a particular Burgers vector. Groups of inclusions would all have the same image with a line of zero contrast normal to the diffraction vector. Confirmation of this

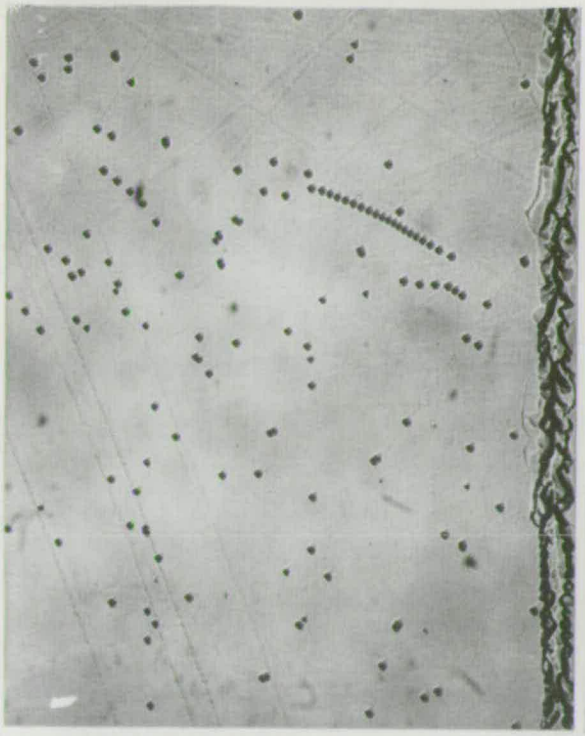

Etch pits on top surface.

Dislocations viewed by polarised light.

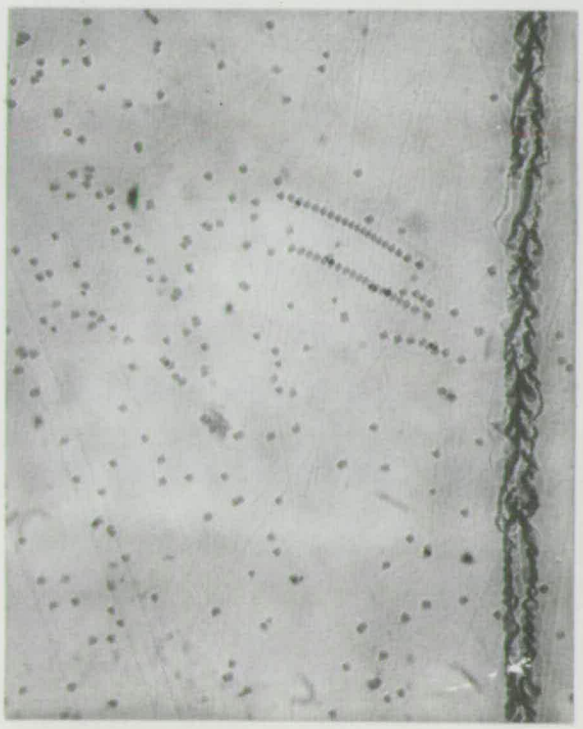

Etch pit patterns of top and bottom surfaces superimposed.

Thickness of slice = 600 μm.

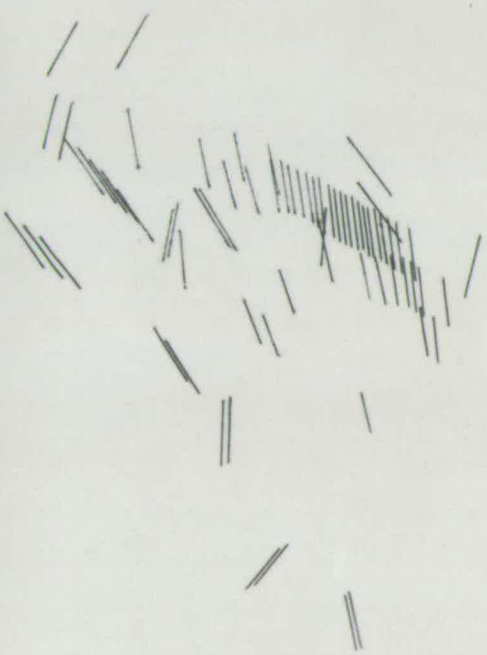

Trace of dislocation lines.

100 μm

Figure 5.6.2

can be obtained by etch pit and polarised light studies on a thicker slice.

If a dislocation line runs through a slice then an etch pit should form at each end of the dislocation where it intersects the surface. Birefringence should allow the dislocation line to be seen in polarised light. Figure 5.6.2 shows a sequence of photographs of etch pits on the two surfaces and the dislocation line. The straight lines of low contrast are the result of residual polishing damage. A double exposure made without any movement of the crystal superimposes the etch pit patterns of the top and bottom surfaces. Certain features such as the long line of etch pits can readily be identified on both surfaces. The angle the dislocation line makes with the growth direction can be determined if the thickness of the slice is known. The angle the dislocation makes varies from 3^{o} to 13^{o}, with most of them at an angle of $6\text{-}7^{o}$ as in this figure. The dislocation lines lie on no particular crystallographic direction apart from being close to [111]. These dislocations must have a large edge component since they are visible both in the topograph and in polarised light. Unfortunately, the inclination of the dislocation lines of $\sim 7^{o}$ is too large to use the stress birefringence pattern to determine Burgers vectors[97] except in a few isolated cases where the edge component of $\underline{b}$ lies in the $\langle 110 \rangle$ directions. Most dislocations are probably of mixed type as they are also visible in double crystal or Lang reflection topographs, see fig. 5.6.3, with the diffraction vector parallel to [111].

Dislocations visible in Double Crystal topographs.

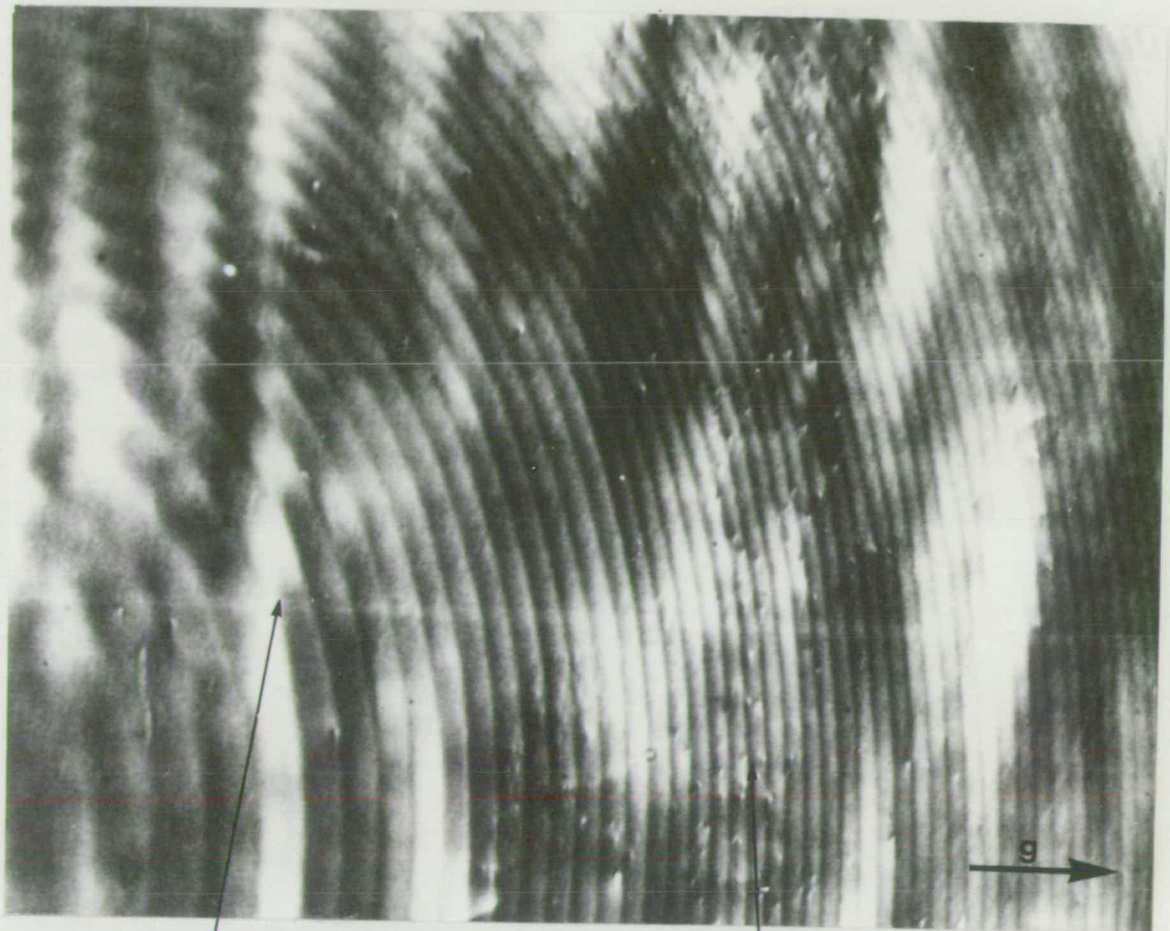

Double crystal (8 8 8) Cu K_α

1 mm

Figure 5.6.3

Dislocations viewed by polarised light.

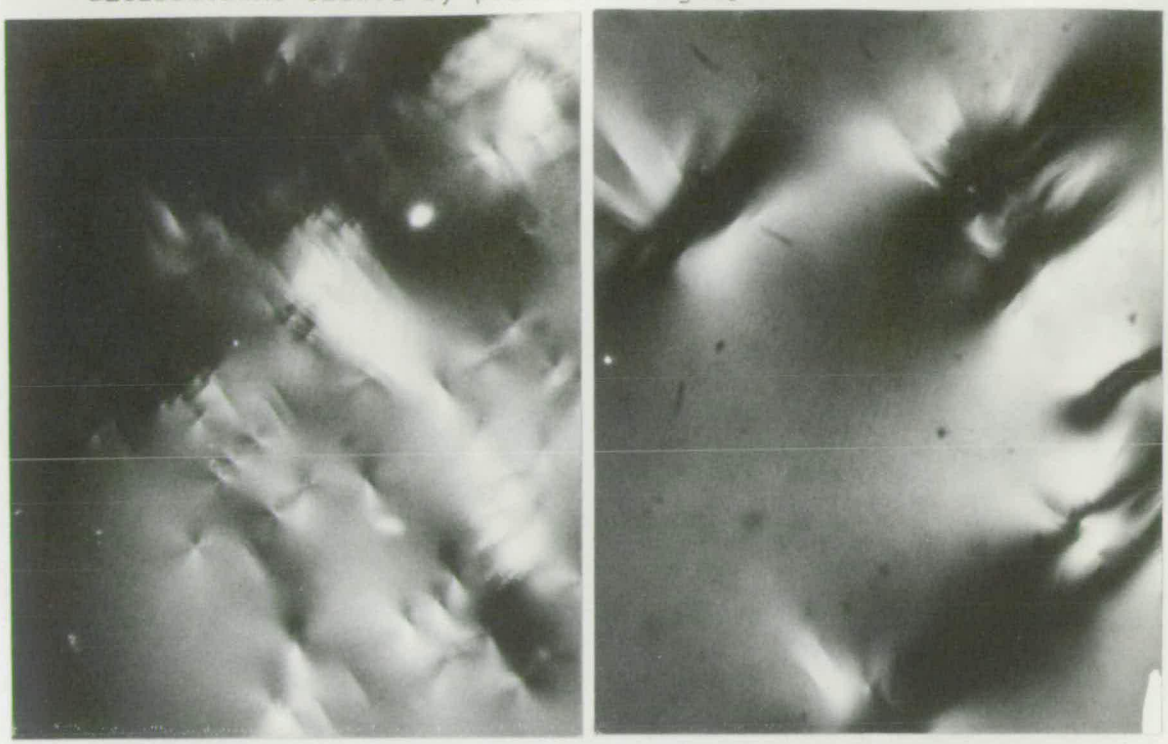

a) Even distribution of dislocations

b) Bunches of dislocations

100 μm

Figure 5.6.4

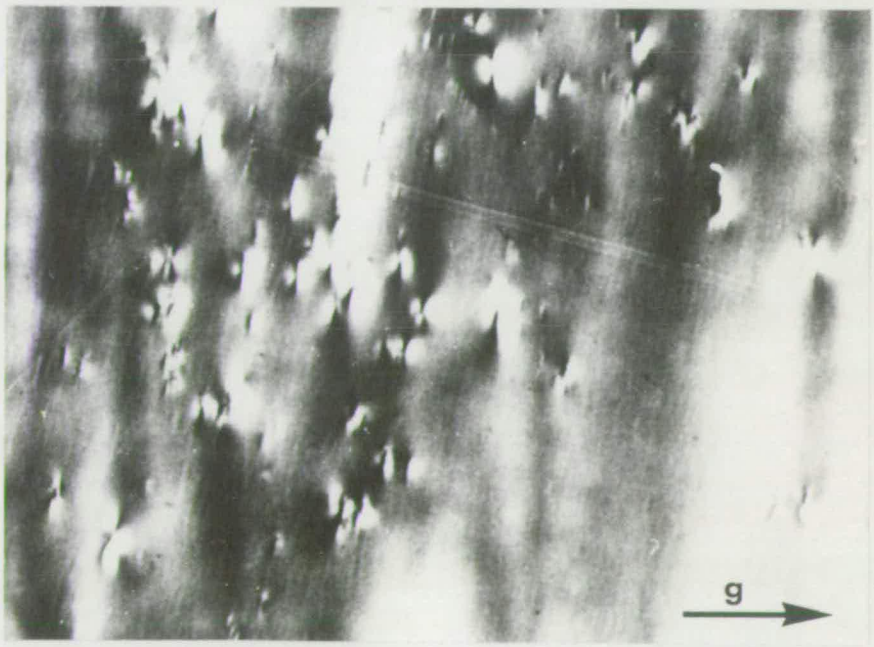

Regions of high strain

Double crystal (8 8 8) Cu K_α

Figure 5.6.5

This boule was not cylindrical in shape but increased from a diameter of 13 mm near the seed end to a maximum diameter of 25 mm a distance 21 mm away. Dislocations, if they are nucleated on the seed, will thus 'fan-out' along the length of the boule and not lie along the [111] axis. A slice taken at the smallest diameter was examined. The dislocations in fig. 5.6.1 are fairly evenly distributed over the region shown. An area with a similar distribution was found in the seed and slice and this is shown in the fig. 5.6.4(a) but there are also some areas of high strain where the dislocations occur in 'bunches', fig. 5.6.4(b). These areas are visible in the topographs of fig. 5.6.5 where the highly strained regions look like images of inclusions. The dislocation lines in each bunch are inclined by a large angle of 10^{o} or more to the [111] direction and appear to radiate from a common point in each bunch, although this point is not contained within this slice. This sample contains a few large inclusions of iridium but the strain field around these is very low and none was identified as being associated with one of the regions of high strain. These dislocations probably were initiated at the seed/crystal boundary or in a region of much higher inclusion density. No inclusions were observed in slices from the wide end of the boule.

Sample 2

The straight dislocations running almost parallel to the $[1\bar{1}1]$ growth direction in the region of high dislocation density are ideally suited to examination by polarised

Rim dislocations

Calculated image

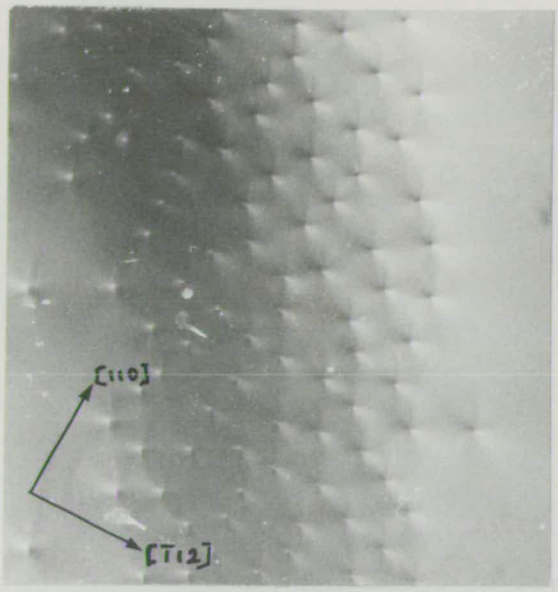

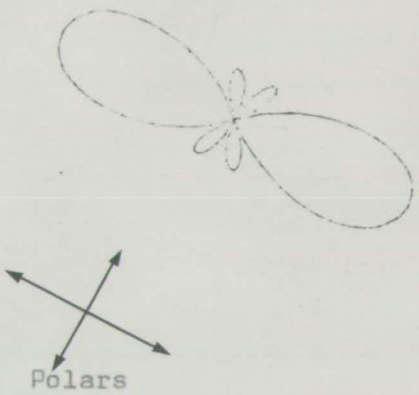

100 μm

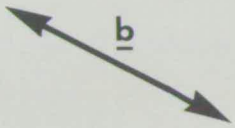

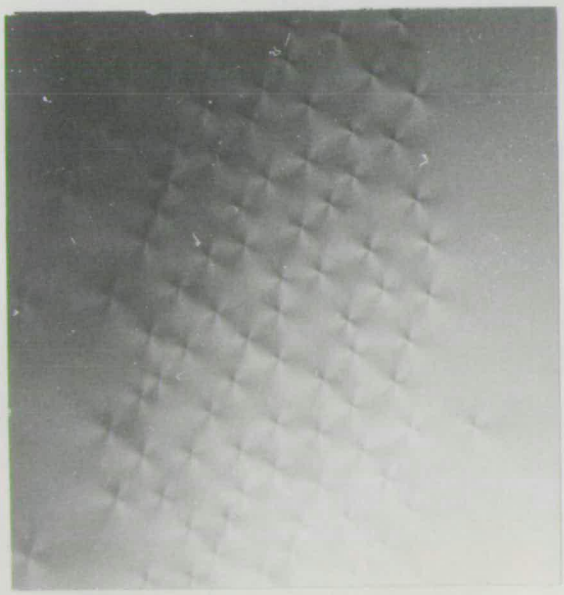

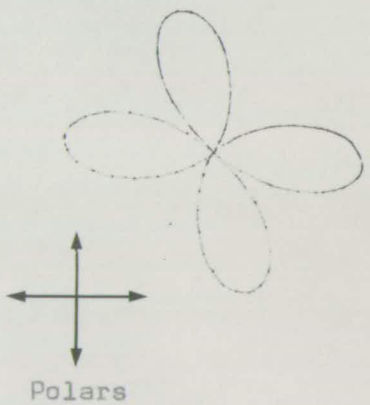

Figure 5.6.6

Orientation of samples.

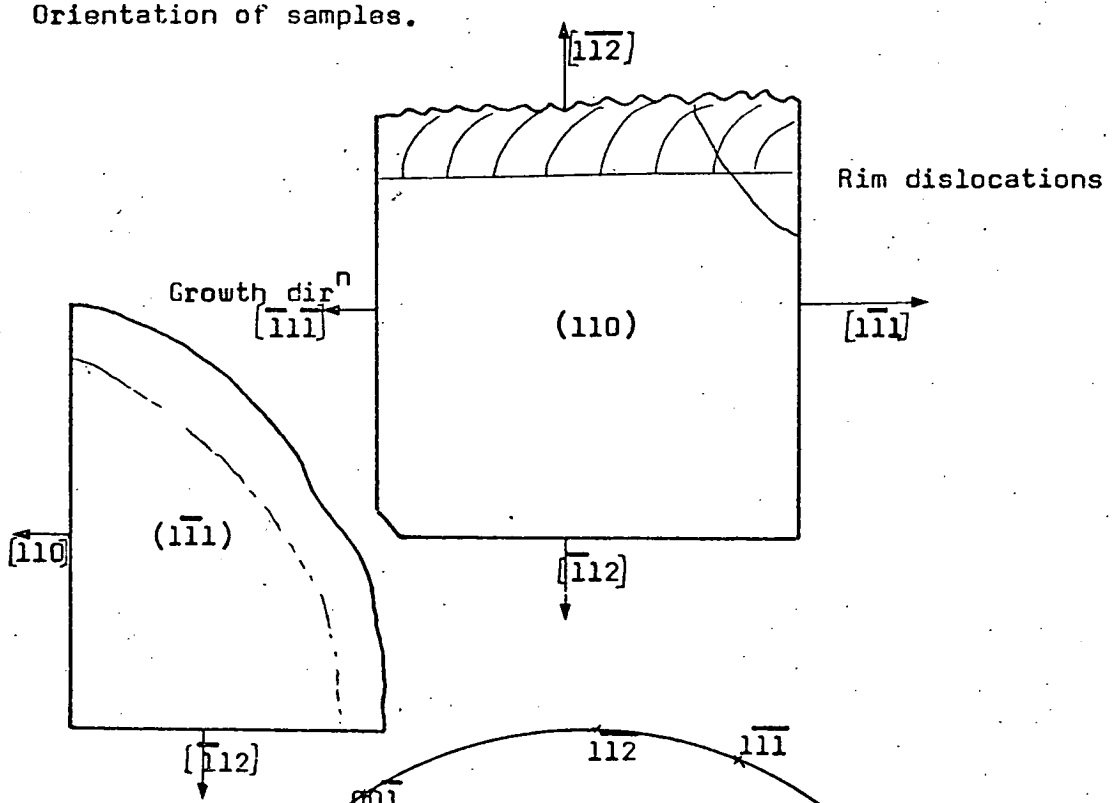

Stereogram

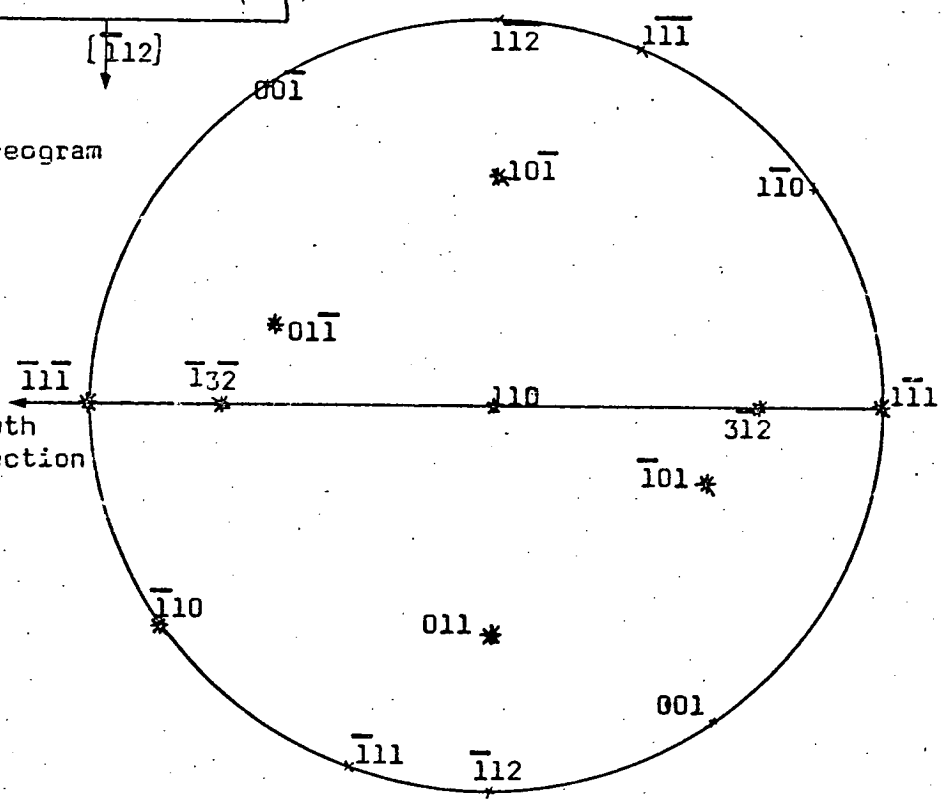

Growth direction

* Planes used for topography

Figure 5.6.7

light in a slice cut normal to the growth direction. Figure 5.6.6 shows two photographs of the dislocations with the polar parallel and at 45° to the Burgers vector direction. The crystallographic directions of the sample are marked. The dislocations all have a large edge component and appear to be all of the same type and of the same size. This is likely to occur if the dislocations are taking up the misfit between the rim, subsection 5.5, and the bulk of the crystal. The direction of the Burgers vector lies in the $[110]$ zone, fig. 5.6.7 describes the arrangement of axes, and is likely to be one of $\pm[1\bar{1}0]$, $\pm[1\bar{1}\bar{1}]$ or $\pm[001]$. The growth direction $[1\bar{1}1]$ is excluded from this list even though it lies in the zone since such a dislocation would be pure screw and thus should not show up by optical means.

Of the three dislocation types given above the $\langle 111\rangle$ type is the most probable since this dislocation has the smallest energy, $|{}^{a}/_{2}\ \langle 111\rangle|^2 < |a\langle 100\rangle|^2 < |a\langle 110\rangle|^2$, and is the closest to a pure edge dislocation which would be best able to relieve the misfit stresses. On these grounds the $\langle 110\rangle$ type Burgers vector would be the least likely. This hypothesis can be tested by x-ray methods although the high density of dislocations means that in even a thin slice there is overlap between the dislocation images.

Table 5.6.1 gives the angle between the various diffraction vectors used in the series of topographs and the possible Burgers vector directions. The cases for

Reflection \ Burgers Vector	001	100	010	110	011	$10\bar{1}$	$1\bar{1}0$	101	$01\bar{1}$	$1\bar{1}\bar{1}$	111	$11\bar{1}$	$1\bar{1}1$
$\bar{1}1\bar{1}$	55	55	55	90	90	90	35	35	35	71	71	71	0
$3\bar{1}2$	58	37	75	68	79	79	41	19	55	72	52	90	22
$1\bar{1}1$	55	55	55	90	90	90	35	35	35	71	71	71	0
$\bar{1}3\bar{2}$	58	75	37	68	79	79	41	55	19	72	90	52	22
$10\bar{1}$	45	45	90	60	60	0	60	90	60	35	90	35	90
011	45	90	45	60	0	60	60	60	90	35	35	90	90
$\bar{1}10$	90	45	45	90	60	60	0	60	60	35	90	90	35
101	45	45	90	60	60	90	60	0	60	90	35	90	35
$01\bar{1}$	45	90	45	60	90	60	60	60	0	90	90	35	35
321	75	37	58	19	55	68	79	41	79	90	22	52	72
110	90	45	45	0	60	60	90	60	60	90	35	35	90
311	72	25	72	31	65	65	65	31	90	80	30	59	59

TABLE 5.6.1

Angles between the diffraction vectors and possible Burgers vectors

which $\underline{g}$ and $\underline{b}$ would be at 90^{o}, and thus the image contrast low, are marked. Since the dislocations are neither pure edge nor pure screw there will be no reflection for which there is a complete absence of contrast. The situation is further complicated by the presence of growth bands which suppress the dynamical image of the dislocation in the cases where the growth band contrast is strong. In other reflections the growth band contrast is weak and the dynamical 'shadow' image is present.

Figure 5.6.8 shows a series of topographs of a small region of crystal near the rim. Consultation of table 5.6.1 indicates that the Burgers vector of the rim dislocations is $\pm\, {}^{a}/_{2}\ [\bar{1}11]$. The sign of the dislocation is not yet determined. Since the rim is of smaller lattice parameter than the bulk the sketch below shows the necessary arrangement of the edge components of the dislocation which will relieve some of the stresses.

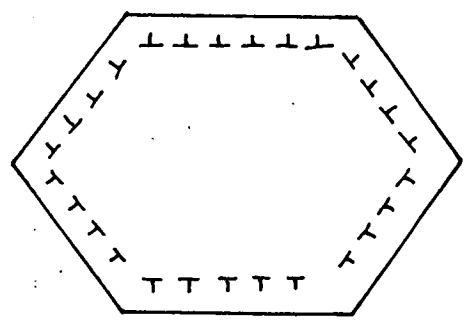

In the interior of the crystal the net stress should be low and there should be less restriction on the type and sign of the dislocations. Towards the centre of the crystal the straight-line dislocations run less exactly parallel to

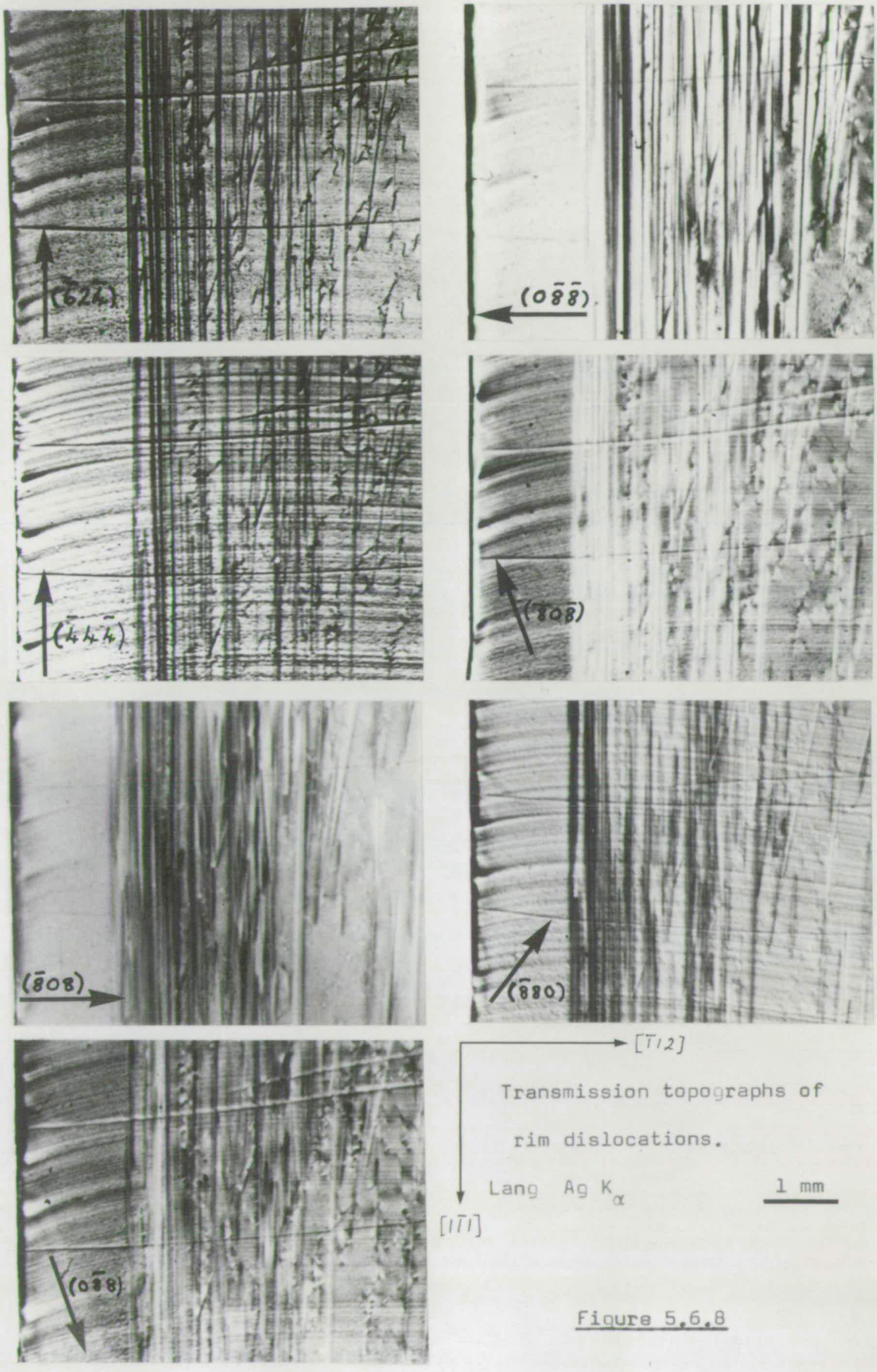

Transmission topographs of rim dislocations.

Lang Ag K_α 1 mm

Figure 5.6.8

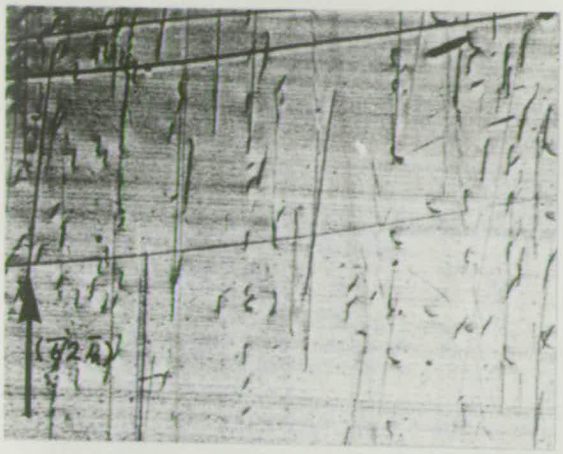

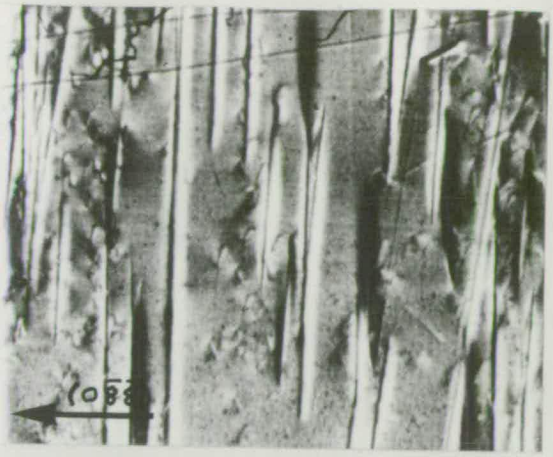

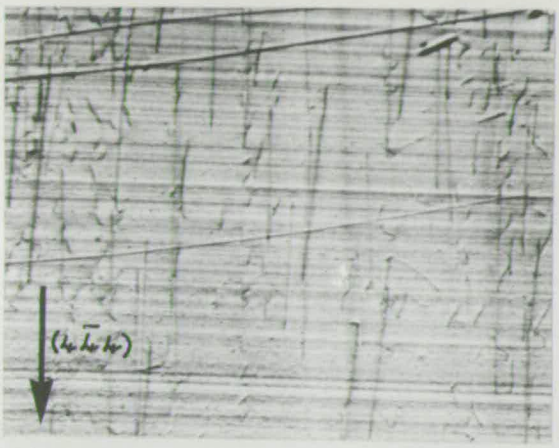

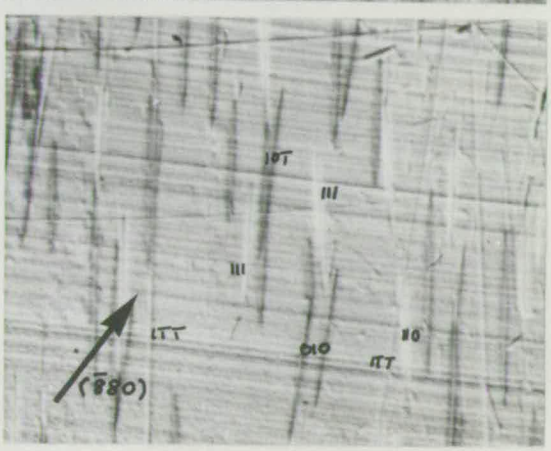

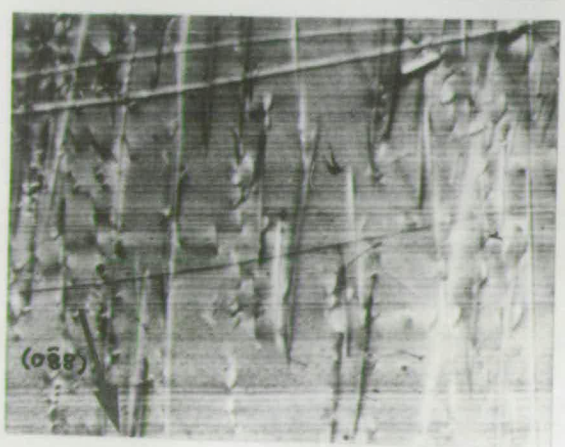

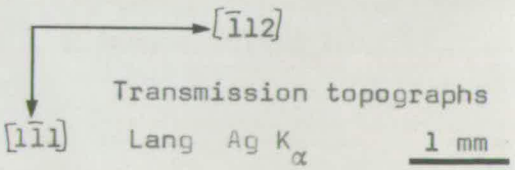

Transmission topographs

Lang Ag K_α 1 mm

Figure 5.6.9

the growth direction and so are not suitable for optical analysis. Many of the short line segments are part of helical dislocations. In most places the dislocation density is high and the images overlap. Figure 5.6.9 shows an area of comparatively low dislocation density. Dislocations of different types, $^{a}/_{2}$ <111> and a <110> are observed and indicated in the figure. These are similar to those found by Glass.(135)

5.6.2 Helical dislocations

Dislocations have been observed in many materials in which the dislocation line, instead of being straight or only slightly curved, takes the form of a helix. These have been observed by electron microscopy in metals.(136),(137),(138) The diameter of these helices is very small at ~1500Å. Larger helices have been found by decoration techniques in CaF_2 and NaCl(139) where the diameter is 40 μm and by x-ray topography in sapphire.(140) These dislocations have a diameter of ~50 μm. The studies by electron diffraction and x-ray topography determined the Burgers vectors of the helices and found them to lie parallel to the axes of the helices.

Helical dislocations have been observed in GGG by optical means(141),(142) and by x-rays.(143),(144) These dislocations were ~200 μm in diameter, which is much larger than those in the other materials mentioned. Helical dislocations were found in two of the crystals examined in this study, samples II and III. The helices could be divided into two types.(145)

Sample II

The helices in this sample run almost exactly along the growth direction and some can be traced over a distance of about one centimetre. If the helix is of a similar type to those mentioned above the Burgers vector should lie parallel to the helix axis and to the growth direction, $[1\bar{1}1]$. Thus topographs with diffraction vector $(1\bar{1}1)$ should show maximum contrast whereas reflections $(10\bar{1})$, (011) and (110) should show zero or minimum contrast. These topographs are shown in fig. 5.6.10. Other reflections give contrast intermediate between these extremes. All of the helices behave in the same way and so they all have Burgers vector $^{a}/_{2}\,[1\bar{1}1]$.

The image of the helices is simple and some of them show complete turns in the sample, which is 160 μm thick. The diameter of these helices is ~120 μm, which is comparable to those observed by other authors. The pitch to diameter ratio is approximately one and constant over the length visible. Neighbouring helices have different pitches. The $(10\bar{1})$ and (011) reflections should show very low contrast since $\underline{g}$ is perpendicular to $\underline{b}$ and very nearly parallel to most of the dislocation line except where the line runs normal to the (110) slice. Slightly higher contrast is visible at these points. A (110) reflection used in the $(1\bar{1}1)$ slice, fig. 5.6.11, has $\underline{g}$ perpendicular to $\underline{b}$ but the dislocation line, which here will appear approximately as a circle, will only be parallel to the diffraction vector at two points. Zero contrast occurs only at these points.

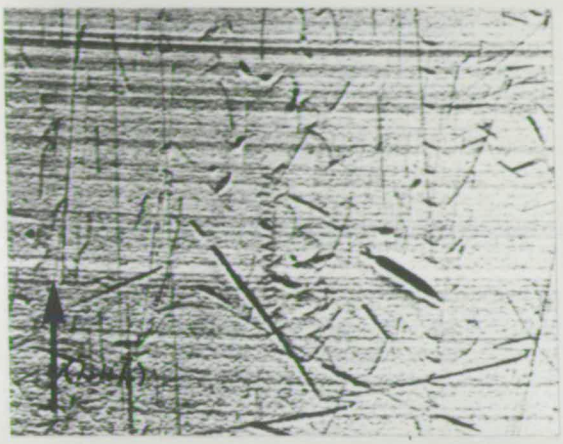

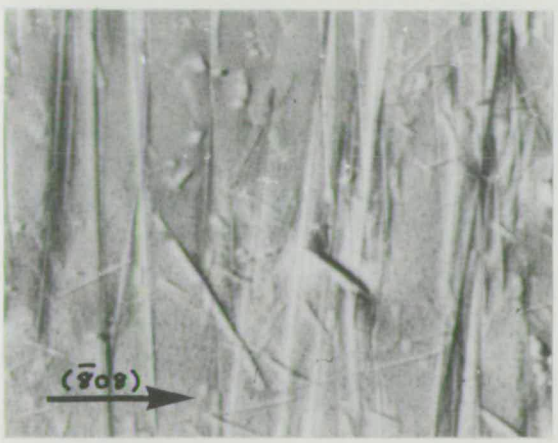

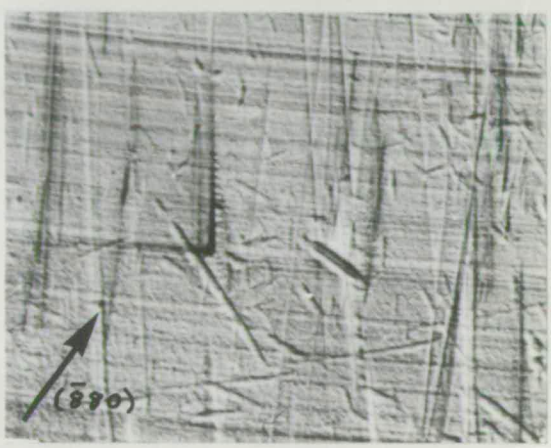

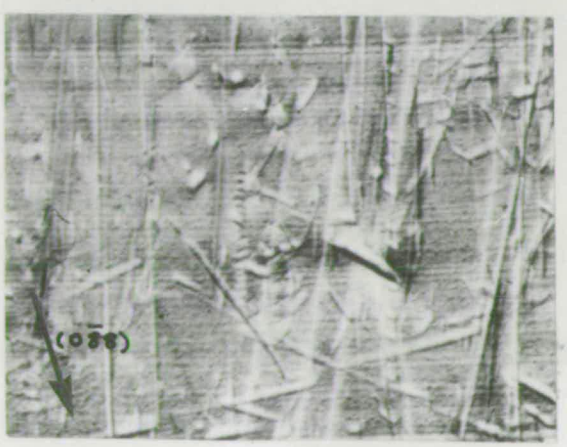

[$\bar{1}12$]

[$1\bar{1}1$]

Transmission topographs of helical dislocations.

Lang Ag Kα 1 mm

Figure 5,6,10

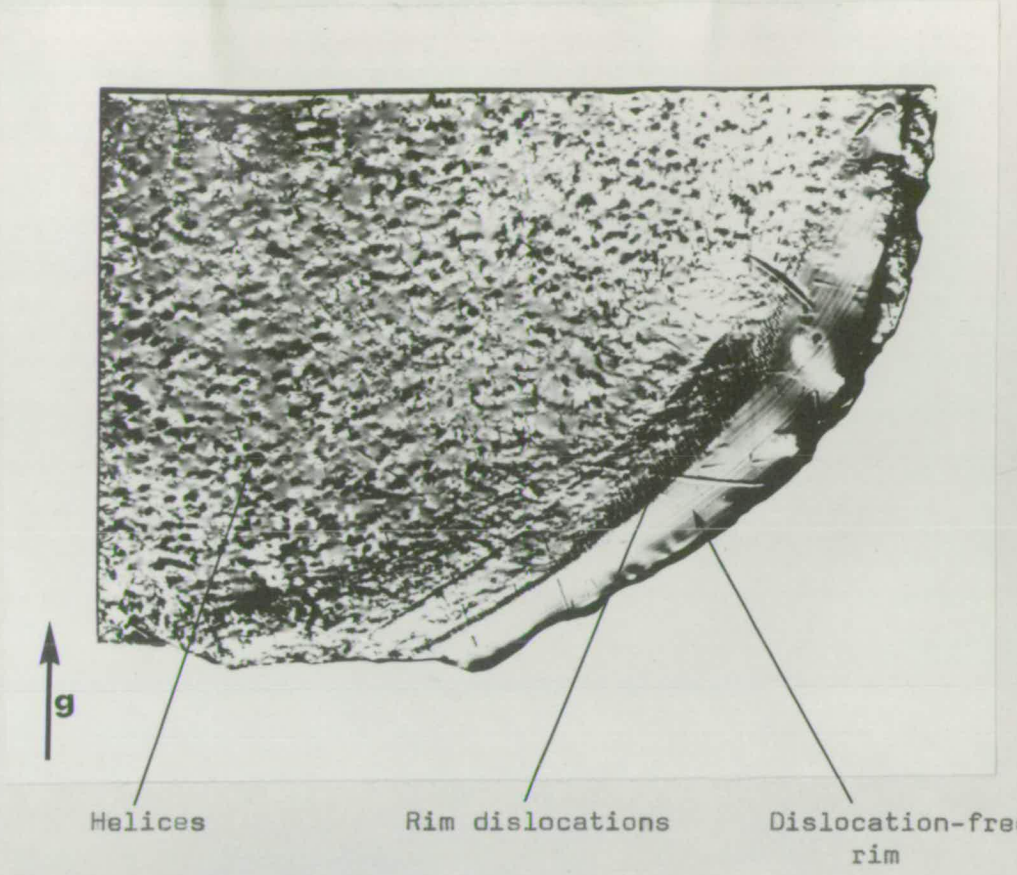

Lang (8 8 0) Ag Kα

2 mm

Figure 5.6.11

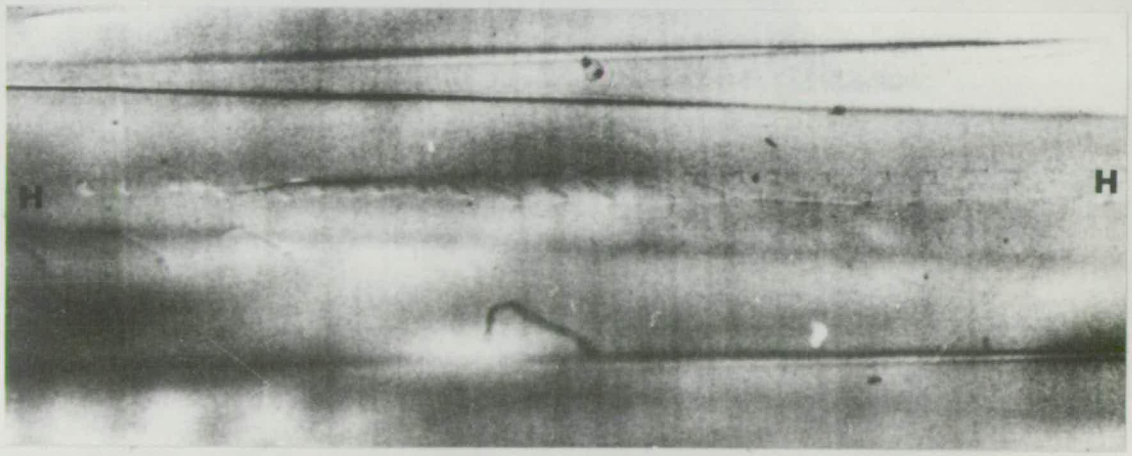

Double crystal (8 8 0) Cu Kα

0.5 mm

Figure 5.6.12

A helical dislocation may also be observed in a (110) slice using double crystal topography. Figure 5.6.12 is a topograph taken with the diffraction vector normal to the Burgers vector of the helix. The dislocation line is visible for the reasons discussed above. The helices can be seen just grazing the surface where they emerge at the 'pointed' end. Complete turns of the helix can be seen but as the dislocation moves deeper only the part of the dislocation line nearer the surface can be seen due to the limited penetration of the x-rays. Even though only segments of the line can be seen, it confirms the long distance over which helices will persist. The weak dislocation image means that any other strain associated with the dislocation will not be masked in the topograph. Figure 5.6.12 shows that there is a 'tube' of strained material with the helix running round the surface of the tube. The sense of the contrast change indicates a very slightly smaller lattice parameter perpendicular to the growth direction.

Sample III

A set of polished slices, 14 mm diameter and 1 mm thick, from one boule was received. These slices contained a small number of very large helical dislocations. A double crystal topograph of one such slice is shown in fig. 5.6.13. About 40 large circular defects are visible, each of which has a diameter of ~700 μm, which is five times greater than the diameter of the helices observed in the previous sample. Also visible are an approximately

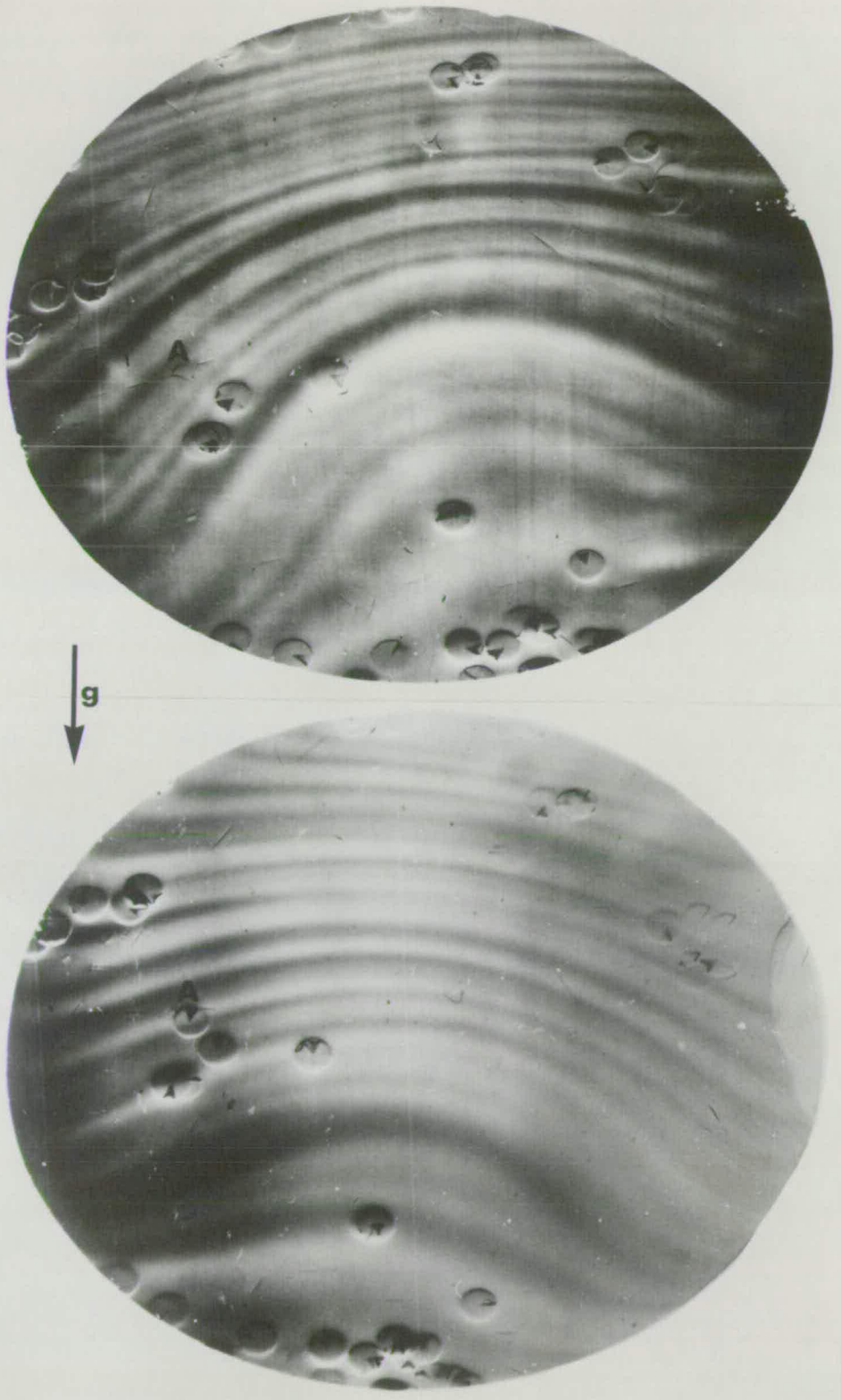

Large helical dislocations.

Double crystal (12 4 4) Cu Kα High θ side of peak.

2 mm

Figure 5.6.13

equal number of defects which appear as a line equal to the radius of the circles with a 'head' at one end. These 'tadpoles' will be discussed in detail later.

Since this sample was received ready-sliced and the slices in an unknown order, the defects can only be traced directly over a distance of 1 mm, i.e. within one slice. The defect distribution can be compared in different slices. If the defects are propagated right through the crystal then it should be possible to identify particular groups of defects in each slice.

Figure 5.6.13 compares topographs of the two sides of the one slice. One of the topographs has been printed in reverse so that a direct comparison of the distribution of the defects may be made. The circular defects run right through the crystal and thus are likely to be helical dislocations. The helix marked A is only just visible in (a) but appears as a complete circle in (b). Since the depth in the crystal at which detail of defects is visible is, at most, 100 μm then it would appear that the pitch of the helix can vary over very short distances. The black/white contrast around the circle is the same in both photographs but the black wedge-shaped regions in the interior of the circles have moved, but the edges of the wedges still appear to lie along particular crystallographic directions, i.e. <110> directions.

Information on variations in lattice parameter or rotation of the crystal planes can be obtained by observing changes in the image of the helix and wedge as the crystal is rotated about the diffraction vector or as the position

on the rocking curve is changed. Figure 5.6.14 shows a set of reflections, each set on the high θ and then the low θ side of the rocking curve. The contrast of the wedge depends solely on the position on the rocking curve and does not depend on the orientation of the slice. The wedge shows dark when set on the high θ side of the peak and light when set on the low θ side. The lattice parameter of the material of the wedge region is smaller than that of the surroundings.

The contrast round the circular part of the defect corresponds to a bending of the crystal planes since the pattern does not rotate with the sample but remains fixed to the diffraction vector. The sense of the contrast corresponds to a curving outward of the diffracting planes at the crystal surface. This implies a larger lattice parameter along the axis of the helix.

Such large helices can be observed by polarised light.[141],[142] A group of helices is shown in fig. 5.6.15. Only the circle is visible in the image; there is no contrast from the wedge which thus must lie approximately parallel to the plane of the slice. The contrast of the dislocation line becomes zero at the four points where the dislocation is approximately parallel and perpendicular to the polariser. As the sample is rotated the pattern stays fixed with respect to the polariser direction. A Burgers vector must stay constant along a dislocation line and so the dislocation must be almost pure edge with the Burgers vector parallel to the growth direction and to the axis of the helix for the contrast to

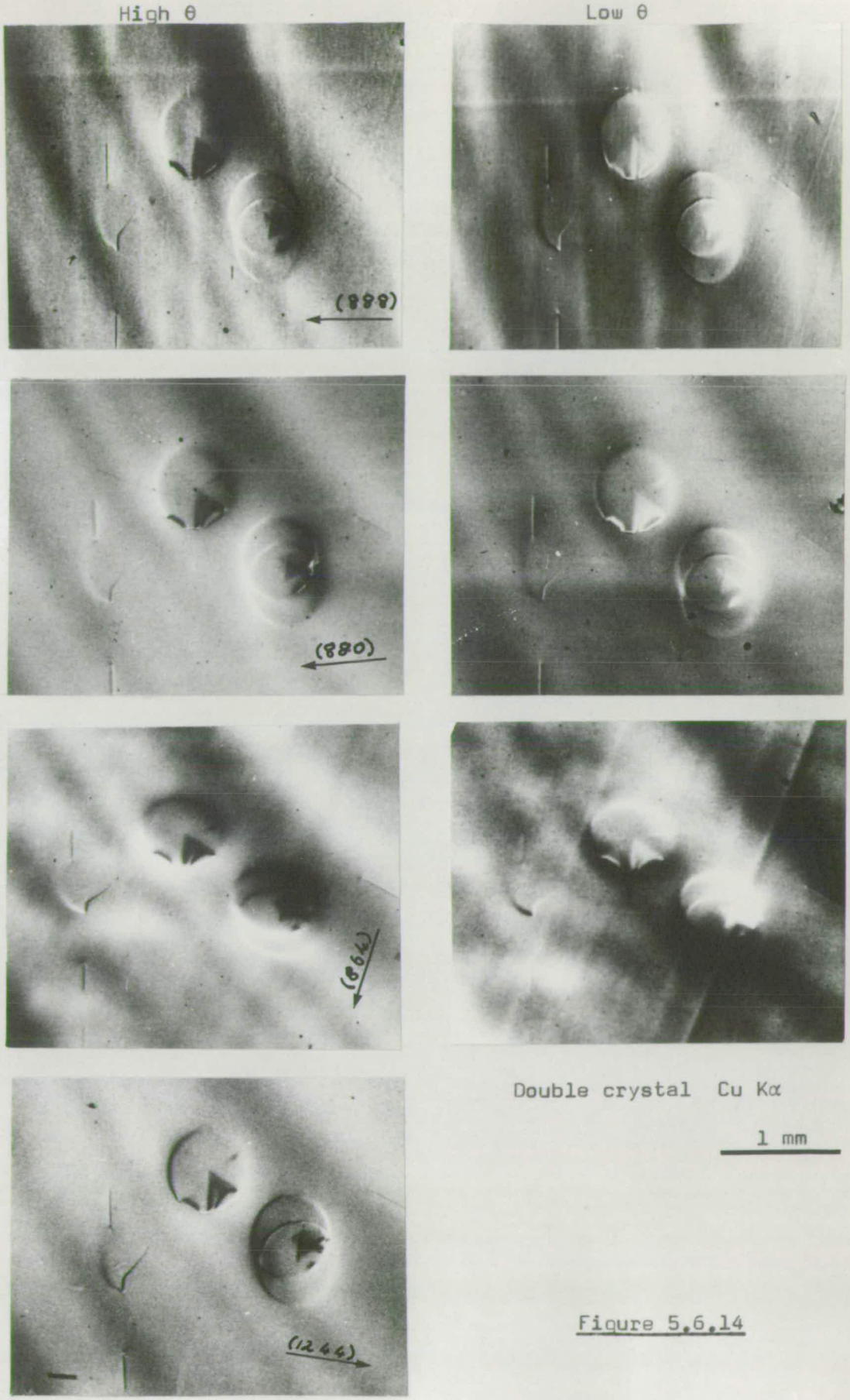

Double crystal Cu Kα

1 mm

Figure 5.6.14

Dislocations viewed by polarised light.

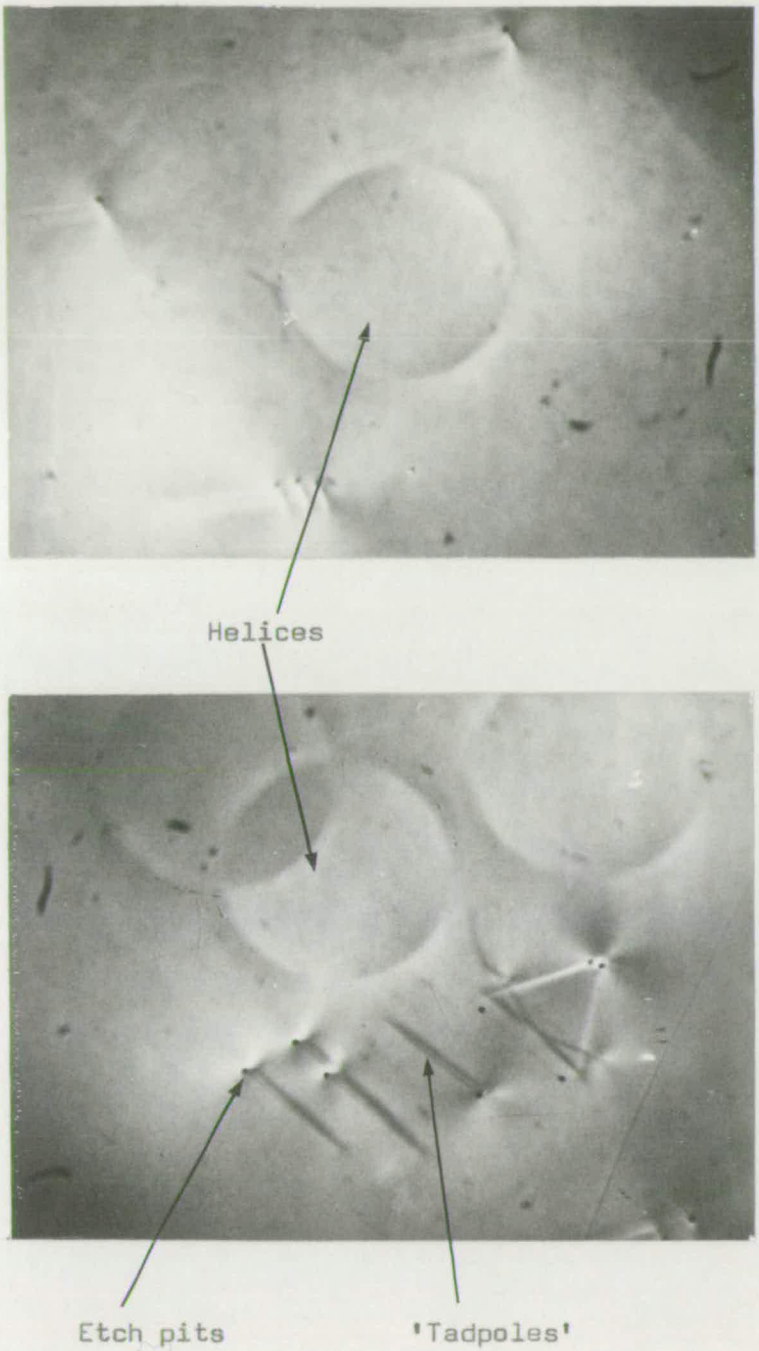

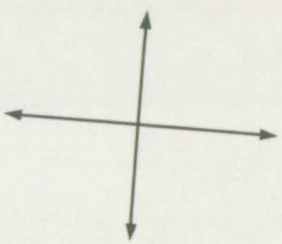

500 μm

Figure 5.6.15

behave in this way.[99]

The structure of the wedge-type contrast and the Burgers vector of the helix were investigated further by transmission Lang topography of a different slice from the same crystal. This slice was thinned to 150 μm and was found to contain at least one turn of most of the helices, as can be seen from fig. 5.6.16 which is set in the same orientation as the slice in fig. 5.6.13. The same groups of helices can be identified in each slice. The image of the dislocation line appears double. This could be because there is a pair of dislocations forming the helix but they would have to be well-separated for them to be resolved in this projection. A doubling of a dislocation image will occur for short wavelengths and high order reflections.[89] The wedges which were visible in the double crystal topographs appear here typically as six 'rays' along the $\langle 110 \rangle$ directions in the plane of the slice. This is somewhat different from the ray system observed by Stacy[143] where the rays extended in all directions.

If the Burgers vector of the helix is along the growth direction, the topographs taken with the diffraction vector normal to this direction should give low contrast in the dislocation line and zero contrast when the line is parallel to the diffraction vector. Figure 5.6.17 shows the series of $\{8\ 0\ 0\}$, $\{8\ 8\ 0\}$ and $\{12\ 4\ 4\}$ type reflections possible on this slice. The $\{8\ 8\ 0\}$ symmetric reflections do indeed give zero contrast where the dislocation line is parallel to $\underline{g}$ and this is linked to the diffraction vector not the crystal. Such a break in the image of the dislocation is

Transmission topograph of helical dislocations.

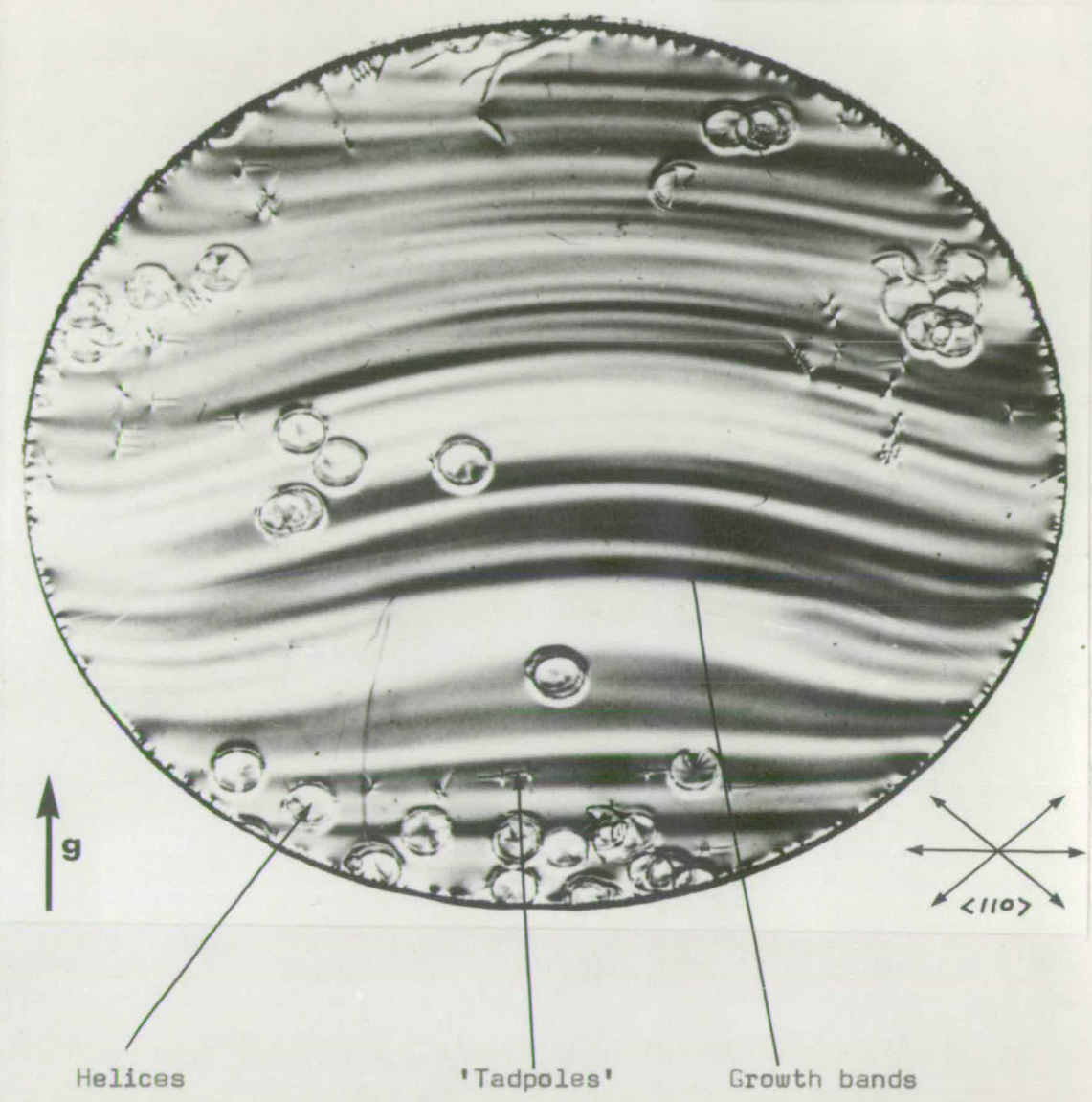

Lang (8 0 0) Ag Kα

1 mm

Figure 5.6.16

Asymmetric

Symmetric

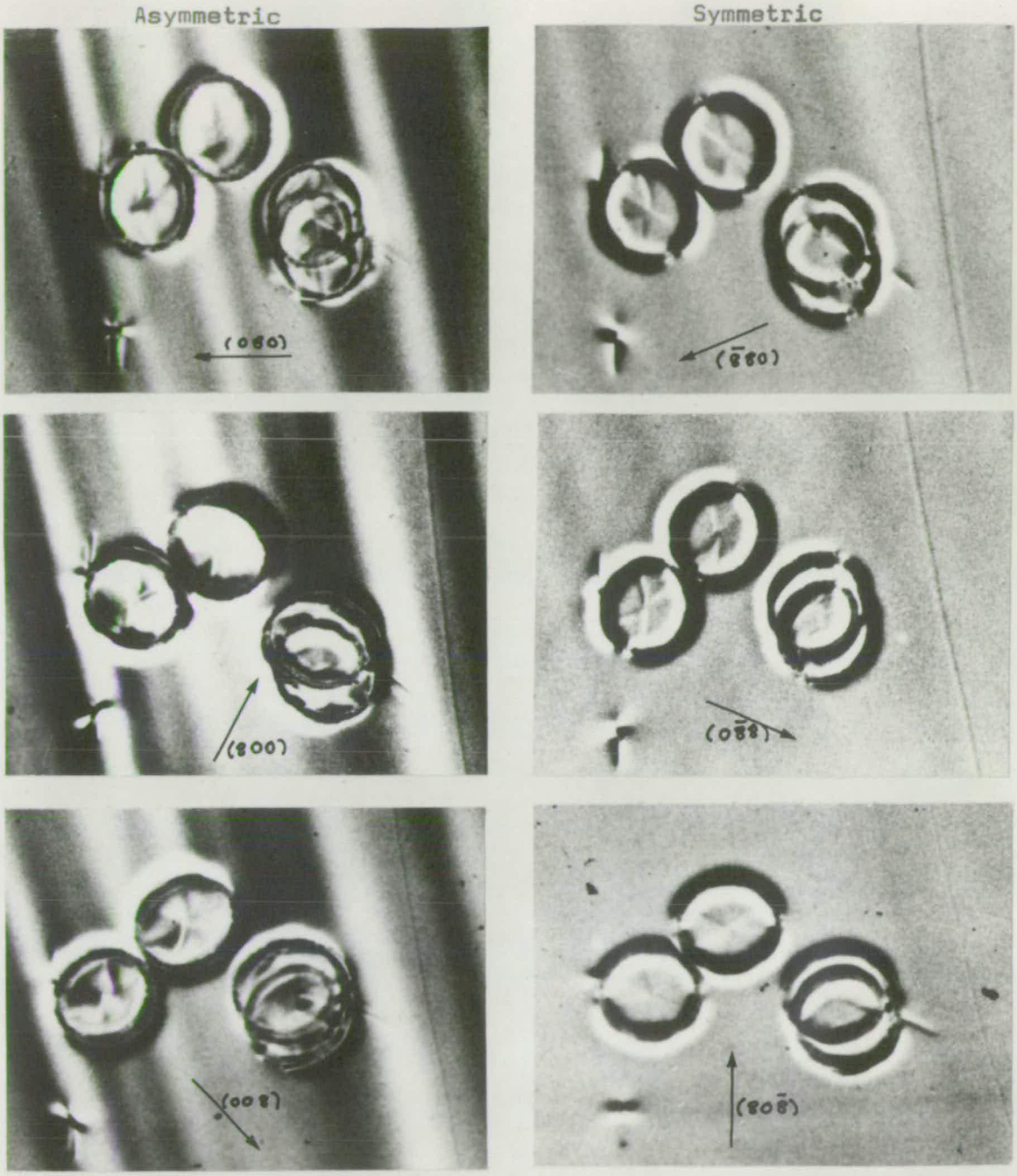

Transmission topographs of large helices.

Lang Ag Kα 1 mm

Figure 5.6.17

not observed for the other two reflection types and so this confirms the Burgers vector as axial. The dislocation line does not appear completely smooth and circular. There are 'flats' along the <211> directions in the plane of the slice (or nodes in <110> directions).

The rays also show variations in contrast, depending on the type of reflection. When the ray is parallel to the diffraction vector or its projection there is zero contrast in the image. A helicoidal fault surface in the form of a helical staircase with steps every 60° would give rise to this type of image. A model of such a surface is shown in fig. 5.6.18. The helical dislocation is marked on the outer edge. If the fault surface were a stacking fault or twin boundary there would have to be a similar dislocation bounding the surface along the axis of the helix. There is no evidence for a dislocation of this type. A thin layer of impurity or precipitate associated with the helical dislocation would not require an inner bounding dislocation; such a layer has been suggested.[143]

This fault surface may be investigated more fully by preparing a thin slice of (110) orientation which contains part of a helix. Such a slice, 80 μm thick, was prepared which went almost through the centres of two interlocking helices. Since the thickness of the slice is 80 μm, and the diameters of the helices $\sim$700 μm, the short segments of dislocation line run almost perpendicular to the (110) surface. The lines visible in the series of topographs in fig. 5.6.19 are the section through the helicoidal surface. Figure 5.6.20 shows the same sample viewed by polarised

Model of large helical dislocation.

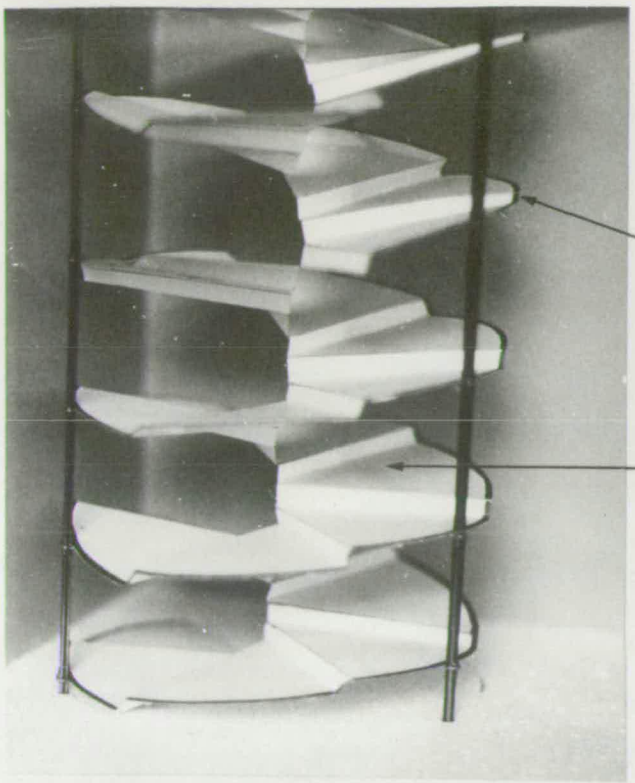

Model viewed down axis.

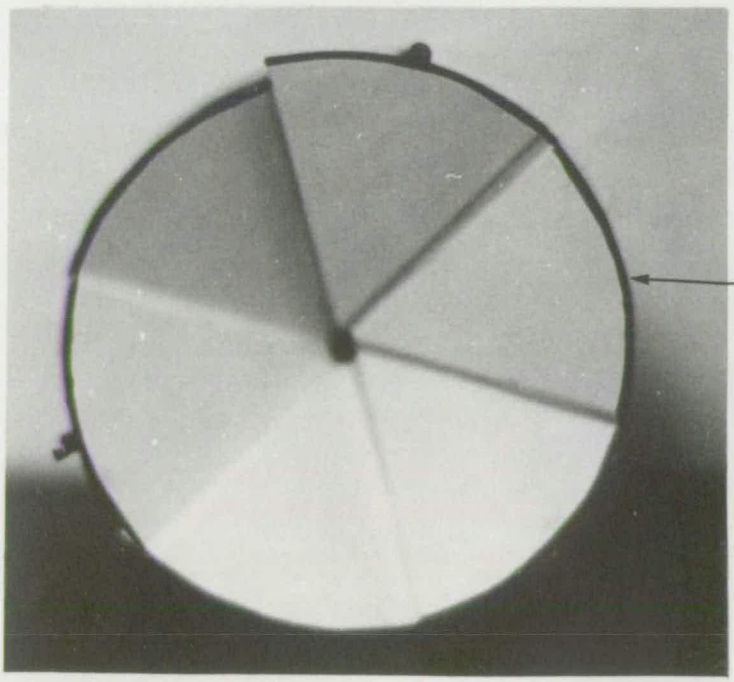

Figure 5.6.18

Asymmetric

Symmetric

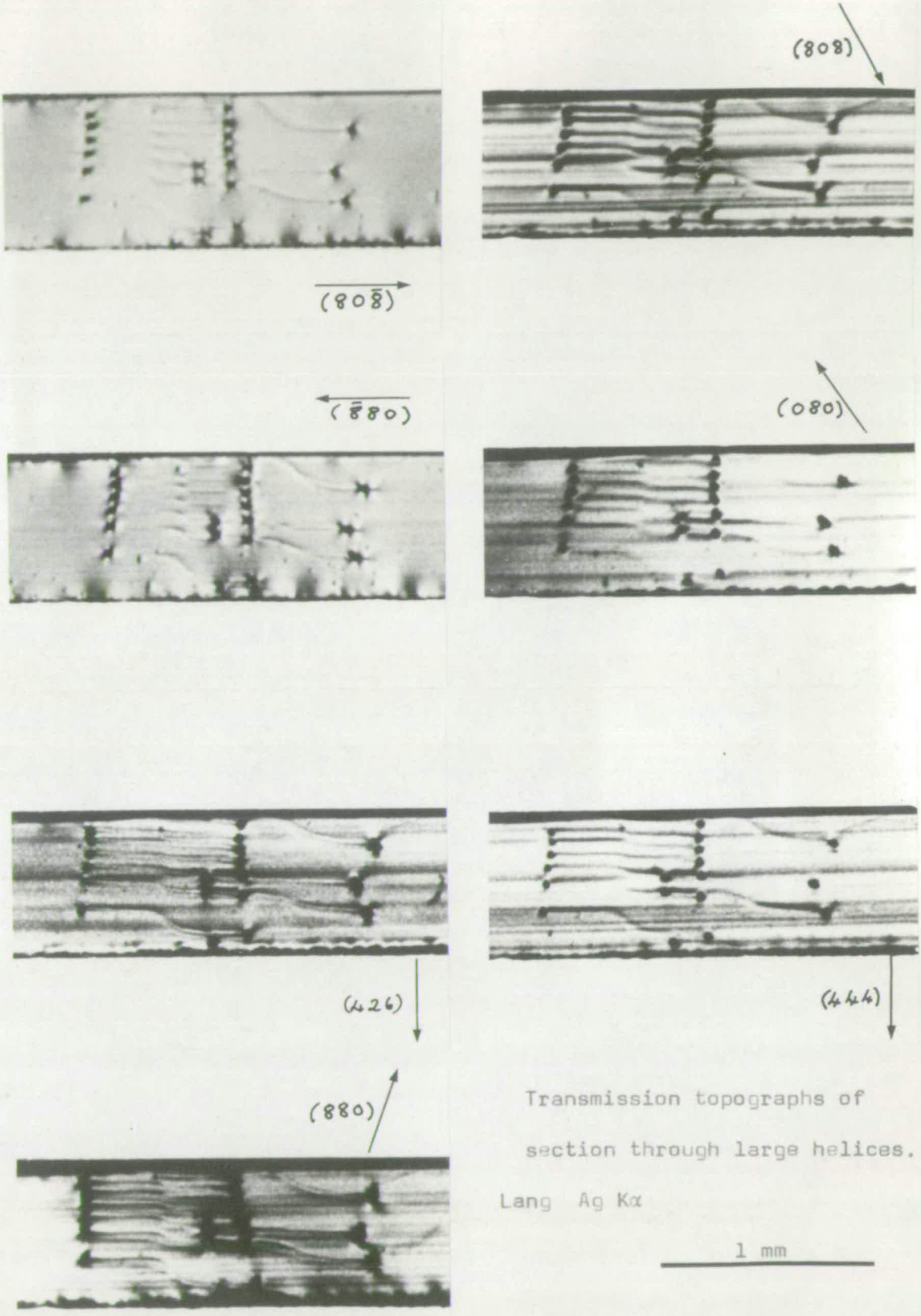

Transmission topographs of section through large helices.

Lang Ag Kα

1 mm

Figure 5.6.19

Section through large helical dislocations viewed by polarised light.

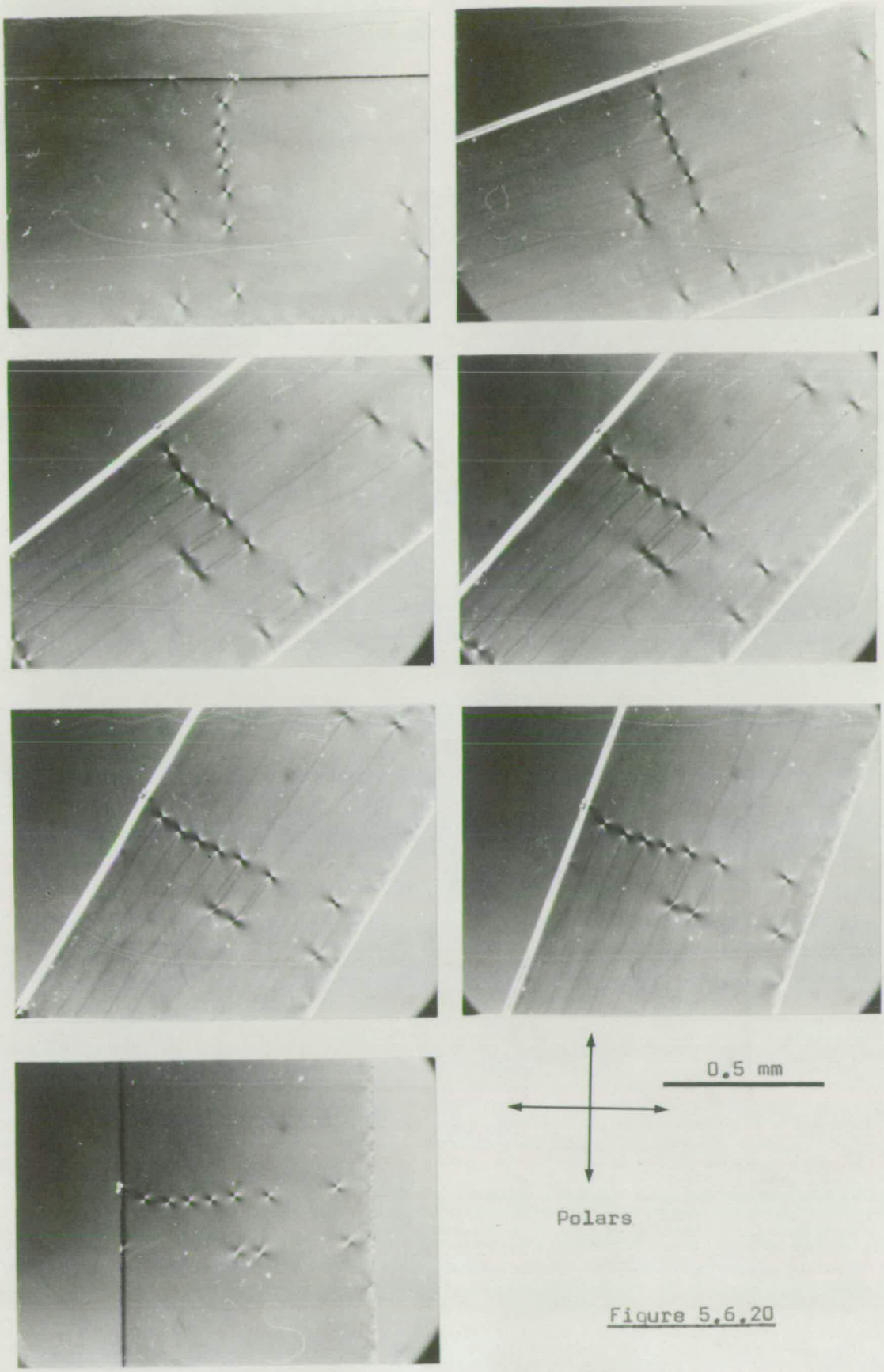

Figure 5.6.20

light. In this orientation the helical dislocation should appear as a row of edge dislocations with the dislocation line running normal to the plane of the slice and the Burgers vector parallel to the rows. The dislocation images in the x-ray and optical cases show complex images which are very much larger than those previously observed. The image would be complicated if the dislocation line were decorated by impurity atoms, particularly if the magnitude of the Burgers vector were $n\frac{a}{2}[111]$ with $n > 1$ or there were a very close bundle of dislocations. Some of the x-ray images look similar to those obtained from inclusions.

The topographs show an apparent double fault surface. This is not a diffraction effect as this is also seen optically when the line is at 45° to the polariser direction. The contrast is zero when parallel or perpendicular. In the topographs the contrast from the surface is at a minimum when the line is parallel to the diffraction vector. A 'sandwich' of impurity atoms would have its fault vector parallel to the growth direction and since this layer has a smaller lattice parameter than the matrix, as determined previously, this layer is likely to be gallium-rich, gadolinium-poor. Analysis by electron beam x-ray microanalysis on this sample did not find any change in the gallium to gadolinium ratio over that due to growth banding in the region containing the fault surface, but there was a very slight increase in the Ga/Gd ratio at the dislocation.

Before considering reasons why a dislocation of this

type should form, the defects which appear as a straight line in fig. 5.6.13 will be examined more closely. A particular group of these is shown for various double crystal and transmission topographs in fig. 5.6.21. Many similarities with the helices are immediately apparent. The lengths of the lines, which run in $\langle 110 \rangle$ directions, are approximately equal to the radius of the helices. There is a dislocation at only one end as shown by x-ray and etch-pit studies. Figure 5.6.22 compares the etch-pit distribution, measured using the vernier x-y stage of a microscope with the defect distribution obtained by a topograph of the same sample and corrected for distortions. There is only one etch pit per 'tadpole' and there is a one-to-one correspondence between the position of the etch pit and the head of the tadpole. It is interesting to note that no etch pits were formed at the shallow intersection of the helical dislocation with the surface.

The 'tail' is a planar fault surface, similar to that in the helix, which does not run exactly parallel to the growth direction. This can be seen from the relative movement of the defects from slice to slice. The double tail image and the variation of the spacing with orientation of the diffraction vector will give the plane of the fault if it is assumed that the two images come from the top and bottom surfaces of the crystal. This gives $\{111\}$ as the plane of the fault.

The dislocation would appear to have a large edge component as it is readily visible in polarised light. Unfortunately, a thin (110) slice was not obtained

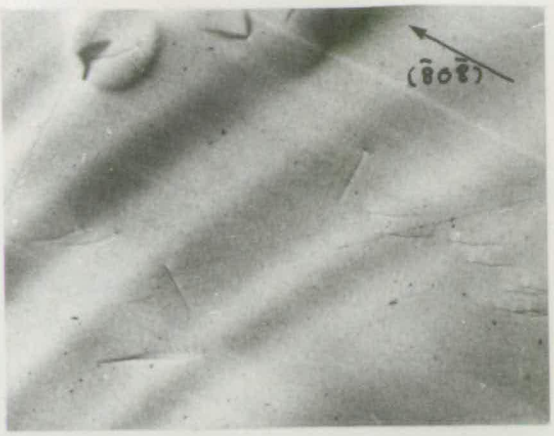

Double crystal Cu Kα

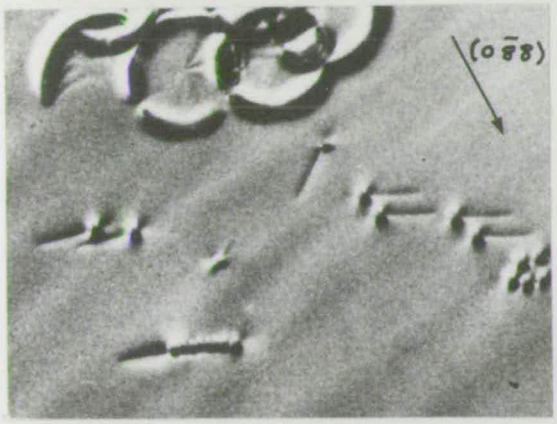

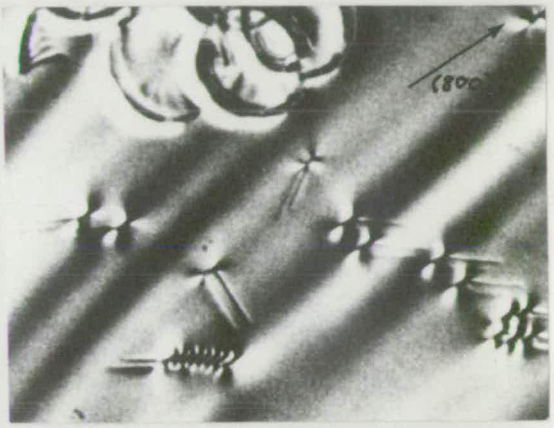

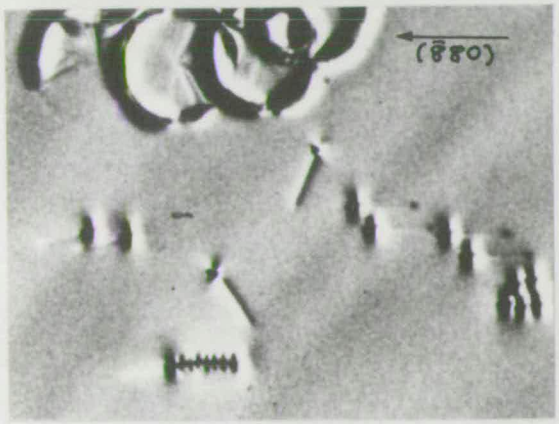

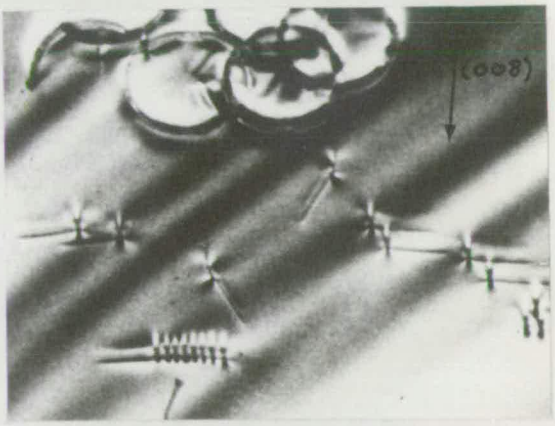

Transmission Lang Ag Kα

1 mm

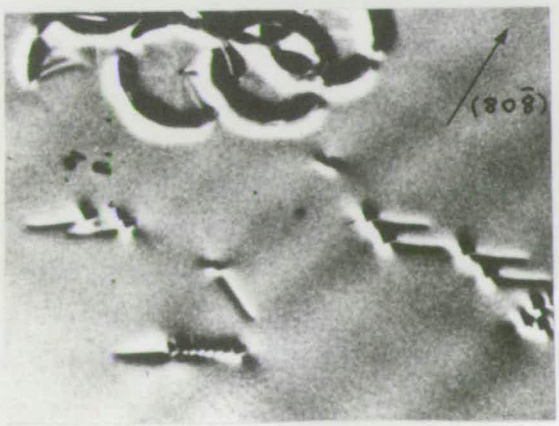

Topographs of 'Tadpoles'

Figure 5.6.21

Double crystal topograph

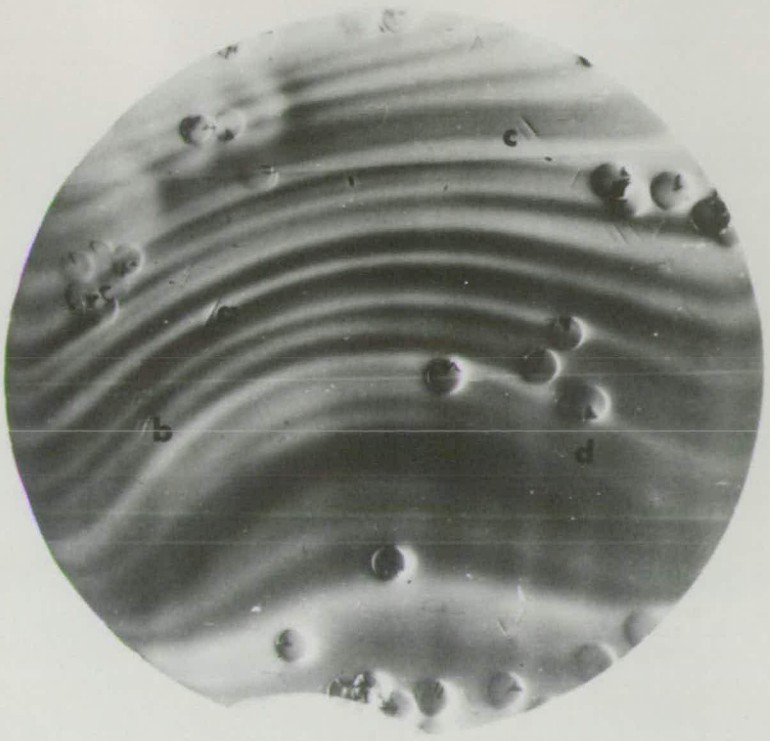

Etch pit pattern of same sample

2 mm

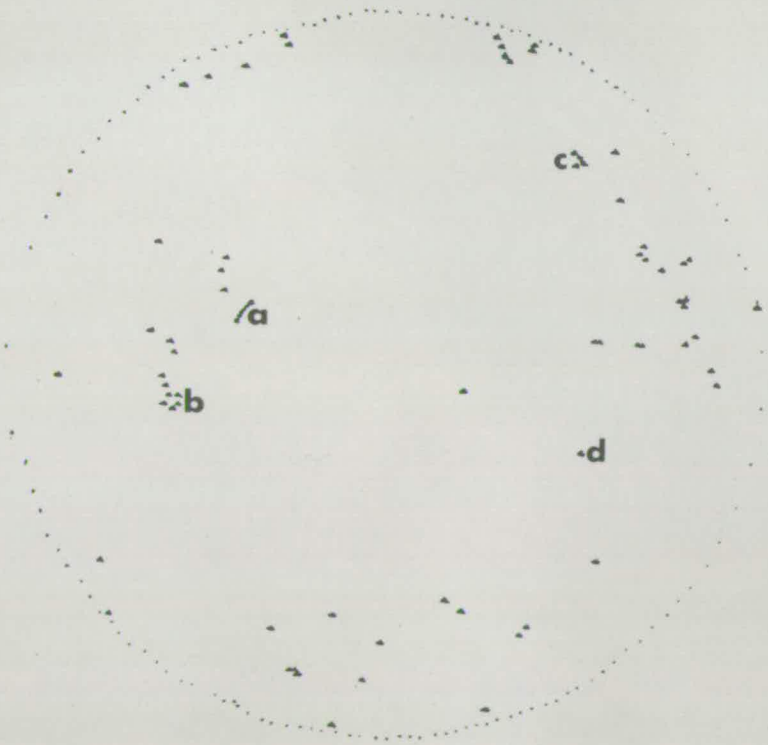

Figure 5.6.22

containing one of these dislocations and so a direct determination of the Burgers vector was not possible. The similarity of the images would suggest that the Burgers vectors were all of the same magnitude. The images in the symmetric {8 8 0} reflections are small and most of the images in the double crystal topographs are small, which would suggest the <111> directions not parallel to the growth axis as likely Burgers vectors.

Only screw dislocations will form a helix if there is a supersaturation of point defects and in forming a helix the line will become mostly pure edge. If the Burgers vector is large then there will be a large compressive stress on the extra half plane and a tensile stress near the core of the dislocation. The hollow region at the edge of the half-plane is a site for oversize impurity atoms. The stress on the extra half plane can be relieved by housing an excess of small atoms there. In this case this can be achieved by housing an excess of gallium on the half plane and ejecting gadolinium to the surrounding matrix. This also relieves stresses at the dislocation core. The greater the strength of the dislocation the more favourable this replacement by gallium will be and the greater the distance over which this will take place. Thus if initially all dislocations had the lines parallel to the growth direction and had all possible Burgers vectors of the <111> type then the left-handed and right-handed screw dislocations would climb into right- and left-handed helices in the presence of point defects. The mixed dislocations,

already having a large edge component, would be unable to climb and so would propagate as straight lines. In both cases stress-relief occurs with the fault surface.

5.7 Other Substrate Materials

A closer match between the lattice parameter of Ga:YIG films and the substrate material may be obtained by substituting dysprosium for some of the gadolinium in GGG. One boule, of nominal composition $Dy_2\ Gd_1\ Ga_5\ O_{12}$, was received which had a lattice parameter as determined by powder methods of 12.341 $\pm$ 0.001 Å. This confirms the composition of the boule if it is assumed that the lattice parameter varies linearly with composition between the limits of GGG at a = 12.383 Å and Dy GG at 12.320 Å.[50]

Mixed rare-earth gallium garnets are more difficult to grow than those of a single rare earth due to the dangerof interface breakdown due to constitutional supercooling if the growth-rate becomes too high. This is reflected in the imperfections in the crystal boule. This boule was subject to stresses sufficient to form a large crack in the interior of the crystal which runs through the centre parallel to the growth direction. The plane of the crack was close to (110) and is seen in fig. 5.7.1 surrounded by a very high density of dislocations. The outer region is fairly good and shows growth bands. The defects are shown more clearly in the transmission topograph of approximately half of the slice in fig. 5.7.2.

Rare-earths are difficult to purify free of other rare-earths. This difficulty is compounded if a mixed

Dysprosium gadolinium gallium garnet.

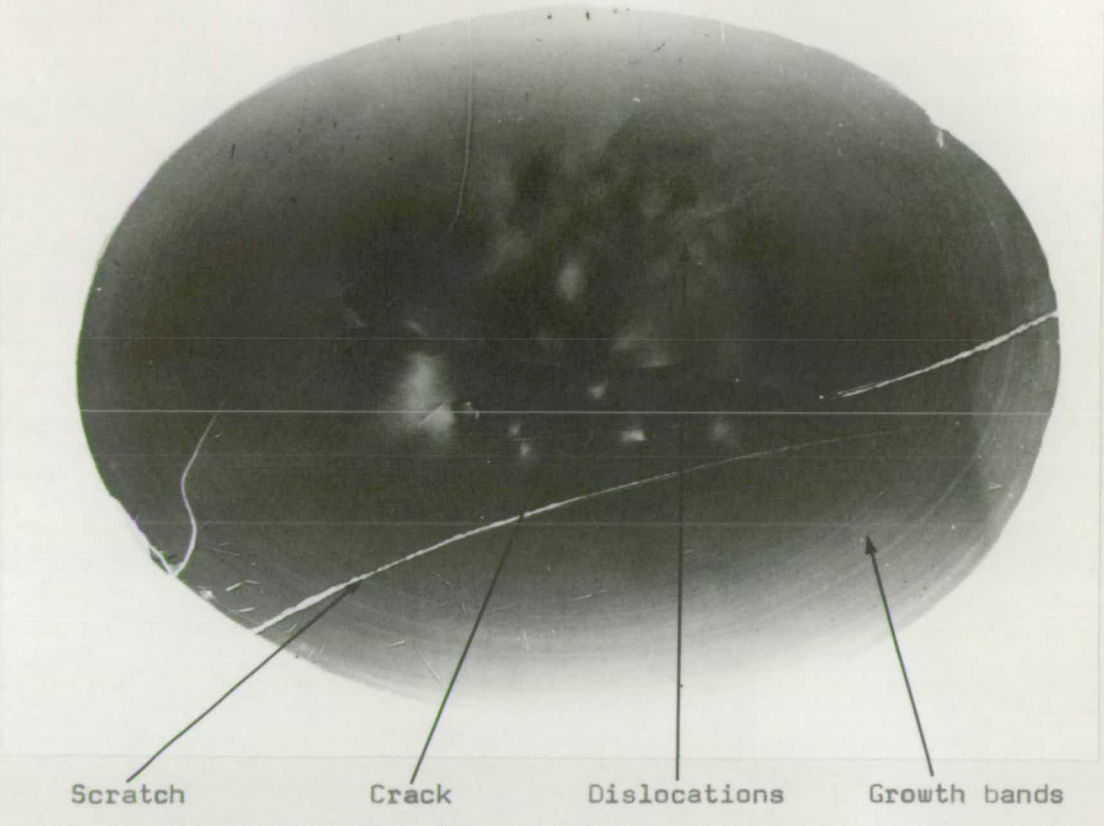

Lang reflection (16 16 16) Mo Kα 1 mm

Figure 5.7.1

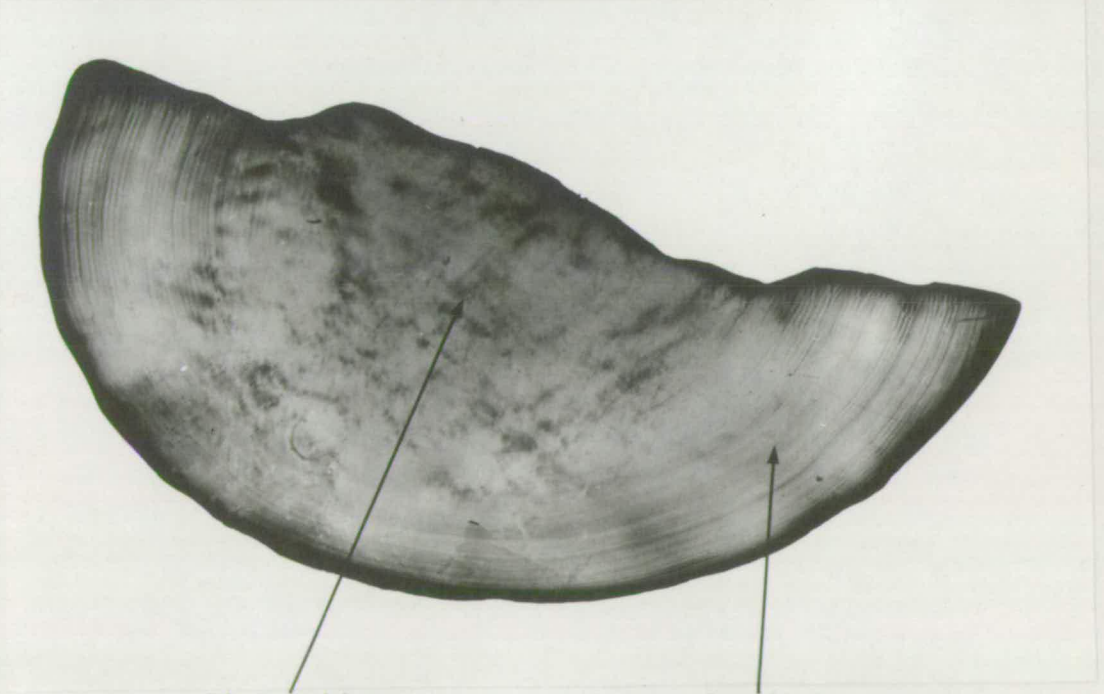

Lang (4 $\bar{4}$ 4) Mo Kα 1 mm

Figure 5.7.2

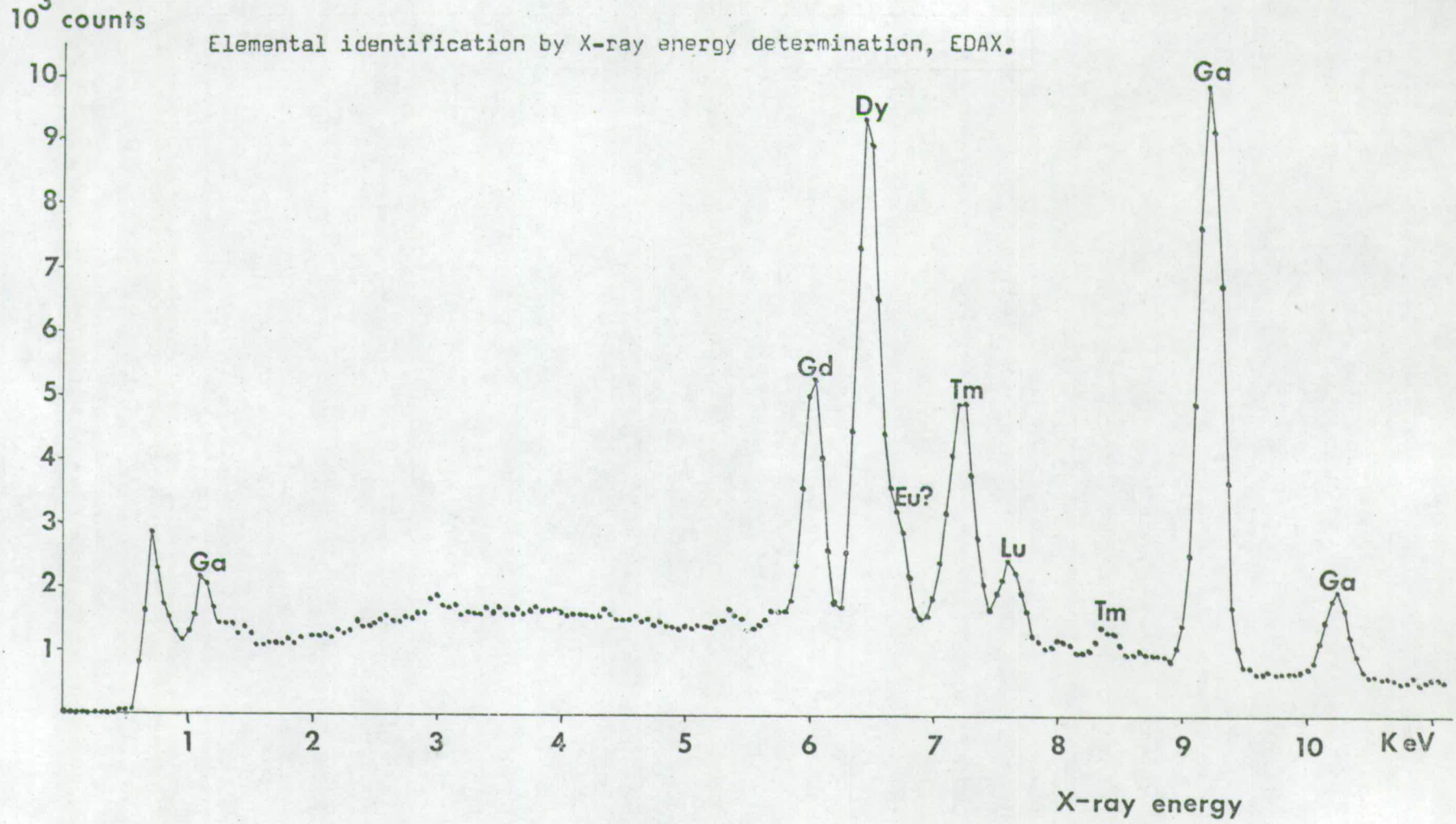
10^3 counts
Elemental identification by X-ray energy determination, EDAX.
10
9
8
7
6
5
4
3
2
1
Ga
Gd
Dy
Eu?
Tm
Lu
Tm
Ga
Ga
1
2
3
4
5
6
7
8
9
10
KeV
X-ray energy

Figure 5.7.3

rare-earth garnet is required, particularly if one of the rare-earths is less commonly used. Figure 5.7.3 shows the identification of the elements present using x-ray energy determination (EDAX). There is substantial contamination by other rare-earths. This does not matter if the lattice parameter is that required. Reproducibility becomes more difficult since different batches of raw materials are likely to have different amounts of impurity.

Conclusions

The following defects were found to have been formed during the growth of GGG.

1. Triangular plates of iridium metal with the plane of the inclusion parallel to the growth interface were found to produce little strain. Some matching of crystallographic orientation with the host material was indicated.

2. Elastic distortions due to composition variations were found in growth bands in all crystals (variation in lattice parameter $\Delta a = 0.0002$ Å), core and/or facets in most crystals ($\Delta a = 0.001$ Å) and a strained rim in one crystal.

3. Plastic distortions, i.e. dislocations, were found in all but one crystal. The main type of Burgers vector, $\underline{b}$, was $\frac{a}{2}\langle 111\rangle$. The dislocation lines were close to the growth direction and for dislocations of mixed type were approximately straight. The dislocations with $\underline{b}$ parallel to the growth direction had the dislocation line in the form of a helix. Two types of helix were found. One was of diameter ~100 μm, the other with diameter ~700 μm. The larger helix had a helicoidal fault surface of impurity associated with it. The mixed dislocations in this sample also had a plane of impurity attached.

CHAPTER 6

DEFECTS IN EPITAXIAL FILMS

6.1 Defects Formed During Growth

This section considers the defects formed in an epitaxial garnet film as a consequence of the growth process and particular growth conditions. Similar classes of defect occur in films grown by both liquid phase epitaxy (LPE) and chemical vapour deposition (CVD) but may differ in detail and severity. The main types of defect considered are variation in thickness, variation in composition, inclusions, cracks and dislocations. Section 6.2 investigates the effect of defects, in the substrate, on the epitaxial film.

6.1.1 Variation in thickness

a) LPE films

i) Effect of methods supporting the substrate

The substrate must be held in, or on the surface of, the melt and rotated during growth of the film. The growth rate depends on temperature[59],[60] and if there is a variation in the temperature of the substrate across the slice then there will be corresponding variations in thickness. The vacuum chuck method of supporting the substrate involves a large mass of platinum, a good thermal conductor, in contact with the substrate. The platinum tube is about 5 cm long and so the top of the tube is in a colder region of the furnace than the sample end and thus will act as a heat sink. This effect will be accentuated if insufficient pre-heating time had been allowed and if the temperature drop up the furnace had not been minimised by a system of

baffles.

An annular region of thicker film in the centre of the sample will be produced and the thickness contours can be seen by optical interference in fig. 6.1.1. A film of uniform thickness is required. A thicker region occurring in the centre of the film is troublesome and may introduce some extra strain. If it is not possible to remove this ring by improved thermal gradient and pre-heating the thicker region may be removed by polishing, but this introduces an unwanted extra step.

Another method of supporting the slice is by small, platinum claws gripping the edge of the substrate. If the platinum wire is sufficiently massive then there may be similar problems of chilling as found with the vacuum chuck. The claws protrude over the surface of the substrate which has several effects on the growing film. Immediately under the claw there will be a region where the growth of the film is very restricted, if it can grow at all. The sample will be rotated so in the lee of the claws there will be less frequent renewal of the melt material. If the rotation rate is too high there may be a breakdown of the flow pattern in the melt at the claws thus giving different rates of growth.

The strain produced in the region of the claws is seen in the topographs of fig. 6.1.2. One of them, (a), shows strain which is exceptionally large, the other shows a more usual amount which is confined to the region close to the edge. This effect would become less troublesome as the size of the substrate increased. This means that

Thickness variation in L.P.E. films viewed by optical interference.

Samples supported by vacuum chuck during the growth of the film.

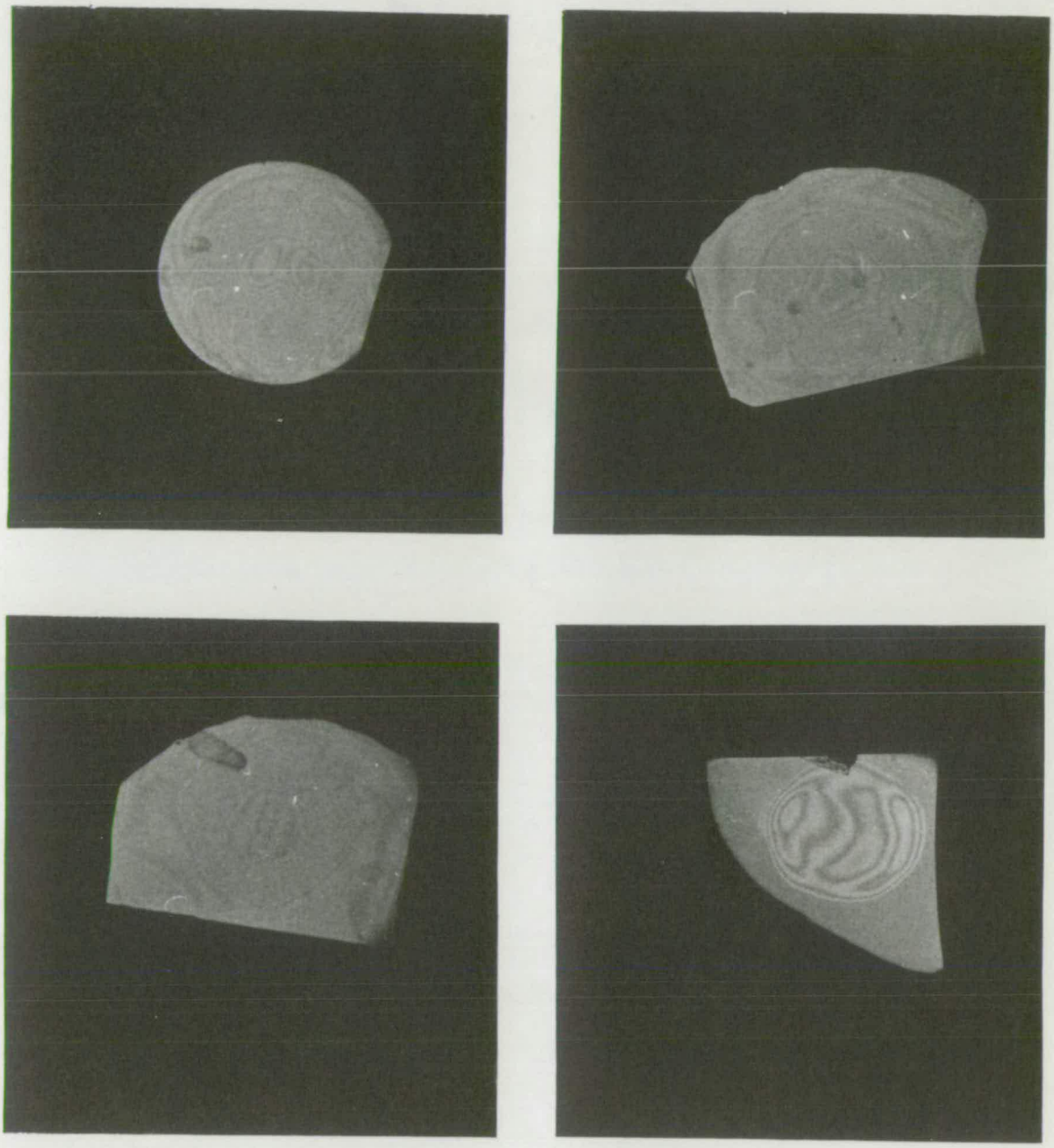

1 cm

Figure 6.1.1

Topographs of strain in L.P.E. films which were supported by claws during the growth of the film.

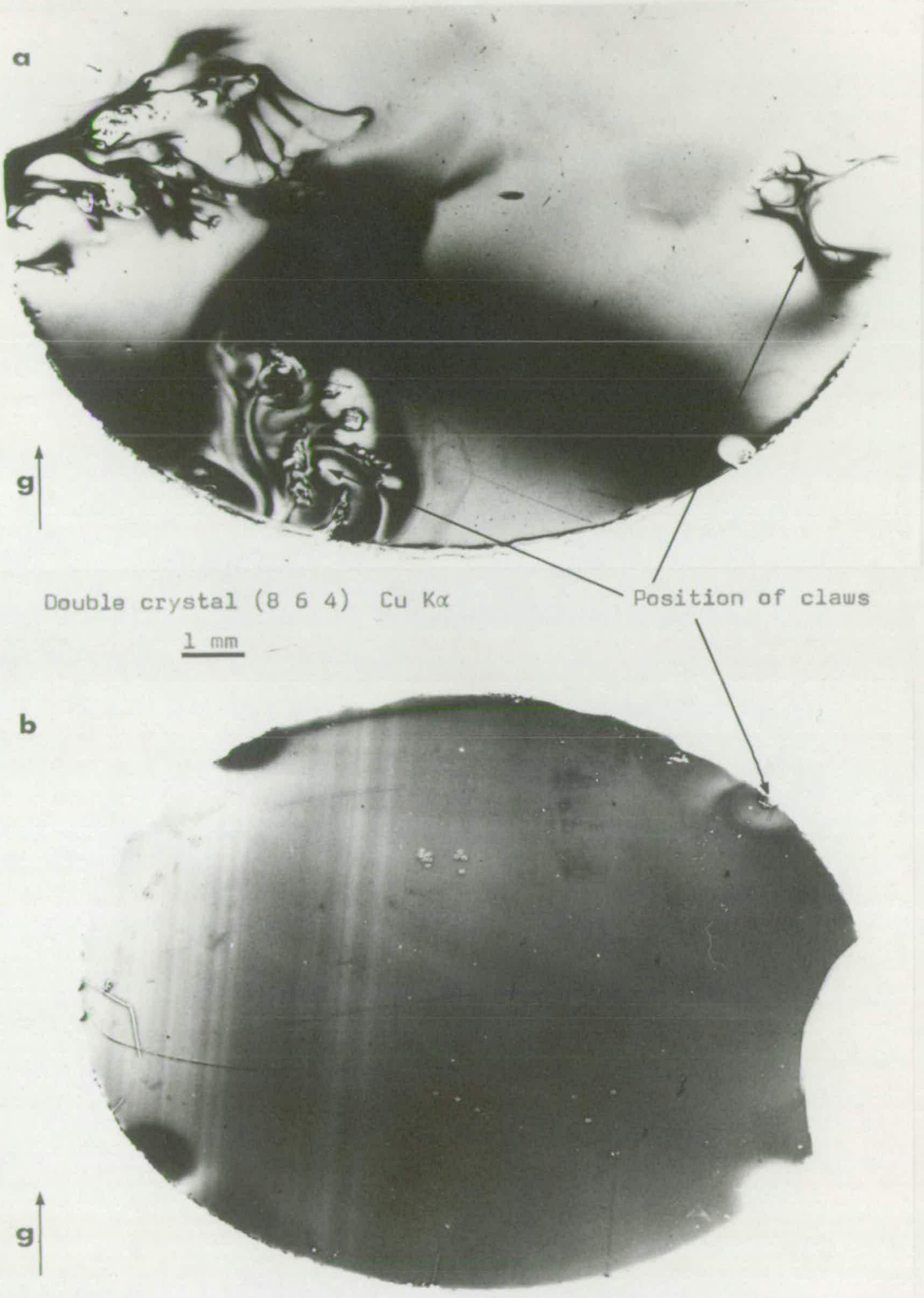

Figure 6.1.2

the edge of the substrate cannot be used for devices but, since this region is also subject to handling damage, there is little extra loss.

ii) Retention of flux

Some of the molten flux, containing garnet in solution, is retained on the surface of the slice in droplet form as the sample is withdrawn from the melt. If these drops of flux are not removed the material in them will solidify to produce a thicker layer of garnet covered by a skin of lead-rich oxide.[146],[147] This oxide skin can be dissolved off by solvents such as glacial acetic acid. A garnet film with thicker regions approximately circular in shape is left. These thicker regions, known as 'mesas' produce strain at the boundary between the thin and thick regions, as seen by the black/white contrast in the topograph in fig. 6.1.3.

The retained flux can be removed, or at least confined to the edge of the sample by spinning the horizontally mounted samples very rapidly just after they have been withdrawn from the melt. Vertically mounted samples should drain the flux off the surface though there is likely to be a drop retained at the bottom. For either method to be successful there should not be too steep a temperature gradient above the melt. There should be time for the flux to be spun off before it cools too much and the flux becomes viscous.

Strain at 'mesa' in an L.P.E. film.

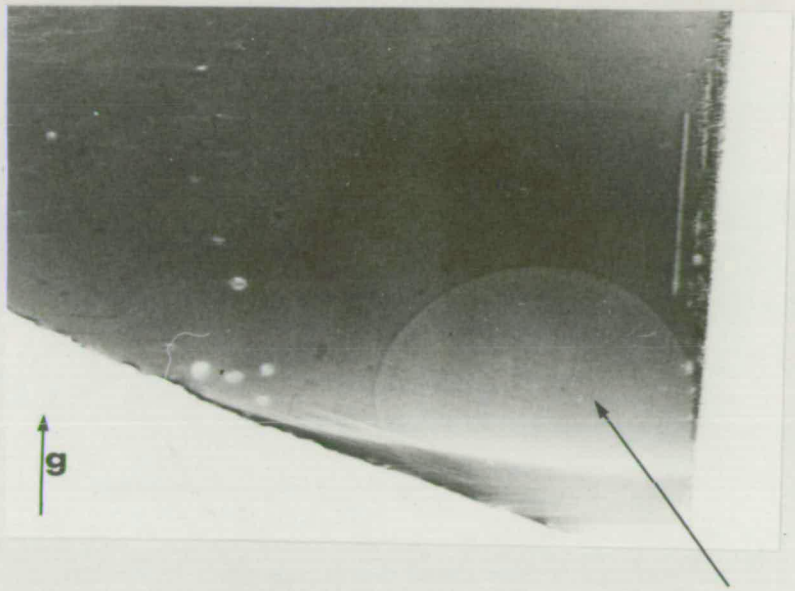

Lang reflection (16 16 16) Mo Kα

1 mm

Figure 6.1.3

Stress relief by faceting in an L.P.E. film.

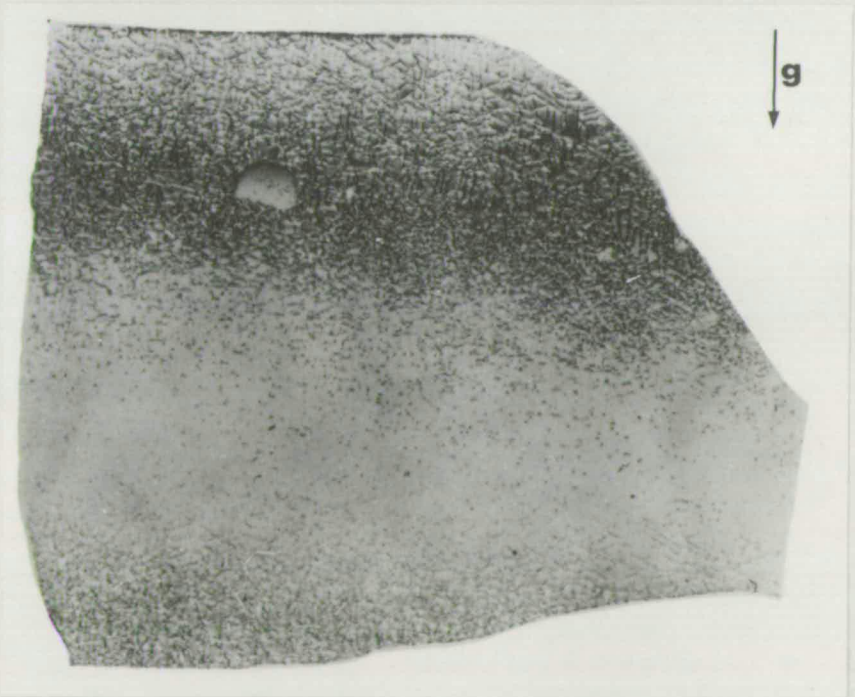

Lang reflection (16 16 16) Mo Kα

5 mm

Figure 6.1.4

iii) Faceting

One sample only was grown with a film of lattice parameter considerably greater than that of the substrate. The stress bent the sample sufficiently to show separate bands diffracted by $k\alpha_1$ and $k\alpha_2$ in a Lang reflection topograph, the sense of which confirms that the film was of larger lattice parameter. Stress relief was obtained to a certain extent by the phenomenon known as 'faceting'. Instead of smooth epitaxial growth the surface consists of a large number of approximately triangular hillocks which form by rapid growth around a dislocation but slower growth over the dislocation itself. Several authors give a figure of 0.018 Å as the maximum amount the lattice parameter of the film can exceed that of the substrate without faceting occurring.[60],[148] The existence of a smooth region in the midst of the faceted region, see fig. 6.1.4, shows that this particular film was just on the limit. The film was too thick to measure the lattice parameter mismatch directly. The faceted region diffracts strongly, except where parts of the film are shadowed by the hillocks and so this is an epitaxial layer, not a collection of randomly oriented crystallites.

b) CVD films

With the CVD system there is an asymmetry imposed by the direction of gas flow over the slice. Ideally, there should be smooth gas flow across the slice and a uniform reaction rate at all parts of the gas stream. The presence of edges to the substrate will disrupt the gas flow,

Thickness variation in C.V.D. films viewed by optical interference.

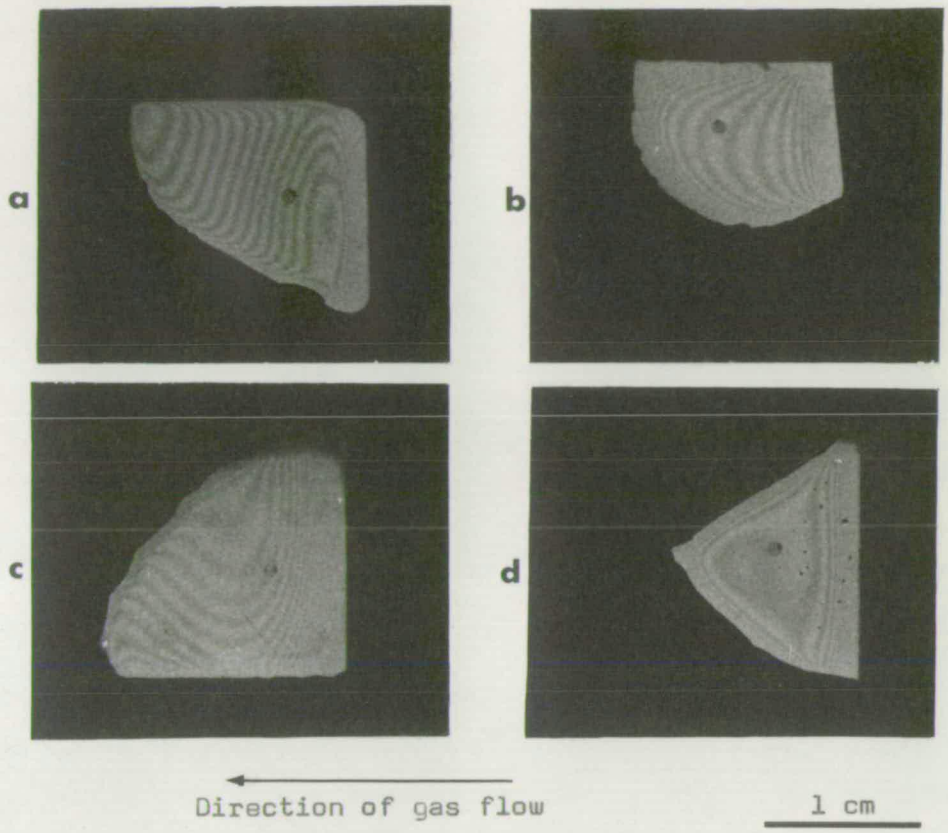

Figure 6.1.5

Pendellösung fringes in a reflection topograph of a thin film.

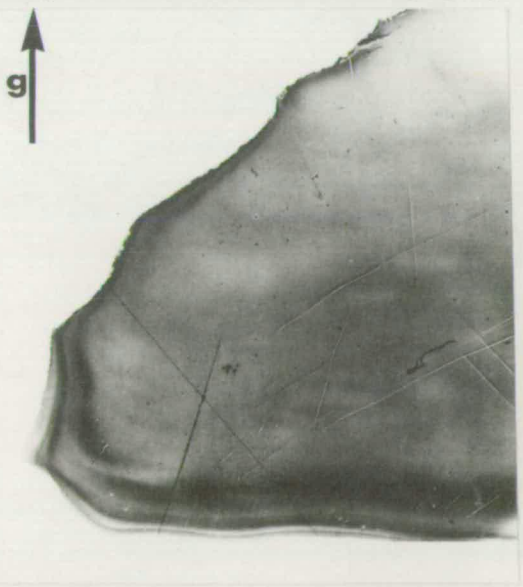

Double crystal (8 8 8) Cu Kα 1 mm

Same sample and orientation as in fig.6.1.5c

Figure 6.1.6

particularly if the substrate is not recessed into a sample holder. These changes in flow will produce corresponding changes in thickness.[70] Figure 6.1.5 shows examples of the contours of variation in thickness seen by interference in monochromatic light. The direction of gas flow is marked in each case. Tilting the specimens in the holder, as shown in the schematic diagram of the CVD furnace, fig. 2.7.2, produced an improvement in the uniformity of thickness as did using larger, more regularly shaped samples.

In thin films the variation in thickness near the edge of the sample can be seen in double crystal topographs as Pendellösung interference fringes.[149] These can only be seen if the crystal is both thin and perfect. Figure 6.1.6 shows part of one of the samples seen in fig. 6.1.5. The x-ray and optical interference fringes may be compared.

6.1.2 Variations in composition

a) LPE films

The variation within a slice is considered here. Variations in composition from slice to slice as a melt becomes depleted, though of undoubted importance for a production run,[150] will not be considered in detail here.

As with substrate materials, the purity of the starting materials to form the melt is important. Non-reproducible impurities will produce uncontrolled changes in lattice parameter which is required to be a close match to that of the substrate. Table 6.1.1 gives the values of $\Delta a^{\perp}$ as determined from double crystal rocking curves for different melt batches.

Melt	Film Comp^{n}	Growth Temp ^{o}C	No of growth run	$\Delta a_{\AA}^{\perp r}$
20.2.73.	YIG	899	1	0.012
		912	3	0.014
		896	6	0.015
23.2.73.	YIG	970	1	0.021
1.3.73.	YIG	905	3	0.005
	spec pure	896	17	0.014
		892	18	0.012
3.5.73.	YIG	930	1	0.0025
	spec pure	900	4	0.0075
26.6.74.	YIG	900	1	0.0047
	spec pure	900	2	0.005
		900	3	0.0047
		900	4	0.005
		900	5	0.006
		900	6	0.009
6.4.73.	GGG	977	1	0.0082
		970	2	0.0055
22.5.73.	GGG	1020	3	0.0058
		1025	4	0.0025
		1030	6	0.0009
22.8.73.	GGG	1000	1	0.0088
23.8.73.	Dy:GGG	1000	1	0.0140

TABLE 6.1.1

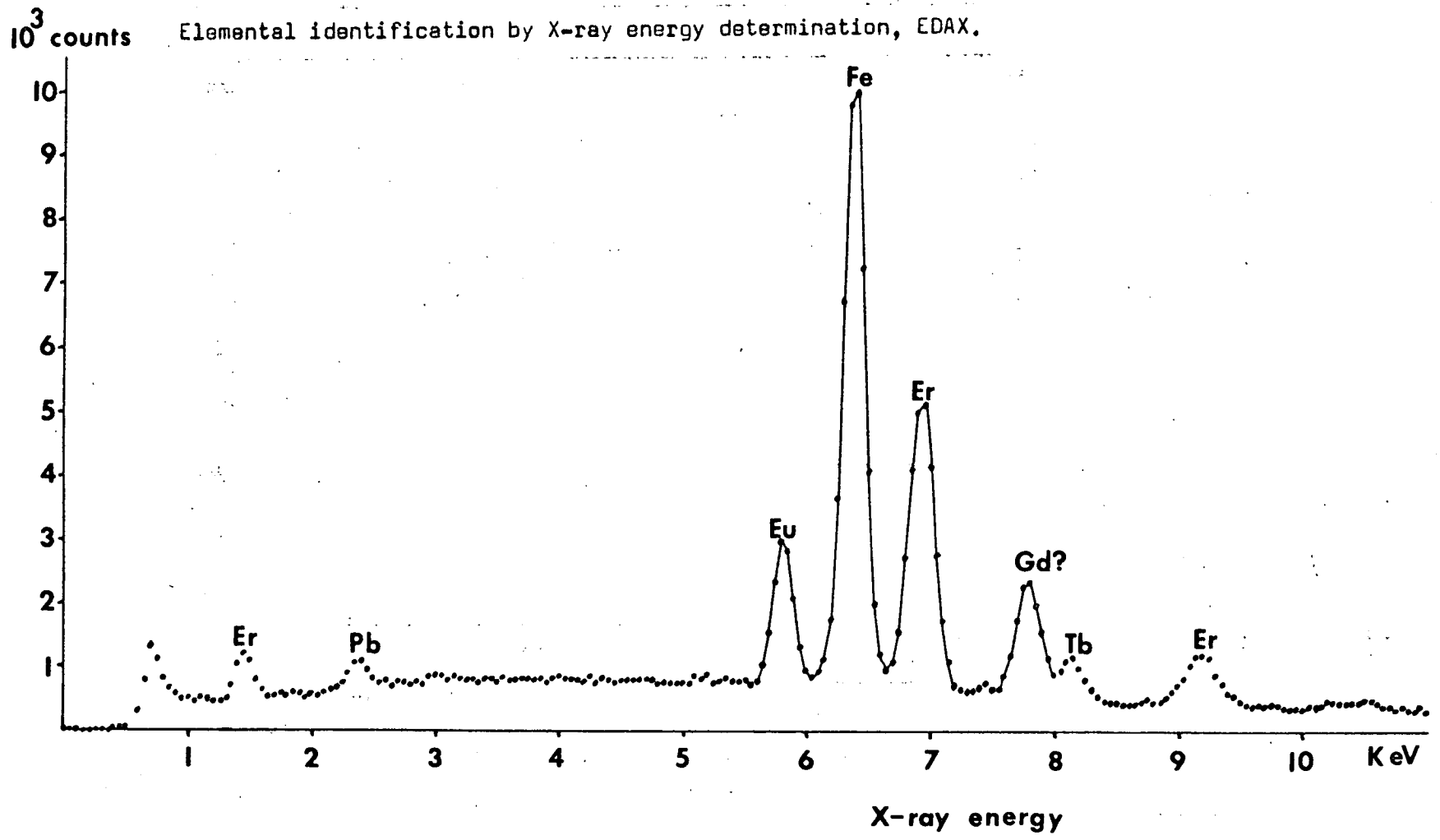
Elemental identification by X-ray energy determination, EDAX.
10^3 counts
10
9
8
7
6
5
4
3
2
1
Fe
Er
Eu
Gd?
Tb
Er
Er
Pb
1
2
3
4
5
6
7
8
9
10
KeV
X-ray energy

Figure 6.1.7

Figure 6.1.7 shows the EDAX analysis of a film of nominal composition, $Eu_2 Er_1 G_{0.7} Fe_{4.3} O_{12}$, grown on a GGG substrate. There is evidence of rare earth impurity. The gadolinium may be a signal from the substrate but this would be accompanied by gallium signal. There is also a peak showing the presence of lead in the film, a fact which is hardly surprising since ~90% by weight of the melt is lead oxide. The amount of lead incorporated in the film has been found to increase as the growth rate increases and as the growth temperature decreases.(60),(65) The lead composition varies through the film.(151),(152)

To minimise the lead content in the films high growth temperatures and slow growth rates are needed. The growth conditions must also be kept constant if a film of a single lattice parameter is required. Double crystal rocking curves have revealed the presence of accidentally produced double film layers in some samples, see fig. 6.1.8. The thicker the film is required to be the more important such control becomes if multiple layers in the film are to be avoided.

Film growth at lower temperatures and at an effective rotation rate of zero occurs in the mesas at the end of the growth cycle. The double crystal topograph in fig. 6.1.9 shows a mesa and the chilled region under the vacuum chuck giving slightly lighter contrast. The topograph was taken on the high θ side of the rocking curve and so the lighter contrast corresponds to regions of slightly larger lattice parameter. Thus there is a variation in the

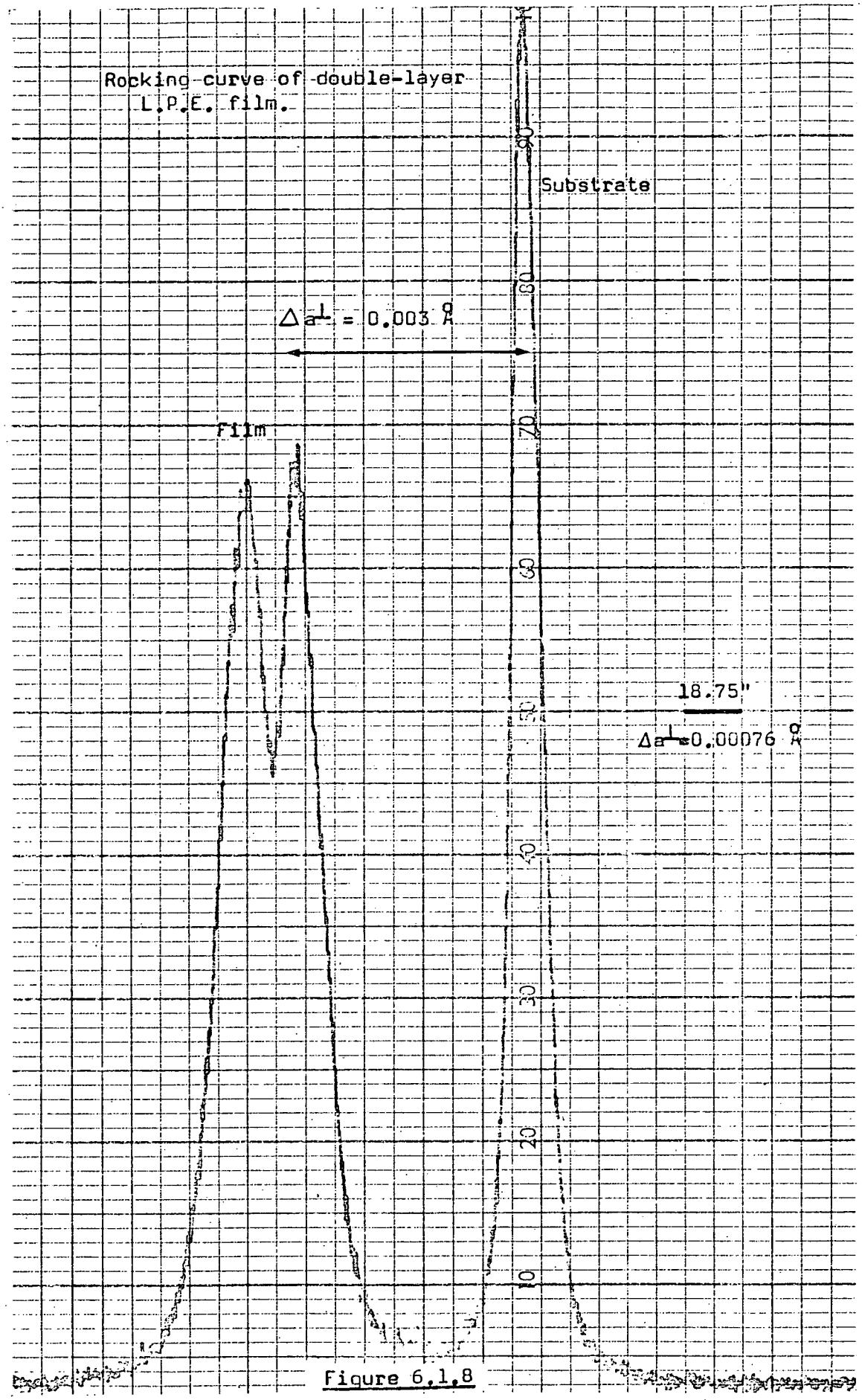
Rocking curve of double-layer L.P.E. film.
Substrate
$\Delta a_{\perp} = 0.003$ Å
Film
18.75"
$\Delta a_{\perp} = 0.00076$ Å
40
30
20
10

Figure 6.1.8

Topograph of L.P.E. film.

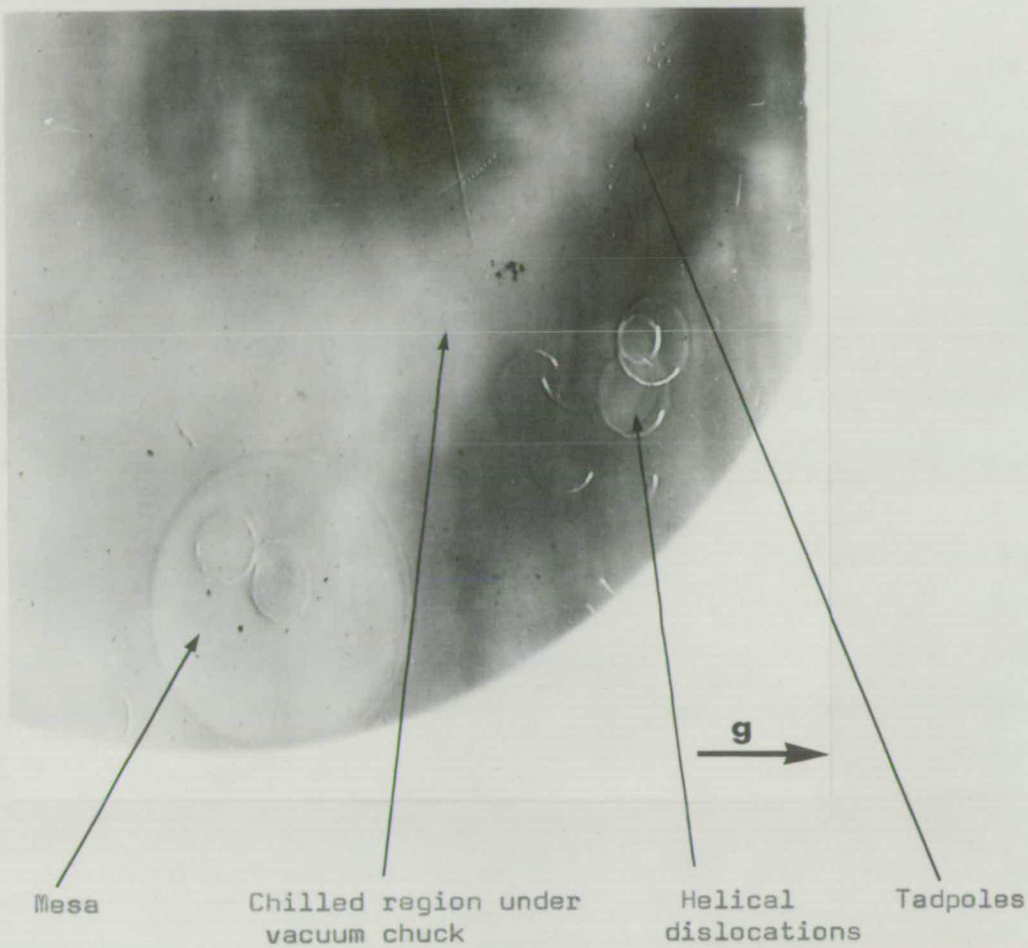

Double crystal (8 8 8) Cu Kα

1 mm

Figure 6.1.9

composition of the film across the chilled region and the possibility of a double, lead-rich film forming at the mesa.

b) CVD films

Films of pure YIG and Ga: YIG were grown by chemical vapour deposition. As for LPE films, the composition of the film will depend on any impurities in the starting materials. High purity reactants were used throughout and so this point will not be considered further.

A single layer film is required which is uniform in composition throughout its area. A similar problem to that of thickness variation along the gas flow direction occurs for composition variations, as can be seen in table 6.1.2.

Sample	$\Delta a^{\perp}$ Upstream	$\Delta a^{\perp}$ Downstream	% Difference
R3C	0.0173	0.0179	+ 3.4
N9	0.0188	0.0187	- 0.5
UC10	0.0195	0.020	+ 2.6
B9	0.0154	0.0141	- 8.4
B10	0.0101	0.0112	+10.9
A11	0.0160	0.0165	+ 3.1

TABLE 6.1.2

Lattice parameter mismatch measurements were made using a small x-ray beam at two points in the sample corresponding to positions upstream and downstream relative to the centre of the sample. The change in lattice parameter mis-

Lattice parameter mismatch versus the HCl gas flow over the Ga metal

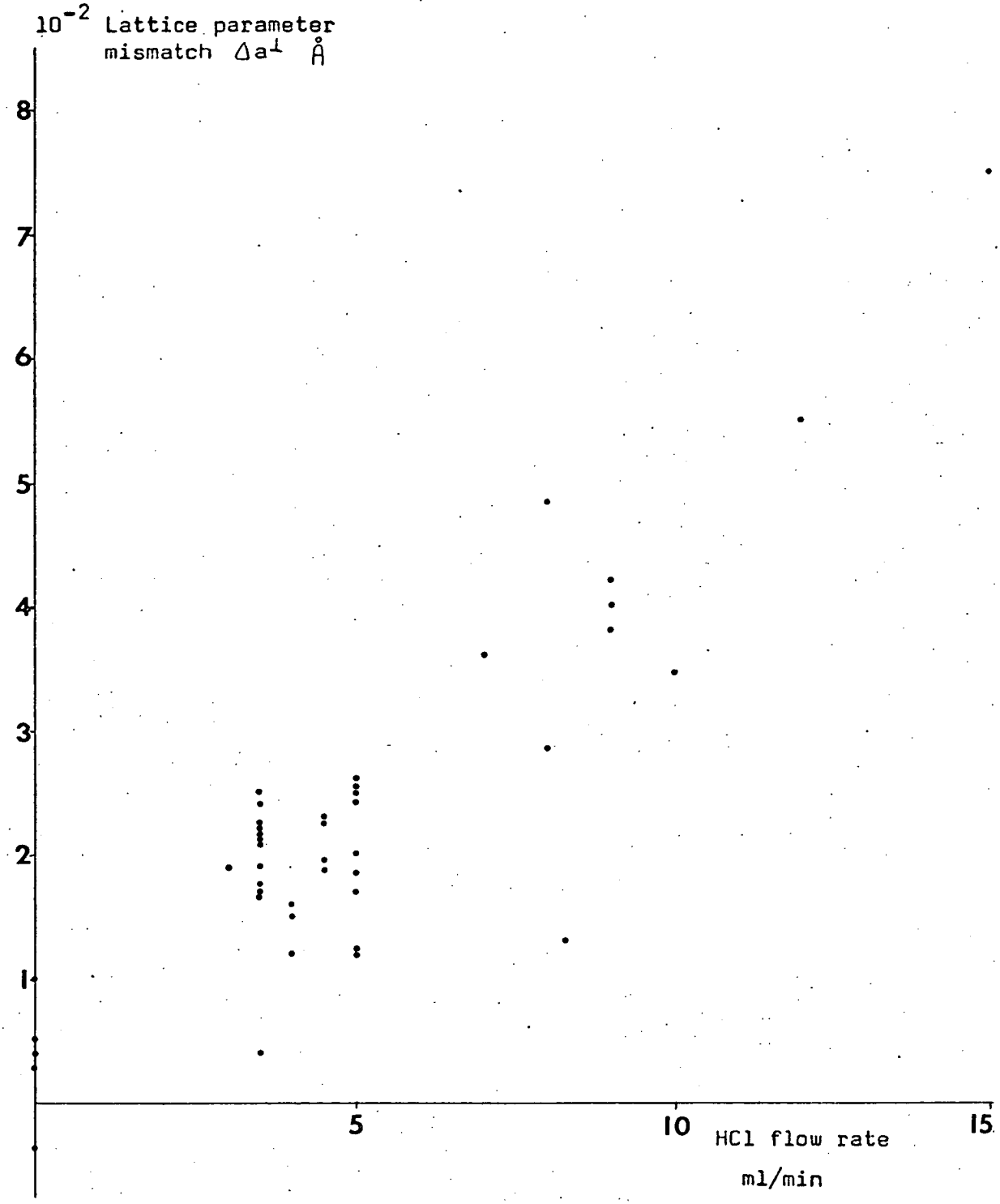

Figure 6.1.10

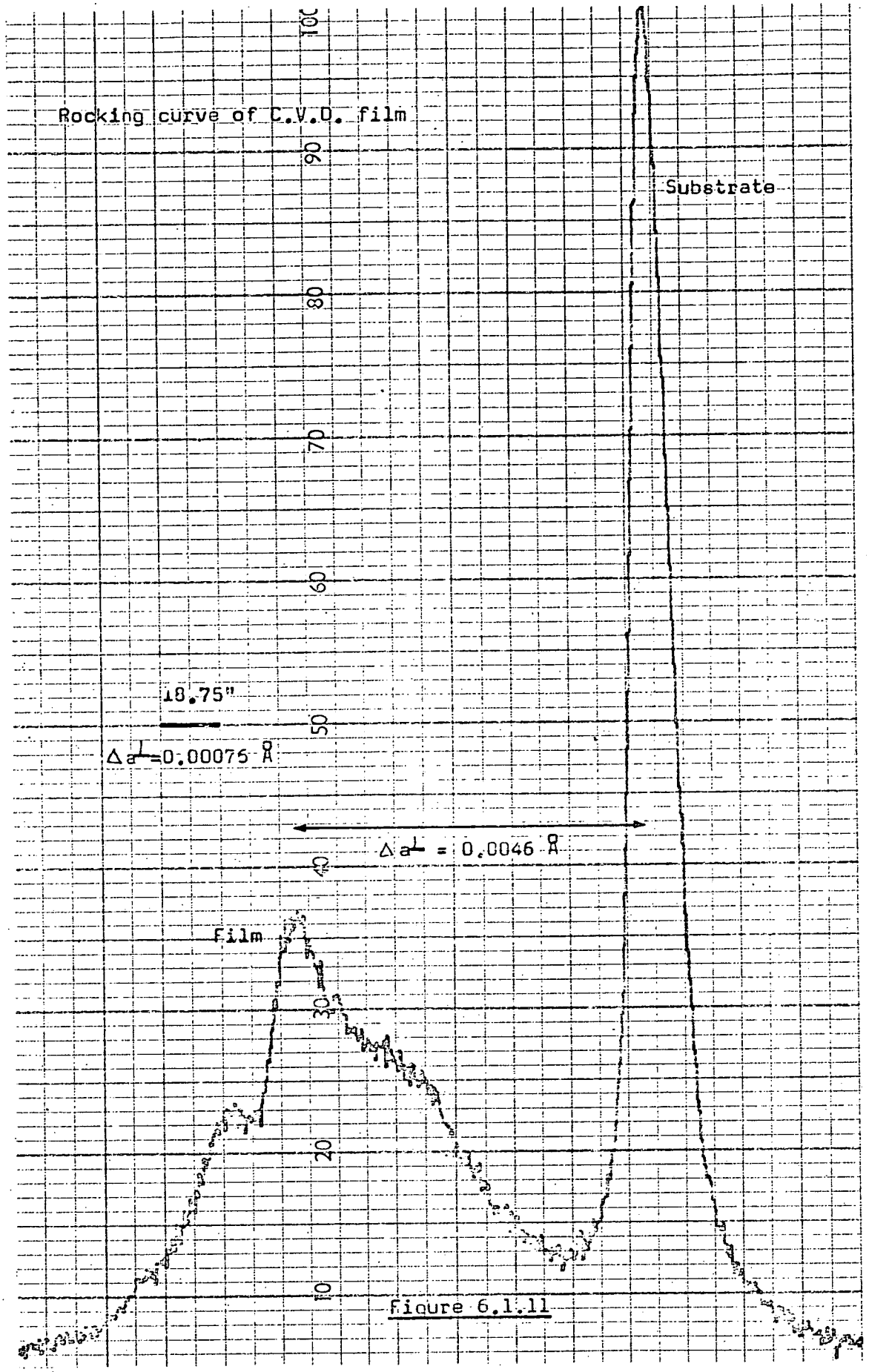
Rocking curve of C.V.D. film
100
90
80
70
60
50
40
30
20
10
Substrate
18.75"
$\Delta a^{\perp}$=0.00075 Å
$\Delta a^{\perp}$ = 0.0046 Å
Film

Figure 6.1.11

match of up to 10% over a distance of, at most, one centimetre reflects a similar change in gallium content. The samples with a large variation in lattice parameter of the film also had a fairly large variation in thickness. Position in the gas stream and the amount of tilt are also important since there is also a large variation in the lattice parameters of the films grown in the same run. The brackets in table 6.1.2 indicate which samples were grown together. Conditions of growth which produced a film of uniform thickness also give uniform composition.

The amount of gallium available to react and hence the amount of gallium incorporated in the growing film will depend on the rate of flow of the HCl carrier gas. The graph, fig. 6.1.10, shows the lattice parameter mismatch, $\Delta a^{\perp}$, measured in 47 samples of Ga:YIG versus the HCl gas flow rate. The general trend is for the lattice parameter mismatch, and hence the gallium content, to increase as the HCl flow rate increases. There is considerable variation in gallium content for a particular measured flow rate. These variations are measured on different samples but may occur within one film. In the long growth times of about 1 hour required for a 5 μm film the flow conditions may change sufficiently to produce multiple layers of different composition in the film. Figure 6.1.11 shows a rocking curve of one such film and the several layers are clearly resolved.

Table 6.1.3 gives the lattice parameters and number of layers found in CVD films. Where several peaks are indicated all values of lattice parameter are listed and

TABLE 6.1.3

Lattice Parameter Mismatch in CVD Films

Sample	Date of growth	Number of layers in film	Composition	Ga HCl flow rate ml/min	Thickness μm	Å	Cracks
B4	27.9.73	1	YIG	0		0.0105	No
B½	11.9.73	3	YIG	0		0.0047 0.0040 0.0030	No
R10B	25.8.73	2	Ga:YIG	4.5	4.7	0.0237 0.0228	Yes
R19C	16.8.73	1	Ga:YIG	3.5	4.8	0.0220	No
R12B	20.8.73	2	Ga:YIG	3.5	5.9	0.0245 0.0230	Yes
~~P4~~	16.8.73	1	Ga:YIG	3.5	5.7	0.0216	No
R8C	14.8.73	1	Ga:YIG	3.5	5.6	0.0213	Yes
R7B	14.8.73	2	Ga:YIG	3.5		0.0237 0.0227	Yes
E4	10.8.73	3	Ga:YIG	3.5	3.4	0.0198 0.0224 0.0236	No
R18A	8.8.73	8	Ga:YIG	3.5	3.6	0.0215 ↓ 0.0145	Yes
A7	10.8.73	3	Ga:YIG	3.5	7.1	0.0217 0.0193 0.0165	Yes

TABLE 6.1.3
(continued)

R4B	3.8.73	2	Ga:YIG	3.5	3.1	0.0042 0.0047	No
R3C	26.6.73	2	Ga:YIG	5	2.8	0.0187 0.0177	No
A26	2.8.73	2	Ga:YIG	3.5		0.0169 0.0154	No
R10C	27.3.73	1	Ga:YIG	8		0.0484	Yes
P7	29.3.73	4	Ga:YIG	7	8.4→4.4	0.0362 0.0358 0.0354	Yes
R9B	12.3.73	2	Ga:YIG	8	6.4→4.0	0.02859 0.0256	Yes
B19	23.8.73	1	Ga:YIG	5	4.2	0.0250	Yes
P9	23.8.73	2	Ga:YIG	5	5.2	0.0263 0.0250	Yes
UC9	20.7.73	1	Ga:YIG	3		0.0191	No
UC3	5.10.73	1	YIG	0		0.0053	No
R9A	25.8.73	1	Ga:YIG	4.5	5.7	0.0228	Yes
E20	26.7.73	1	Ga:YIG	3.5	3.2	0.0193	No
R3C	26.7.73	1	Ga:YIG	3.5	7.1	0.0176	Yes
B9	21.6.73	1	Ga:YIG	4	4.3	0.0148	No

TABLE 6.1.3
(continued)

B10	21.6.73	4	Ga:YIG	4	4.9	0.0108 0.0116 0.0129 0.0153	No
N9	22.6.73	1	Ga:YIG	4.5	4.4	0.0188	No
A11	21.6.73	2	Ga:YIG	4	3.6	0.0162 0.0174	No
UC10	22.6.73	1	Ga:YIG	4.5	3.0	0.0196	No
R9A	11.5.73	1	Ga:YIG	5	3.6→2.1	0.02545	No
R16A	13.5.73	4	Ga:YIG	5	5.5→3.3	0.0232 0.0248 0.0259 0.0275	Thick side
R19A	13.5.73	1	Ga:YIG	5	6.6→2.6	0.02439	Thick side
R20A	11.5.73	3	Ga:YIG	5	10.8→4.1	0.0174 0.0195 0.0211	Thick side
R4C	17.4.73	3	Ga:YIG	5	7.2→8.3	0.012	No
R18C	17.4.73	1	Ga:YIG	5	2.5→2.8	0.017	No
R20B	23.4.73	1	Ga:YIG	5	11 → 17	0.012	Yes
N9	26.3.73	2	Ga:YIG	9	9 4.4	0.038	Yes

TABLE 6.1.3
(continued)

R25B	26.3.73	1	Ga:YIG	9	2.9 1.5	0.042	Thick side
R14A	27.3.73	1	Ga:YIG	9	3.7 1.4	0.040	Yes
R8A	5.3.73	?	Ga:YIG	8.25	8.3 5.5	0.013	Yes
B19	30.1.73	?	Ga:YIG	20	1.1	0.078	Yes
B20	30.1.73	?	Ga:YIG	15	1.2	0.075	Yes
R3A	26.2.73	1	Ga:YIG	12	1.2	0.055	Yes
R3B	26.2.73	1	Ga:YIG	10	3.7 2.1	0.0346	Yes

that of the dominant peak is underlined. Evidently, the gas flow meters were not sufficiently sensitive to detect small changes in flow rate. Changes in the arrangement of the furnace and any leaks would produce long term changes. Note that the sample B½, which is supposedly of pure YIG, has three discrete layers in the film. This suggests contamination from deposits on the walls of the furnace. The early films had very broad rocking curves. Later films had narrow rocking curves which indicates a general improvement in the quality of the films with time.

6.1.3 Inclusions

a) LPE films

The composition of the melt should be chosen to produce garnet as the primary phase. After several growth runs the composition of the melt will change. If there is a reduction in the PbO content by evaporation, or in Fe_3O_4 by depletion, then the melt will approach the garnet/orthoferrite phase boundary. This increases the possibility of formation of orthoferrite crystals. These will form readily if the temperature of the melt is more than 5^{o} below saturation temperature in the orthoferrite region, or if there are sites for crystal nucleation such as dust or particles from the furnace lining. These small orthoferrite crystals float on the surface of the melt and will be incorporated into the growing film, particularly with the vacuum chuck method of support. Some of these inclusions are seen in fig. 6.1.12. These crystals are only loosely attached to the film and may fall out,

Inclusions in L.P.E. films.

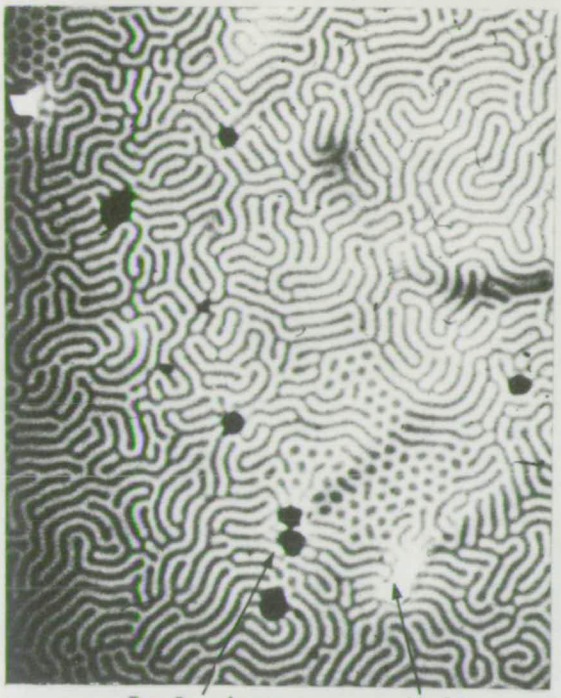

Polarised light

0.25 mm

Lang reflection topograph of film.

(16 16 16) Mo Kα 1 mm

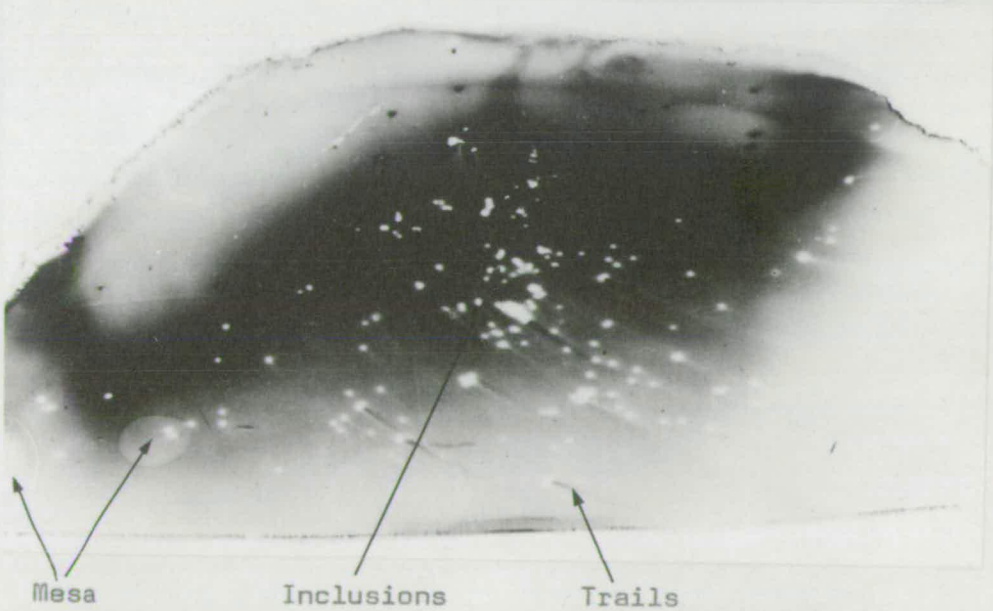

Double crystal topograph of film (8 8 8) Cu Kα 1 mm

Figure 6.1.12

leaving a crystal-shaped hole in the film. The topograph (b) of the same crystal shows that the crystallites do not diffract and so are not related to the substrate. They have affected the film by making the area of film immediately round the inclusion much thinner, thus the substrate reflection immediately by the inclusion shows stronger since the absorption is less. The crystallite was picked up from the beginning of growth and has upset the flow pattern of liquid over the surface of the rotating sample, as can be seen in the 'trails' of topograph of fig. 6.1.12(c).

b) CVD films

Phases other than garnet are produced at different points in the gas stream. The region immediately prior to the garnet field produces orthoferrite. If small particles of orthoferrite are produced in the gas stream, or become detached from the surface on which they formed, they can be swept onto the garnet substrate by the gas flow. A substrate put into the region which gives orthoferrite on the fused quartz surface will still have garnet deposited on it[70],[153] but any perturbation such as dust or scratches will encourage the formation of orthoferrite.

The growth of the garnet film around the orthoferrite crystallite is prevented. The crystallite will continue to grow, thus extending its adverse influence further. This can be seen in fig. 6.1.13. The variations in thickness of the film are seen by the changes of absorption of the substrate reflection. A few large crystallites have formed

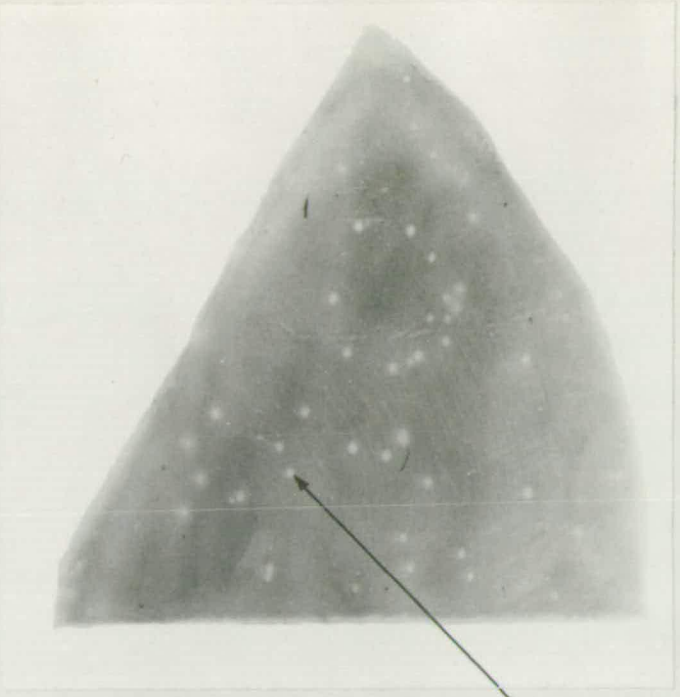

Topograph of film

Holes in film around inclusions

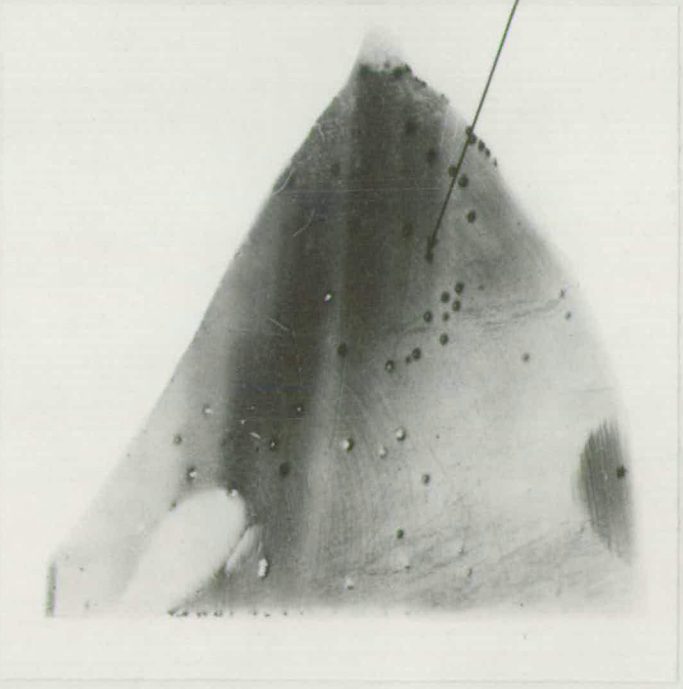

Topograph of substrate through film

Double crystal (8 8 8) Cu Kα

2 mm

Figure 6.1.13

with an extensive ring of thinner material around them.

6.1.4 Elastic strain

A film which would have a free lattice parameter less than that of the substrate will grow with tensile stresses in the plane of the film. The strains produced will mean that the film is no longer cubic. This is what produces the magnetic anisotropy in CVD films and is also important for LPE films. This strain has been assumed to be elastic and this was demonstrated in the following way. Figure 6.1.14 shows the schematic arrangement of crystal planes when an epitaxial film is grown on a substrate. All of the strain is located in the film and there is perfect matching at the interface of the crystal planes normal to the slice.

		Angle between planes
Planes normal to surface	$d_s^{\parallel} = d_f^{\parallel}$	0
Planes parallel to surface	$d_s^{\perp} > d_f^{\perp}$	0
Any other set of planes	$d_s > d_f$	$\psi > 0$

Double crystal rocking curves show, in general, two peaks, one from the substrate and one from the film.[82] For reflections from planes parallel to the surface the spacing between the peaks should be independent of the orientation of the sample. Any other reflection will give a different separation as the crystal is rotated about the diffraction vector and this difference will depend on the amount of strain in the film.[84],[154]

A sample of Ga:YIG grown by CVD was chosen which was

Model of elastic strain in an epitaxial film.

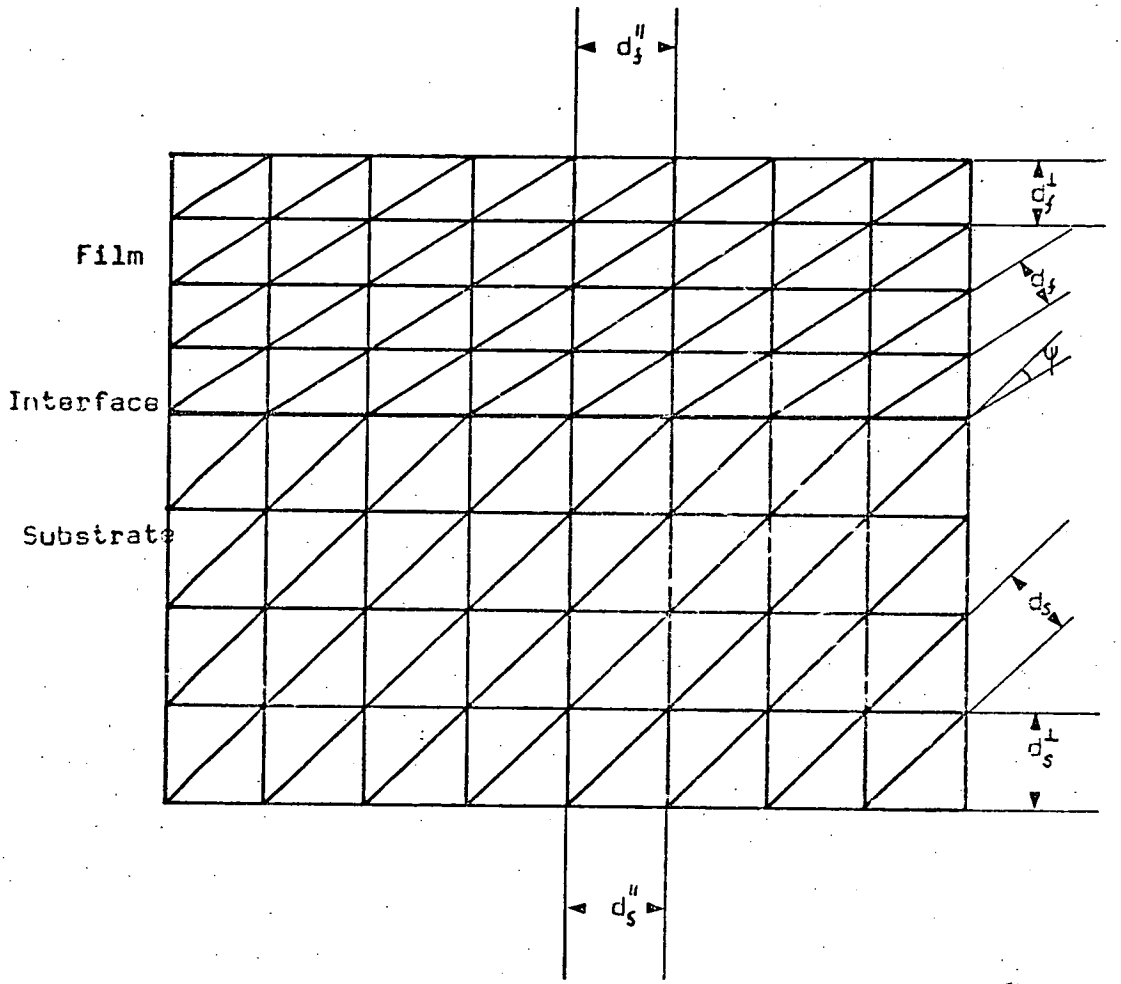

Figure 6.1.14

a single layer film of fairly constant thickness and composition and of good quality. The reflecting planes used were (8 8 8) symmetric, three {8 8 0} and three {12 4 4} asymmetric reflections. The (8 8 8) symmetric rocking curves were measured four times for four different orientations of the crystal. The asymmetric reflections were each measured twice in the non-dispersive setting but in two different orientations, so that the effects of plane rotations and dilatations could be separated. The settings are described as type 1 where the (111) surfaces of the sample and reference crystals are parallel, and type 2 when the reflecting planes are parallel but the (111) surfaces are not. Table 6.1.4 summarises the results. The arrow in the column marked 'orientation' shows the direction of gas flow across the crystal when the measurement was made. The larger angular separation between the peaks corresponds to $\Delta\theta_d + \psi$, the smaller gives $\Delta\theta_d - \psi$ where $\Delta\theta_d$ is the change in Bragg angle due to change in d-spacing. The final column in the table gives the value of Δa calculated for the model shown in fig. 6.1.14. The agreement is within the limits of experimental error, particularly as composition gradients in the film are not entirely absent.

The symmetry in the angles between the planes of the substrate and the film indicate a rhombohedral distortion of the basic cubic lattice. Instead of the angles between the <100> directions being 90° they are all $\alpha > 90^\circ$. An estimate of α was obtained from the angles between the

Reflection	Orientation	Angle Rad	$\Delta\theta_d$ Rad	ψ Rad	$\Delta\bar{\theta}_d$	$\bar{\psi}''$	Δa	Δa model
12 4 4	2	0.002199	0.001563	0.000636				
	1	0.000927						
	1	0.001218	0.001814	0.000595	0.0017 ±0.0002	130	0.014 ±0.002	0.017 ±0.001
	2	0.002408						
	2	0.002309	0.001645	0.000664				
	1	0.000982						
8 8 8	1	0.002763	0.002695	0.000068				
	1	0.002627			0.0026 ±0.0001	17	0.019 ±0.001	0.019 ±0.001
	1	0.002691	0.002591	0.000010				
	1	0.002491						
8 8 0	1	0.000545	0.001210	0 000754				
	2	0.002054						
	2	0.001963	0.001118	0.000845	0.0012 ±0.0001	164	0.015 ±0.001	0.016 ±0.001
	1	0.000273						
	2	0.001963	0.001172	0.000791				
	1	0.000382						

TABLE 6.1.4

{110} and (111) planes in the film since these planes are more sensitive to changes than the {311} planes

$$110 \wedge 111 \quad \cos\phi = \frac{2 + 4\cos\alpha^*}{(2+2\cos\alpha^*)(3+6\cos\alpha^*)}$$

$$\cos\frac{\alpha^*}{2} = \frac{1}{2\cos\alpha/2}$$

Results

$110 \wedge 111$	In cubic	Expt in film	$\alpha = 90^\circ 3'$	$\alpha = 90^\circ 4'$
	35.264	35.219	35.229	35.217

Thus in this sample for a $\Delta a^{\perp}$ of 0.019Å the film is rhombohedral with an angle $\alpha = 90^\circ 4'$ and all distortions are elastic and can be considered confined to the film.

This experiment, performed on an LPE film before and after annealing to remove the growth-induced anisotropy, would be interesting.

The previous analysis has assumed that the lattice parameter mismatch for planes perpendicular to the surface is zero. This assumption can be checked by zebra patterns of a thick film on a substrate which has been cut normal to the (111) plane. A sample with a YIG film 70 μm in thickness was cut on a (110) plane in this way. Zebra patterns of the polished edge were taken using Si (440) as reference and GGG (880) on the sample. The stripe was photographed for two known positions of the sample. The

Zebra pattern of section through substrate and thick film.

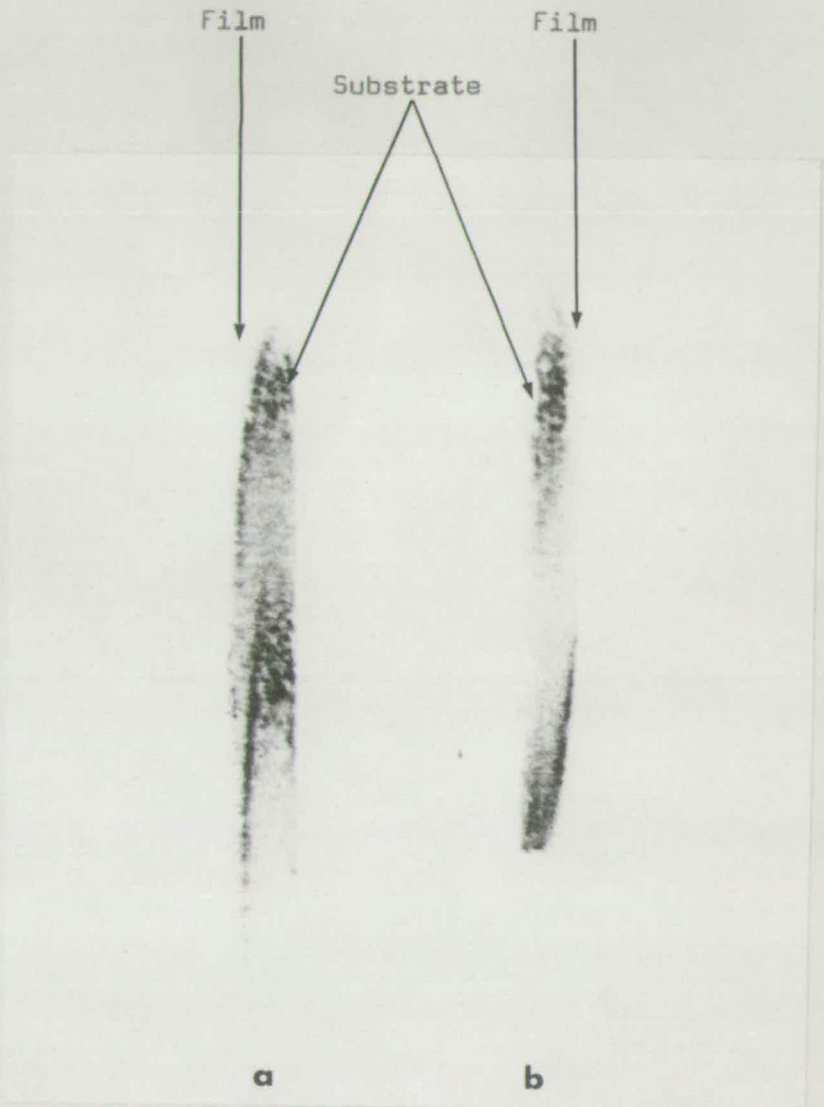

Double crystal (8 8 0) Cu Kα

1 mm

Figure 6.1.15

effects of dilatation and rotation were separated by repeating the experiment with the sample inverted. Figure 6.1.15 shows the set of photographs. Photograph (a) shows the effect of $\Delta\theta_d + \psi$ and (b) shows $\Delta\theta_d - \psi$. These give a value of $\Delta a''$ of 0.0012Å and a rotation of one minute of arc in a film for which $\Delta a^{\perp}$ is 0.01Å. Such a large rotation of the planes was not indicated by the rocking curve measurements which were made in the centre of the sample. This rotation can occur by relaxation of the stresses at the cut edge of the sample and this will allow the small change in lattice parameter in the (110) planes near the edge. This is illustrated in fig. 6.1.16. Therefore these Zebra pattern measurements do not contradict the model in fig. 6.1.14.

6.1.5 Cracks

If the tensile stress is sufficiently large the film will crack.[45] This may be aided by a notch of some sort in the film. The cracks will produce a change in spacing and tilting of the crystal planes as occurred for the edges of the slice. This means that cracks will be readily visible by x-ray topography, as can be seen in fig. 6.1.17. This shows two samples, one grown by LPE, the other by CVD. In both cases the cracks tend to run in straight lines in particular directions, except where influenced by scratches or the proximity of other cracks. The positions of the cracks visible in topograph (a) were measured using the micrometer stage of a microscope and corrected to remove the distortion inherent in the topograph. The

Relaxation of strained film at crack or edge of sample.

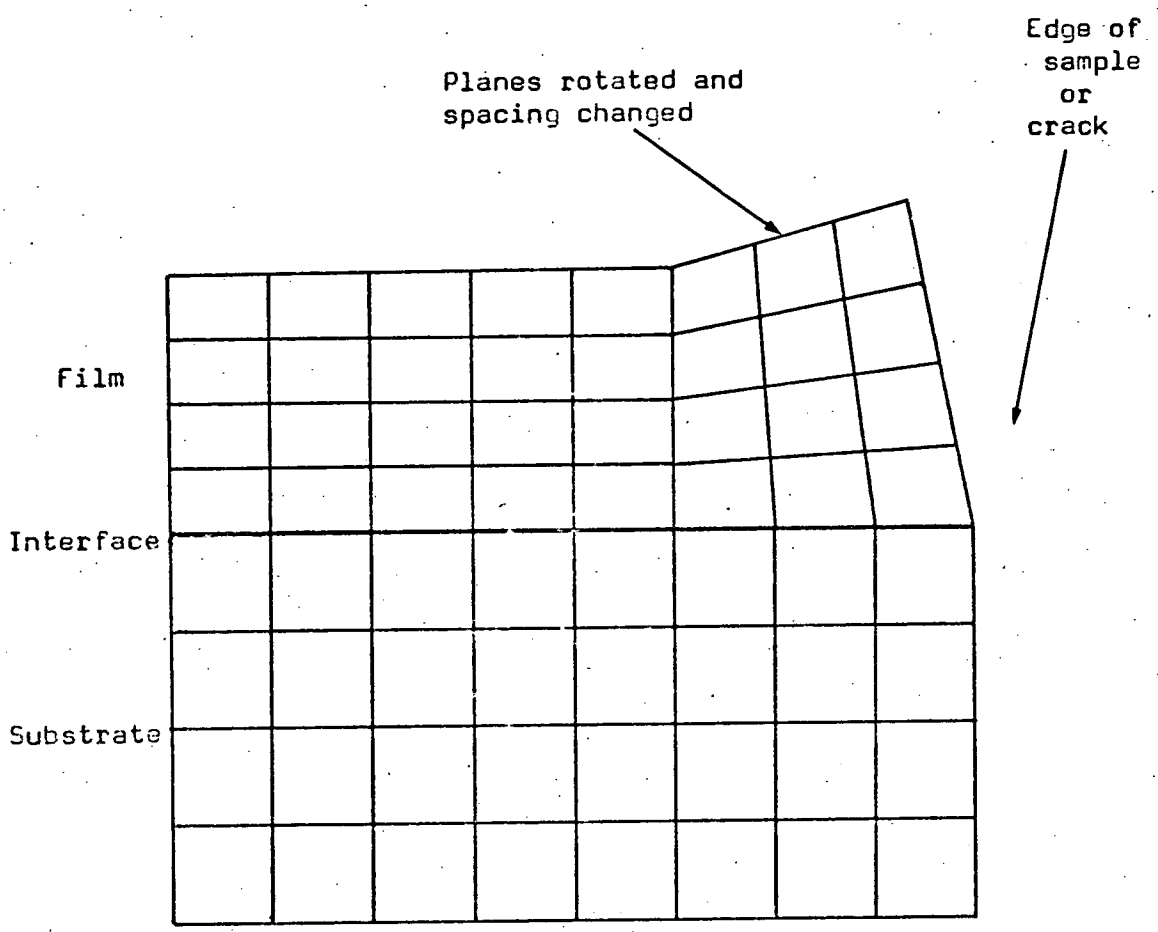

Figure 6.1.16

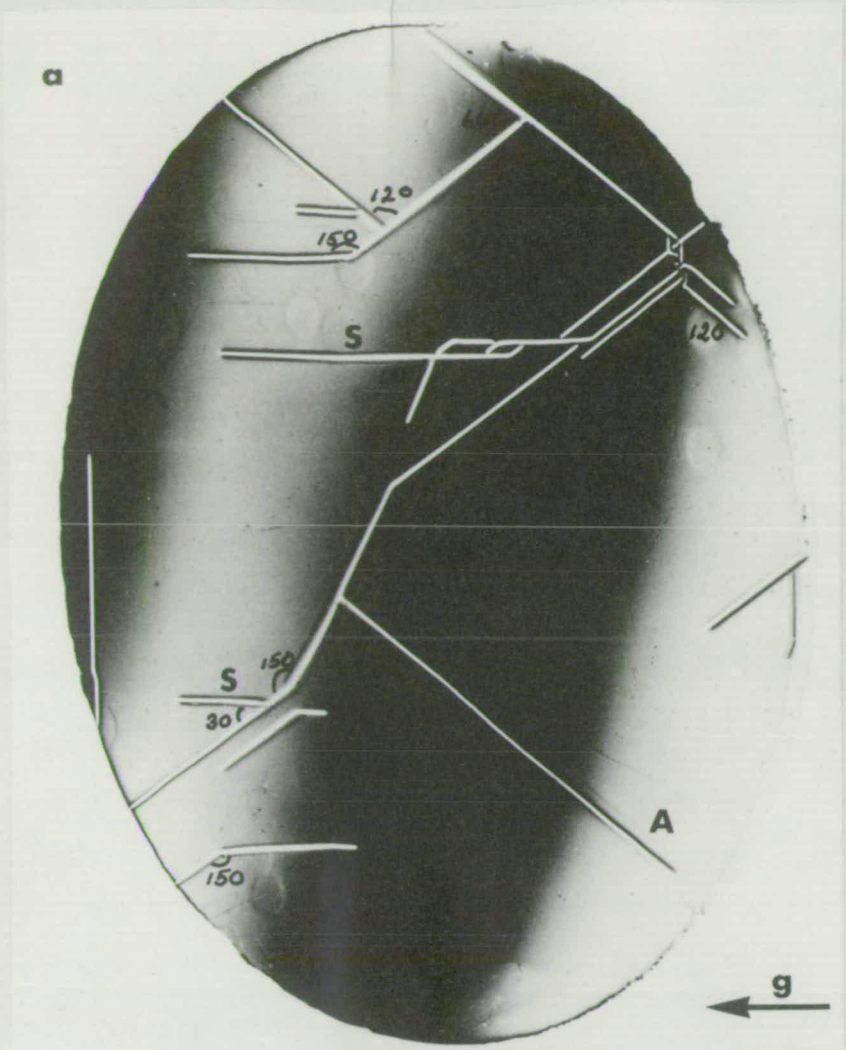

Cracks in L.P.E. film

Double crystal (8 8 8) Cu Kα

1 mm

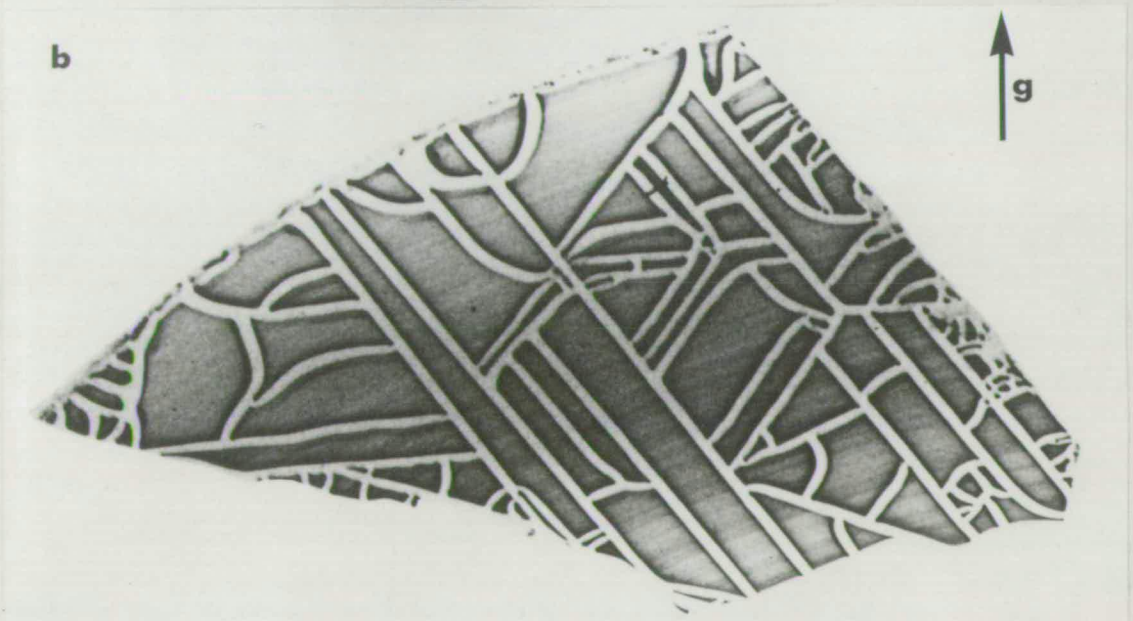

Cracks in C.V.D. film

0.5 mm

Lang reflection (16 16 16) Mo Kα

Figure 6.1.17

angles between the cracks are marked on the topograph. These angles are consistent with the cracks being mostly along the {211} and {110} planes which lie normal to the plane of the slice. Laue photographs confirm that the crack marked A is in the (110) plane.

The x-ray images of the cracks extend a large distance either side of the cracks and come from the combinations of rotations and dilatations. The sample as a whole is bent into a saucer-shape, as can be seen by the $k\alpha_1$ and $k\alpha_2$ bands. Immediately by the cracks the rotations of the planes are so great that there can be no diffraction. Further from the crack the rotations will be smaller but the lattice parameter $\Delta a^{\perp}$ will be larger than in the uncracked region of the film since it is more nearly cubic. The horizontal cracks show contrast away from the crack which depends just on these changes in lattice parameter. The horizontal cracks in the non-diffracting region between the $k\alpha_1$ and $k\alpha_2$ bands show two dark stripes either side of the white stripe. This is where the curvature of the sample allows the Bragg condition for diffraction in the regions of larger $\Delta a^{\perp}$, i.e. smaller θ, to be satisfied. This effect is seen in cracks running in other directions but the dark images are displaced due to the rotations of the planes.

The vapour phase grown films of $Y_3Ga_xFe_{5-x}O_{12}$ require a fairly high gallium content, with x about one, to produce magnetisations of the required values. This amount of gallium produces a large mismatch. Cracking occurs if the fracture stress is exceeded. Cracks are propagated

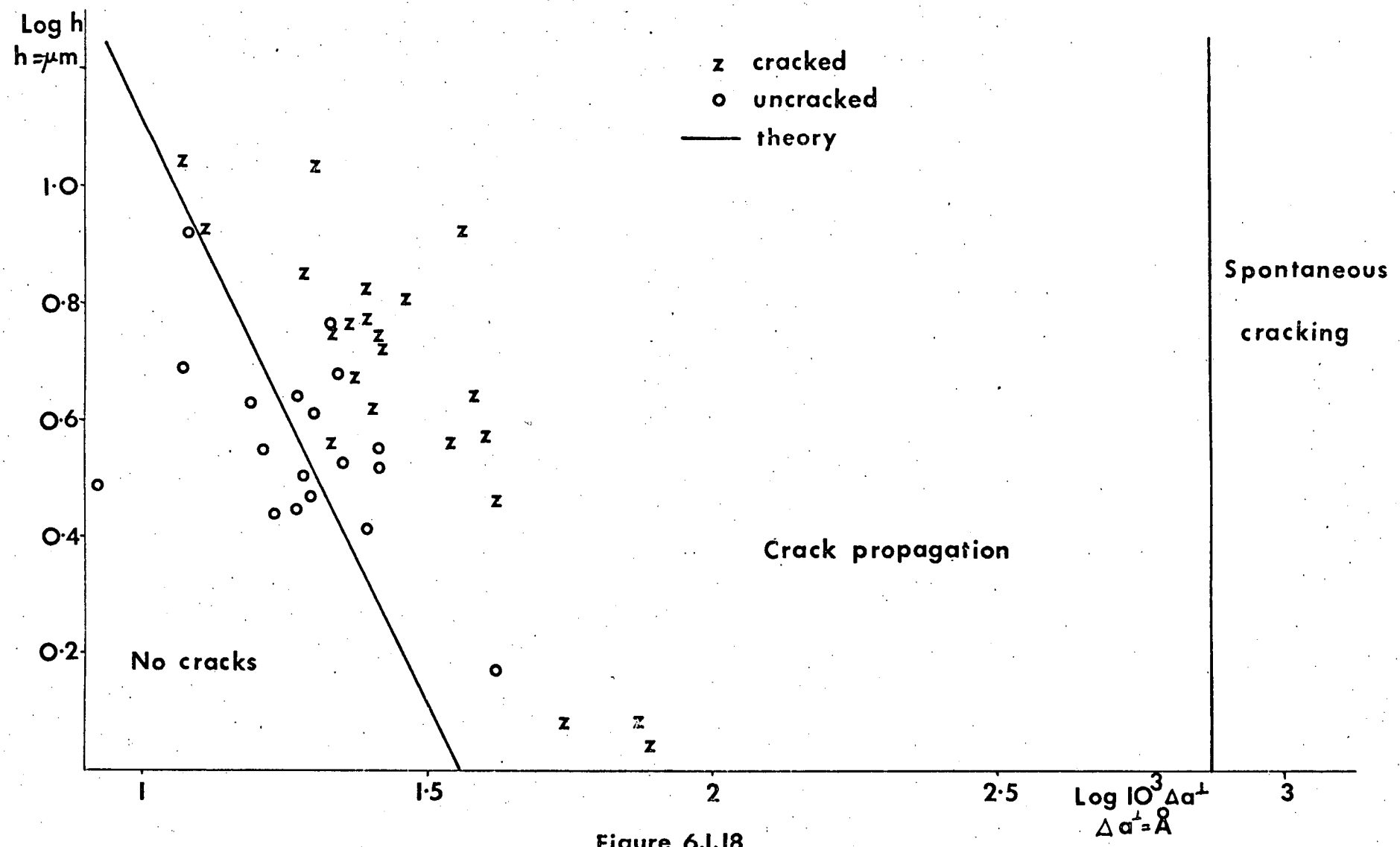
Log h
h = μm
1·0
0·8
0·6
0·4
0·2
z cracked
o uncracked
theory
Spontaneous
cracking
Crack propagation
No cracks
1
1·5
2
2·5
3
Log 10³ Δa⊥
Δa⊥ = Å

Figure 6.1.18

from a notch if the thickness of the film is greater than half the Griffith crack length.[45] Table 6.1.3 includes data on the thickness of the film and the presence or absence of cracks. These data are summarised in the graph in fig. 6.1.18. Matthews[45] gives a theoretical expression which predicts that the thickness at which cracks are propagated is proportional to $^{1}/_{\Delta a^2}$. This theoretical curve is marked in fig. 6.1.18 and is supported by the experimental points. Below the line none of the samples was cracked. Above the line most of the samples were cracked as this is the region where cracks will propagate. None of the samples was near the region where spontaneous cracks would occur.

In one early LPE sample the film was in compression and the stresses were sufficiently great[155] to fracture the film at the film/substrate interface. No measurements were made on this sample.

6.1.6 Misfit dislocations

According to the amount of mismatch found in the YIG and Ga:YIG films it would have been energetically more favourable for misfit dislocations to have formed to relieve the stress rather than cracks.[45] That cracks have formed and misfit dislocations were absent in all but one film, as observed by x-ray topography, would indicate that such dislocations are difficult to generate.

In just one sample, what appears to be a network of misfit dislocations was formed in a YIG film grown by CVD. A topograph of this sample is seen in fig. 6.1.19.

Misfit dislocations in a C.V.D. film.

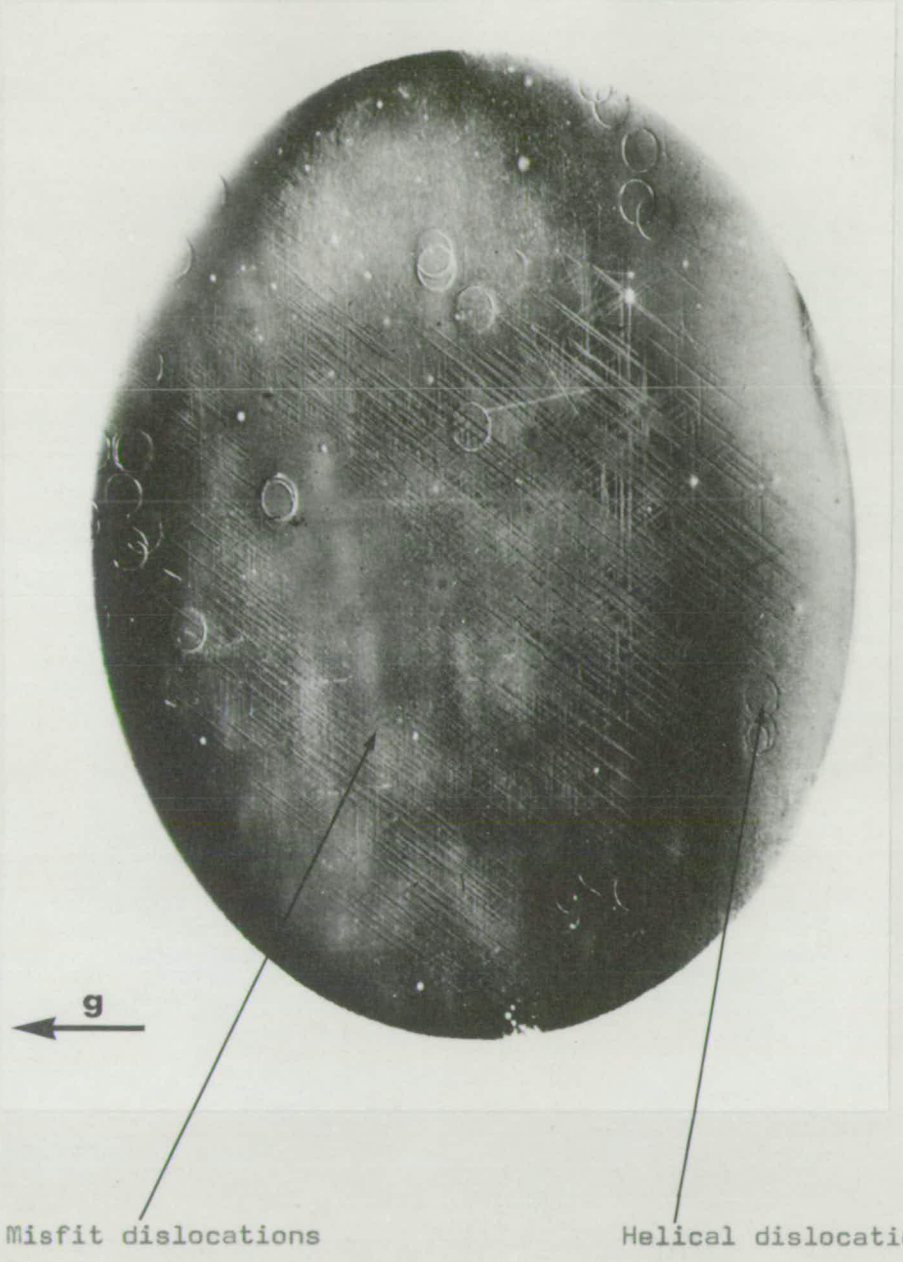

Double crystal (8 8 8) Cu Kα

1 mm

Figure 6.1.19

This sample was of rather poor general appearance and had a very high density of small crystals of orthoferrite in the film. These would be sites of stress concentration, particularly if there were large thermal fluctuations. There is a symmetry in the direction of the bands which run in the ⟨110⟩ directions in the plane of the slice. In a few places individual dislocation lines can be resolved. These dislocations appear similar to misfit dislocations observed in P-diffused silicon.(156)

Misfit dislocations, to have the maximum effect in relieving stress, would be pure edge with both the dislocation line and the Burgers vector lying in the plane of the film. No further x-ray work was done on this film because of its general poor quality. From this one topograph the following information is available. The dislocation line runs along ⟨110⟩. A Burgers vector of ⟨211⟩ type in the plane of the film is unlikely but there is a ⟨111⟩ direction normal to ⟨110⟩ and not normal to the plane of the film. This would give an edge dislocation of the smallest, and energetically most favourable, Burgers vector lying at only 20° to the plane of the film, which would be nearest the optimum configuration. The low dislocation contrast would help to confirm this.

6.2 Effect of Substrate Defects

In the previous section the type of defect observed in the film depended on the method of growth of the film. In this section the effects of the defects in the substrate on the epitaxial film are considered. In general the

effects are independent of the method of growth except in a few cases which will be indicated.

6.2.1 Preparation of surface

The flatness, or otherwise, of the substrate does not affect the growth of the film. The film will follow the shape of the substrate. Scratches and dirt on the surface have a bad effect on the film.

At the high temperatures involved during growth dust and organic material on the substrate will become charred and firmly attached to the substrate. This will have the effect of masking, partly or completely, the substrate from the melt or gas flow. The particle will be a nucleation site for unwanted phases such as orthoferrite and large inclusions may form as seen previously.(65) It would seem to be a matter of common sense that good films will not grow on dirty substrates.

Scratches are regions of high local strain and for deep scratches the misorientations can be very large and extend several hundred microns. An epitaxial film grown over a scratched region will tend to match the local variations in orientation and in extreme cases may form nucleation sites either for isolated islands of garnet or for orthoferrite. The continuation of misorientations in the film meansthat scratches will be visible in topographs of films and can be seen in figs. 6.1.2, 6.1.5, 6.1.9, 6.1.17. In figure 6.1.17 some of the scratches have caused cracks to form and these parts can be identified as being less straight and the contrast of the parallel black bands

either side of the crack is rippled instead of smooth. This is marked S on the topograph.

If thick, crack-free films are required then scratches must be eliminated since the thickness and likely mismatch bring the sample into the region where cracks, once formed, will propagate even from shallow scratches. This also means that scratches must not be introduced by the handling of the slice after the film has been grown.

6.2.2 Inclusions

No defect in the films directly attributable to inclusions in the substrate was observed here. Pitting in the film due to inclusions near the surface have been observed by scanning electron microscopy by Gill and Fairholme.[157]

6.2.3 Growth bands

In the discussion on tensile stress in the film it was found that the film is strained elastically. The planes normal to the film/substrate interface are continuous and straight across the boundary. If the spacing of these planes in the substrate varies then the variation will be matched by the planes in the film and thus produce a complementary change in the spacing of the planes parallel to the interface. An increase in $d_s^{//}$ will give an equal increase in $d_f^{//}$ and thus cause $d_f^{\perp}$ to decrease.[158] The local value of $\Delta a^{\perp}$ will increase. Thus if growth bands in the substrate cause variations in $d_s^{//}$ then the growth band pattern will be replicated in the film.

The analysis of topographs of growth bands in substrate

materials showed that the variation in d parallel to the lamellae was much less than the value of d perpendicular since the growth bands are constrained by the neighbours. The amount of variation in d parallel to the (111) slice depends on the angle at which the growth bands intersect the surface and on the amount of composition variation. Thus for growth bands in the form of a spherical cap, the variation in d parallel to (111) would be greatest near the edge of the sample and almost zero at the centre.(159)

Epitaxial films, both CVD and LPE, grown on slices from the two boules which had almost flat growth bands did not show any replication of the growth band pattern. This is seen in figs. 6.1.9, 6.1.12, 6.1.17 and others from the same boules. For the other substrates the effect of substrate growth bands was much more pronounced for CVD films than LPE films. The contrast from growth bands was reduced in the film since the film is only sensitive to part of the lattice parameter variations of the substrate. Figure 6.2.1 compares topographs of films and substrates. The LPE film in this figure showed the greatest growth band pattern of the LPE films, for most LPE films the growth bands were barely visible.

There should be no difference between the sensitivity of CVD and LPE films to growth bands in the substrate if the model of elastic strains described above were the only mechanism operating. One major difference between CVD and LPE films is the rate of growth which is approximately an order of magnitude greater for LPE films which also tend to be thicker films. There may be time for a

The effect of growth bands on epitaxial films

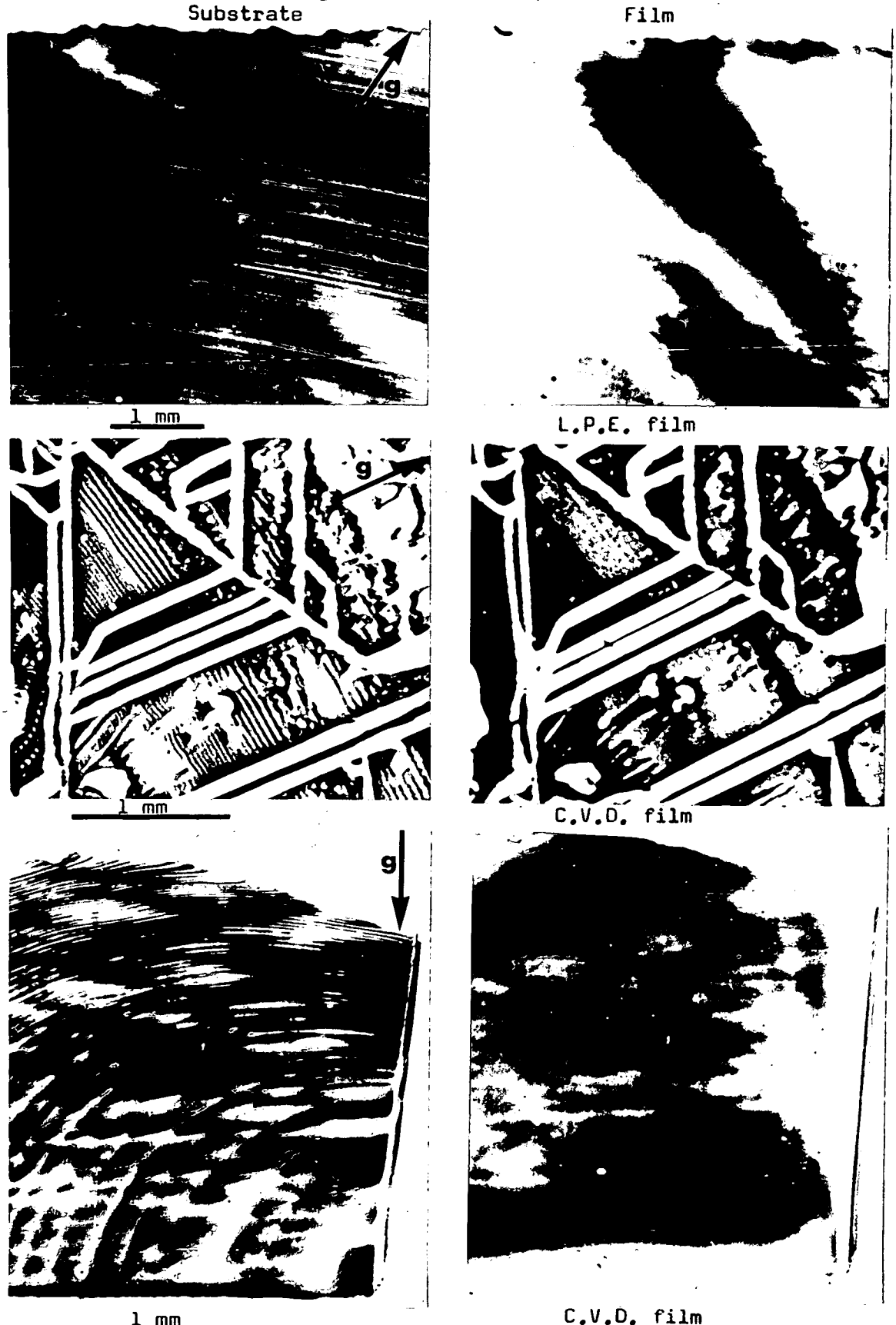

Double crystal (8 8 8) Cu Kα

Figure 6.2.1

The effect of growth bands on epitaxial films

Substrate

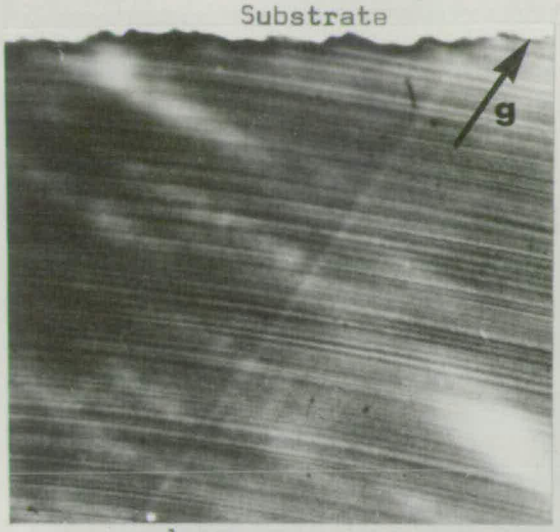

1 mm

Film

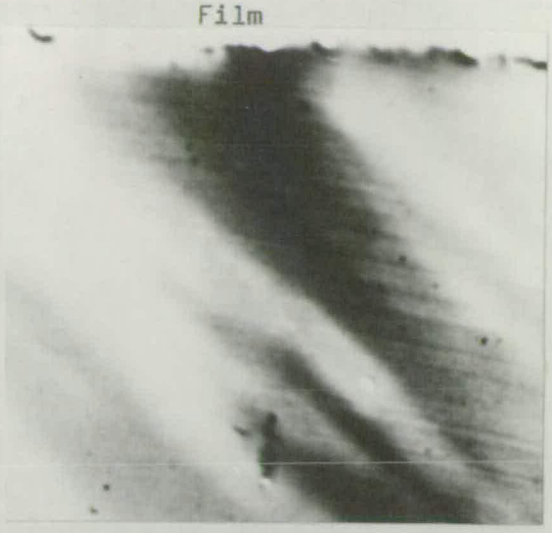

L.P.E. film

1 mm

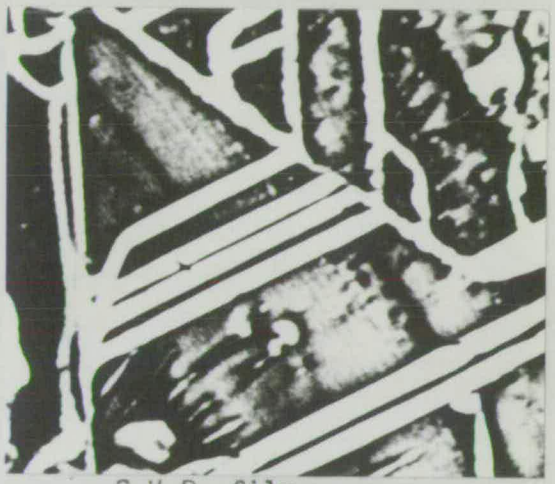

C.V.D. film

1 mm

Double crystal (8 8 8) Cu Kα

C.V.D. film

Figure 6.2.1

redistribution of components in CVD films[160] but this would mean that pure YIG films should show no banding, which is not the case. High gallium content CVD films will have a much greater mismatch than LPE films which can be more easily designed to low mismatch. Since the contrast comes from the elastic strain in the film if there were zero mismatch there would be no strain and thus no replication of growth bands. Conversely, the greater the mismatch the greater the contrast seen in the film from growth bands.

6.2.4 Coring and faceting

The effect on epitaxial films from a core is equivalent to a large growth band, of greatly increased lattice parameter, running perpendicular to the (111) slice. Thus the full effect of the core should be found in the film. The value of d parallel to the slice is greater in the cored region that the matrix and this causes extra tensile stress over the facet in the film of smaller free lattice parameter.[159],[160]

Figure 6.2.2 shows topographs of film and substrate for cored samples and fig. 6.2.1 shows a sample with an edge facet. One sample of fig. 6.2.2 is bent into a saucer-shape and the cored region is diffracting even though the $k\alpha_1$ diffracting band does not pass through it. The core is set at a higher angle of incidence to the $k\alpha_1$ beam and so, for it to diffract, the lattice parameter $a^{\perp}$ must be smaller over the core than for the surrounding film. This confirms the above argument.

Effect of coring on films.

Substrate

L.P.E. film

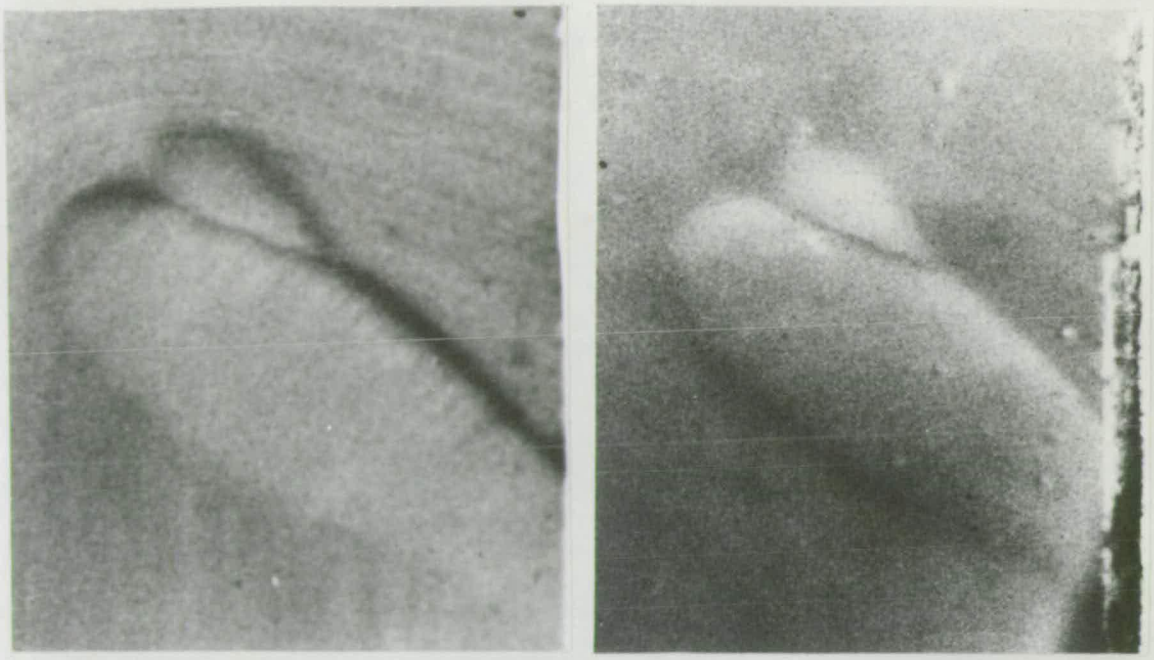

Lang reflection (16 16 16) Mo Kα

1 mm

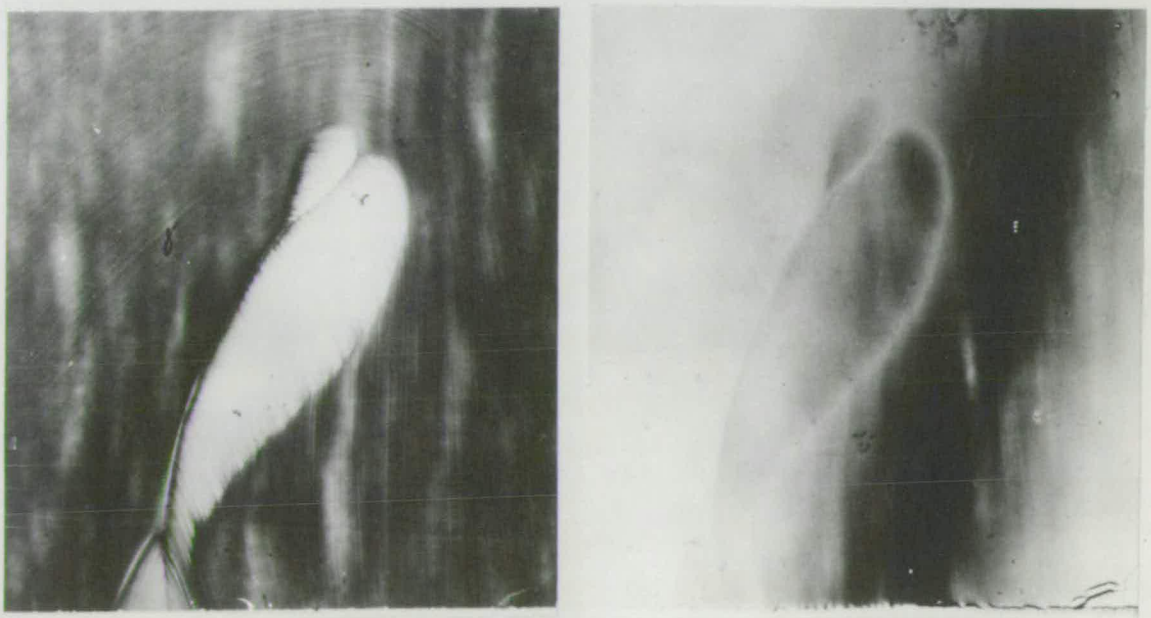

Double crystal (8 8 8) Cu Kα

1 mm

Figure 6.2.2

In thick epitaxial films the film over the core is thinner. This suggests that the extra strain makes the film more difficult to grow. This should apply even to facet-free films in that the growth rate would be dependent on the lattice parameter mismatch. Thus for fast growth of films zero mismatch would be best. This effect is not due to crystal orientation[147] because the slice is cut parallel to (111).

6.2.5 Strained rim

The rim has a smaller d'' than the bulk of the crystal and so the film would be given a slightly larger $d^{\perp}$ than the rest of the film in a process similar to that for coring and growth bands. The effect of the rim is observed in fig. 6.2.3 which compares topographs of film and substrate.

6.2.6 Dislocations

A dislocation cannot terminate inside a crystal and so a dislocation intersecting the substrate surface will propagate into the film unless it interacts with another dislocation or an inclusion.

Figure 6.2.3 shows the high-density band of straight-line dislocations next to the strained rim of the crystal. The images of dislocations can be identified in both the film and the substrate topograph. Figure 6.2.4 is of the centre region of the same crystal containing helical and straight-line dislocations which also appear in the topograph of the CVD film. Even though the diffracted peaks from the film and substrate were quite distinct it is possible that the dislocation images in the film are due

Propagation of dislocations into film.

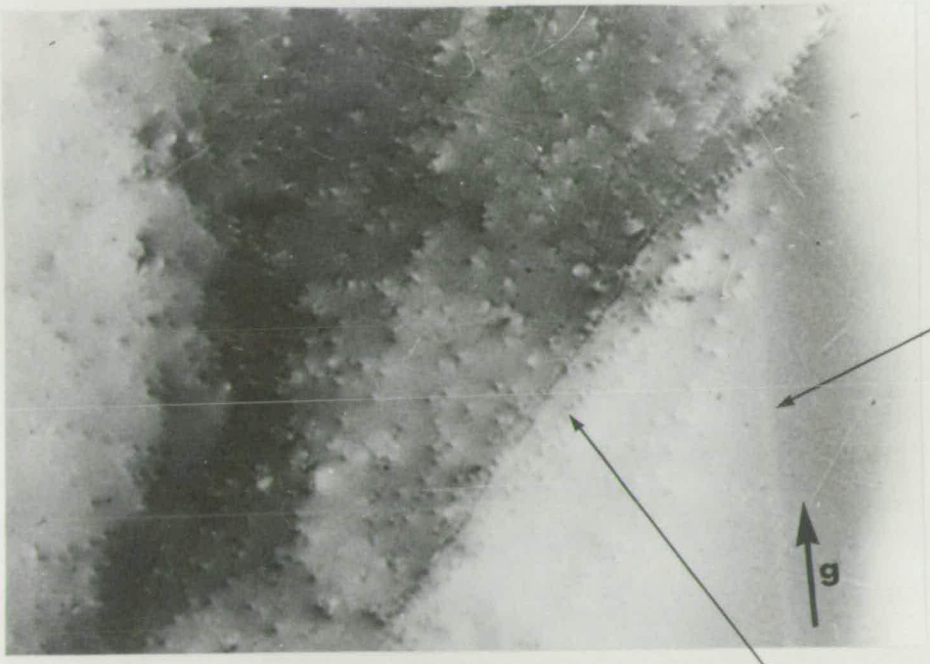

Substrate

Straight dislocations in rim

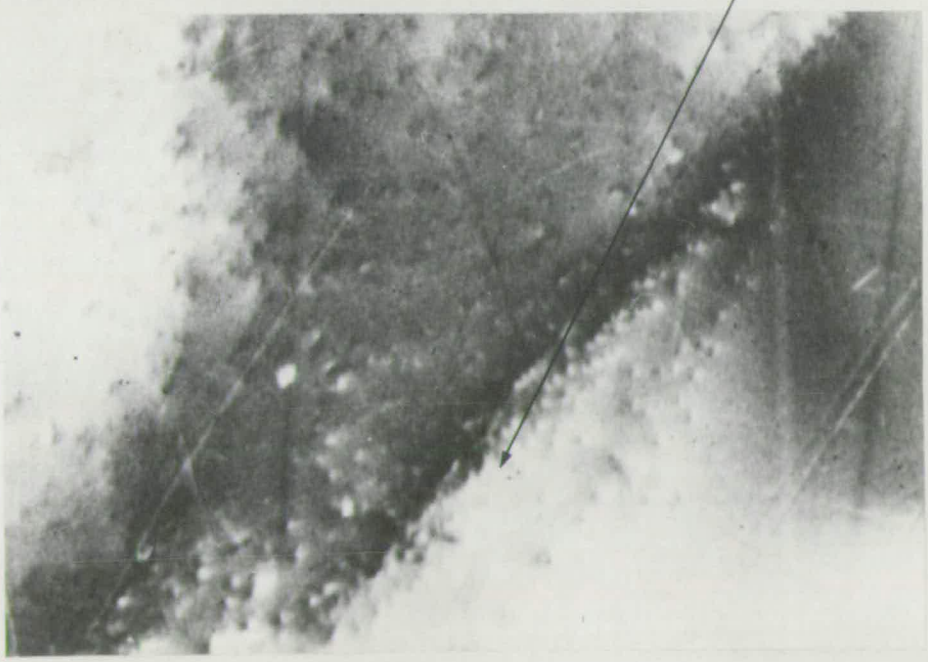

C.V.D. film

Double crystal (8 8 8) Cu Kα

1 mm

Figure 6.2.3

Propagation of dislocations into film.

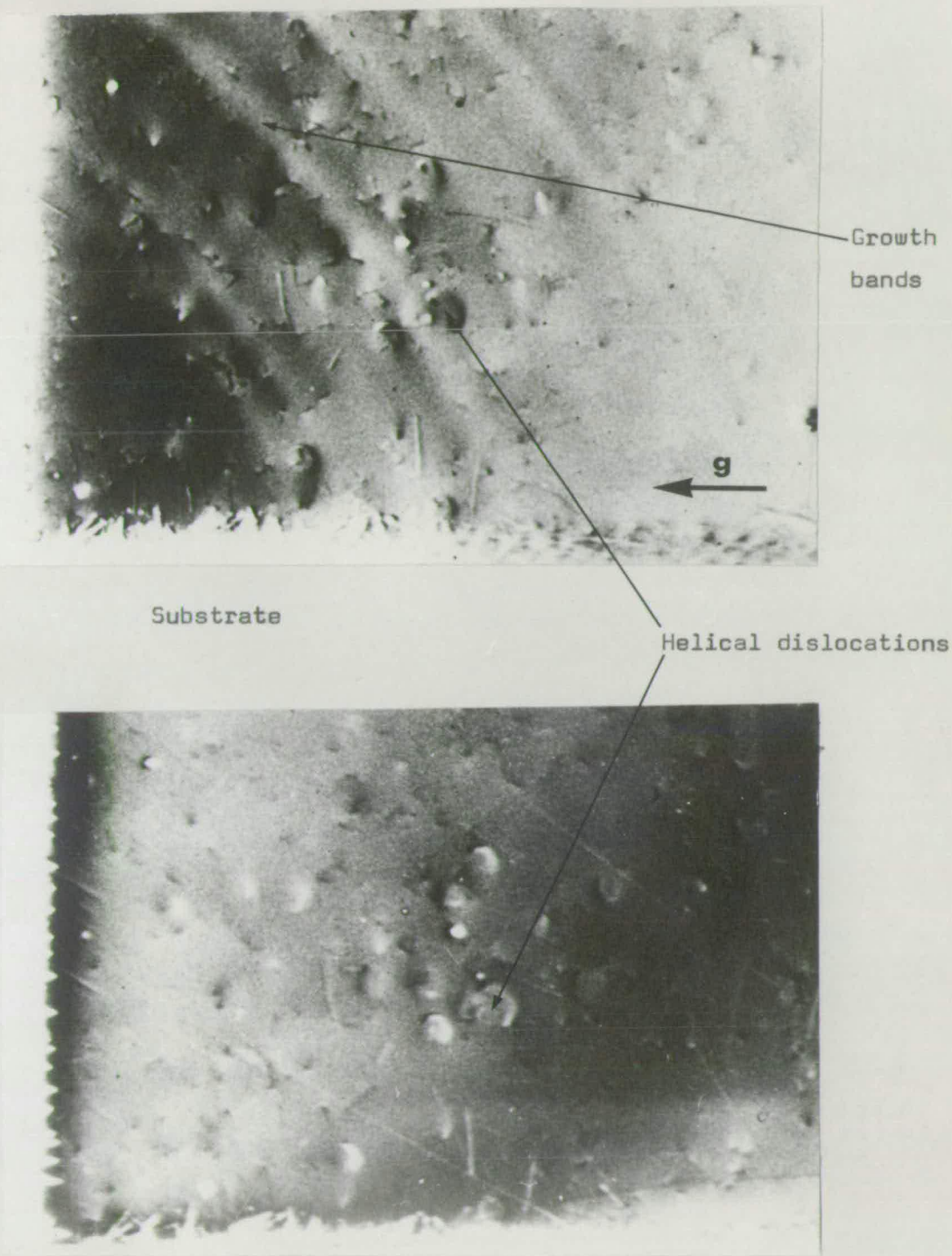

C.V.D. film

Double crystal (8 8 8) Cu Kα

1 mm

Figure 6.2.4

just to the strain in the substrate and the dislocation itself has not propagated. A thick film of YIG was grown by LPE on a similar substrate cut from the same boule. The substrate was then mostly removed by taper polishing.

Figure 6.2.5 shows the transmission topograph of the free part of the film. Although the sample is slightly bent the distribution of dislocations can be recognised as containing helical dislocations fairly evenly distributed and the high density band of straight dislocations near the dislocation-free rim. Thus these dislocations propagate into the film.

Topographs of films grown on substrates containing the very large helical dislocations have already been seen in figs. 6.1.9, 6.1.17, 6.1.19. These show that the helices appear to grow into the film for both LPE and CVD films. Figure 6.2.6 compares topographs of a particular helix in the substrate with its appearance in epitaxial films. The dislocation lines appear in the film topographs but the wedge-shaped contrast is missing since the conditions for the formation of a fault surface of impurity are not met. Similarly, for the 'tadpoles' the head propagates but not the tail. Figure 6.2.7 shows a transmission topograph of a thick film with the substrate removed and this is compared with a topograph of the substrate before the film was grown. Again, it is clear that the dislocation has grown into the film. It is interesting to note that in this topograph the magnetic stripe domains show faint contrast. This would not be expected for 180° domains.

Dislocations in a free film.

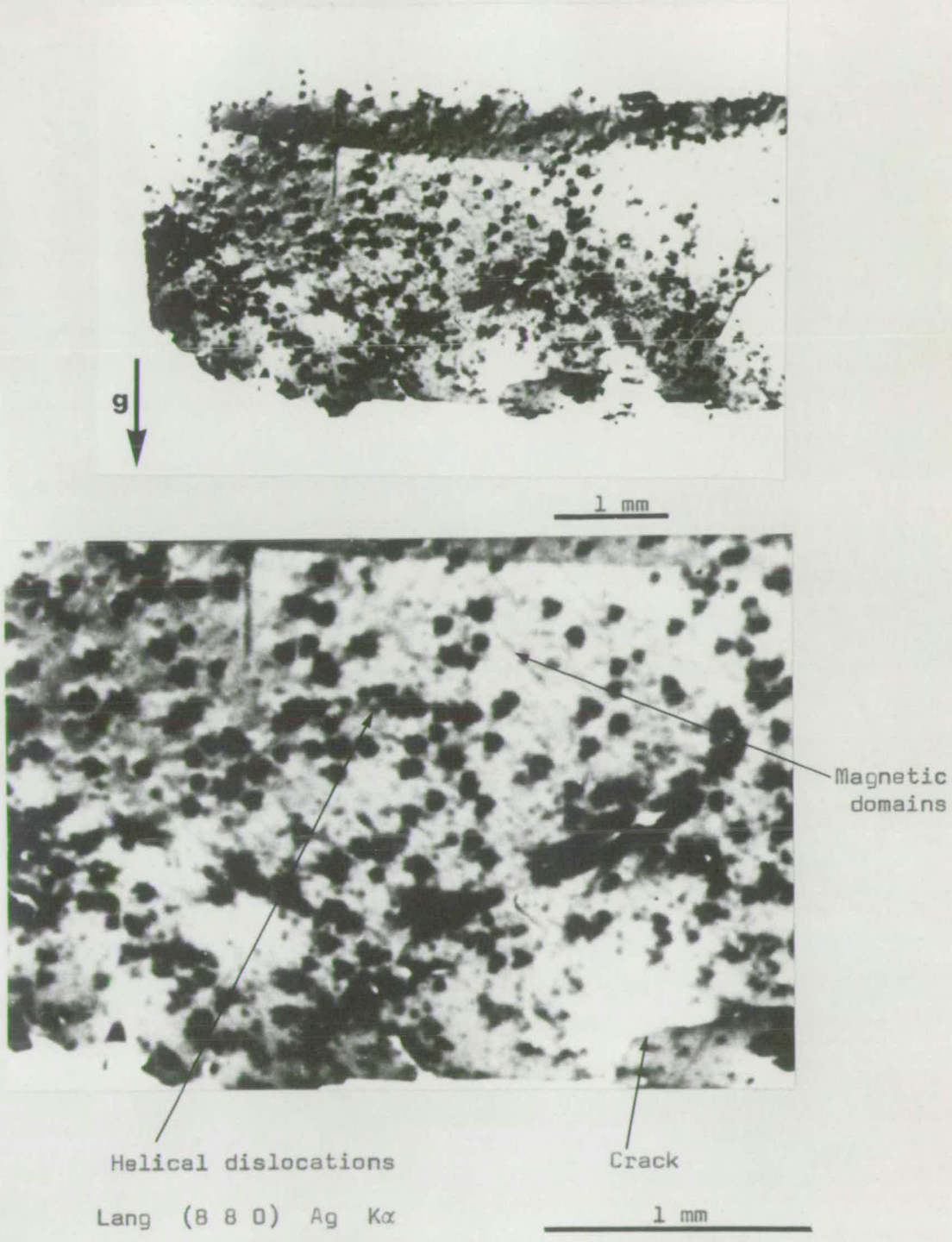

Figure 6.2.5

Propagation of large helical dislocations into film.

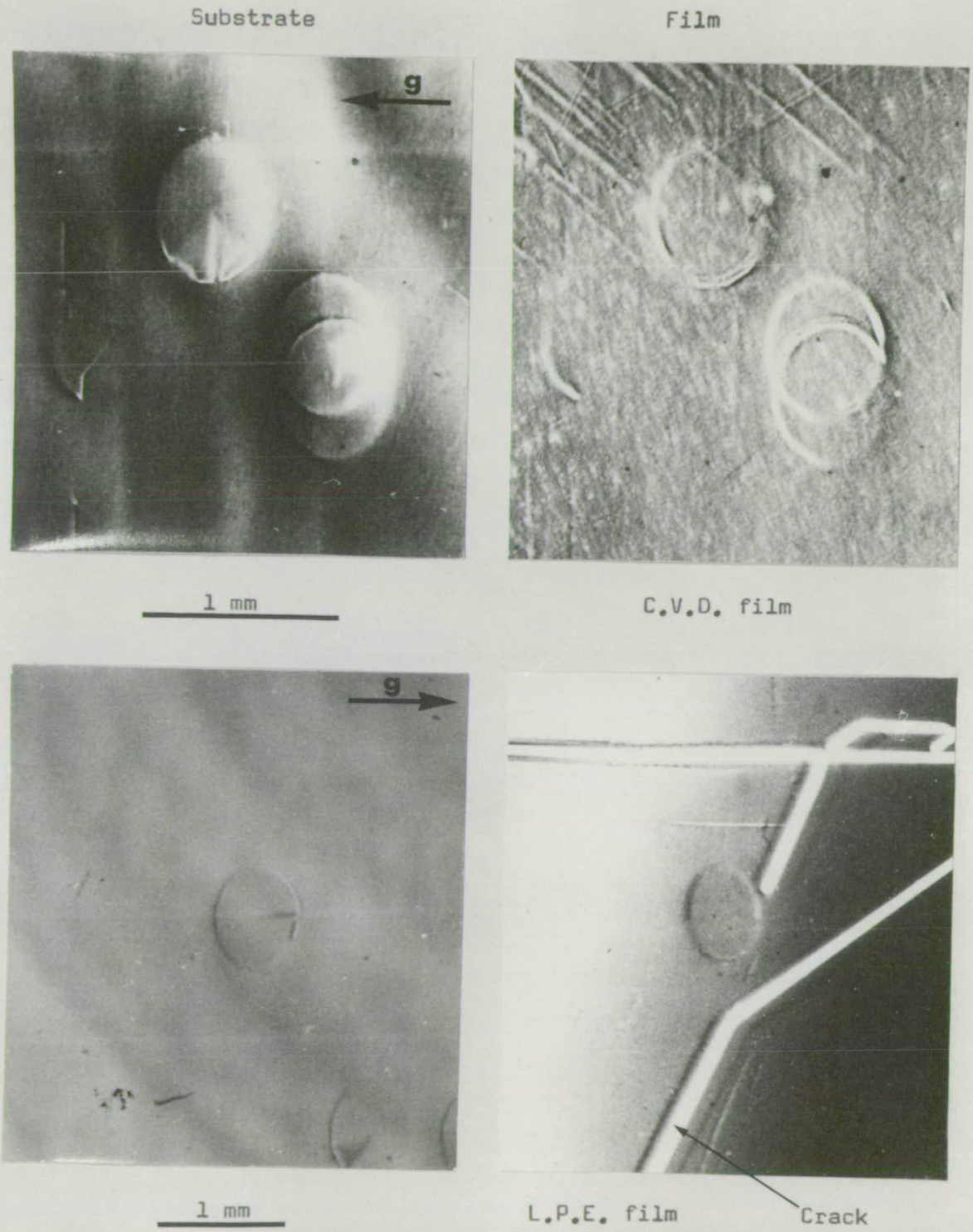

Double crystal (8 8 8) Cu Kα

Figure 6.2.6

Large helical dislocations in a free film.

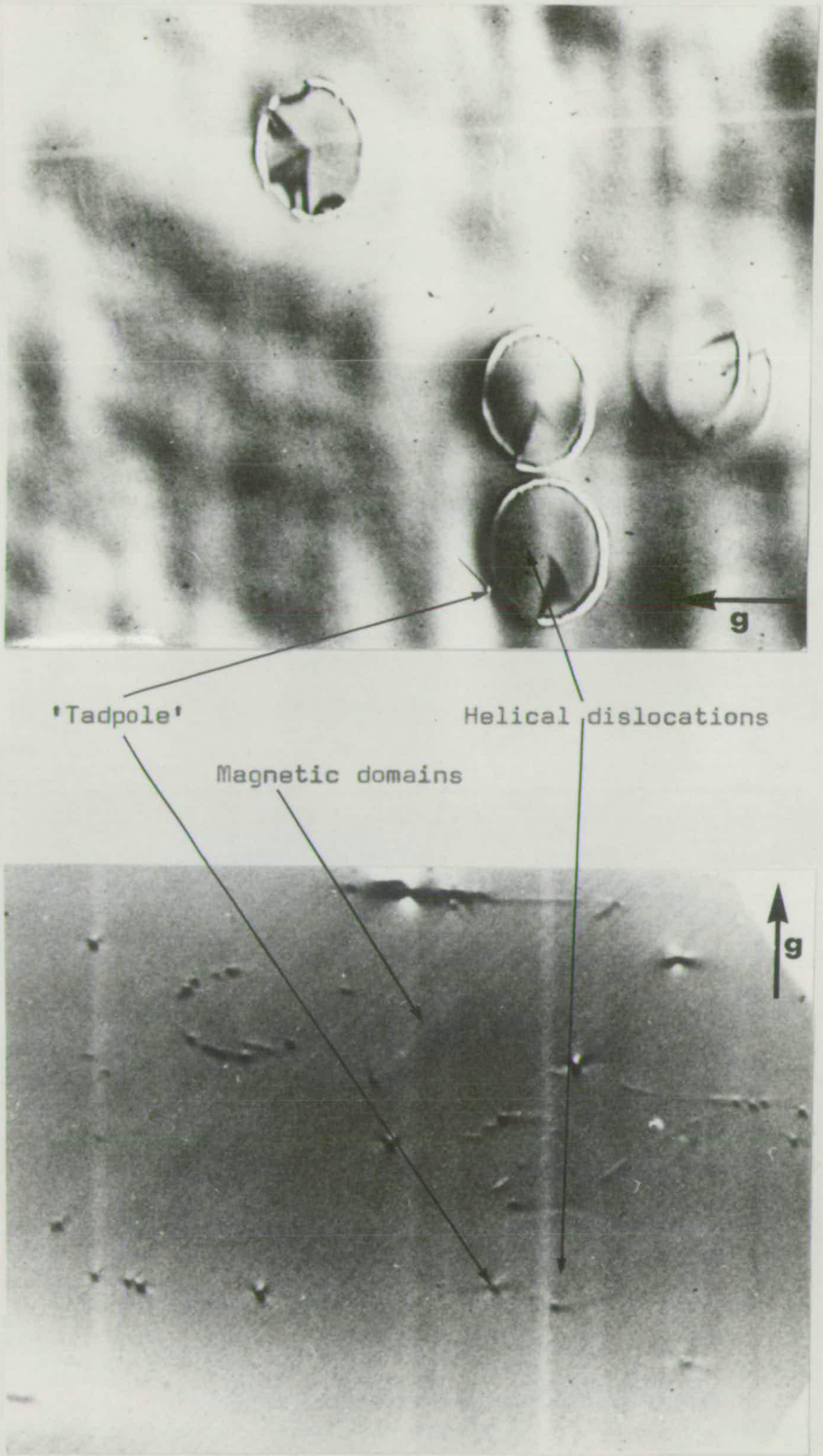

Substrate on which film was grown.

Double crystal

(8 8 8) Cu Kα

Free film with substrate removed.

Lang (8 8 0)

Cu Kα

Figure 6.2.7

The only differences in the films grown by LPE and CVD is the tendency in CVD growth for these large Burgers vector dislocations occasionally to be etched preferentially by the HCl gas with the formation of an etch pit. The high concentration of stress near the surface over the helix due to the shallow pitch of the helix encouraged the film to crack.

In thin films generally there is no observable effect on the surface relief due to dislocations. Any additional stresses around the dislocation can be accommodated elastically. Thick LPE films, of order 50 μm or greater, grown on (111) GGG substrates have triangular pits associated with the point of emergence of the dislocation line. The [111] direction is a fast growing direction and a dislocation in the substrate, possibly assisted by slight etching by the flux, will reveal slow growing directions and thus a pit will form.[161] By the same argument, hillocks should form over dislocations in {211} and {110} oriented slices and this has been observed.

The relationship between dislocations and surface relief for dislocation lines nearly normal to the (111) plane is shown in fig. 6.2.8. A transmission topograph of one quarter of a boule slice is compared with a photograph of a thick LPE film of YIG under oblique incidence illumination. This slice is from the same boule and there is a correspondence between the distribution of the growth pits and the dislocations. The shape of the growth pits is clearly seen by phase contrast microscopy in the figure. This is from the same sample in a region of high

Effect of dislocations on a thick film.

Substrate

Lang (8 8 0) Cu Kα

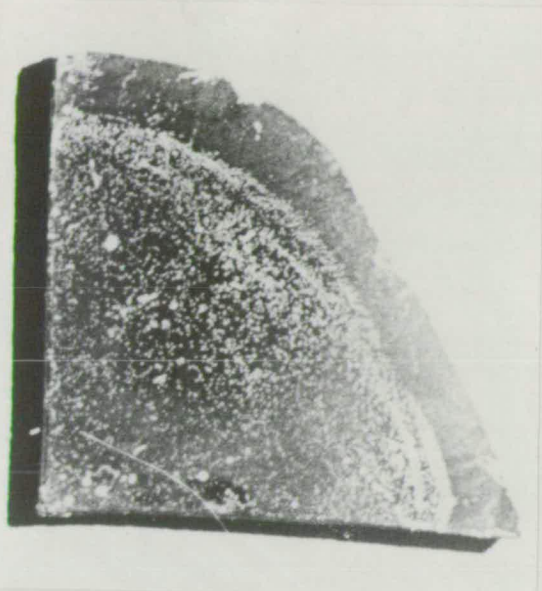

Thick L.P.E. film on a similar slice

Oblique illumination

1 mm

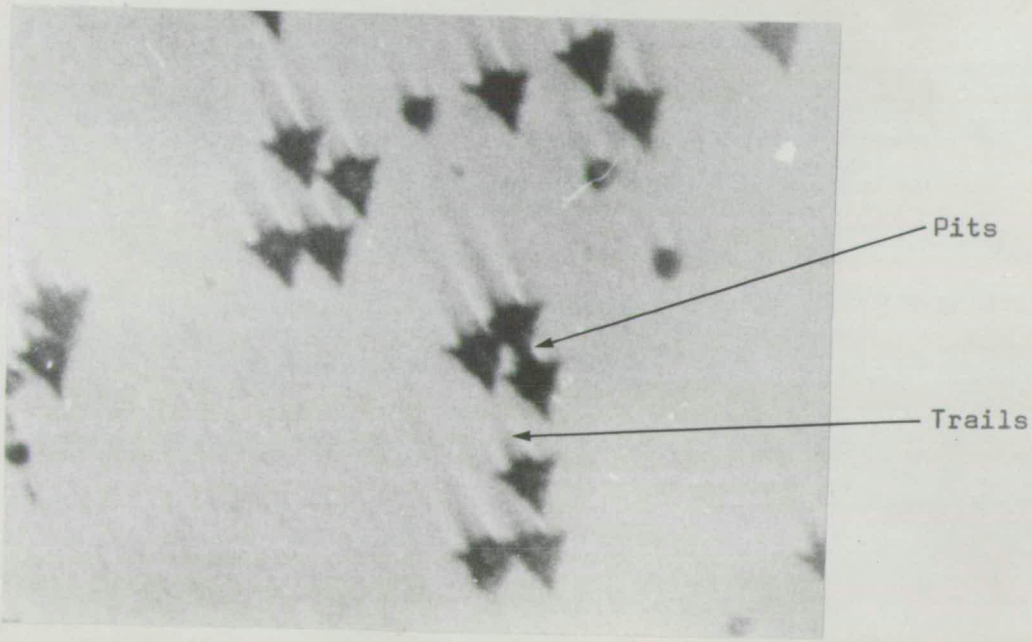

Pits at dislocations in thick film

Phase contrast illumination

100 μm

Figure 6.2.8

Effect of a large helical dislocation on a thick film.

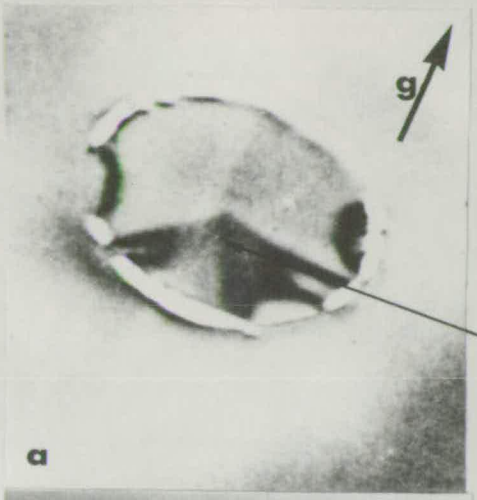

Substrate

Double crystal (8 8 8), Cu Kα

0.5 mm

Rays

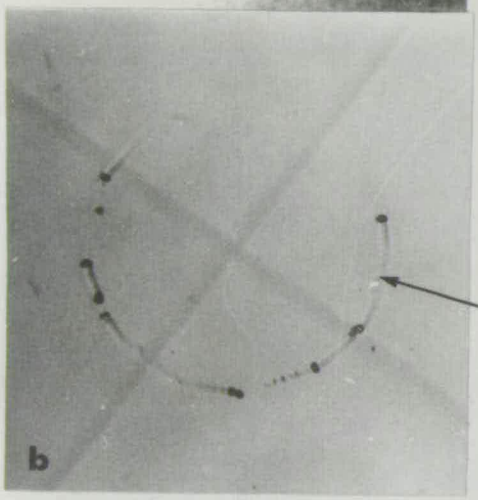

L.P.E. film, 40 μm in thickness

Phase contrast illumination

0.5 mm

Groove over dislocation line

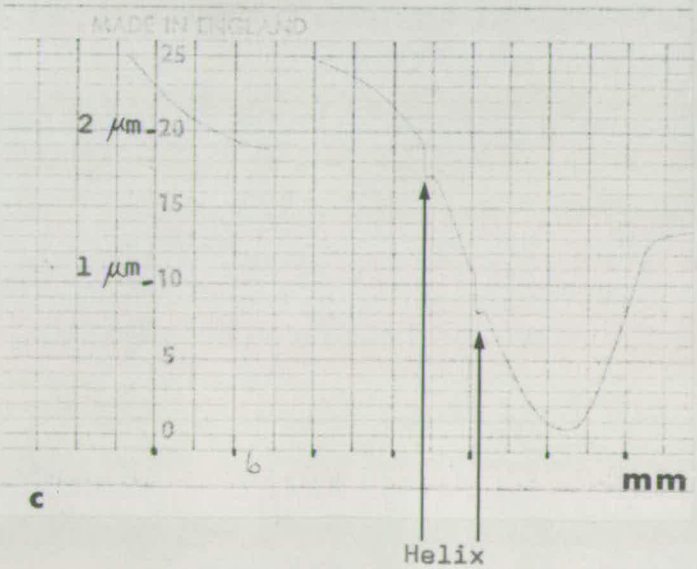

Talysurf trace over helical dislocation

Figure 6.2.9

dislocation density. Evident in this photograph are 'tails' of thickness variation arising from local disturbance of the liquid flow as the substrate was rotated.

The large helical dislocations with their large radius and small pitch have a significant length of dislocation line close, and nearly parallel, to the surface. Figure 6.2.9(a) shows a topograph of a substrate showing a single helix with a complex arrangement of 'rays' inside. A film of YIG, 40 μm in thickness, was grown by LPE on this substrate. Figure 6.2.9(b) shows the variation in thickness of this film by phase contrast microscopy. This change in thickness was found to be approximately 0.2μm. The Talysurf trace across the helix is shown in fig. 6.2.9(c). The sample as a whole was tapered, which gives the background slope in the trace.

Conclusions

Cracks, inclusions, misfit dislocations and variations in thickness ($\Delta d = \sim 1$ μm) and composition ($\Delta a = \sim 0.005$ Å) can be formed during the growth of LPE and CVD films. These defects can be eliminated or confined to the edge of the sample by careful growth and choice of composition.

Elastic strains in the substrate will produce corresponding strains in the film. This effect is reduced if the lattice parameters of film and substrate are approximately matched. Dislocations of all types propagate into the film from the substrate and perturb the growth of thick films. These can only be eliminated by using a dislocation-free substrate.

CHAPTER 7

THE EFFECT OF DEFECTS ON MAGNETIC PROPERTIES OF FILMS

The way in which imperfections in the film affect the static and dynamic behaviour of stripe and bubble domains is considered in this chapter. The static properties include the zero field pattern and the alteration of this pattern when a D.C. bias field is applied. The range of field over which the bubbles are stable is of particular importance. The movement of stripe domains and bubbles in the plane of the film is investigated by the application of bias field gradients in addition to the D.C. bias field.

These experiments were performed on a limited number of samples. None of the home-grown CVD films was found to support bubbles. Five LPE films and two CVD were examined and between them had examples of all of the defects previously discussed. The two CVD films were grown elsewhere. The results will be presented in sections, each section dealing with one magnetic property and the effect of defects upon it. Since many of the defects have a similar effect on the magnetic properties subdividing this chapter by defect, as was done in chapters 5 and 6, will lead to unnecessary repetition.

7.1 Static Properties

7.1.1 Zero field stripe pattern

In bubble domain materials the domains should form a serpentine pattern with no preferred direction when there is no external field applied. The domains in pure YIG or Ga:YIG with a low concentration of gallium form domains which are straight over long distances and change direction sharply to form a chevron-like pattern. The direction and width of the straight and serpentine domains are influenced by the imperfections in the magnetic film in the manner described below. Except where indicated, the effect is the same for both LPE and CVD films.

a) Edge:

The boundary of the sample can be classed as a defect and will influence the pattern of domains. A domain at the centre of the sample is at a lower energy than a domain nearer the edge. Thus there is a force tending to repel a domain from the boundary. If a stripe is joined to the boundary it will remain attached unless extra energy is supplied to form the domain wall to close the end.[162] A domain not held by the boundary and repelled by it will have an equal force along its length if it lies parallel to, but some distance from, the boundary. The domain joined to the boundary at one end can minimise its energy by running perpendicular to the boundary until this effect becomes weaker than domain-domain interactions.

The total pattern would thus tend to consist of sections of domain running either perpendicular or parallel

Magnetic domains near edge of sample.

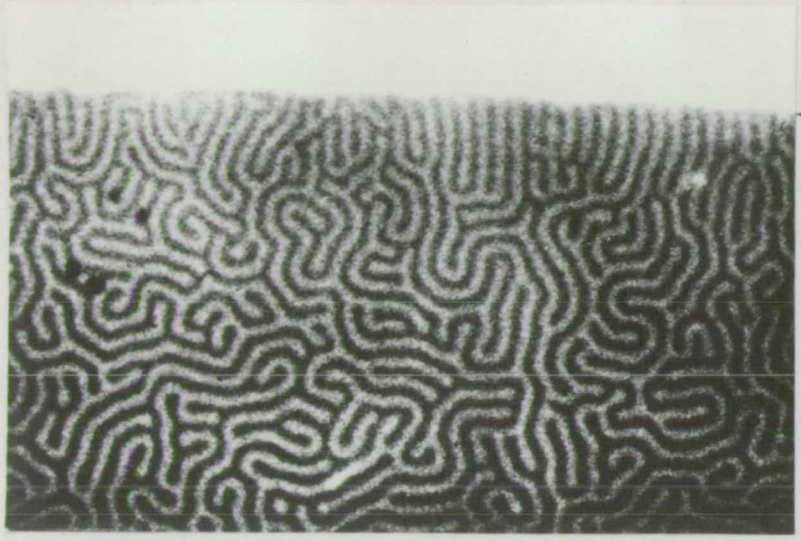

Sample 5 μm thick

25 μm

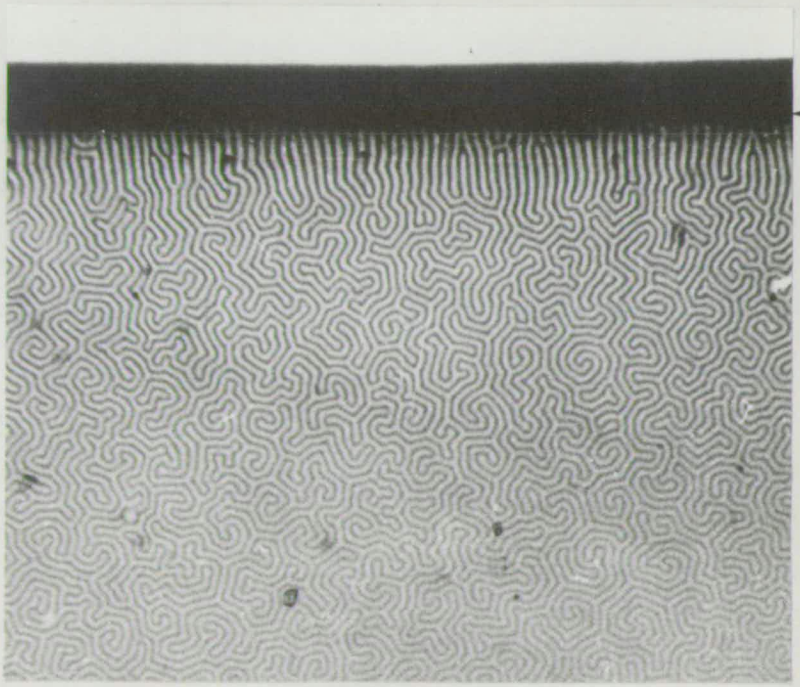

Sample 19 μm thick

100 μm

Domains viewed by Faraday effect.

Figure 7.1.1

Straight magnetic domains.

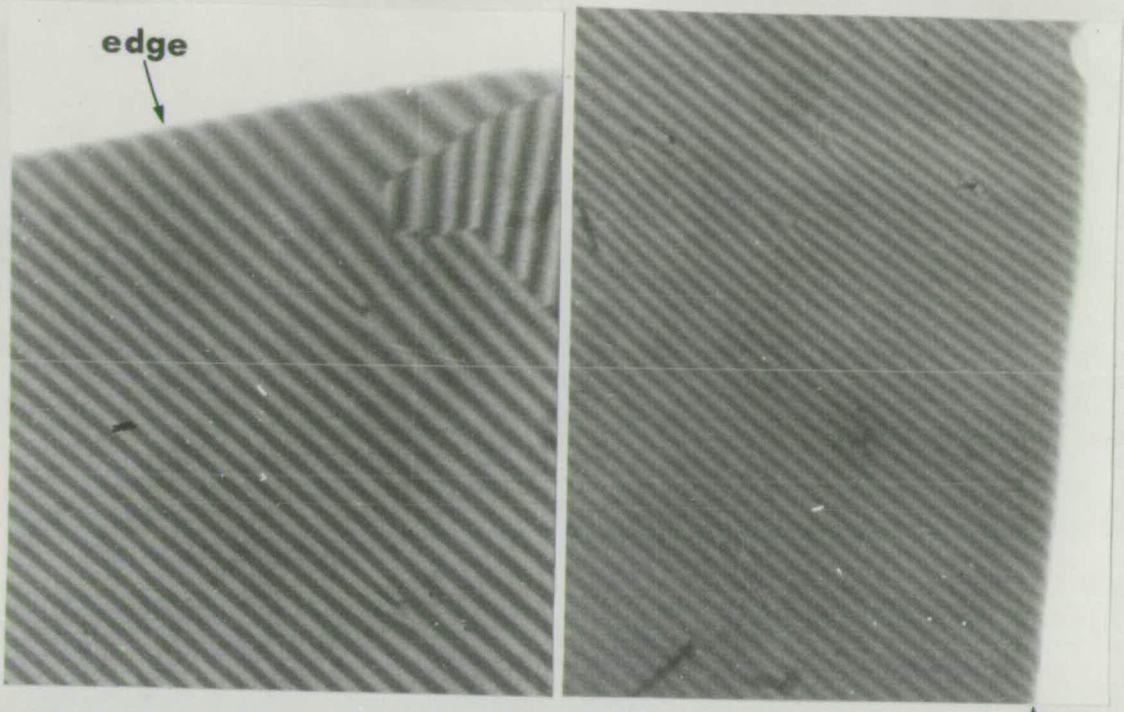

Straight domains in a free film of YIG

Sample 40 μm thick

100 μm

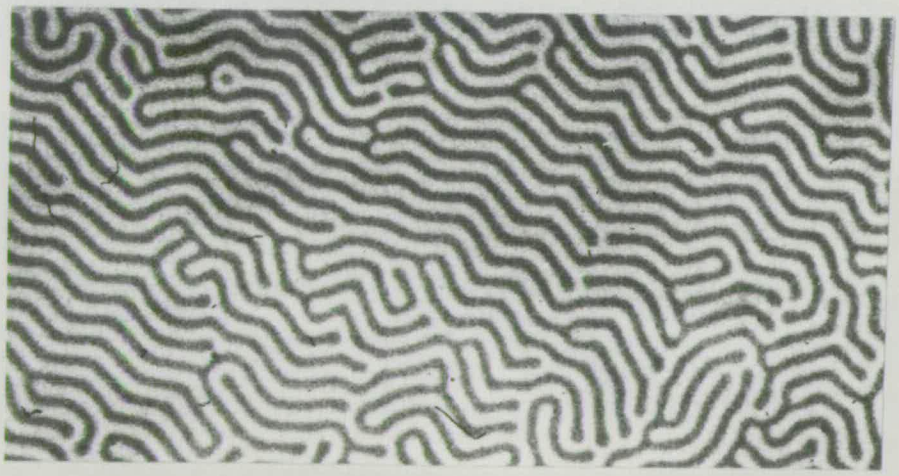

Chevron pattern in a bubble film

Sample 5 μm thick

25 μm

Figure 7.1.2

to the edge near the boundary. This pattern will become modified by the serpentine pattern nearer the centre of the slice. Examples of this behaviour can be seen in fig. 7.1.1. Except for the film which was thicker the serpentine domain pattern becomes established quite quickly close to the edge.

For pure YIG films the effect of the boundary is less than that of the underlying crystallography. This gives straight domains or a chevron pattern with the domain walls on {110} planes. This type of pattern can also be produced in bubble films by perturbing the sample with varying in-plane fields[162] but it occurs spontaneously for YIG. Figure 7.1.2 shows the domain pattern in YIG and a chevron pattern in a bubble film.

b) Cracks:

A crack acts as a boundary in the film in the same way as the edge of the sample does. The important difference is that the magnetic field at the crack, due to the film's own magnetisation, is very small instead of the large value found at the edge. This means that the crack is important since, as well as acting as a physical barrier which a domain cannot cross, the stress relief in the film produced by the crack changes the amount of stress-induced uniaxial anisotropy in the film. This is particularly important for CVD films since stress is the only source of magnetic anisotropy in the film. Cracks tend to break the film up into islands of different sizes and thus each island will have a different amount of

Effect of cracks on magnetic domains.

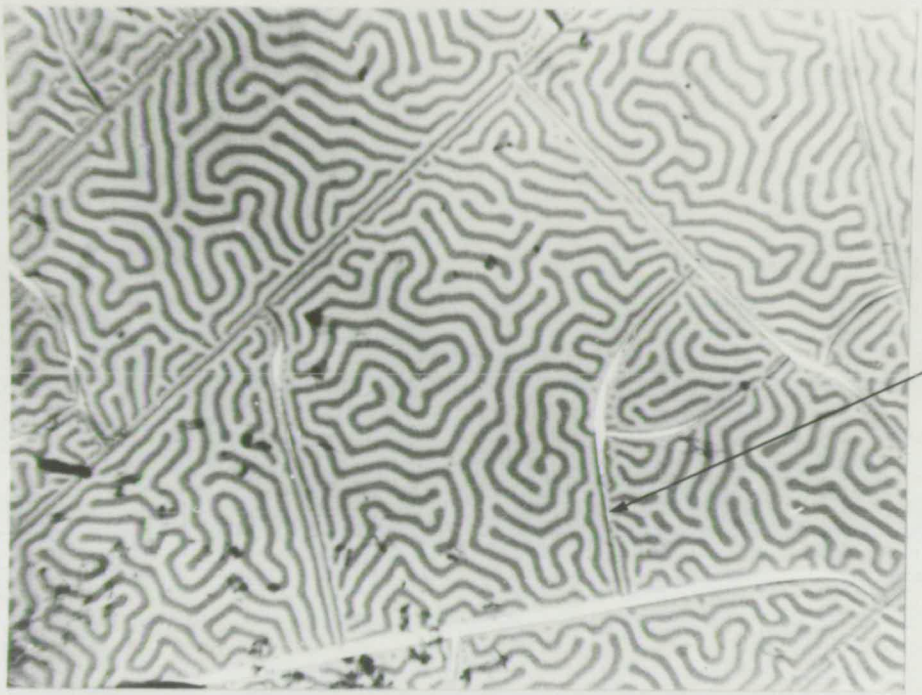

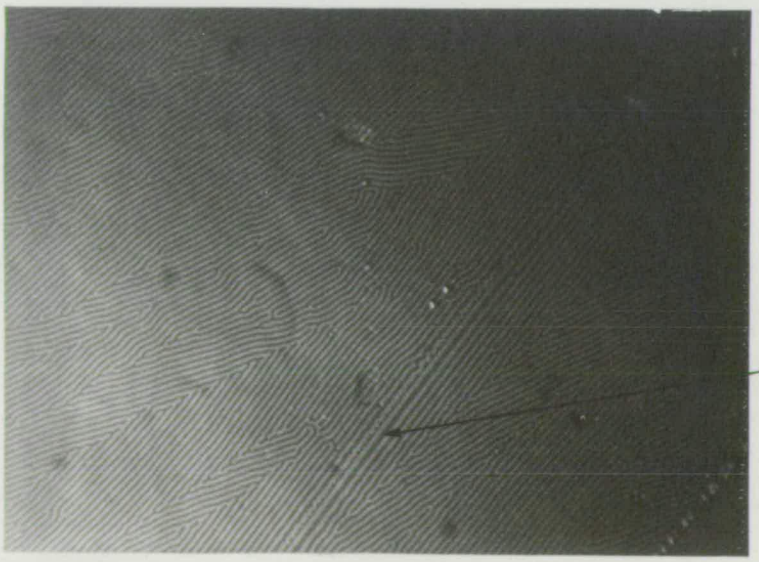

Figure 7.1.3

stress-induced anisotropy.[147]

The stripe domains tend to run parallel to the crack except when one end of the domain is pinned on the crack. Then the domains run normal to the crack. The domains are encouraged to lie parallel since {110} is a low energy plane for the domain walls and also a plane on which the film is most likely to crack. Examples of the domain pattern near cracks are shown in fig. 7.1.3.

c) Scratches:

Scratches in the substrate grow through to produce disordered regions in the film. Additional scratches can be produced when handling the film. These disordered regions act as regions of higher coercivity and changed anisotropy.[163] The effect of this is for a domain wall lying along the scratch to be in a state of lower energy than if it were in a damage-free part of the film. In very severe cases the domains will be unable to cross the scratch which acts as a physical barrier similar to a crack. In less severe cases there will be a tendency for the domains to line up along the crack. This pattern can be modified by the serpentine pattern of the other domains and the domain can cross the scratch. The effect of scratches, of varying severity, on the domain pattern are seen in fig. 7.1.4.

d) Variations in thickness:

The width of a stripe domain depends on the thickness of the film, as discussed in section 4.1. Gradual changes in the thickness of the film produce corresponding effects

Magnetic domains around scratches of varying severity.

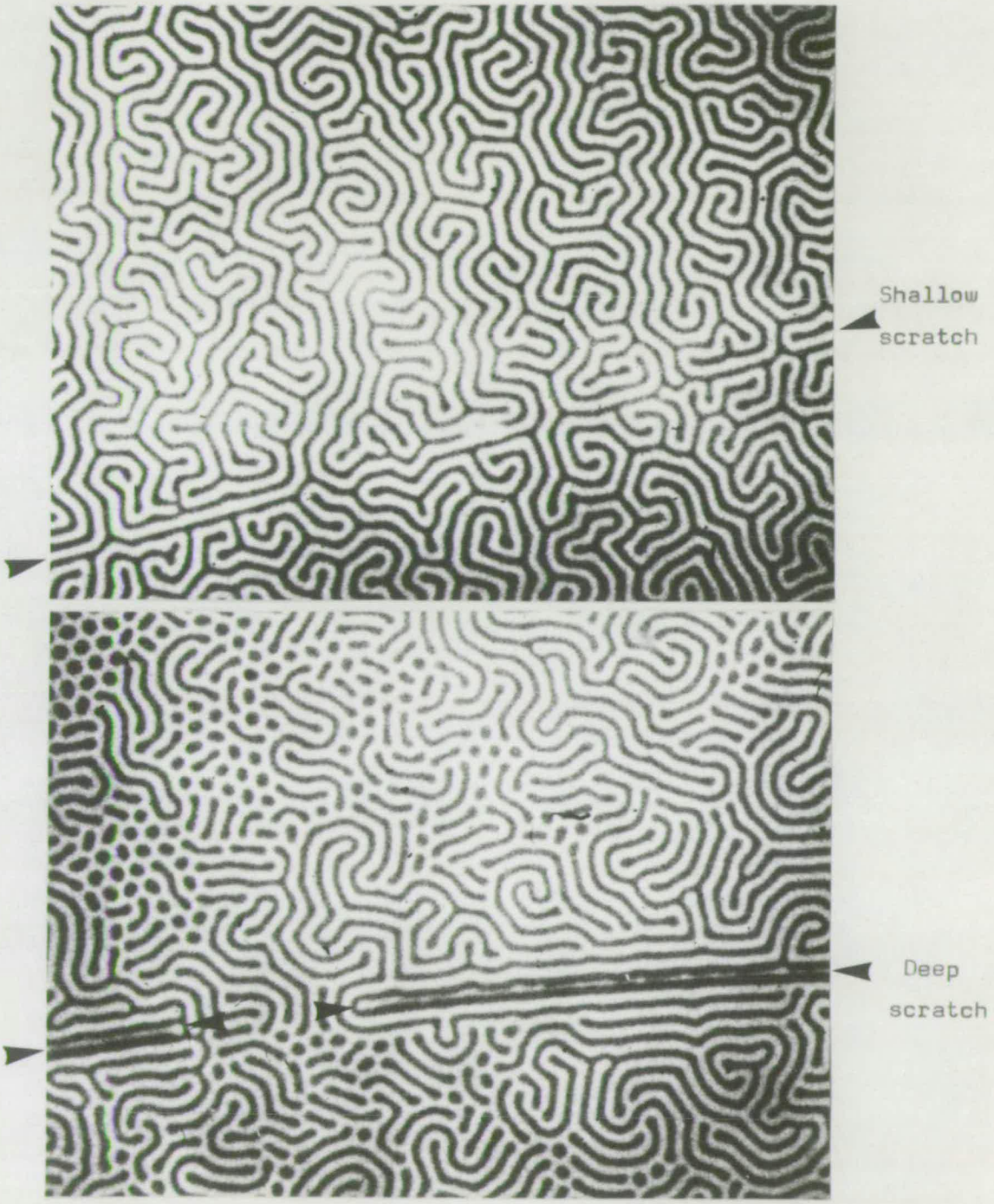

Sample 5 μm thick

25 μm

Figure 7.1.4

in the domains and this is most visible in the domain pattern of pure YIG films. The straight domain pattern becomes 'dislocated' and a stripe terminates in the film when there are more thick stripes than is energetically favourable. Such a domain pattern is seen in fig. 7.1.5.

An abrupt change in thickness occurs at 'mesas' in LPE films. This would be expected to produce a local increase in the width of the stripe domains. There is also strain at the mesa boundary which was revealed by x-ray topography. This strain acts as a partial barrier to the domains which, particularly in the thinner region, lie along the boundary. Figure 7.1.5(b) shows a sample where the film was thin and the relative change in thickness large. Thicker films, where the difference in thickness was not so great, show similar, but less pronounced, effects.

Crystallites of orthoferrite which form in both LPE and CVD films mask the garnet film growth. This produces a small, thin region or even a hole in the film. The domains become narrower and terminate at the inclusion. This perturbs the domain pattern, as seen in fig. 7.1.5.

e) Growth bands:

In none of the samples studied here was the strain in the film due to growth banding very large and the strain gradients were small. No effect was observed on the domain pattern.

Growth bands have been reported to affect the domain pattern in one sample of a low magnetisation film.[164]

Variation in domain pattern with film thickness.

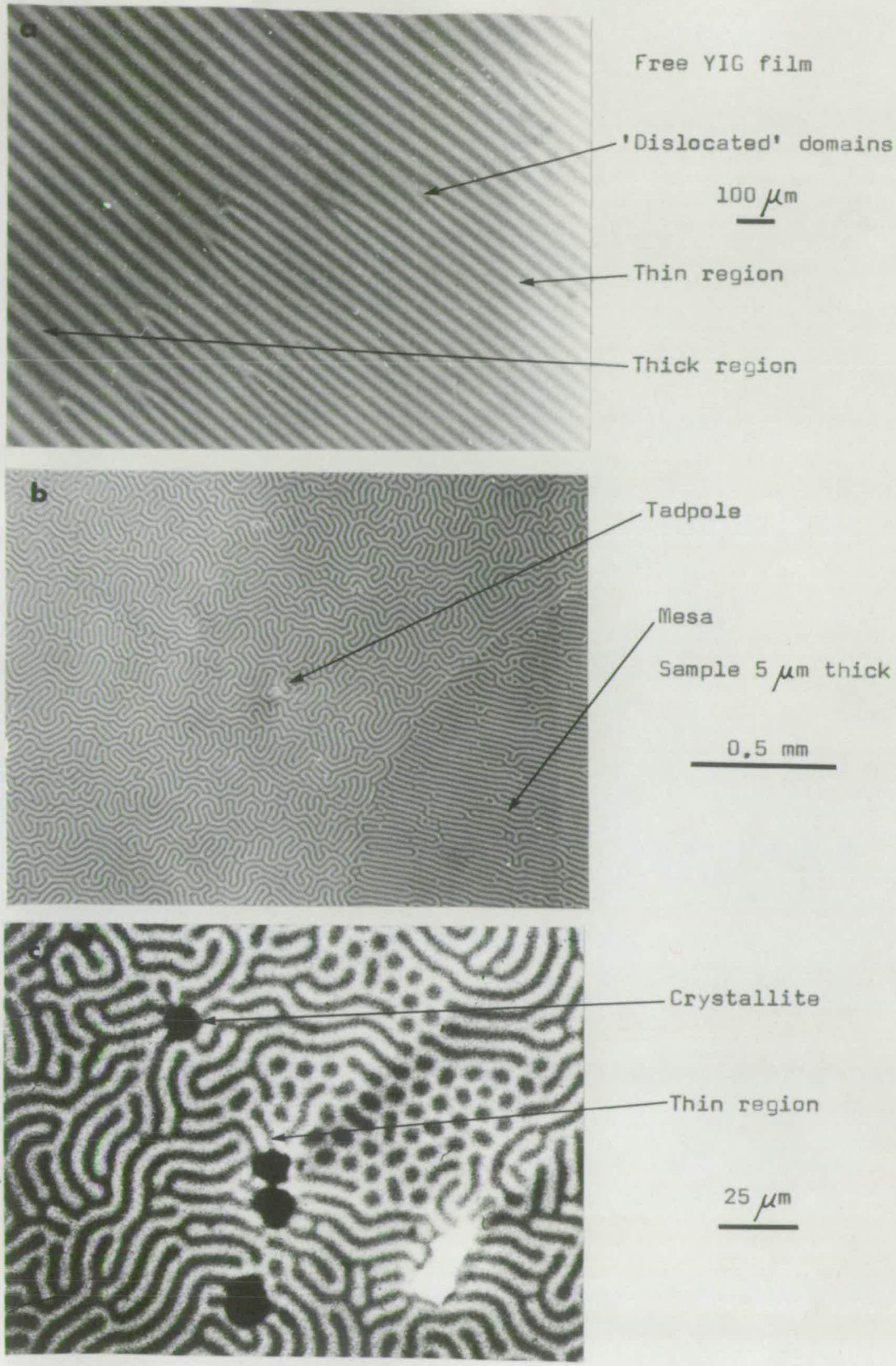

Figure 7.1.5

f) Core:

The core is a region of different lattice parameter which has, generally, a sharp boundary with the bulk of the crystal. It has been reported[158] that the zero field domain width is greater inside the core than outside. This is confirmed by the following measurements obtained on one bubble film and two pure YIG films:

Sample	Inside core μm	Outside core μm
YIG	6.64 ± 0.1	6.36 ± 0.1
YIG	6.65 ± 0.3	6.23 ± 0.1
Bubble film	21.5 ± 0.2	20.3 ± 0.6

The measurements were taken fairly close to the core boundary and at the same distance from the crystal edge to minimise the effect of variations in thickness of the film.

There is also a slight effect on the domain pattern, particularly for the pure YIG films. The straight, parallel domains in YIG change direction at the core boundary as can be seen in fig. 7.1.6. The domains change direction in other parts of the film but there the 'fold' occurs on a straight line. The core boundary is curved and this is followed closely by the point at which each domain bends. The serpentine domain pattern in the bubble film shows much less effect from the core boundary. There are slightly more chevrons with the domain lined up approximately along the boundary than there are in the rest of the sample, see fig. 7.1.6.

Effect of core on magnetic domains.

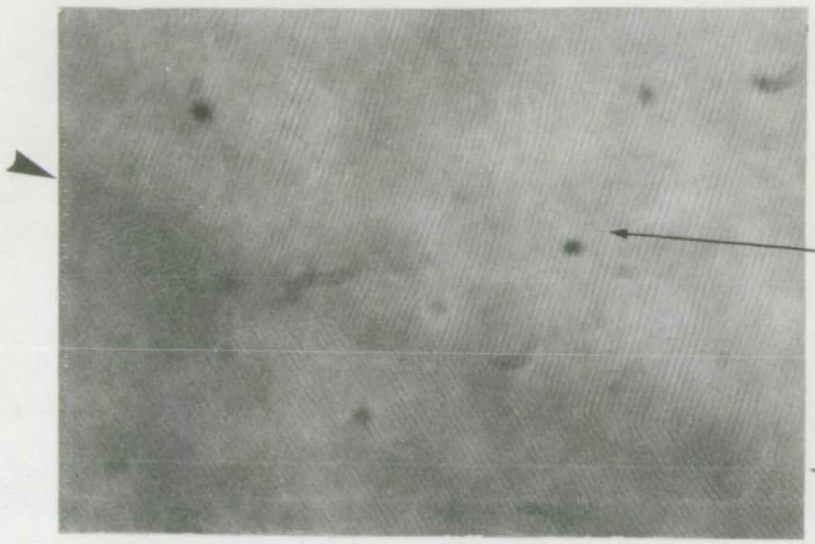

YIG film

Core

Core boundary

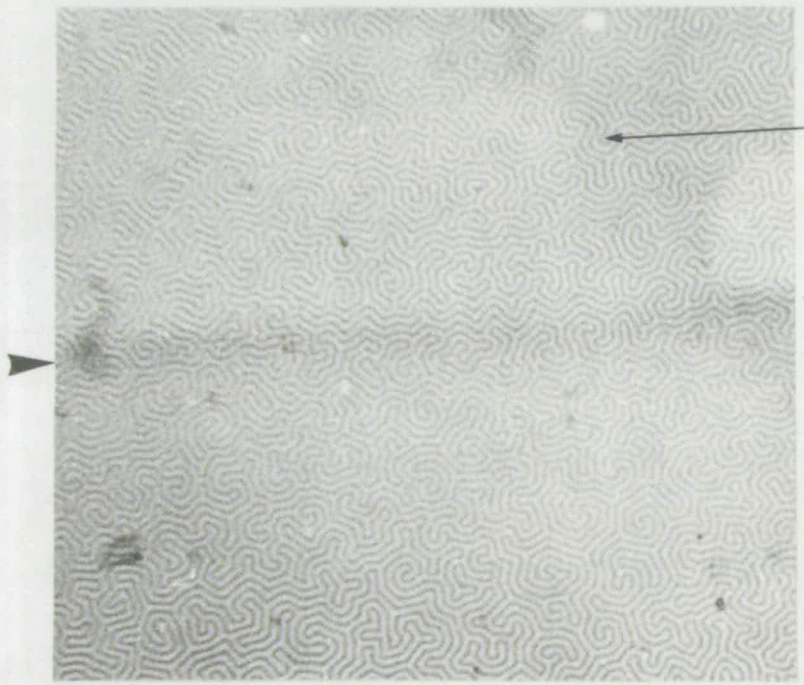

Bubble film

Core

Core boundary

100 μm

Figure 7.1.6

g) Variations in surface quality:

One sample was polished and then given an etch in phosphoric acid. The etch removed the surface damage but the phosphoric acid or reaction products could not be removed from the substrate at one corner. A bubble film was grown which was smooth everywhere except in this one corner where it appeared matt. The film in this corner was highly strained. The domain patterns in the smooth and rough areas of film may be compared in fig. 7.1.7. The domains form a smooth, serpentine pattern in the region where the film is of good quality but form a jagged pattern in the rough area.

h) Dislocations:

Straight line dislocations running almost perpendicular to the film do not have a long-range effect on the serpentine domain pattern. The domain stripe terminates at the point of emergence of the dislocation, as can be seen in fig. 7.1.8(a) and fig. 7.1.5, where the head of a 'tadpole' emerges. There is no particular influence on serpentine domains from a large helical dislocation or a 'tadpole' tail. In a thick film of pure YIG the domain pattern is perturbed by the presence of the helical dislocation, fig. 7.1.8(b). There are 'dislocations' in the straight domain pattern at the helix boundary, initiated by the change in thickness over the helix. This pattern is emphasised if a bias field is applied. The discontinuity becomes greater, fig. 7.1.8(c), round the edge of the helix.

Variation in surface quality.

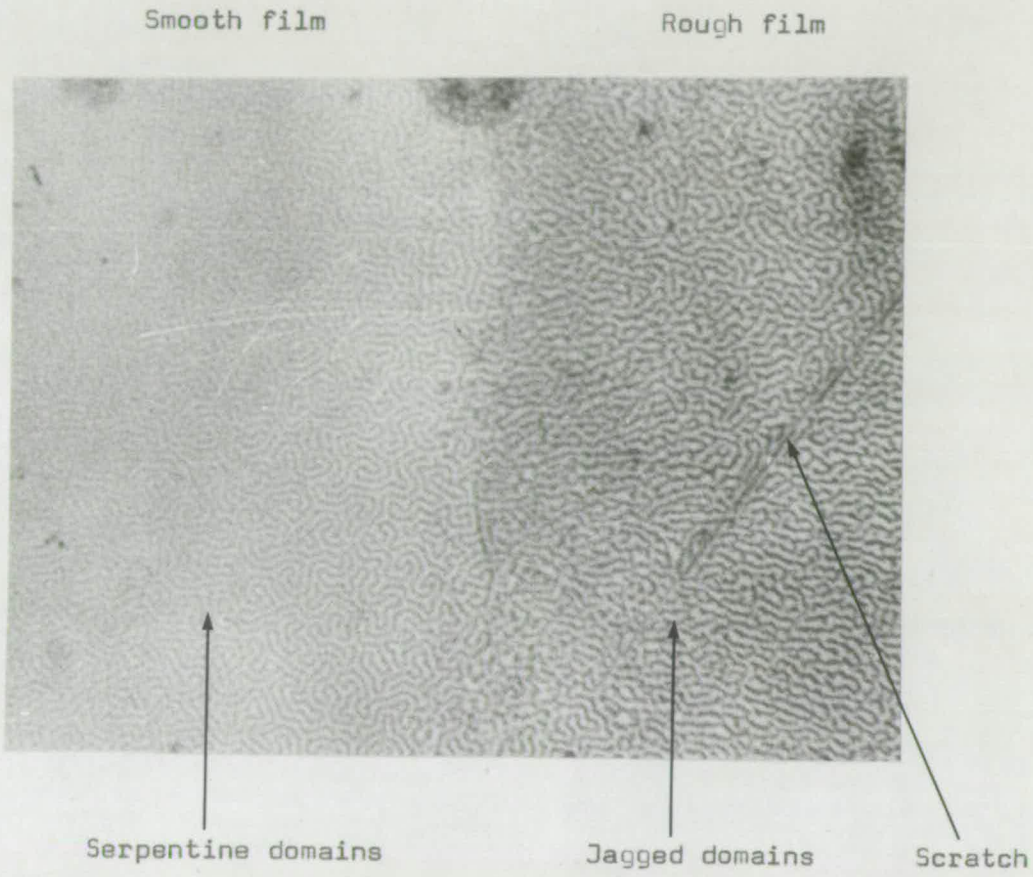

Figure 7.1.7

Variation in surface quality.

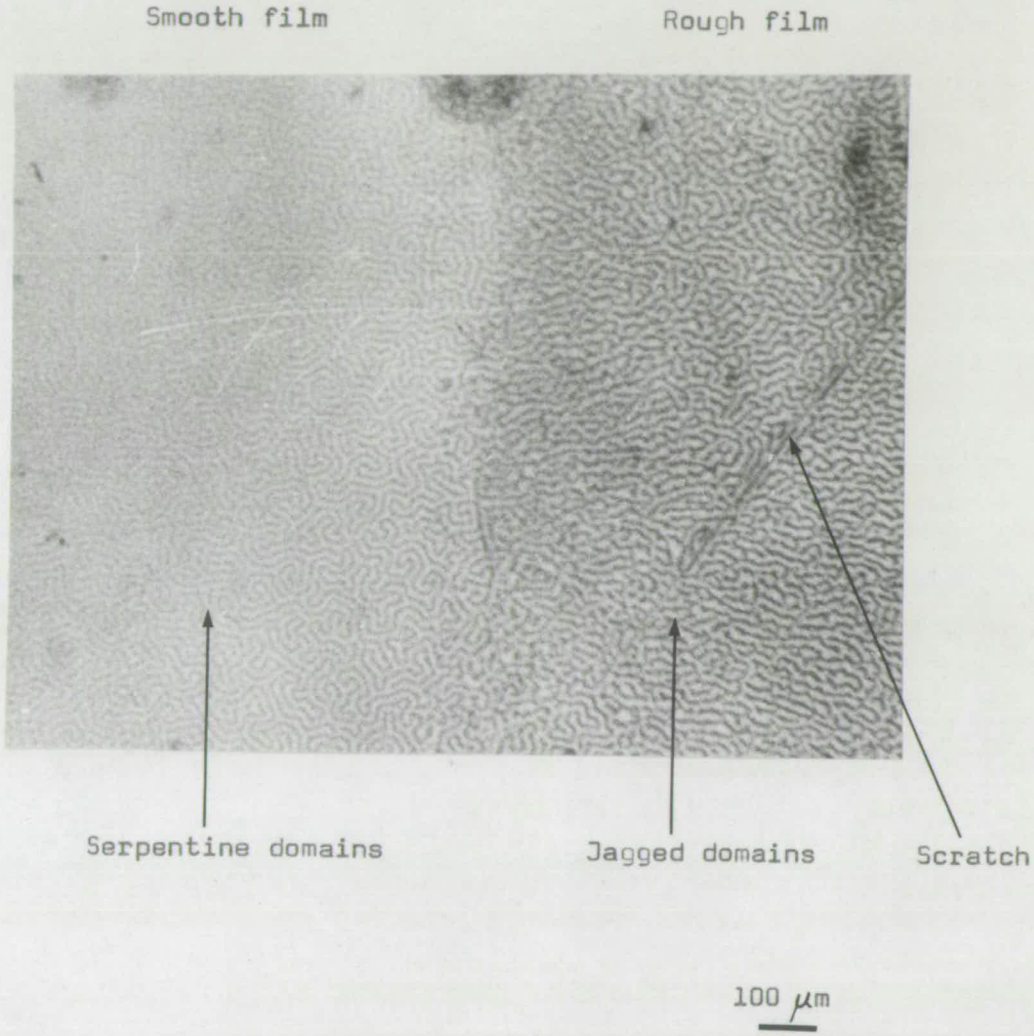

Figure 7.1.7

7.1.2 D.C. bias field applied to stripes

a) Variations in thickness:

The field at which a particular part of a film becomes saturated depends on the thickness of the film. Thus, in LPE films, mesas and the thicker regions under the vacuum chuck will retain reverse domains at higher D.C. bias fields than the surrounding film. This effect can be seen in fig. 7.1.9 which shows the variation of density of short strip domains with thickness. The dark curved line was made by the vacuum chuck on the back of the slice and indicates the position of the thickest part of the film. As the bias field is increased the small stripes collapse to bubbles and some of the bubbles in the thinner areas collapse, fig. 7.1.9(b). The fields for collapse of stripe domains inside and outside mesas is given below:

Thickness of lowlands μm	Δh μm	Inside mesa G	Outside mesa G
18.8	4	144 $\pm$ 1	149 $\pm$ 1
4.86	4	110 $\pm$ 1	74 $\pm$ 1

The extra thickness due to the mesa is estimated to be 4 microns in each case. As might be expected, the film with the greatest percentage change in thickness produces the greatest change in the field required to saturate the film.

Variations in thickness

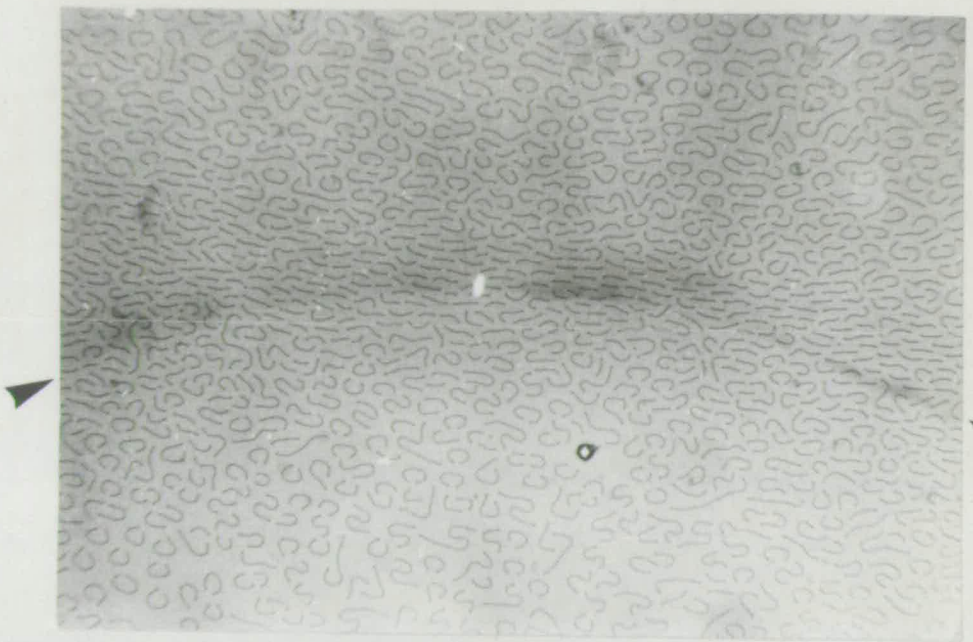

a) Small bias field applied

100 μm

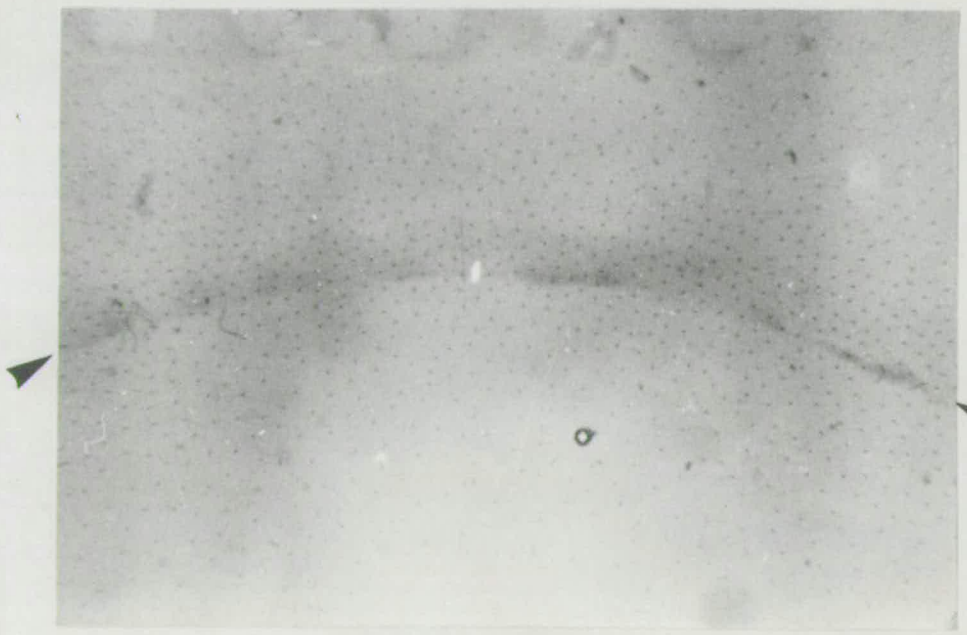

b) Bias field increased

Figure 7.1.9

b) Core:

The core had no significant effect on the field at which the stripe domains disappeared. The field required was 157 ± 1 G in the core and 155 ± 1 G outside. Comparable changes would be produced from more pinning points in the core.

c) Growth bands:

No effect was observed.

d) Other defects:

In section 7.1.1 it was noted that a domain stripe may be terminable on the edge, crack, scratch, inclusion and dislocation. As a bias field is applied those domains held at one or more points will persist to a higher field than the domains in the regions which are defect free. These field domains are said to be pinned by the defect which stabilises the domain.

7.1.3 Static bubble properties

This section considers the effect of defects on the fields at which bubbles collapse or run out into stripes.

a) Variation in composition - double layer films:

A multiple layer film may be formed in CVD films by a change in gas flow and in LPE films by the formation of mesas. This may aid the formation of 'half-bubbles' or 'floating-bubbles'.[165] Two types of bubble domain were observed in a CVD Ga:YIG film. One bubble, (I), was large and gave strong Faraday contrast. The other, (II), was

smaller, gave less contrast and appeared less well-defined at the edges. The two types could co-exist over a range of bias field. Either type of bubble could be produced by applying an A.C. bias field. At a fixed D.C. bias the type I bubbles were formed for the lower A.C. amplitude or if the A.C. amplitude were fixed, a lower D.C. bias produced the type I bubbles.

Figure 7.1.10(a) shows short segments of type I domains generated with D.C. bias = 15.5 G and the mutual interaction between them. In 7.1.10(b) the strips have been collapsed to type I bubbles as the field is raised to 23 G. Some stripes remain along the cracks and in both photographs a few type II bubbles are visible along the edges of the cracks. Bubbles generated at D.C. field of 23 G and displayed at the same field are seen to consist of type II bubbles except for a few type I domains which appear to be pinned at the cracks.

The type I bubbles transform abruptly into type II as the bias field is raised. The reverse transformation does not occur as can be seen in the sequence of photographs in figure 7.1.11. The bias field is gradually increased and then decreased. As the field is increased the type I bubbles decrease in size and then transform to type II. These bubbles become larger as the field is decreased but at lower fields, instead of transforming back to type I, they fade away as type I stripe domains are

Double layer films

a) Interaction between short segments of Type 1 domains

Bias field = 15.5 G

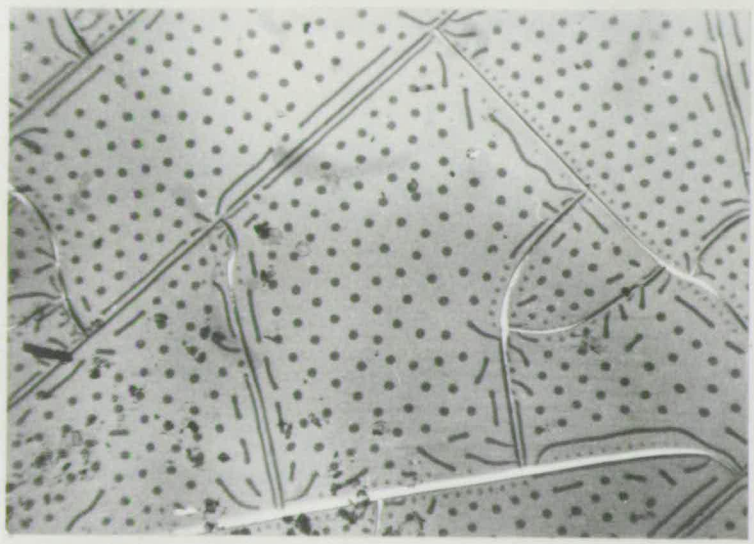

b) Type 1 bubbles

Bias field = 23 G

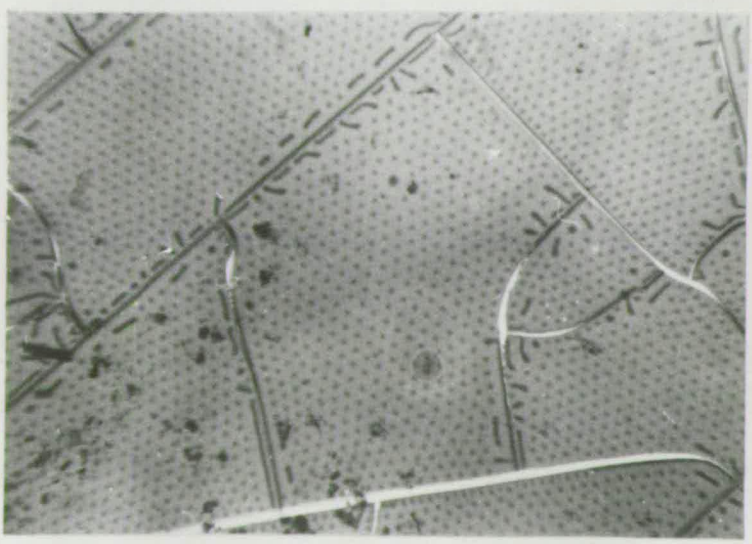

c) Type 11 bubbles

Bias field = 23 G

100 μm

Figure 7.1.10

Variation of domains with bias field.

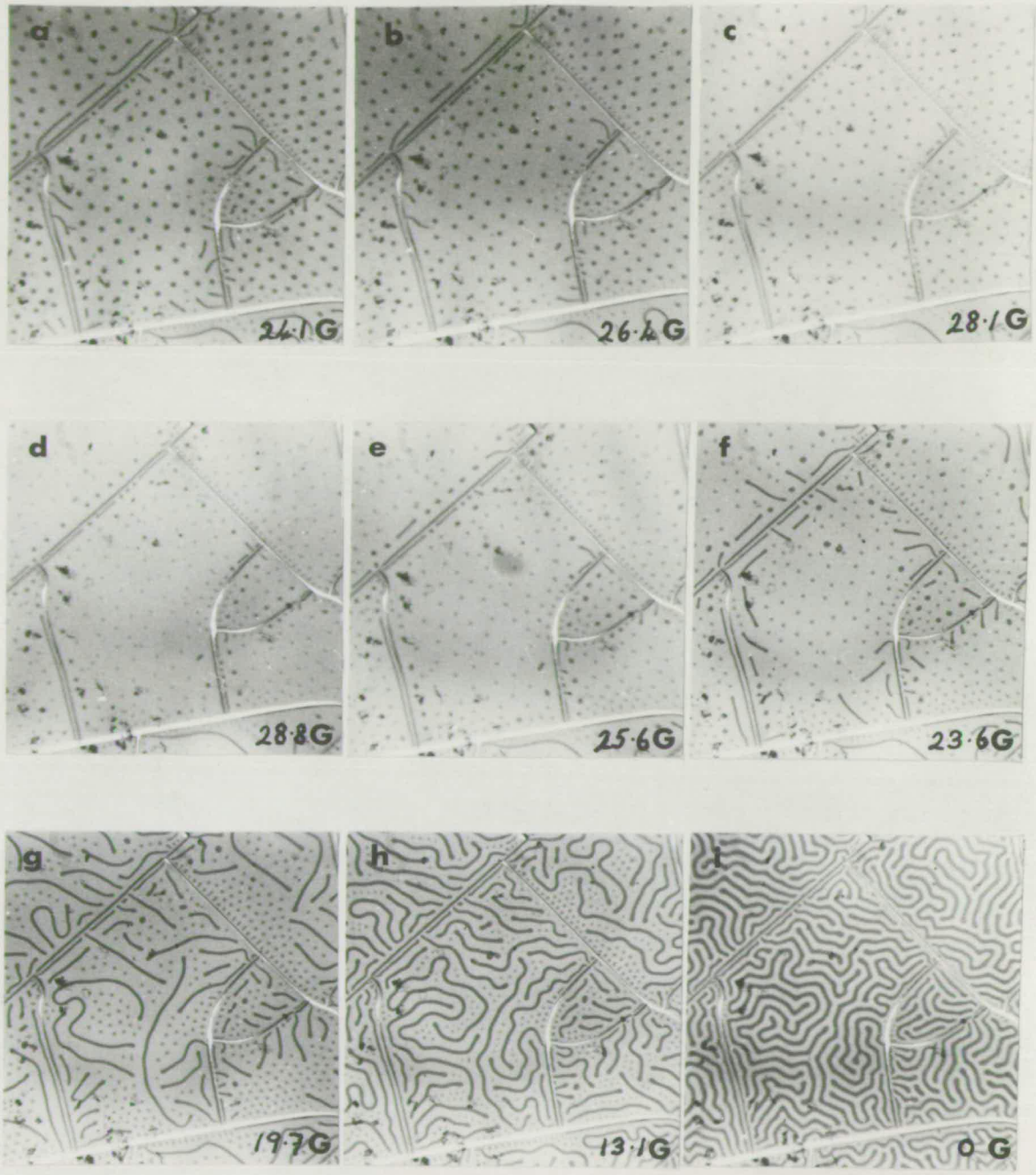

200 μm

Figure 7.1.11

nucleated at the cracks. Finally, only type I stripe domains remain. The type II bubbles can be collapsed if a high enough field is applied.

	Collapse Field G	Runout Field G
Type I	31 ± 1	17 ± 1
Type II	38 ± 1	-

The variation of bubble diameter with field for each type of bubble is shown in the graph in figure 7.1.12. The two types of bubble appear similar to those of Braginski et al. [165] It seems reasonable to suppose that the type I bubbles are cylindrical domains extending right through the film and the type II bubbles are approximate hemispheres floating at the free film surface.

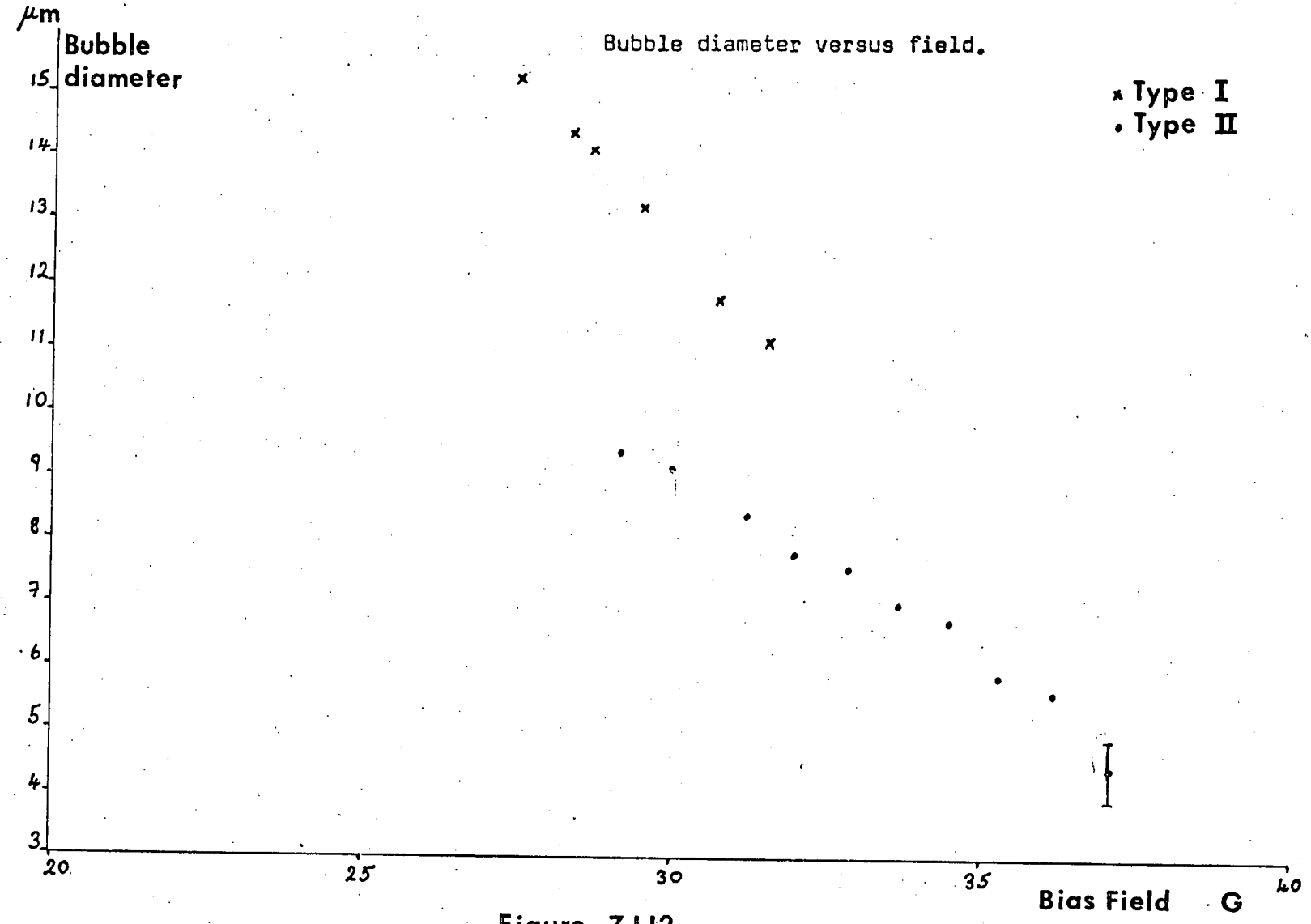
μm
Bubble diameter
Bubble diameter versus field.
x Type I
• Type II
15
14
13
12
11
10
9
8
7
6
5
4
3
20
25
30
35
40
Bias Field G

Figure 7.1.12

A related type of behaviour was observed in a mesa in an LPE film of Sm, Ga:YIG. In this film the bubble diameter decreased as the bias field increased until the bubble apparently collapsed. However, if the field was then reduced the same bubble pattern reappeared. The pattern was destroyed only if the bias field was raised to a much higher value.

	In helix G	Outside helix G
Apparent collapse	118 ± 1	120 ± 0.5
Permanent collapse	127 ± 2	130 ± 1
Run out	97 ± 1	104 ± 2

In this case a half bubble may be formed bounded by the bottom surface of the film. This film in the mesa suppressed the formation of hard bubbles.

b) Variation in thickness:

The following data were obtained for variation in collapse and runout fields with thickness for LPE films containing mesas.

Thickness μm	Δh μm		Collapse G	Runout G	Range G
4.86	4	Inside mesa	128 ± 1	100 ± 1	28 ± 2
		Outside mesa	95 ± 1	70 ± 1	25 ± 2
18.8	4	Inside mesa	167 ± 1	135 ± 1	32 ± 2
		Outside mesa	165 ± 1	133 ± 1	32 ± 2

The range of field over which the bubble is stable is essentially unchanged by the change in thickness but is displaced to higher fields as the thickness of the film increases. This shows that care must be taken, when making measurements at various points in the film, that the variations are due to the defect under study and not just variations in thickness.

c) Core:

Measurements were made at two points, one inside and one outside the core. To minimise the effect of thickness variations these points were not more than 0.5 mm apart, i.e. the core boundary was in the centre of the microscope field of view. The bubbles inside the core collapsed and ran out at slightly lower fields from those in the matrix.

	Runout G	Collapse G
Inside core	147.4 ± 0.5	176.5 ± 0.5
Outside core	150.4 ± 0.5	178.5 ± 0.5

d) Growth bands:

No effect on collapse or runout observed.

e) Dislocations:

Bubbles are held at the point of emergence of dislocations and are smaller than free bubbles, as can be seen from the graph in fig. 7.1.13. It was found that the bubbles on the dislocations collapsed and ran out at lower fields than the other bubbles. The range of stability was

Bubble diameter versus field.

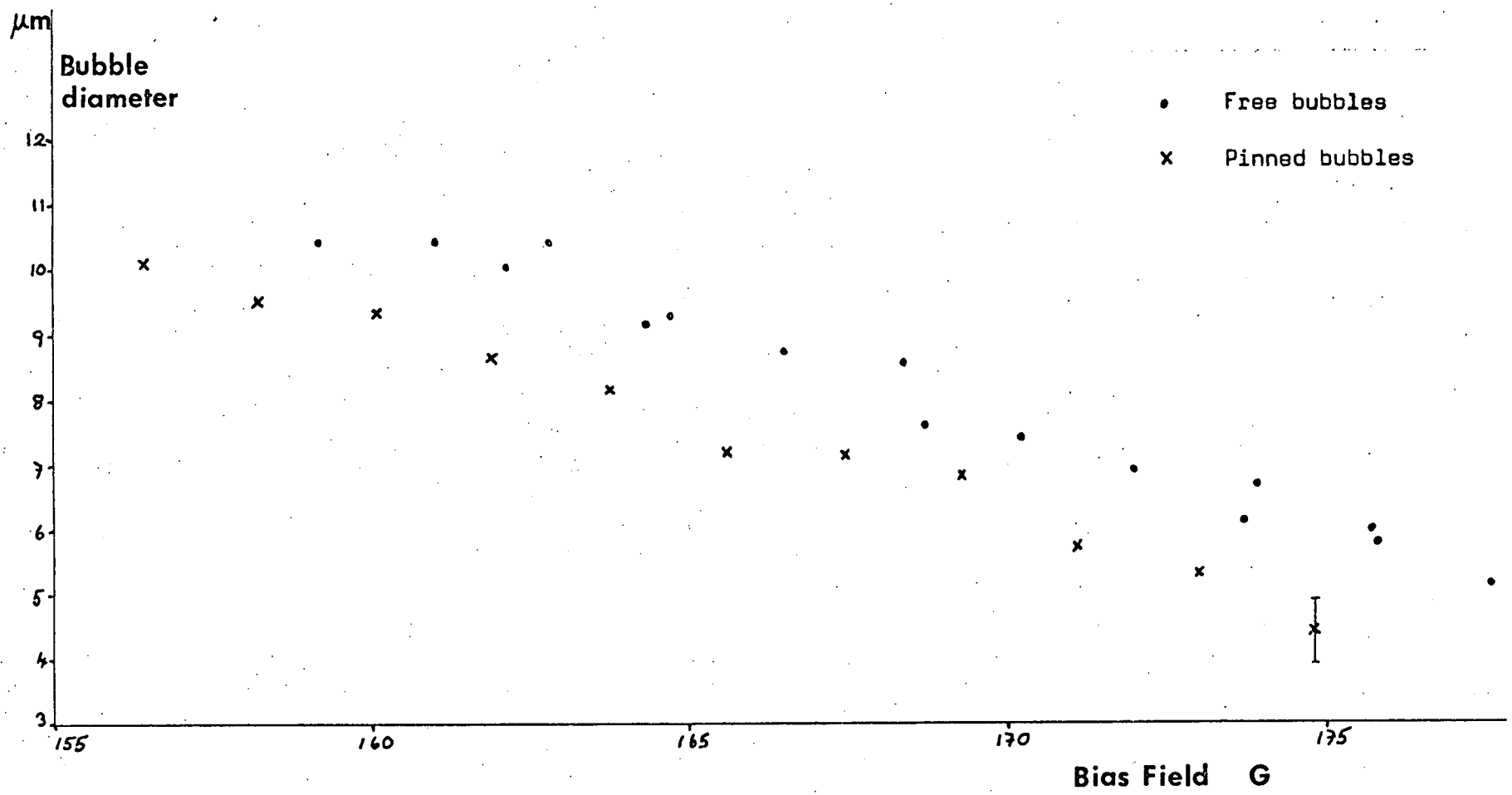

Figure 7.1.13

increased.

	Collapse G	Runout G
Dislocation-free	179 ± 1	147 ± 1
Plus dislocation	176 ± 1	135 ± 2

The effect, particularly for runout, is greater than would occur by thickness variations alone.

f) Cracks and scratches:

Figure 7.1.11 shows that stripe domains remained near the cracks at fields where the bubbles in the centre of each fragment of film had collapsed. Where bubbles are formed they are at a much higher density and persist to much higher fields. A scratch produces less extreme behaviour but a higher than average density of bubbles will form along the scratch.

g) Other films:

One sample of a CVD film was received half-covered with a film of SiO_2. This may affect the magnetic properties depending on heat treatment[10] or due to elastic strain. The history of this sample was not available. A small strain gradient exists at the boundary between the coated and uncoated parts since the bubbles lie in a row along the boundary and the hexagonal bubble pattern is perturbed. The following data were obtained:

	Collapse G	Runout G
Without SiO_2	123 ± 1	103 ± 1
With SiO_2	122 ± 1	108 ± 1

The change in the runout field implies a higher magnetisation under the film. This would suggest that the effect is due to strain but more information is needed.

h) Variations in composition:

The magnetisation of a film may be obtained from the data on bubble collapse, runout and zero field stripe period. Sources of error in obtaining these values are discussed by Pierce.[121] The main source of error, particularly for thin films of high magnetisation is in the measurement of domain widths. The average result for each film, ignoring any effects of defects, is given below:

Sample	Composition	$\mu_o M_s$ G	Range G
Eu 18	$Eu_2Er_1Ga_{0.7}Fe_{4.3}O_{12}$	246	± 20
A 4	"	241	± 15
RRE 2	"	255	± 15
R3C	"	168	± 10
UC 9	$Sm_{0.25}Y_{2.75}Ga_1Fe_4O_{12}$	176	± 50
A	Ga:YIG	137	?
B	"	237	± 20

7.2 Dynamic Properties

7.2.1 A.C. field

By suitable choice of D.C. bias field and A.C. bias field amplitude and frequency, bubbles or stripe domains can be made to move in the film. In a perfect film the domains move smoothly and uniformly and the contrast in

the polarising microscope is uniform. If there is a defect present which perturbs or slows the motion of a domain then, locally, the amount of light transmitted is altered and the source of domain pinning is revealed.

Scratches, cracks, dislocations, rough areas of film and inclusions all impede bubble motion. Boundaries of elastic strain such as in the core, the edge of the mesa and the SiO_2 over layer all perturb bubble motion. Examples of these may be seen in the sequence of photographs in fig. 7.1.14.

This method gives a qualitative overall picture of the pinning of domains but some of the weaker pinning points may be missed. This method will not show up variations in mobility in different areas of otherwise perfect crystal such as the change in mobility inside and outside the core.

7.2.2 Bubble mobility

Bubble mobility was determined by a translation method which gives a quantitative measure of variations in mobility and coercivity as might be encountered in device operation. Bubble collapse methods were investigated and abandoned as not being sufficiently sensitive nor taking account of coercivity. Measurements were made in regions of varying elastic strain such as cored regions and near dislocations. The qualitative effect of scratches and cracks were observed.

a) Cracks and scratches:

Bubbles could not be propagated across cracks or severe scratches. Even very small scratches would turn the motion of the bubble to go parallel to the scratch, even if it were originally travelling normal to the scratch. This would give an effective mobility of zero if the drive field is normal to the scratch. If the scratch and field gradient are parallel then the bubble will move faster than in the defect-free region. This will occur even for hard bubbles and was observed in one case to increase the velocity by a factor of 5 when moving along the crack. This underlines the principle of grooved track propagation in devices.

b) Variations in composition - double layer films:

The composition of the top layer of a mesa is rich in lead and may contain small inclusions. This would tend to impede the motion of a bubble, as is shown below:

	Mobility $ms^{-1}G^{-1}$	Coercivity B_c G
In film	1.85 ± 0.1	0.31 ± 0.04
In mesa	1.17 ± 0.14	0.45 ± 0.1

The mobility is lower and the coercivity greater in the mesa. Even if a device over the mesa did not cross the mesa boundary its performance would not be so good as a device in the thin area of the film.

c) Type of bubble:

One film of CVD Ga:YIG was a double layer film which could contain two types of bubbles. Both bubbles were mobile, one was cylindrical the other floated as a half-bubble. These two bubbles had different mobilities but both were 'normal' bubbles.

	Mobility $ms^{-1}G^{-1}$	Coercivity B_c G
Large bubble	0.19 ± 0.08	0.1 ± 0.4
Small bubble	0.66 ± 0.2	0.057 ± 0.02

The film of $Sm_{0.25}$ $Y_{2.75}$ Ga_1 Fe_4 O_{12} had hard bubbles in the thin areas and normal bubbles in the mesas. In this case the double layer in the mesa has a beneficial effect.

	Mobility $ms^{-1}G^{-1}$	Coercivity B_c G
Mesa	4.1 ± 1	0.2 ± 0.1
Lowlands - motion parallel to field gradient.	0.75 ± 0.7	0.2 ± 0.5

d) Core:

There is an adverse effect on the mobility in the cored region, fig. 7.2.1 . Two pairs of readings are given below:

	Mobility $ms^{-1}G^{-1}$	Coercivity G
In core	0.74 ± 0.02	0.26 ± 0.02
Outside core	1.12 ± 0.02	0.28 ± 0.02
In core	0.82 ± 0.06	0.19 ± 0.05
Outside core	0.93 ± 0.1	0.25 ± 0.08

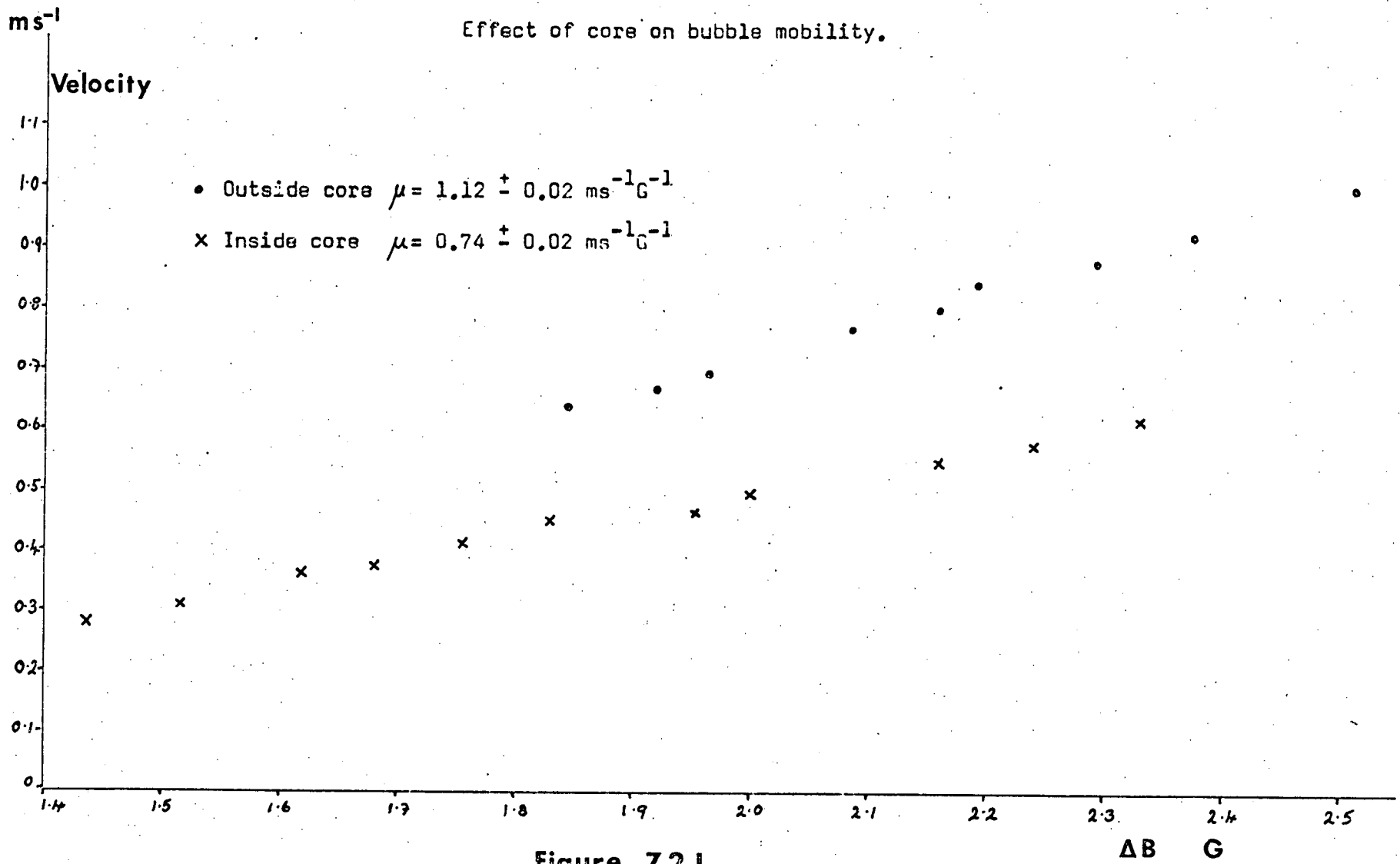
Effect of core on bubble mobility.
ms⁻¹
Velocity
• Outside core μ = 1.12 ± 0.02 ms⁻¹G⁻¹
× Inside core μ = 0.74 ± 0.02 ms⁻¹G⁻¹
1·1
1·0
0·9
0·8
0·7
0·6
0·5
0·4
0·3
0·2
0·1
0
1·4
1·5
1·6
1·7
1·8
1·9
2·0
2·1
2·2
2·3
2·4
2·5
ΔB G

Figure 7.2.1

e) Growth bands:

Since the core affects mobility it might be expected that there would be a similar effect with growth bands. A bubble travelling parallel to a growth band 'sees' a path of constant strain. The bubble running perpendicular to the growth bands is in a varying strain field. Thus a higher mobility along the growth band would be expected.

	Mobility $ms^{-1}G^{-1}$	Coercivity G
Perpendicular to growth bands.		
All data	0.72 ± 0.02	0.13 ± 0.03
Omitting lowest point	0.75 ± 0.02	0.14 ± 0.03
Parallel to growth bands		
All data	0.91 ± 0.08	0.37 ± 0.08
Omitting lowest 2 points	0.74 ± 0.02	0.16 ± 0.02

These measurements were made over a very wide range of bubble diameters. The uncertainty in the smallest, lowest velocity bubbles is great and so it is reasonable to omit these values, fig. 7.2.2. The experiment was performed at the same position on a film which was grown on a substrate with the most severe growth banding available. There is no significant change in the mobility or coercivity with direction.

f) Dislocations:

A bubble travelling within 10-15 μm of a dislocation is liable to become pinned by the dislocation, particularly

Effect of growth bands on bubble mobility.

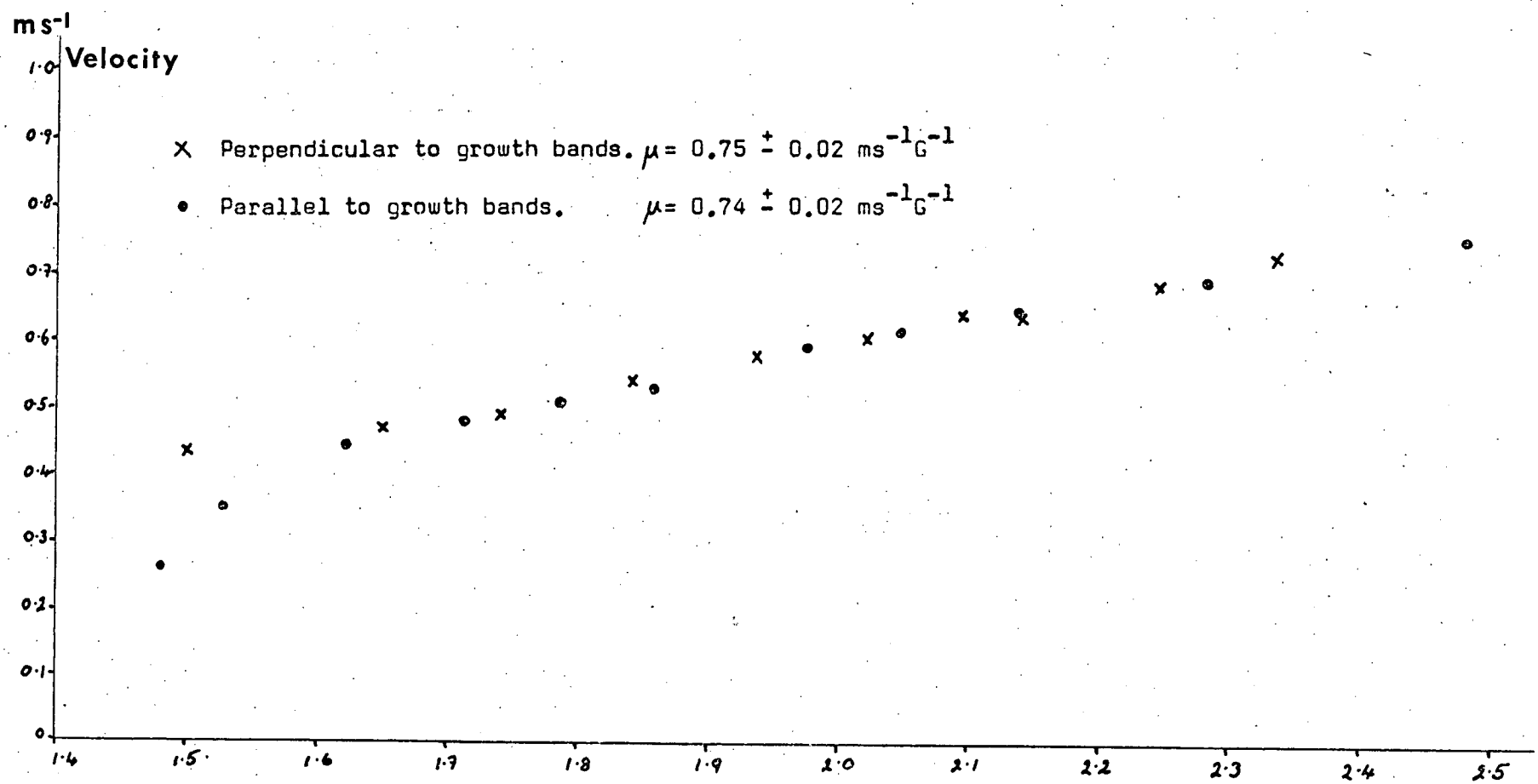

Figure 7.2.2

when the bubble is travelling at low velocities. Measurements were taken on moving bubbles only and stopped as soon as the bubble was pinned. Measurements on the mobility of a bubble at different distances from a dislocation were made.

Distance μm	Mobility $ms^{-1}G^{-1}$	Coercivity G
12 pinned	0	—
12	1.00 ± 0.06	0.30 ± 0.04
30	0.62 ± 0.06	0.25 ± 0.09
150	0.93 ± 0.1	0.20 ± 0.09
300	1.17 ± 0.04	0.42 ± 0.03

The high value of mobility for the closest bubble to the dislocation occurred as the bubble was attracted to the dislocation. It deviated from a straight path and could not be propagated past the dislocation. Otherwise there is a systematic increase in the mobility as the distance between the bubble and the dislocation increases.

Helical dislocations also affect the mobilities. The mobility of a bubble inside the helix is reduced and a bubble becomes pinned on the dislocation line. In this sample there were also other sources of pinning, and in the thin region of film only hard bubbles could be produced.

Position		Mobility $ms^{-1}G^{-1}$	Coercivity G
Mesa	In helix	3.10 ± 0.8	0.17 ± 0.1
	Outside helix	4.75 ± 1.4	0.14 ± 0.1
Lowlands	In helix	0.41 ± 0.4	0.24 ± 0.5
	Outside helix	1.07 ± 0.6	0.23 ± 0.3

7.3 Discussion

From the previous results it is apparent that the only type of defect which can be tolerated in the centre of a substrate material is growth banding. Even for growth bands it is preferable for them to be flat and parallel to the (111) slice. The composition fluctuations should also be small to maintain reproducibility. These stringent requirements may be relaxed a little at the edge of the sample. The edge is subject to handling damage and so edge facets and a strained rim will cause little extra loss of good devices, particularly if the diameter of the substrate is large.

Dislocations of all types, although interesting in themselves because of their large size and variety, must be excluded. This means that the conditions of growth of the boule must be carefully controlled. The atmosphere must be controlled to prevent inclusions which may nucleate dislocations. The interface shape must not become concave so it, and also the melt composition, must be controlled. Neither must the interface become too convex, else a central core is formed.

Magnetic domains observed by x-ray topography and polarised light.

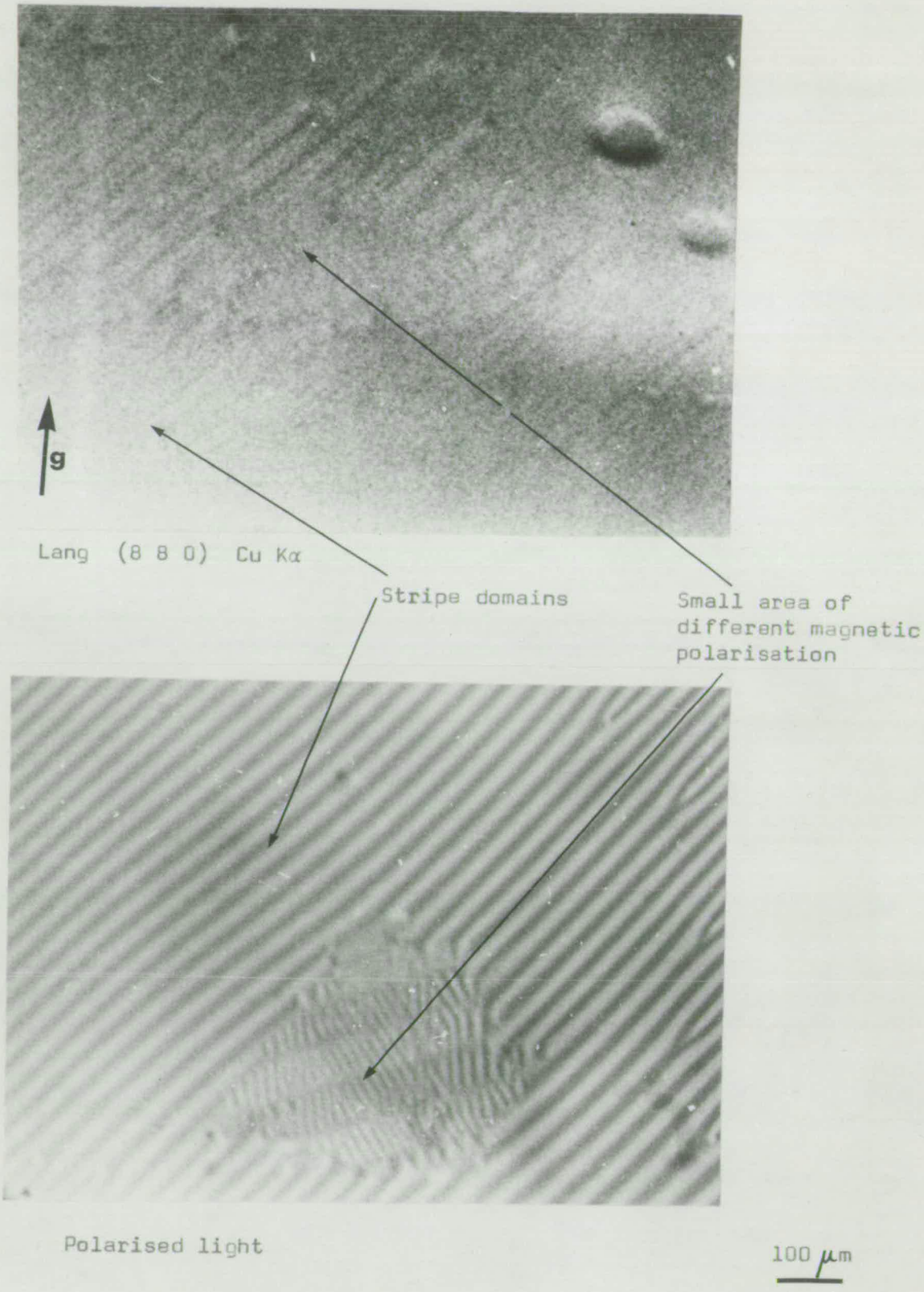

Figure 7.3.1

Having produced a dislocation-free, core-free, strain-free substrate the surface polishing must be of a similar high quality with no scratches and the surface must be clean. A clean, scratch-free high-quality substrate will allow the growth of good films but no extra defects, unless confined to the edge of the sample, can be allowed. The film should be flat and of uniform composition with no inclusions. The lattice parameter should be tailored to give good growth with no cracks or faceting but with sufficient mismatch to produce the required stress-induced uniaxial magnetic anisotropy.

This work has stopped short at considering the defects and strain produced by the fabrication of devices. Any strain so produced should be visible by x-ray topography. There has also been no discussion on the effects of heat-treatment by annealing of films, the temperature dependence of magnetic properties, nor the effect of irradiation. Irradiation by x-rays has been found to improve the mobility of bubbles[166] but the mechanism of this improvement is uncertain.

It was observed during the x-ray experiments that a GGG slice placed close to the x-ray source suffered radiation damage. The colourless GGG turned an orange-brown colour similar to that observed in x-ray irradiated lithium fluoride. This suggests that colour centres of some kind have been formed. They were rapidly bleached by sunlight or ultraviolet light. The absorption spectrum at room temperature showed the sharp bands characteristic of gadolinium in the ultra-violet region and a broad

absorption in the visible region due to the colour centres. Further investigation may produce some information on the mechanism operating in bubble films if it assumed that the damage is the same in each case, since examination of a transparent material is easier.

It was also noted, as mentioned previously, that supposedly 180^{o} domains had been observed by x-ray topography in a film which had been removed from the substrate. The optical and x-ray pictures can be correlated, see fig. 7.3.1. Most of the magnetic anisotropy must have been growth induced since the domain pattern was unchanged after the substrate was removed. None of the bubble films had bubbles large enough to be resolved on the x-ray plate and were too thin to be removed from the substrate. A similar experiment to that on the thick YIG film, performed on a thick bubble film, would be interesting since the direction of magnetisation in the domains would be known if the film can support bubbles. An investigation of the domain pattern, as observed by x-rays, as a function of temperature would also be of interest.

REFERENCES

1. Bobeck A.H., 1967 Bell Syst. Tech. J. 46 1901

2. O'Dell T.H., 1974 Magnetic Bubbles (London:Macmillan)

3. Bobeck A.H., Fischer R.F., Perneski A.J., Remeika J.P. and van Uitert L.G., 1969 IEEE Trans. Magnetics MAG-5 544

4. Copeland J.A., Elward J.P., Johnson W.A. and Ruch J.G., 1971 J. Appl. Phys. 42 1266

5. Perneski A.J., 1969 IEEE Trans. Magnetics MAG-5 554

6. Danylchuk I., 1971 J. Appl. Phys. 42 1358

7. Parzefall F., Littwin B. and Metzdorf W., 1973 IEEE Trans. Magnetics MAG-9 293

8. Reekstin J.P., 1971 J. Appl. Phys. 42 1362

9. Spencer E.G., Schmidt P.H. and Fischer R.F., 1970 Appl. Phys. Lett. 17 328

10. Le Craw R.C., Byrnes P.A., Johnson W.A., Levinstein H.J., Nielsen J.W., Spiwak R.R. and Wolfe R., 1973 IEEE Trans. Magnetics MAG-9 422

11. Copeland J.A., Josenhans J.G. and Spiwak R.R., 1973 IEEE Trans. Magnetics MAG-9 489

12. Solomons B. and Owens J.M. 1973 Private communication

13. Nelson T.J., Chen Y. and Geusic J.E., 1973 IEEE Trans. Magnetics MAG-9 289

14. Chang H., Fox J., Lu D. and Rosier L.L., 1972 IEEE Trans. Magnetics MAG-8 214

15. Strauss W., 1971 J. Appl. Phys. 42 1251

16. Almasi G.S., 1973 IEEE Trans. Magnetics MAG-9 663

17. Chen T.T., Bohning O.D., Tocci L.R., Archer J.L. and Stermer R.L., 1974 IEEE Trans. Magnetics MAG-10 739

18. Seny R.S. and Irons H.R., 1973 AIP Conf. Proc. No 18 p.90

19. Williams R.A., Henry R.D., Chen T.T. and Archer J.L., 1973 IEEE Trans. Nucl. Sci. NS-20 229

20. Bonyhard P.I., Danylchuk I., Kish D.E. and Smith J.L., 1970 IEEE Trans. Magnetics MAG-6 447

21. Lee S.Y. and Chang H., 1974 IEEE Trans. Magnetics MAG-10 746

22. Gianola U.F., Smith D.H., Thiele A.A. and van Uitert L.G., 1969 IEEE Trans. Magnetics MAG-5 558

23. Remeika J.P., 1956 J. Amer. Chem. Soc. 78 4259

24. Bobeck A.H. and Della Torre E., 1975 Magnetic Bubbles (Amsterdam: North-Holland)

25. Varnerin L.J., 1971 IEEE Trans. Magnetics MAG-7 404

26. Bobeck A.H., Spencer E.G., van Uitert L.G., Abrahams S.C., Barns R.L., Grodkiewicz W.H., Sherwood R.C., Schmidt P.H., Smith D.H. and Walters E.M., 1970 Appl. Phys. Letters 17 131

27. Grundy P.J., Hothersall D.C., Jones G.A., Middleton B.K. and Tebble R.S., 1972 phys. stat. sol. (a) 9 79

28. Middleton B.K., 1972 phys. stat. sol. (a) 9 617

29. Finbow D.C. and Jones G.A.,1973 phys. stat. sol. (a) 20 K91

30. Gambino R.J.,Chaudhari P. and Cuomo J.J., 1974 AIP Conf. Proc. No. 18 p.578

31. Chaudhari P., Cuomo J.J. and Gambino R.J., 1973 IBM J. Res. Develop. 17 66

32. Menzer G., 1926 Z. Kristallogr. 63 157

33. Menzer G., 1928 Z. Kristallogr. 69 300

34. International Tables for X-Ray Crystallography 1969 Vol. I p.345 (Birmingham:Kynoch Press)

35. Wyckoff R.W.G., 1965 Crystal Structures, Vol. 3 p.222 (New York:Interscience)

36. Beevers miniature models, Simon Square Centre, Pleasance, Edinburgh

37. Gilleo M.A. and Geller S., 1958 Phys. Rev. 110 73

38. Pauthenet R., 1959 J. Appl. Phys. 30 (Suppl.) 2905

39. Bertaut F. and Pauthenet R., 1957 Proc. Instn. Elect. Engrs. 104B (Suppl.) 261

40. Heinz D.M., Besser P.J., Owens J.M., Mee J.E. and Pulliam G.R., 1971 J. Appl. Phys. 42 1243

41. Nielsen J.W., 1958 J. Appl. Phys. 29 390

42. Rosencwaig A. and Tabor W.J., 1971 J. Appl. Phys. 42 1643

43. Rosencwaig A., Tabor W.J. and Pierce R.D., 1971 Phys. Rev. Lett. 26 779

44. Rosencwaig A., Tabor W.J., Hagedorn F.B. and van Uitert L.G., 1971 Phys. Rev. Lett. 26 775

45. Matthews J.W. and Klokholm E., 1972 Mater. Res. Bull. 7 213

46. Stacy W.T., Janssen M.M., Robertson J.M. and van Hout M.J.G., 1973 AIP Conf. Proc. No. 10 p.314

47. Rosencwaig A. and Tabor W.J., 1972 AIP Conf. Proc. No. 5 p.57

48. Cronemeyer D.C., Giess E.A., Klokholm E., Argyle B.E. and Plaskett T.S., 1972 AIP Conf. Proc. No. 5 p.115

49. Wolfe R., North J.C., Barns R.L., Robinson M. and Levinstein H.J., 1971 Appl. Phys. Lett. 19 298

50. Brandle C.D. and Barns R.L., 1974 J. Cryst. Growth 26 169

51. Geller S., Espinosa G.P. and Crandall P.B., 1969 J. Appl. Cryst. 2 86

52. Geller S., Espinosa G.P., Fullmer L.D. and Crandall P.B., 1972 Mater. Res. Bull. 7 1219

53. Brandle C.D. and Valentino A.J., 1972 J. Cryst. Growth 12 3

54. Cockayne B. and Roslington J.M., 1973 J. Mater. Sci. 8 601

55. O'Kane D.F., Sadagopan V. and Giess E.A., 1973 J. Electrochem. Soc. 120 1272

56. Brandle C.D., Miller D.C. and Nielsen J.W., 1972 J. Cryst. Growth 12 195

57. Linares R.C., 1968 J. Cryst. Growth 3,4 443

58. Shick L.K., Nielsen J.W., Bobeck A.H., Kurtzig A.J., Michaelis P.C. and Reekstin J.P., 1971 Appl. Phys. Lett. 18 89

59. Levinstein J.H., Licht S., Landorf R.W. and Blank S.L., 1971 Appl. Phys. Lett. 19 486

60. Blank S.L. and Nielsen J.W., 1972 J. Cryst. Growth 17 302

61. Giess E.A., Kuptsis J.D. and White E.A.D., 1972 J. Cryst. Growth 16 36

62. Blank S.L., Hewitt B.S., Shick L.K. and Nielsen J.W., 1973 AIP Conf. Proc. No.10 p.256

63. Ghez R. and Giess E.A., 1973 Mater. Res. Bull. 8 31

64. Ghez R. and Giess E.A., 1974 J. Cryst. Growth 27 221

65. Robertson J.M., Tolksdorf W. and Jonker H.D., 1974 J. Cryst. Growth 27 241

66. Suemune Y. and Inoue N., 1974 Japan J. Appl. Phys. 13 204

67. Hiskes R., 1974 J. Cryst. Growth 27 287

68. Mee J.E., Pulliam G.R., Archer J.L. and Besser P.J., 1969 IEEE Trans. Magnetics MAG-5 717

69. Stein B.F., 1971 J. Appl. Phys. 42 2336

70. Robinson McD., 1973 J. Cryst. Growth 18 143

71. Besser P.J., Mee J.E., Elkins P.E. and Heinz D.M., 1971 Mater. Res. Bull. 6 1111

72. Besser P.J., Mee J.E., Glass H.L., Heinz D.M., Austerman S.B., Elkins P.E., Hamilton T.N. and Whitcomb E.C., 1972 AIP Conf. Proc. No.5 p.125

73. Basterfield J., 1969 Brit. J. Appl. Phys. (J.Phys.D) Ser.2 2 1159

74. Szaplonczay A.M. and Quon H.H.D., 1972 J. Mater. Sci. 7 1280

75. Miller D.C., 1973 J. Electrochem. Soc. 120 1771

76. Newkirk J.B., Bonse U. and Hart M., 1967 Adv. in X-ray Analysis 10 1

77. Lang A.R., 1957 Acta Met. 5 358

78. Lang A.R., 1958 J. Appl. Phys. 29 597

79. Lang A.R., 1959 J. Appl. Phys. 30 1748

80. Lang A.R., 1959 Acta Cryst. 12 249

81. Bonse U., 1962 In Direct Observations of Imperfections in Crystals (New York:Interscience)

82. Howard J.K., Dobrott R.D., 1966 J. Electrochem Soc. 113 567

83. Renninger M., 1963 In Crystallography and Crystal Perfection edited by G.N. Ramachandran (London: Academic Press)

84. Hattanda T. and Takeda A., 1973 Japan J. Appl. Phys. 12 1104

85. Forsyth J.B. and Wells M., 1959 Acta Cryst. 12 412

86. International Tables for X-ray Crystallography, 1968 Vol III p.157 (Birmingham:Kynoch Press)

87. Hart M., 1963 PhD Thesis, University of Bristol

88. Gerward L., 1970 phys. stat. sol. (a) 2 143

89. Authier A., 1967 Adv. in X-ray Analysis 10 9

90. Read W.T., 1953 Dislocations in Crystals (New York: McGraw-Hill)

91. Polcarová M., 1969 IEEE Trans. Magnetics MAG-5 536

92. Basterfield J. and Prescott M.J., 1967 J. Appl. Phys. 38 3190

93. Pétroff J.F. and Mathiot A., 1974 Mater. Res. Bull. 9 319

94. Mathiot A., Pétroff J.F. and Bernard Y., 1973 phys. stat. sol.(a) 20 K1

95. Patel J.R., Jackson K.A. and Dillon J.F., 1968 J. Appl. Phys. 39 3767

96. Bullough R., 1958 Phys. Rev. 110 620

97. Prescott M.J. and Basterfield J., 1967 J. Mater. Sci. 2 583

98. Nikitenko V.I. and Dedukh L.M., 1970 phys. stat. sol. (a) 3 383

99. Tanner B.K. and Fathers D.J., 1974 Phil. Mag. 29 1081

100. Dillon J.F., 1958 J. Appl. Phys. 29 1286

101. Cooper R.W., Crossley W.A., Page J.L. and Pearson R.F., 1968 J. Appl. Phys. 39 565

102. Bongers P.F., 1969 IEEE Trans. Magnetics MAG-5 472

103. Crossley W.A., Cooper R.W., Page J.L. and van Stapele R.P., 1969 J. Appl. Phys. 40 1497

104. Thiele A.A., 1969 Bell Syst. Tech. J. 48 3287

105. Fowlis D.C. and Copeland J.A. 1972 AIP Conf. Proc. No. 5 p.240

106. Shaw R.D., Hill D.E., Sandfort R.M. and Moody J.W., 1973 J. Appl. Phys. 44 2346

107. Callen H. and Josephs R.M., 1971 J. Appl. Phys. 42 1977

108. Thiele A.A., 1971 Bell Syst. Tech. J. 50 725

109. Bobeck A.H., Danylchuk S., Remeika J.P., van Uitert L.G. and Walters E.M., 1970 Proc. Intntl. Conf. on Ferrites, Japan, p.361

110. Slonczewski J.C., 1972 AIP Conf. Proc. No.5 p.170

111. Callen H., Josephs R.M., Seitchik J.A. and Stein B.F., 1972 Appl. Phys. Lett. 21 366

112. Vella-Coleiro G.P. and Tabor W.J., 1972 Appl. Phys. Lett. 21 7

113. Kryder M.H. and Hu H.L., 1974 AIP Conf. Proc. No.18 p.213

114. Tabor W.J., Bobeck A.H., Vella-Coleiro G.P. and Rosencwaig A., 1973 AIP Conf. Proc. No. 10 p.442

115. Grundy P.J., Hothersall D.C., Jones G.A., Middleton B.K. and Tebble R.S., 1971 IEEE Trans. Magnetics MAG-7 483

116. Dunk P. and Jones G.A.,1974 AIP Conf. Proc. No.18 p.162

117. Rosencwaig A., 1972 Bell Syst. Tech. J. 51 1440

118. Milne A.D., Owens J.M., Solomons B. and Thornley S.J., 1973 AIP Conf. Proc. No. 10 p.414

119. Geusic J.E., Levinstein H.J., Licht S.J., Shick L.K. and Brandle C.D., 1971 Appl. Phys. Lett. 19 93

120. Argyle B.E. and Chaudhari P., 1973 AIP Conf. Proc. No. 10 p.403

121. Pierce R.D., 1974 J. Cryst. Growth 27 299

122. Shumate P.W., 1971 J. Appl. Phys. 42 1274

123. Robertson J.M., van Hout M.J.G., Janssen M.M. and Stacy W.T., 1973 J. Cryst. Growth 18 294

124. Keig G.A., 1973 AIP Conf. Proc. No.10 p. 237

125. Matthews J.W., Klokholm E. and Plaskett T.S., 1973 AIP Conf. Proc. No.10 p 271

126. Brandle C.D., Miller D.C. and Nielsen J.W., 1972 J. Cryst. Growth 12 195

127. Matthews, J.W., 1973 phys. stat. sol. (a) 15 607

128. Matthews J.W., Klokholm E., Sadagopan V., Plaskett T.S. and Mendel E., 1973 Acta Met. 21 203

129. Damen J.P.M. and Robertson J.M., 1972 J. Cryst. Growth 16 50

130. Belt R.F. and Moss J.P., 1973 Mater. Res. Bull. 8 1197

131. Glass H.L., 1973 Mater. Res. Bull. 8 43

132. Brice J.C., 1970 J. Cryst. Growth 6 205

133. Cockayne B., Roslington J.M. and Vere A.W., 1973 J. Mater. Sci. 8 382

134. Glass H.L., 1972 Mater. Res. Bull. 7 1087

135. Glass H.L., 1972 Mater. Res. Bull. 7 385

136. Thomas G. and Whelan M.J., 1959 Phil. Mag. 4 511

137. Guyot P., 1971 phys. stat. sol. (a) 5 95

138. Morton A.J., 1970 Phil. Mag. 22 483

139. Amelinckx S., Bontinck W. and Maenhout-van Der Vorst W., 1957 Physica 23 270

140. Caslavsky J.L. and Gazzaron C.P., 1971 J. Mater. Sci. 6 1139

141. Matthews J.W., Klokholm E., Plaskett T.S. and Sadagopan V., 1973 phys. stat. sol. (a) 19 671

142. Matthews J.W., Klokholm E. and Plaskett T.S., 1973 IBM J. Res. Develop. 17 426

143. Stacy W.T., Pistorius J.A. and Janssen M.M., 1974 J. Cryst. Growth 22 37

144. Imamura Y. and Shinoyama S., 1974 Japan J. Appl. Phys. 13 379

145. Thornley S.J. and Milne A.D., 1974 Second European Crystallographic Meeting, Keszthely, Hungary

146. Giess E.A., Guerci C.F. and White W.H., 1974 IBM Tech. Disclos. Bull. 16 3049

147. Tolksdorf W., Bartels G., Espinosa G.P., Holst P., Mateika D. and Welz F., 1972 J. Cryst. Growth 17 322

148. Miller D.C. and Caruso R., 1974 J. Cryst. Growth 27 274

149. Stacy W.T. and Janssen M.M., 1974 J. Cryst. Growth 27 282

150. Stein B.F. 1974 AIP Conf. Proc. No. 18 p.48

151. Robertson J.M., van Hout M.J.G. and Verplanke J.C., 1974 Mater. Res. Bull. 9 555

152. Glass H.L. and Elliott M.T., 1974 J. Cryst. Growth 27 253

153. Braginski A.I., Oeffinger T.R. and Takei W.J., 1972 Mater. Res. Bull. 7 627

154. Isomae S., Kishino S. and Takahashi M., 1974 J. Cryst. Growth 23 253

155. Klokholm E., Matthews J.W., Mayadas A.F. and Angilello J., 1972 AIP Conf. Proc. No. 5 p.105

156. Ghezzi C. and Servidori M., 1974 J. Mater. Sci. 9 1797

157. Gill G.P. and Fairholme R.J., 1973 J. Mater. Sci. 8 115

158. Glass H.L., Besser P.J., Hamilton T.N. and Sterner R.L., 1973 Mater. Res. Bull. 8 309

159. Stacy W.T., 1974 J. Cryst. Growth 24/25 137

160. Glass H.L. and Hamilton T.N., 1972 Mater. Res. Bull. 7 761

161. Miller D.C., 1973 J. Electrochem. Soc. 120 678

162. Capé J.A. and Lehman G.W., 1971 J. Appl. Phys. 42 5732

163. White E.A.D. and Wood J.D.C., 1972 J. Cryst. Growth 17 315

164. Isherwood B.J., 1973 Private communication

165. Braginski A.I., Oeffinger T.R., Patterson R.W. and Charap S.H., 1973 AIP Conf. Proc. No.10 p.354

166. Eisenberger P., Schmidt P.H. and Walters E.M., 1970 Appl. Phys. Lett. 17 533

167. Cape J.A., 1972 J. Appl. Phys. 43 3551

REPRINTS OF PAPERS

Milne A.D., Owens J.M., Solomons B. and Thornley S.J., 1973 AIP Conf. Proc. no. 10 p.414

Thornley S.J. and Milne A.D., 1974 Second European Crystallographic Meeting, Keszthely, Hungary

features are identifiable in both topographs but the change in the relative positions shows that these defects do not grow exactly along the [$\bar{1}$11] axis.

Many differences from the helices of type I are apparent. The diameter of each helix is much larger (~750μm) but the pitch of the helix is not correspondingly large (~100μm). The pitch also varies considerably over a few turns.

The image of the dislocation line, seen in fig.3 nearly end-on, is broad and complex which would suggest a dislocation with a very large Burgers vector or a close association of dislocations with a more usual size of Burgers vector.

By analogy with the helices of type I, a topograph taken with a reflection in the zone normal to the helix axis should show low contrast for the dislocation if the Burgers vector is along this axis. Such a Burgers vector is suggested by Matthews, Klokholm, Plaskett and Sadagopan (Physica Status Solidi A 19, 671 (1973)) from optical studies of similar dislocations and by Stacy, Pistorius and Janssen (to be published) from x-ray work. However, for reflections of the necessary type the dislocation image did not disappear but remained strong which suggests that these dislocations are more complex than those previously studied. The crystal in fig.4 is viewed in transmission approximately down the axes of the helices. The diffraction vector is normal to [$\bar{1}$11] but the diffraction contrast is strong. The thickness of the slice is 150μm and is such that at least one turn of each helix is visible. The dislocation line is not smooth but hexagonal with the 'flats' along the ⟨211⟩ directions in the ($\bar{1}$11) plane.

Associated with this complex dislocation line is a helicoidal fault surface which is confined to particular crystallographic planes. Figure 4 shows 'rays' in the centres of the helices, the rays running in ⟨110⟩ directions. Figure 3 shows the turns of the helix linked by a double surface which keeps close to ($\bar{1}$11). This surface would appear to be in the form of a helical 'staircase' with steps every 60°. The nature of this surface is linked to the nature of the boundary dislocation and is not yet completely determined. However, it could be a double layer of stacking fault or twin boundary stabilised by a change in impurity concentration.

Other interesting defects are visible in fig.4 as lines with dislocations at one end. This dislocation gives strong contrast similar to that seen in fig.3. The line is a planar defect which runs in the same direction as a ray inside the helices and for the same distance. These could be helices manqué, dislocations and planar defects of the same type as in the helices but for which the local conditions are not suitable for growth as a helix e.g. the sense of rotation of the crystal during pulling could suppress the growth of helices of one hand and allow the growth of helices of the other hand.

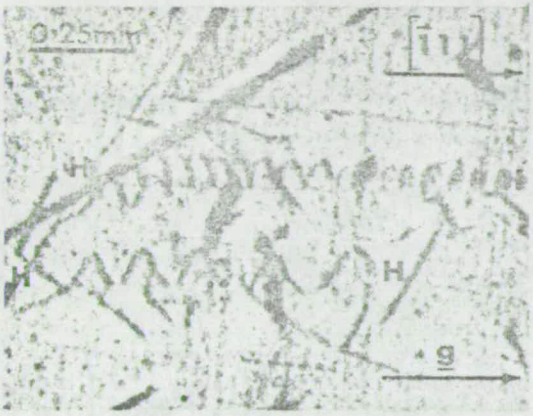

Fig. 1 ($\bar{2}64$) reflection

Fig. 2 ($08\bar{8}$) reflection

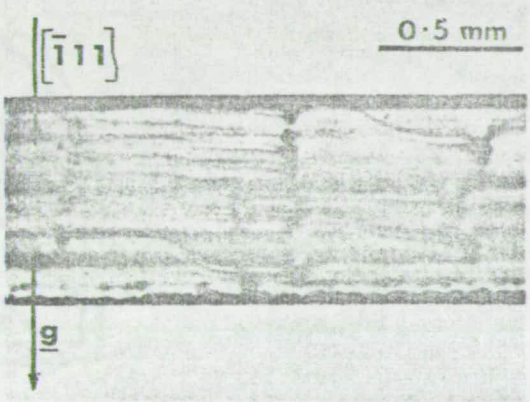

Fig. 3 ($\bar{2}64$) reflection

Fig. 4 ($\bar{8}08$) reflection

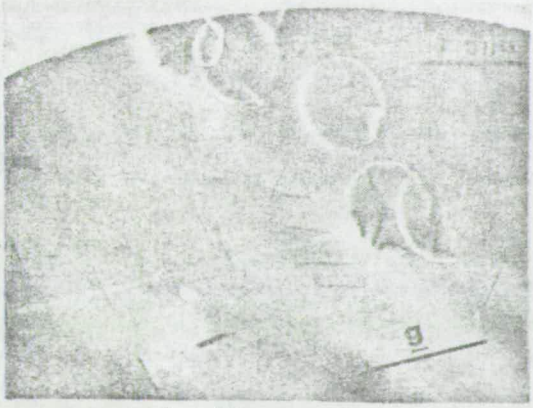

Fig. 5 ($\bar{4}124$) reflection

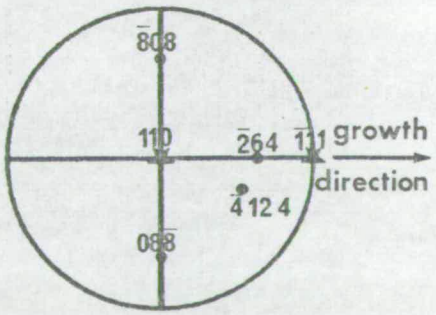

Stereographic projection showing orientation of slices ✶ and reflections • used above.

GIANT HELICAL DISLOCATIONS IN $Gd_3Ga_5O_{12}$

S.J. Thornley and A.D. Milne
Wolfson Microelectronics Liaison Unit
Department of Electrical Engineering,
University of Edinburgh, Scotland

Gadolinium gallium garnet has become of great importance as a substrate material for magnetic bubble domain and microwave devices. As defects in the substrate have an adverse effect on the performance of these devices it is important to understand fully the nature of the defects. A study has been made of these defects using Double Crystal and Lang topography.

One defect of particular interest, which has been found in the Czochralski-grown crystals, is a helical dislocation. This type of dislocation is not uncommon and has, for example, been observed by electron microscopy in Al-4% Cu alloys (Thomas and Whelan, Phil.Mag.4, 511 (1959)) and by x-ray topography in sapphire (Caslavsky and Gazzaron, J.Mat. Sci. 6, 1139, (1971)). In both these cases the Burgers vector was determined by choosing diffraction conditions such that the diffraction vector (g) was perpendicular to the Burgers vector (b) giving zero, or near zero, contrast in the dislocation image. The Burgers vectors were found to be parallel to the axes of the helices which is to be expected if the helix has been formed by condensation of vacancies onto a screw dislocation.

A similar analysis was attempted on gadolinium gallium garnet. Large helices were found which fall into two types.

Type I

These helices, fig.1, are typically 120μm in diameter and are considerably larger than those found in metal systems. Two helices (H-H) can be seen in this transmission topograph of a (110) slice which is 160μm in thickness. From the section which shows complete turns the ratio of pitch to diameter can be determined as approximately one to one. It should be noticed that the pitch of the helix is constant over the length visible. The same region of crystal is shown in fig.2 where the diffraction vector was chosen to be perpendicular to the growth direction. The images of the helices have disappeared for this reflection and for others in the $[\bar{1}11]$ zone. The Burgers vectors of these helical dislocations are parallel to the growth direction and to the axes of the helices with a probable magnitude $^{a}/_{2}\ [\bar{1}11]$.

Type II

Figure 3 is a transmission topograph of a (110) slice, 80μm in thickness, taken from a different crystal. It shows a section through two interlocking giant helices. Figure 4 is a transmission topograph and figure 5 a double crystal topograph of different $(\bar{1}11)$ slices from the same crystal as that shown in fig.3. Comparison of figs. 4 and 5 shows that these defects grow right through the crystal. The same

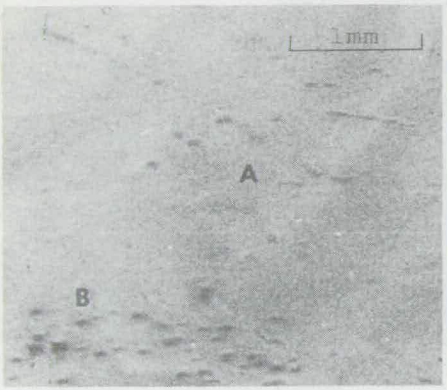

Fig. 1

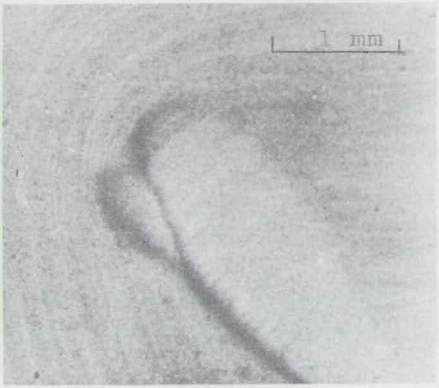

Fig. 3

X-ray images of substrates

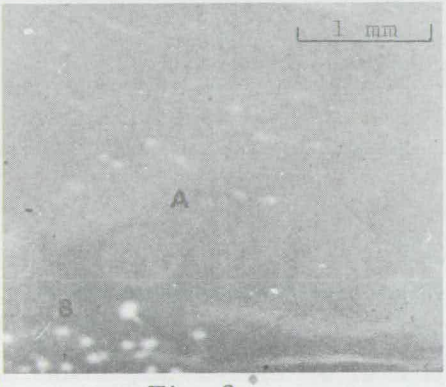

Fig. 2

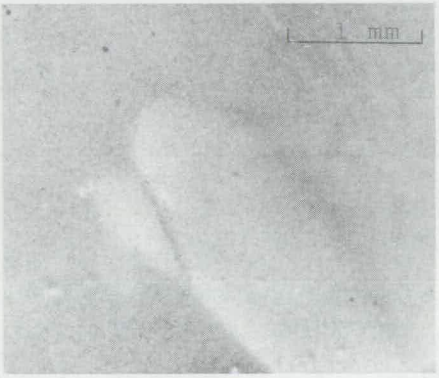

Fig. 4

X-ray images of films

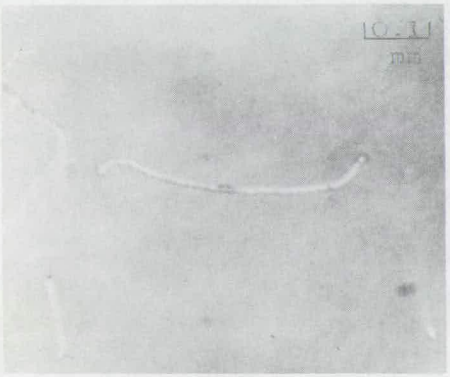

Fig. 5
AC Bias Field Domain Pattern

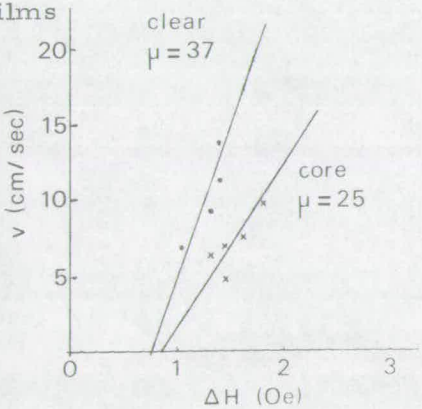

Fig. 6
Mobility Measurement

as growth banding can be suppressed if there is sufficient difference between film and substrate lattice parameters. When the difference is small (e.g. $\Delta d < 5 \times 10^{-4}$) lattice parameter variations are observed in the film but do not appear to affect the mobility. Faceted areas on the other hand are bounded by localised regions of higher strain which allows the film to adopt a modified lattice parameter. Bubble mobility in such regions will be modified to an extent dependant on the difference of lattice parameter.

TABLE I

Substrate Defect	VPE	LPE
Inclusions	Pinning points	Pinning points
Dislocations	Pinning points	Pinning points
Surface Microstrain	Pinning points	Pinning points
Growth Banding	Some correlation of relaxed pattern, no mobility reduction	Little effect
Faceting	Mobility reduction	Mobility reduction

REFERENCES

1. W.T. Stacy, W. Tolksdorf, AIP Conference Proc. American Institute of Physics, New York, No. 5 pp 185 (1972).
2. H.L. Glass, Mat. Res. Bull. V.7, 385 (1972).
3. J.M. Robertson, M.J.G. van Hout, M.M. Janssen, W.T. Stacy, to be published.
4. J.E. Geusic, et al, Appl. Physics Letters V.19, No. 4. 93 (1971)
5. J.A. Cape, J..Appl. Physics, V.43, No. 8 (1972), 3551.

ACKNOWLEDGEMENTS

This paper incorporates work carried out under a CVD contract and is published by permission of the Ministry of Defence (Procurement Executive), and the British Post Office.

serpentine domains. This static pattern has been compared with the strain contours demonstrated with X-rays. Secondly, an oscillatory A.C. bias field was applied to the samples and the resulting domain patterns observed. Geusic[4] has shown that this is a highly sensitive indicator of defects with impede bubble motion. Finally, translation mobility was measured in selected areas utilizing a pulsed uniform field gradient generated by two parallel wires with equal currents, after the technique of Cape[5]. This technique provides a direct measure of translational mobility, and is highly sensitive to defects and imperfections.

We have found that the relaxed domain patterns have shown that only in extreme cases of lattice parameter fluctuation in the substrate is the imperfection reflected in the domain pattern. This has been observed in one instance in a VPE Ga - YIG film. Strain induced anisotropy films of this formulation would be expected to be more prone to this type of problem due to the large variation of total anisotropy with lattice constant. Liquid phase samples have not, in general, shown this characteristic.

The AC bias field domain pattern clearly shows defects and pinning points. Fig. (5) shows the pinning points at residual surface microstrain and inclusions in the sample whose topographs are shown in Figs. 1, 2. This technique provides an excellent method of studying defects and reveals virtually all defects which impede propagation. It has become clear from the study that all localised regions of strain (inclusions, dislocations, etc.) which show in the topograph of the substrate will act as pinning points in the film. Detailed mobility measurements have been made in regions where mobility reduction might be expected and in "perfect" areas for comparison. In only one case has a drop in mobility been observed in an area corresponding with a structural defect in the substrate (in this case a facet) which appears perfect by optical examination. Topographs of the faceted region are shown in Figs. 3 and 4. The data from this set of measurements, Fig. 6, shows a clear mobility reduction in the faceted region.

CONCLUSION

The results of the correlation of magnet defects and topographic defects is shown in Table I. In general there is a one to one correspondence between localised defects in topographs (inclusions and dislocations) and magnetic pinning points.

In the case of general lattice strain, the situation is more complex. Slowly varying strains, such

In the case of liquid phase films, the lattice parameter of the films was 12.390 ± 0.001 so that it was possible to obtain topographs separately from film and substrate after growth. Figure 1 taken through an 8.0 μm thick film shows a substrate which has been Syton polished to remove surface damage. Residual strain, A, not detected optically can be clearly seen as can the dark images of inclusions, B, which form during the growth of the film. The uneven background results from gentle lattice strains associated with temperature fluctuations during growth of the substrate. As can be seen from the topograph of the film, fig. 2, the defects with the exception of the growth banding, appear also in the film. The loss of the small lattice parameter fluctuations ($\frac{\Delta d}{d} \sim 10^{-5}$) due to temperature cycling is however not surprising in view of the magnitude of the difference between the lattice parameters of the film and substrate.

Another crystal, shown in Fig. 3 before the film had been grown, illustrates more clearly the growth banding but in this case the periodicity is much greater although the strain is similar. In addition, two faceted regions can be observed. These result from growth on (211) planes and they are important because they have a slightly different lattice periodicity ($\frac{\Delta d}{d} \approx 10^{-4}$). A liquid phase film of the same composition to that above which was grown on this substrate also exhibit the core although the growth bands are again suppressed. Another important defect is the dislocation which has an extensive strain field. They are rarely found in good quality substrates due to their large energy of formation but when they occur they propagate directly into the film.

In the case of vapour phase films with strain induced anisotropy, the difference in lattice parameter between film and substrate must be rigorously controlled to generate the required anisotropy. A limited range of samples have been examined in which the lattice mismatch between film and substrate is small ($\Delta d < 0.007$Å) and it is found that all defects described above propagate into the film.

MAGNETIC STUDIES

The magnetic characteristics of the samples which were analysed topographically, have also been investigated. For these studies three techniques have been used. First the samples were annealed above the Curie point to produce the minimum energy configuration of the

THE EFFECT OF STRUCTURAL IMPERFECTIONS ON MAGNETIC PROPERTIES OF EPITAXIAL GARNET BUBBLE FILMS

A.D. Milne, J.M. Owens, B. Solomons and S.J. Thornley
University of Edinburgh, Edinburgh, Scotland.

ABSTRACT

X-ray topographic studies using the Berg-Barrett reflection technique have been made on $Gd_3Ga_5O_{12}$ substrates grown under various conditions. The crystals exhibit coring, faceted growth, growth banding, iridium inclusions and dislocations. Liquid and vapour phase films have been grown on these substrates and the films examined by reflection topography. In general the substrate defects propagate directly into the films, however the degree to which general lattice strain appears in the film depends both on film thickness and lattice parameter mismatch.

The epitaxial films have also been examined to study their bubble characteristics. Static relaxed domain patterns have been correlated with the substrate strain patterns. Dynamic measurements using AC field gradients on a DC biased sample to provide domain motion and point out defects have been correlated with substrate and film defects.

INTRODUCTION

Since the earliest realisation of magnetic bubble domain devices, people have been aware that a major factor controlling device performance is material perfection[1,2]. In the epitaxial magnetic garnet system, there are two ways in which imperfections can arise[3]. There can be discrete defects or strain gradients in the substrate material which propagate into the epitaxial film and there can be interfacial defects, such as inclusions which produce growth defects in the magnetic film. These different types of defects have been studied and their influence on the magnetic characteristics analysed.

DEFECT ANALYSIS

The crystal perfection of the substrates and films was assessed by reflection scanning Berg-Barrett topography using $MoK\alpha_1$ radiation and 16,16,16 reflections.

The substrates were nominally $Gd_3Ga_5O_{12}$ and had a lattice parameter of 12.382 $\pm$ 0.001. The films were either $Er_1Eu_2Ga_{.7}Fe_{4.3}O_{12}$ and grown by liquid phase epitaxy or Ga:YIG and grown from the vapour phase method.

Reprinted From

AIP Conference Proceedings

Number 10

Magnetism and Magnetic Materials - 1972

(18th Annual Conference-Denver)

New York 1973